DEGRADATION BEHAVIOR OF FIBER REINFORCED COMPOSITES IN WATER ENVIRONMENT

1994

Toru Mori

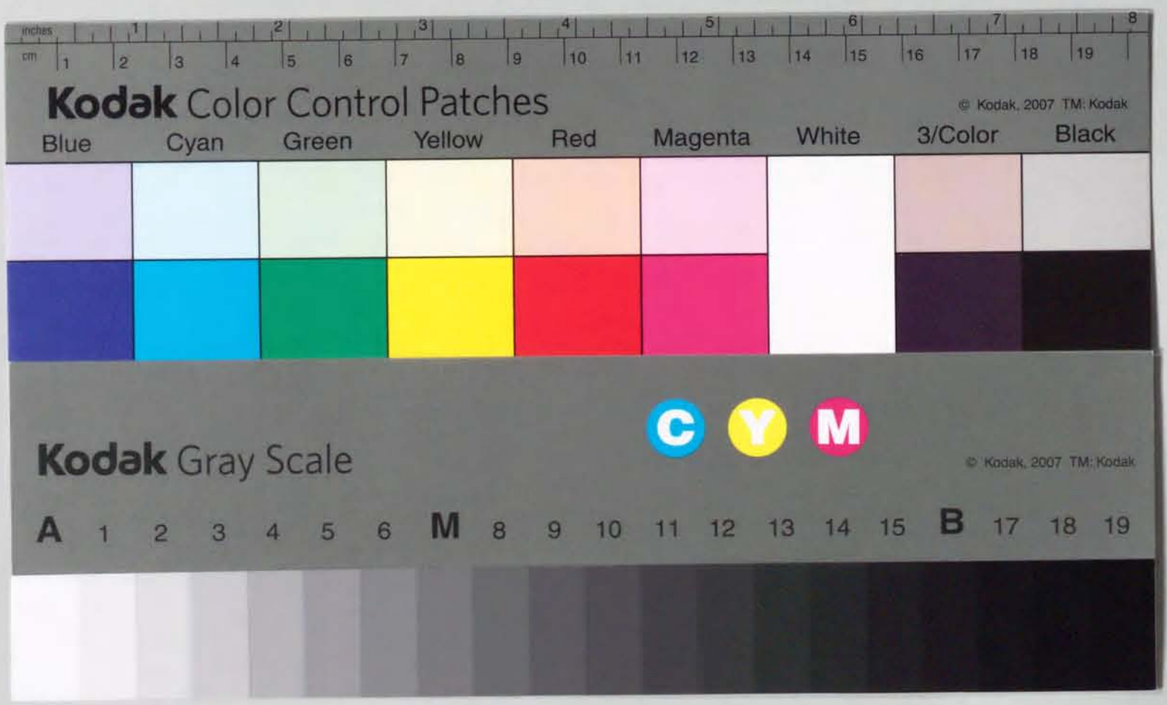

DEGRADATION BEHAVIOR OF FIBER REINFORCED COMPOSITES IN WATER ENVIRONMENT

1994

Tohru Morii

Contents

Chapter 1 Introduction

1.1 Composite Material

Composite material has been defined as the material that consists of two or more different materials, and that possesses the characteristic properties which never be obtained in the individual components.[1] Wood, bamboo and bone are listed as the natural composite materials, and metallic alloys, concrete, reinforced rubber and reinforced plastics are also listed as the composite materials for industrial applications. The definition of composite material for use in structural applications includes three main points as follows.[2]

(i) It consists of two or more physically distinct and mechanically separable materials.

(ii) It can be made by mixing the separate materials in such a way that the dispersion of one material in the other can be done in a controlled way to achieve optimum properties.

(iii) The properties are superior, and possibly unique in some specific respects, to the properties of the individual components.

The composite material in a narrow sense has been classified into particle dispersed composites and fiber reinforced composites by the reinforcing structure.[1] Moreover the fiber reinforced composites have been classified by matrices into fiber reinforced rubber (FRR), fiber reinforced plastics (FRP), fiber reinforced metal (FRM) and fiber reinforced ceramics (FRC). FRP among these is widely used as the structural material in various fields. Fibers as reinforcement have high modulus and strength, however, they are usually brittle. Plastics as matrix is ductile, however, they usually have excellent resistance to chemical (corrosive) environments. Therefore the material combining fibers and plastics has modulus and strength close to that of the fibers and chemical resistance of the plastics. Moreover the weight of FRP is very light, and so high specific modulus and specific strength can be obtained. The higher specific modulus and specific strength signify that the weight of structural components can be reduced. For this reason, FRP has been flourishingly applied to the aero- and astronautics fields, and it has been developing with the advancement of the aero- and astronautics technologies. As mentioned above, FRP has excellent corrosion resistance as well as high specific modulus and strength. Utilizing this advantage, FRP has been used as the structural components of shipping, boat, tank and vessel and as the housing and building materials. The demands of the composite materials in these fields keep on increasing in recent years. In FRP physical and chemical properties can be designed by optimum choices of matrices and reinforcing fibers. The reinforcing fibers mainly affect the mechanical properties, while the matrices do the corrosion resistance. At present, glass, carbon and aramid fibers have been used as reinforcing fibers, and due to the reinforcing fibers FRP has been classified into glass fiber reinforced plastics (GFRP), carbon fiber reinforced plastics (CFRP) and aramid fiber reinforced plastics (AFRP). Glass fiber is the first to be used as the reinforcement for FRP. Glass fiber has isotropic properties, and the effective bonding between glass fiber and matrix resin can be obtained. Moreover glass fiber has high specific modulus and strength although its cost is

comparatively low. Therefore it has been widely used in various fields. In recent years FRP with higher modulus and strength than GFRP has been in great demand, and so carbon fiber and aramid fiber have often been used as reinforcement. However, these fibers are much expensive than glass fiber, and therefore, the application of CFRP and AFRP is necessarily limited in the specified fields such as aeronautics, astronautics and sports equipments. On the other hand, glass fiber is generally used in large scale FRP structures because they require low cost materials due to the use of the material in quantities. In particular, GFRP is mainly used in the fields where the excellent corrosion resistant materials are demanded. Thus, GFRP is generally used as the structural components of shipping, boat, tank, vessel, housing and building.

1.2 Application of Fiber Reinforced Composites under Various Environment

Plastics have excellent water, chemical and weathering resistance in comparison with metal, and therefore, FRP also has this excellent resistance. In addition to this, FRP has high specific modulus and strength, and so FRP has been necessarily used as the structural materials in various corrosive environments. Table 1.1 lists the examples of the applications for FRP structures in corrosive environments. The building and housing materials require the weathering and water resistance, the shipping and boat do the water and alkaline resistance, and the industrial equipments do the chemical resistance. In addition, these products also require the ease of manufacturing and the flexibility of shape. From these viewpoints, FRP has widely spread by the replacement of traditional material, primarily metals. Especially, FRP water storage tanks and bath tubs have often been used in our daily life.

FRP water tanks have some advantages to metals that they are rustproof and completely hygienic and that their maintenance is very simple. The assembly of FRP water storage tanks is very simple because of the development of the prefabricated system. From these facts, FRP panels (compression molded and sheet molding compound (SMC) panels) have rapidly applied to the water storage tanks by the replacement of the steel panels. FRP water tanks are constructed by some small FRP panels as shown in Fig.1.1. Bath tubs are made of earthenware or wood for a long time. However, the earthenware is very brittle and the wood is currently very expensive. Therefore the replacement of the raw materials has ever been demanded, and then, the bath tubs have been usually made of FRP in recent years. FRP bath tubs are superior in the touch and the keeping warmth. The common features required in water tanks and bath tubs are the simple and short cycle molding process for mass product and the durability under hydrothermal environment for long life time. FRP on the basis of these requirements is generally made of glass fiber and unsaturated polyester resin. In water tanks and bath tubs, the physical properties must be isotropic. Therefore the orientation of the glass fiber must be random, and the randomly oriented glass fiber continuous or chopped strand mats are usually used as the reinforcement. The water tanks and bath tubs are generally fabricated by compression molding such as matched metal die (MMD) method and SMC. In MMD method, FRP panels are fabricated from the premix resin compound and randomly oriented continuous (or chopped) strand mat preformed in the mold. In

Table 1.1 FRP structures in corrosive environments and its requirements.

Examples	Requirements
Building & Housing Materisls	Weathering & Water Resistance
Water Storage Tank	Weathering, Water & Thermal Resistance
Chemical Container	Chemical Resistance
Shipping & Boat	Water & Alkaline resistance
Body Parts in Automobile	Weathering Resistance

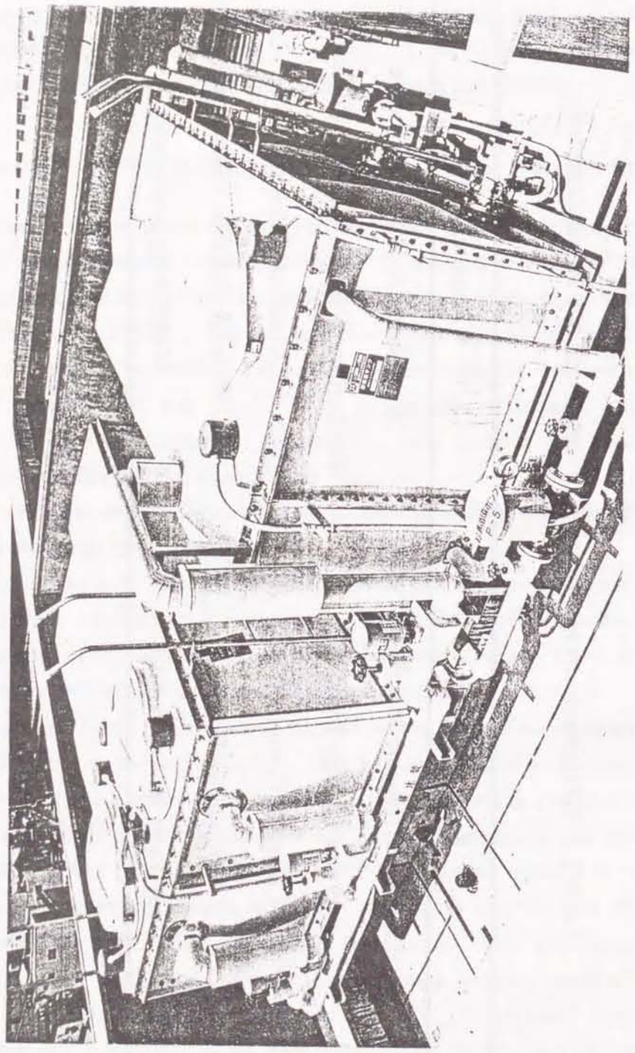

Fig.1.1 FRP water storage tank.

SMC, the chopped strand mat is impregnated with the resin in advance, which is led to the preformed sheet. These sheets are set in the mold, and then SMC panels are fabricated by compression with heating.

1.3 Degradation Problem on Fiber Reinforced Composites under Wet and Water Environment

The common principal problem in the water tanks and the bath tubs is the water and/or hydrothermal resistance of FRP. In particular, it is essential that the degradation of FRP due to water (or moisture) must be considered for the design of the structures and for the prediction of the life time. Therefore the environmental testing of FRP has been widely performed, and the degradation behavior and the life-time prediction have been discussed on the basis of the great amount of such test results. Here, the research works for the effects of moisture on the properties of FRP have bee reviewed.

The works on the effects of moisture on the various properties of FRP are classified into two groups; that is the works for the weight changes and those for the reduction of mechanical properties. The environmental tests are usually performed in water or in humid air. The water environment may be similar to the moist environment at relative humidity of 100%, however, the water environment may often be severer than the moist environment. Therefore, the degradation behavior under the respective environments may be different each other.

Springer et al. have widely studied the environmental effects on FRP.[3,4] They discussed both the moisture absorption and desorption processes[5-9] and the changes of various mechanical properties.[10-13] The moisture absorption kinetics in humid air and in liquids were discussed for unsaturated polyester and vinylester based SMC panels[8,12] and carbon fiber reinforced epoxy resin.[5,7] The moisture absorption kinetics were discussed on the basis of Fick's law. In other works, the weight changes were also discussed on the basis of Fick's law.[14-19] Fick's law is the established theory of diffusion. Fig.1.2 shows the typical Fickian diffusion behavior of carbon fiber reinforced epoxy resins immersed in distilled water. In this figure the moisture content is represented by the weight gain due to immersion in water. In Fickian diffusion, the moisture content increases linearly against the square root of exposure time at short immersion time, and gradually approaches a constant level. As a result, the moisture content reaches an equilibrium at long immersion time. Fig.1.3 shows the changes of the moisture content of SMC panels due to immersion in distilled water. At short immersion time the changes of the moisture content apparently indicate Fickian diffusion. However, the moisture content does not keep equilibrium, but decreases gradually at long immersion time. Such phenomenon never be considered in Fick's law. Loos et al. explained that such decrease of moisture content was caused as a result of the loss of resin particles from the developed microcracks owing to the moist, high temperature environment.[8] They called such weight changes as "non-Fickian". In this paper, however, the mechanism of loss of moisture content was never clarified well, and moreover the effect of the fiber/matrix interface was never considered in the discussion of the weight change mechanism. In

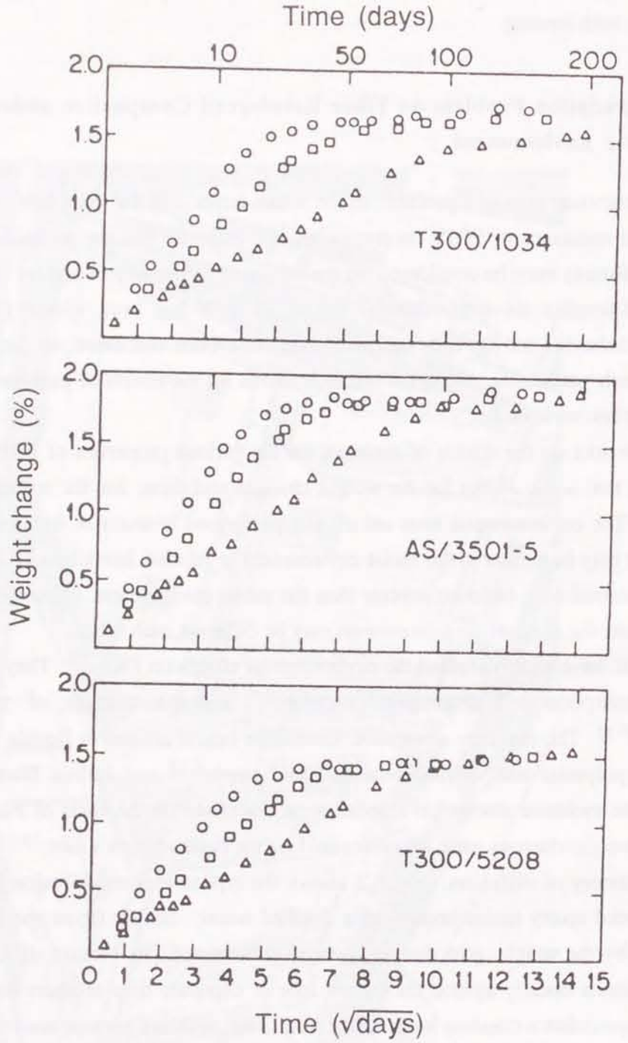

Fig.1.2 Weight changes of carbon fiber reinforced epoxy resins immersed in distilled water.[7]

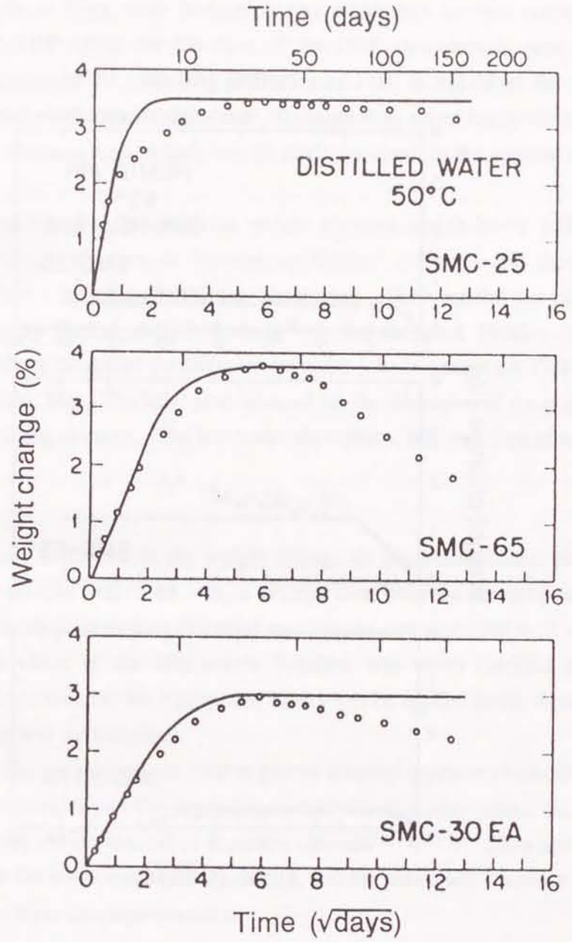

Fig.1.3 Weight changes of SMC panels immersed in distilled water.[8]

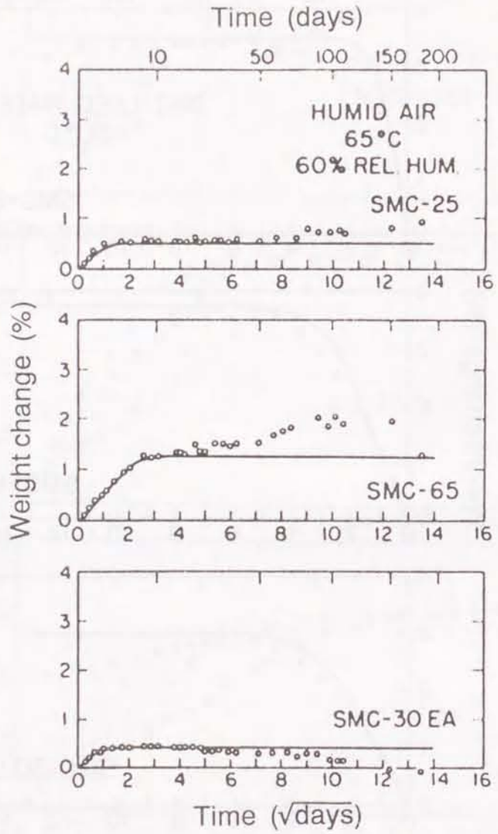

Fig.1.4 Weight changes of SMC panels exposed in humid air.[8]

addition, it is inadequate that the weight changes with the loss of the material are discussed on the basis of Fick's law. Fig.1.4 shows the changes of moisture content of SMC panels due to exposure in humid air. In this figure the moisture content increases again after once it reaches the equilibrium level. Also such phenomenon never be considered in Fick's law. This non-Fickian diffusion appears at long term immersion (or exposure) in wet environment. The long term properties of FRP affect the life time of the FRP structures in wet environment, and therefore, the evaluation of the long term properties of FRP is important for the safe design of FRP structures in wet environment. However, Springer et al. never clarified the mechanism of the long term property changes, and so their works made no sense in the application to the industrial fields.

Pritchard and Speake discussed the weight changes which never follow Fick's law.[20] They called such weight changes as "anomalous Fickian" diffusion and these weight changes included the remarkable increase of moisture absorption. They applied the diffusion theory for polymers proposed by Berens and Hopfenberg[21] to the abnormal Fickian diffusion for FRP. Berens and Hopfenberg classified the diffusion behavior into two stages; a Fickian term, M_F, and a resin relaxation term, M_R. The latter term allowed for the relaxation of the polymer matrix under the influence of swelling stresses. The true water absorption, M_t, was then given by:

$$M_t = M_F + M_R . \tag{1.1}$$

Pritchard and Speake expanded to the weight change of glass/unsaturated polyester laminates. Fig.1.5 shows the comparison of the weight change data between the proposed theory and the experiment. The theory proposed by Pritchard and Speake corresponded well to the experimental data, however, the effect of the fiber/matrix interface was never clarified also in this work. Therefore it is doubtful whether such proposed theory can be applied to the various weight change behaviors of FRP in wet environment.

The weight change behavior of FRP is greatly affected by the environmental condition such as temperature and humidity. The temperature and the humidity affect the rate of diffusion (diffusion coefficient) and the maximum moisture content.[14,15,22-24] Shen and Springer clarified the relation between the environmental humidity, ϕ, and the maximum moisture content, M_m, and the relation between them was represented as;

$$M_m = a\phi^b \tag{1.2}$$

where a and b were constants.[5] The weight change behavior was discussed for the various FRP which was different in matrices and in fibers.[7-9,12-19] Moreover the weight changes have been discussed for the damaged FRP owing to the stress rupture, the thermal spiking and the periodic exposure.[25-30]

The moisture diffusion behavior has often been evaluated analytically by Fick's law.[31-37] Most of these works dealt FRP as homogeneous isotropic material, and neglected the existence of the fiber in the matrix. The orientation dependence of the physical properties is determined by the configuration of the reinforcement, but FRP is essentially heterogeneous material because of the

combination of fiber and matrix. Kondo and Taki proposed the evaluation method of the weight change of unidirectional FRP by the sum of those for fiber and matrix which obeyed Fick's law, and theoretical results were compared with the experimental data.[38] The similar evaluation of weight change for glass-filled polyester was conducted by Janas and McCullough.[39] Moreover, Dewas and Favre, and Lee and Peppas theoretically analyzed the moisture diffusion by considering the composition of fiber and resin.[40,41]

In FRP the interface is necessarily produced between fiber and matrix. Especially in case of FRP containing filler, the interface is also produced between filler and matrix. As mentioned above, there are many works for the moisture diffusion of FRP in wet environment. Most of them, however, have never considered the effect of the interface between fiber and matrix on the diffusion behavior, and few have considered the existence of the fiber/matrix interface.[42,43] It has been reported that the fiber/matrix interface greatly affects the mechanical properties of FRP.[44-55] Therefore it can be easily supposed that the interface also affects the moisture diffusion behavior. Nevertheless the effect of the interface on the diffusion behavior never be clarified well. Then, it is currently essential to clarify the effect of the interface on the diffusion.

The mechanical properties of FRP have been also affected by the environmental exposure such as water and humid air. Therefore many works have studied the reduction of both the static and the dynamic properties. The reductions of the static properties, such as the tensile, bending and compressive moduli and strengths, have been measured after the exposure under water or wet environments, and the reduction mechanisms have been discussed.[10,11,56-66] For the dynamic properties, it has been discussed how the moisture affects the viscoelastic, the fatigue and the creep behaviors.[67-78] Moreover some works have attempted the predictions of the long-term properties under the various environments from the experimental data.[79-83] These works have dealt with the reduction behavior and the effect of components in FRP owing to the environmental exposure, however, they have never dealt phenomenologically with the reduction mechanisms in detail. The effects of fibers and matrices on the reduction of mechanical properties have ever been discussed by many researchers. Nevertheless the effects of the degradation of the fiber/matrix interface have been discussed by few researchers.[84,85] In addition, the qualitative or quantitative discussions have been scarcely done for the relations between the mechanical properties and the weight changes[10,11,20]. Pritchard and Speake attempted the prediction of the long-term properties using the following equation from the short-term experimental data[20]

$$p = a\left(1 - e^{-b\exp(-cM_t)}\right) + d \qquad (1.3)$$

where p was the residual property, M_t was the water absorption, and a, b, c and d were empirical constants. Eqn(1.3) was derived from the approximation of the experimental data, and the phenomenological discussion was not done for the reduction of the mechanical properties. Essentially, to predict the property changes during long-term exposure in water and wet environments requires the exact modeling of the degradation mechanism of FRP, and therefore, the degradation mechanism must be clarified in detail by the experimental observation and evaluation. In addition, the internal damage may be caused by the degradation due to

environmental exposure, and also this point must be considered in the prediction of property changes. The strength reduction due to environmental exposure may often be caused as a result of the changes of fracture process under loading. Therefore some works have evaluated the fracture process under the various loading conditions of aged FRP.[86] It is important to clarify the fracture process of aged FRP to predict precisely the long-term strength.

As mentioned above, many FRP structures such as water storage tanks have been used in wet and water environments. In case that FRP is used as the structural material, some FRP parts are joined. Typical joint structures are the mechanically fastened joints and the adhesive bonded joints. Especially, the mechanically fastened joints have advantages in the maintenance and the replacement to the adhesive bonded joints. In the mechanically fastened joints, some holes are required in joined parts. At the holes the reinforcing fibers are necessarily cut off, and as a result, the stress concentration occurs around the hole. Moreover, water may be absorbed from the edge of the holes, and then local degradation around a hole can occur. Then, the strength reduction in this region is induced. The fibers at the holes are directly exposed to the environments, and so the environmental effects at the holes are more rigorous than those at the other parts. Many works have discussed the strength of the mechanically fastened joints.[87-96] However, few works have clarified the environmental effects on the joint strength.[97,98] Therefore the environmental effects at the joined parts must be clarified for safe design of the FRP structures.

Thermosetting resins have been mainly used as the matrices of FRP until recently. In recent years, however, the disposal of the waste of fiber reinforced thermosettings becomes an issue since the reuse and the recycling of thermosetting composites are very difficult. From this view point, the thermoplastics have gotten much attention as the recyclable matrix resins for FRP. Thermoplastic matrices are normally used with short fiber reinforcement for applications in products made by injection molding. In general, short fiber reinforced thermoplastics have more excellent corrosion resistance but have poorer mechanical properties than thermosetting composites. In recent years, however, the applications of thermoplastic composites to the structural components have spread owing to the development of long fiber reinforced thermoplastics known as stampable sheet. Stampable sheet has been applied to the bumper of automobile. Moreover the applications of stampable sheet to the structural components under corrosive environments have been recently investigated, but there is few data for the property changes in corrosive environments.

1.4 Summary of Paper

As mentioned above, FRP is applied as the structural material in water environments. In particular, GFRP has raised the importance as the main component of the water storage tanks and the bath tubs. Therefore the degradation mechanism of GFRP in wet environment must be clarified to design the higher water resistant materials and structures than the conventional GFRP. From this view point, this paper deals with the degradation behavior and mechanisms of randomly oriented glass fiber mat reinforced plastics in hot water environment.

In Chapter 2, the weight change behavior is macroscopically discussed for FRP immersed in hot water. A new evaluation method for weight changes is proposed to clarify the weight change mechanism in water environment. This proposed method considers the weight loss which may be caused by the generated cracks, the dissolution, etc. Based on this evaluation method, a concept of the weight change mechanism is discussed and formulated theoretically. This proposed concept for weight change is applied to the experimental results of water immersion on randomly oriented glass fiber mat reinforced unsaturated polyester resins, and the weight change mechanisms of these materials are discussed by the proposed concept. In addition, the effect of water temperature on weight change behavior is also discussed.

In Chapter 3, the more detailed discussion is done for the weight change behavior of FRP in consideration of the influence of the interface between fiber and matrix. A quantitative evaluation method on the basis of the weight change measurement of FRP and its neat resin specimens is proposed for the weight changes of the fiber/matrix interface. This proposed evaluation method is applied to the weight changes of FRP in Chapter 2, and the weight change mechanism associated with the interface is clarified. Moreover, the weight loss behavior of FRP is discussed by the chemical analyses of the dissolved matters from glass fiber mat into the environmental water.

The weight changes investigated in Chapters 2 and 3 may often induce the reduction of mechanical properties. Therefore Chapter 4 deals with the changes of the elastic property of FRP immersed in hot water. The reduction process and mechanism of the elastic property of FRP in water are discussed from the relation between the weight changes and the elastic property. From the experimental results of the elastic property, the theoretical estimation method of the elastic moduli of the aged FRP is derived by introducing the damage mechanics.

In Chapter 5, the fracture mechanisms and the strength reductions are investigated for FRP immersed in hot water. The fracture process is clarified roughly by the relation between the weight changes and the strength, and the detailed discussion is done by introducing the acoustic emission (AE) measurement and the microscopic observation. From the experimental results, the estimation method of fracture mechanisms by AE characteristics is suggested, and it is applied to the damage estimation of the aged FRP.

FRP parts have been joined with other parts in case of the industrial application, especially in water tanks. Therefore, Chapter 6 deals with the degradation of mechanically fastened FRP joints immersed in hot water. The effects of water on the joint strength reduction and the failure modes are discussed for the joints with various joint geometries. The main cause of joint strength reductions is discussed from the tensile test results of notched specimen and the bearing test results. Utilizing these experimental results, the predictions of joint strength and failure mode are performed by introducing the finite element analyses. This prediction method is based on the macroscopic failure criterion and the characteristic length.

The material investigated in Chapter 2 to Chapter 6 is randomly oriented glass fiber continuous strand mat reinforced unsaturated polyester resins, which are thermosetting composites. On the other hand, the degradation behavior of thermoplastic composite immersed in

hot water is discussed from the various view points in Chapter 7. The material investigated is randomly oriented glass fiber continuous strand mat reinforced polypropylene. The property changes are discussed for the weight changes, the bending properties, and the strength and the failure mode of the mechanically fastened joints as same with those in Chapter 2 to Chapter 6.

At the end Chapter 8 puts together some conclusions derived from this paper. Moreover the concept is proposed for the material design in order to improve the water resistant.

Chapter 2 Weight Change Behavior of Glass Fiber Reinforced Plastics under Water Environment

2.1 Introduction

Fiber reinforced plastics (FRP) have often been used as water tanks on account of their excellent corrosion resistance. However, FRP degrades as a result of long-term exposure in wet environments. Therefore degradation behavior of FRP in wet environments has been widely studied. In particular, much of this work has dealt with the weight changes in wet environments. Most of the authors, however, have investigated the weight changes of FRP in humid air,[5,14-25], and a few studies have dealt with the weight changes in water.[7,8] In humid air, the weight changes are caused only by water absorption, and their mechanism has often been discussed on the basis of Fick's law. On the other hand, it has been reported that both water absorption and material loss are caused when FRP is immersed in water.[8] Water absorption induces the weight gain of FRP, while material loss induces the weight loss of FRP. Fick's law can be applied to the weight change due to only water absorption, and it cannot deal with the weight changes accompanied by the material loss. In previous works on weight changes of FRP immersed in water, however, the material loss has not been much mentioned and the weight change mechanism has been discussed with reference only to Fick's law. Then, the amount of absorbed water measured in these works must conclude to be inaccurate, and the mechanism of material loss has never been clarified. Therefore the weight change mechanism during long-term immersion must be discussed by introducing an appropriate evaluation method, which can evaluate both the weight gain and the weight loss behavior, in order to predict the long-term properties of FRP.

FRP is composed of fiber, resin, filler, etc., and it is microscopically regarded as a heterogeneous material. However, in most of works on weight changes FRP is macroscopically regarded as a homogeneous material. In the heterogeneous materials, boundaries exist between each components, and furthermore, some differences in boundary conditions of each components originate in case of contact with water. These facts lead to the complexity of weight changes in the heterogeneous materials such as diffusion which never obey Fick's law, material loss, etc.

This chapter proposes a new evaluation method for weight changes of FRP immersed in water. By this evaluation method, weight loss during water immersion is considered. Using this evaluation method, a concept of the weight change mechanism is discussed, and the weight change behavior is theoretically formulated. In addition, this concept is applied to the experimental results of water immersion on randomly oriented glass fiber mat reinforced unsaturated polyester resin, and the weight change mechanism of this material is discussed by the proposed concept.

2.2 Weight Change Evaluation

2.2.1 Weight change mechanism

The mathematical theory of diffusion[99] is based on the hypothesis that the rate of transfer of diffusing moisture through unit area of a section is proportional to the concentration gradient measured normal to the section, i.e.,

$$F = -D\frac{\partial c}{\partial x} \tag{2.1}$$

where F is the rate of transfer per unit area of section, c is the concentration of diffusing moisture, x is the space coordinate measured normal to the section, and D is called as the diffusion coefficient. The fundamental differential equation of diffusion is derived from eqn(2.1) as (see Fig.2.1);

$$\frac{\partial c}{\partial t} = D\frac{\partial^2 c}{\partial x^2}\,. \tag{2.2}$$

Expressions (2.1) and (2.2) are usually referred to as Fick's first and second laws of diffusion. If the initial and boundary conditions are

$$\begin{array}{lll} c = c_i & 0 < x < h & t \le 0 \\ c = c_0 & x = 0\,;\, x = h & t > 0 \\ c = c_{0\infty} & x < 0\,;\, x > h & t > 0 \end{array} \tag{2.3}$$

where h is the thickness of the material, t is the immersion time, c_i is the initial moisture concentration in the material, c_0 is the moisture concentration at the surface of the material and $c_{0\infty}$ is the moisture concentration around the material, the solution of eqn(2.2) is obtained as

$$\frac{c-c_i}{c_0-c_i} = 1-\frac{4}{\pi}\sum_{j=0}^{\infty}\frac{1}{(2j+1)}\sin\frac{(2j+1)\pi x}{h}\exp\left[-(2j+1)^2\pi^2\left(\frac{Dt}{h^2}\right)\right]. \tag{2.4}$$

By multiplying the integration of eqn(2.4) from 0 to h by the density of moisture (γ_w), the moisture content in the material (A_m) is given by

$$A_m = \gamma_w\int_0^h c\,dx. \tag{2.5}$$

Units of γ_w and A_m are "g/mm^3" and "g", respectively. Since the one-dimensional diffusion is assumed here, the lengths of the material in y- and z-direction are defined as unit length in three-dimensional coordinates. Under this assumption, A_m is represented as the weight of moisture in the material. On substituting for c from eqn(2.4) in eqn(2.5), the amount of moisture at time t ($A_m(t)$) is given by

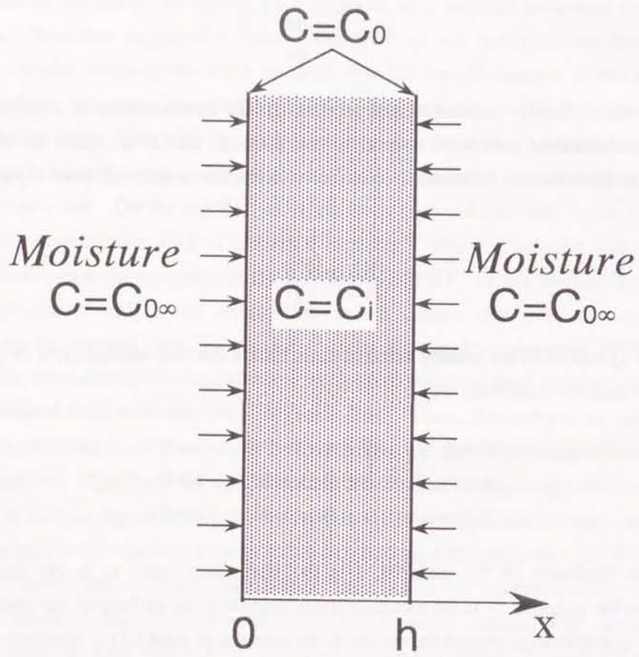

Fig.2.1 Boundary condition for moisture diffusion.

$$A_m(t) = \gamma_w \left[c_0 h - \frac{8h(c_0 - c_i)}{\pi^2} \sum_{j=0}^{\infty} \frac{\exp\left[-(2j+1)^2 \pi^2 \left(\frac{Dt}{h^2}\right)\right]}{(2j+1)^2} \right]. \tag{2.6}$$

From eqn(2.5) the initial amount of moisture ($A_m(0)$) and the amount of moisture at saturation ($A_m(\infty)$) are given by

$$\begin{aligned} A_m(0) &= \gamma_w c_i h \\ A_m(\infty) &= \gamma_w c_0 h \,. \end{aligned} \tag{2.7}$$

From eqns(2.6) and (2.7), the ratio of the amount of moisture at time t to that at saturation, G(t), is given by

$$G(t) = \frac{A_m(t) - A_m(0)}{A_m(\infty) - A_m(0)} = 1 - \frac{8}{\pi^2} \sum_{j=0}^{\infty} \frac{\exp\left[-(2j+1)^2 \pi^2 \left(\frac{Dt}{h^2}\right)\right]}{(2j+1)^2}. \tag{2.8}$$

Introducing the initial material weight W_i, the weight gain of the material by moisture diffusion, M(t), is expressed as

$$M(t) = \frac{A_m(t)}{W_i}. \tag{2.9}$$

Thus, G(t) is represented as

$$G(t) = \frac{A_m(t) - A_m(0)}{A_m(\infty) - A_m(0)} = \frac{M(t) - M(0)}{M(\infty) - M(0)} \tag{2.10}$$

where $M(\infty)$ is the weight gain at saturation and $M(0)$ is the initial weight gain. If $M(0)=0$, M(t) is derived from eqns(2.8) and (2.10) as

$$M(t) = M(\infty) \left[1 - \frac{8}{\pi^2} \sum_{j=0}^{\infty} \frac{\exp\left[-(2j+1)^2 \pi^2 \left(\frac{Dt}{h^2}\right)\right]}{(2j+1)^2} \right]. \tag{2.11}$$

Shen and Springer reported that eqn(2.11) might be approximated as the expression[5]

$$M(t) = M(\infty) \left[1 - \exp\left[-7.3 \left(\frac{Dt}{h^2}\right)^{0.75}\right] \right]. \tag{2.12}$$

Fig.2.2 displays the comparison between the diffusion curves obtained by eqns(2.11) and (2.12). The approximation curve by eqn(2.12) shows good agreement with the curve by eqn(2.11). Eqn(2.12) is also represented as

$$M(t) = M(\infty) \left[1 - \exp(-D_a t^{0.75}) \right] \tag{2.13}$$

where D_a is determined as the apparent diffusion coefficient given by

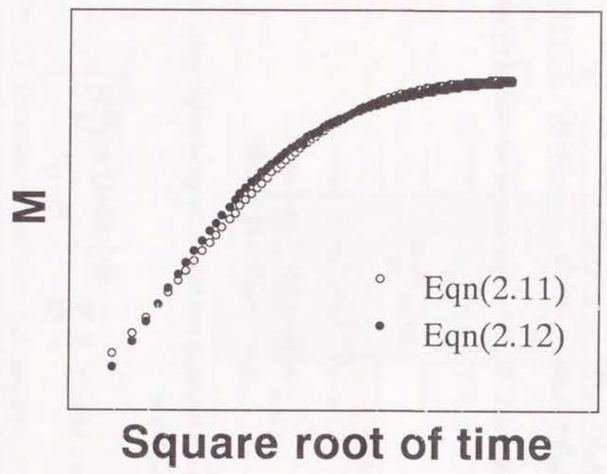

Fig.2.2 Comparison with the diffusion curves obtained by eqn(2.11) and eqn(2.12).

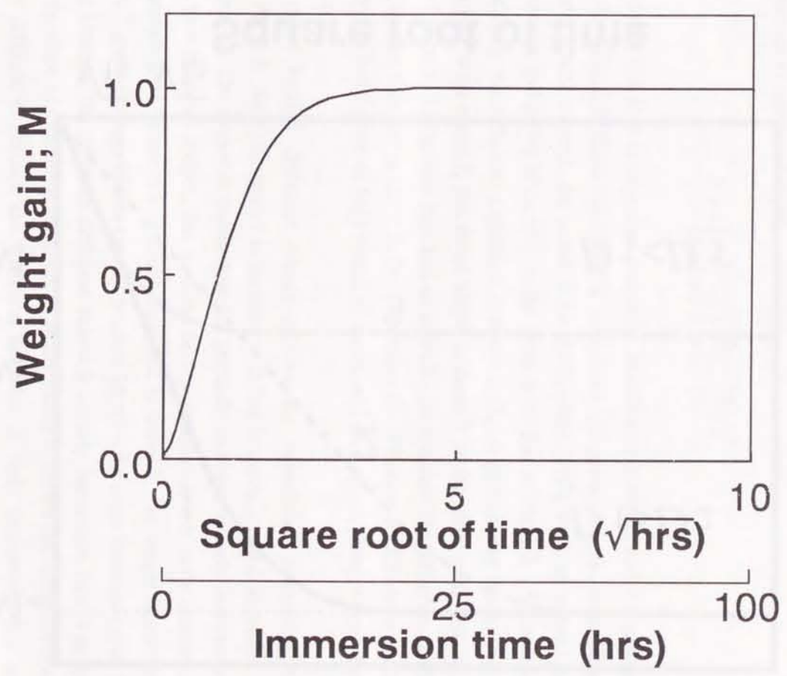

Fig.2.3 Weight gain curve obtained by eqn(2.12); M(∞)=1, D=5×10^{-2}mm^2/h and h=1mm.

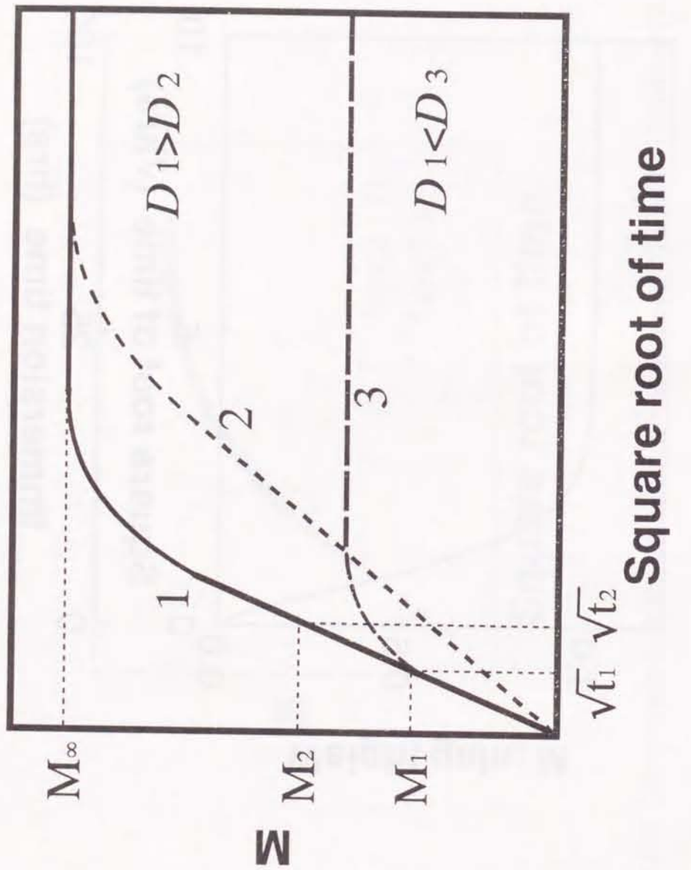

Fig.2.4 Fickian diffusion curves with different D and M(∞).

$$D_a = \frac{7.3^{4/3} D}{h^2}. \tag{2.14}$$

This equation is used as the approximated equation for experimentally measured weight gain. Fig.2.3 shows the weight gain curve obtained by substituting M(∞)=1, $D=5\times10^{-2}$mm²/h and h=1mm for eqn(2.12), and then D_a obtained is 0.772.

Fig.2.4 shows the various typical Fickian diffusion curves. In the typical Fickian diffusion curve, M(t) linearly increased against the square root of immersion time in early immersion time, and gradually reaches a saturation level. The diffusion coefficient D is obtained from the initial slope of M(t) versus √t curve and M(∞)

$$D = \pi\left(\frac{h}{4\,M(\infty)}\right)^2\left(\frac{M(t_2) - M(t_1)}{\sqrt{t_2} - \sqrt{t_1}}\right)^2. \tag{2.15}$$

The diffusion coefficient D is an important parameter in diffusion kinetics, and it characterizes the diffusion curve. Fig.2.4 illustrates various imaginary diffusion curves with different D. Comparing curve 1 with curve 2, the initial slope $((M(t_2)-M(t_1))/(\sqrt{t_2}-\sqrt{t_1}))$ of curve 1 is greater than that of curve 2, and M(∞) in curve 1 is the same with that in curve 2. Substituting these values for eqn(2.15), the diffusion coefficient in curve 1, D_1, is greater than that in curve 2, D_2. Comparing curve 1 with curve 3, the initial slope in curve 1 is the same with that in curve 3, however, M(∞) in curve 1 is greater than that in curve 3. In this case the diffusion coefficient in curve1, D_1, is smaller than that in curve 3, D_3. Therefore the diffusion coefficient is defined both by M(∞) and by the initial slope of M(t) versus √t curve, and as a result, these values characterize the diffusion curve.

Two typical Fickian diffusion curves against the logarithmic immersion time are represented in Fig.2.5. M(∞) in curve 1 is the same with that in curve 2, and D in curve1 is larger than that in curve 2. The slopes in curves 1 and 2 gradually increase in early immersion time as the immersion time becomes longer, that is, these curves are nonlinear in early immersion time. The rate of increasing M in curve 1 is faster than that in curve 2. In longer immersion time, however, curve 2 gradually approaches curve 1 because M(∞) is the same between curve 1 and 2. In the diffusion kinetics, the moisture diffusion behavior in early immersion time is an important problem since the slope of increasing M versus √t is necessary to define the diffusion coefficient. However, it is difficult to discuss the diffusion behavior in early immersion time using the diffusion curve versus logarithmic time as Fig.2.5 because of the nonlinearlity of the diffusion curve. The plots in Fig.2.5 are re-drawn against the square root of time in Fig.2.6. The diffusion curve versus √t indicates the linearity in early immersion time, and therefore it is easy to compare the material dependence of weight change behavior. Owing to this fact, the square root of immersion time is used as the time axis in this paper.

The weight gain due to water absorption is experimentally obtained by

$$M(t) = \frac{W_w(t) - W_i}{W_i} \tag{2.16}$$

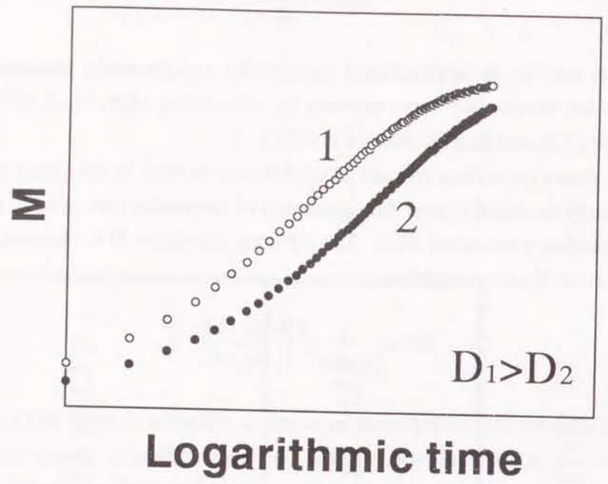

Fig.2.5 Fickian diffusion curves against the logarithmic immersion time.

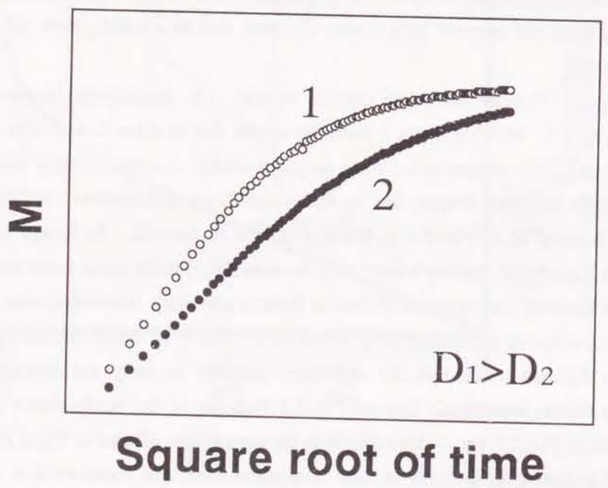

Fig.2.6 Fickian diffusion curves against the square root of immersion time.

where $W_w(t)$ is the weight of wet specimen (containing moisture) after immersion for time t. $W_w(t)$ is expressed as

$$W_w(t) = W_i + W_m(t). \tag{2.17}$$

where $W_m(t)$ is the weight of the absorbed water. Fig.2.7 is an example of the change of M for FRP induced by water immersion. Generally, the weight change behavior of homogeneous materials obeys Fickian diffusion as shown in Fig.2.4. In heterogeneous materials, however, there are some cases that the weight change behavior does not obey Fickian diffusion as shown in Fig.2.7, even if the weight changes of each component obey it. Thus, the weight change behavior of the heterogeneous materials is more complicated than that of the homogeneous ones. For example, in the heterogeneous material consisted of matrix containing fiber as imaginarily shown in Fig.2.8, only matrix comes in contact with water directly from the start of water immersion. On the other hand, contained fiber comes in contact with water after the matrix around the fiber absorbs water. As a result, the boundary conditions of each component are different, and it complicates the diffusion behavior inside the material. Delay of water absorption process between each component may occur as shown in Fig.2.8, and so the diffusion coefficient and maximum water absorption of the heterogeneous material may change during water immersion. More complicated problem in the heterogeneous materials may be the lack of some components associated from the crack generation in the material by water absorption.[8] This phenomenon may cause the loss of material weight as shown in Fig.2.7. Moreover new surfaces of the material are produced by such crack generation, and as a result, water can diffuse from the produced surfaces into the material. From these causes, there are some cases that the diffusion behavior of the heterogeneous material does not obey Fickian diffusion.

Under the consideration of the above-mentioned problems, net weight gain due to water absorption ($M_g(t)$) and weight loss ($M_l(t)$) after immersion for time t are proposed as the weight change parameter in this paper. $M_g(t)$ and $M_l(t)$ are given by

$$M_g(t) = \frac{W_w(t) - W_d(t)}{W_i}$$
$$M_l(t) = \frac{W_i - W_d(t)}{W_i} \tag{2.18}$$

where $W_d(t)$ is the weight of dried specimen after immersion. M(t) given by eqn(2.16) is treated as the apparent weight gain ($M_a(t)$). Relationship between these parameters are illustrated in Fig.2.9 and are expressed as

$$M_a(t) = M_g(t) - M_l(t). \tag{2.19}$$

The net weight gain and the weight loss for neat resin ($M_{gr}(t)$ and $M_{lr}(t)$) are also given by

$$M_{gr}(t) = \frac{W_{wr}(t) - W_{dr}(t)}{W_{ir}}$$
$$M_{lr}(t) = \frac{W_{ir} - W_{dr}(t)}{W_{ir}} \tag{2.20}$$

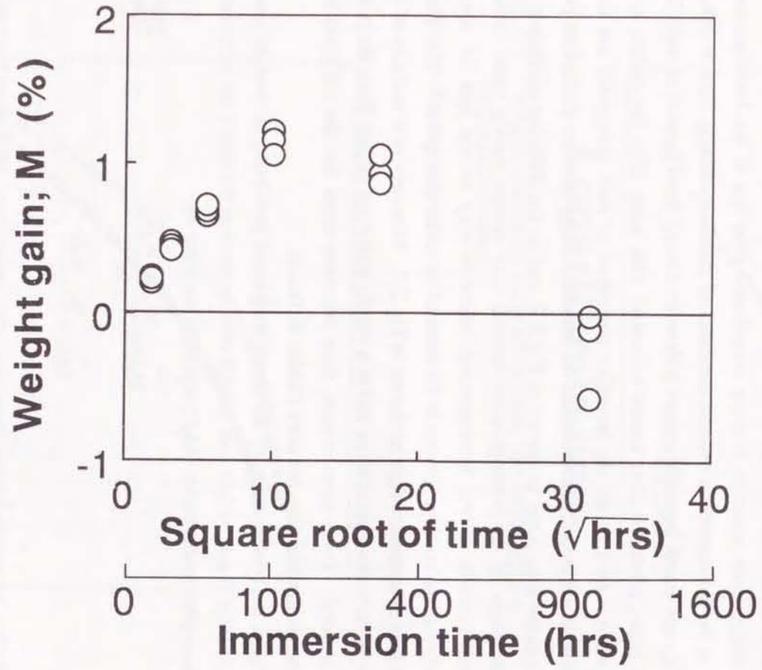

Fig.2.7 Change of M for FRP immersed in water.

- Randomly oriented fiber mat reinforced composite is composed of various kinds of mono-filament composites.
- The effect of intersection of fibers is neglected because of the simplification of the model.

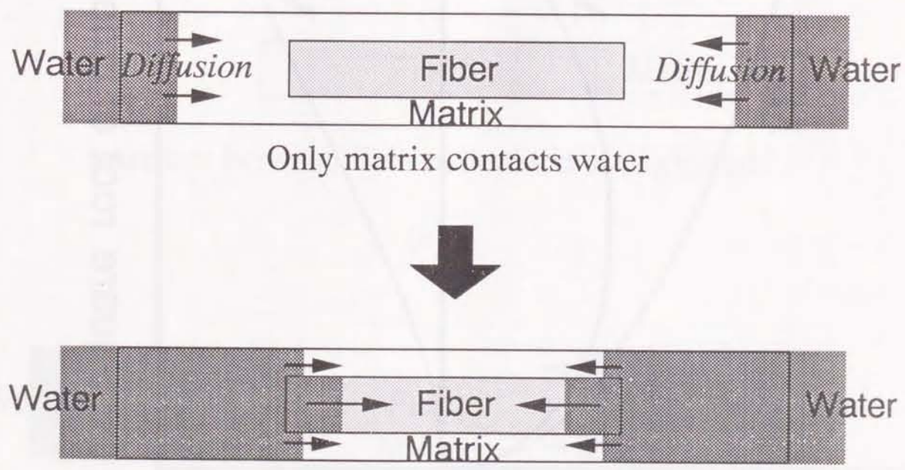

Fig.2.8 Water diffusion in imaginary heterogeneous material.

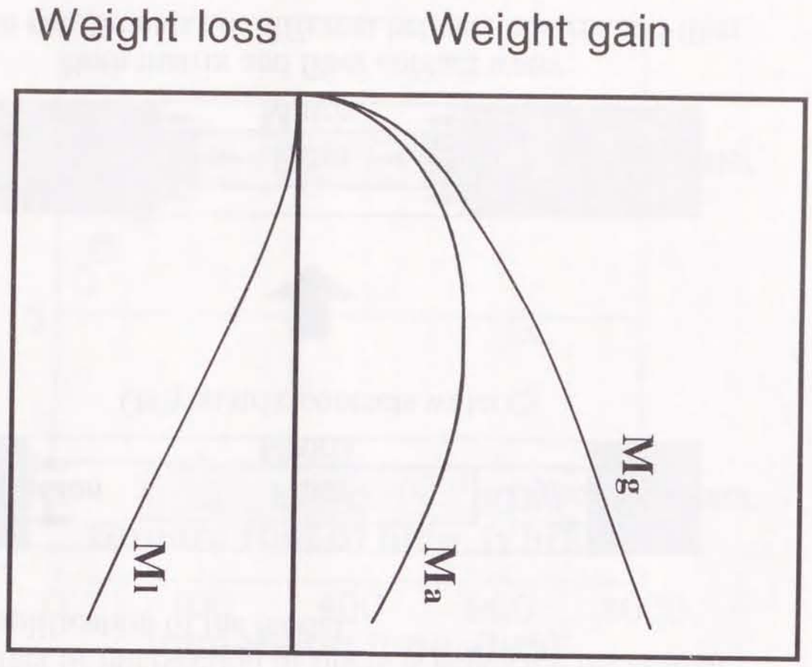

Fig.2.9 Schematic representation of M_a, M_g and M_l.

- Randomly oriented fiber mat reinforced composite is composed of various kinds of mono-filament composites.
- The effect of intersection of fibers is neglected because of the simplification of the model.

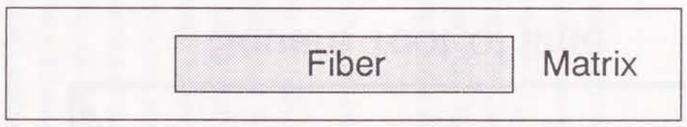

Interface between fiber and matrix is neglected.

(a)

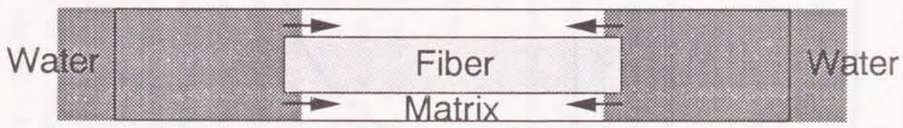

Water diffuses only in matrix.
Fiber never affect the weight changes of FRP.

(b)

Fig.2.10 Concept of weight change on resin part of ideal FRP; (a) ideal FRP model and (b) water absorption in ideal FRP.

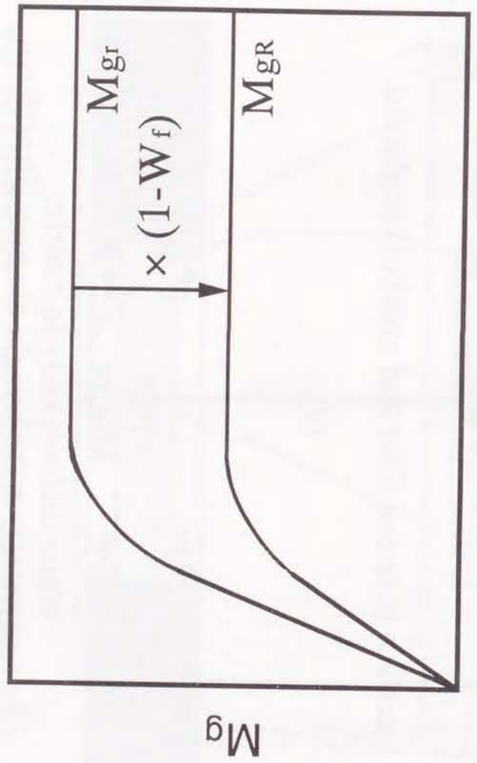

Fig.2.11 M_{gR} calculated from M_{gr}.

where W_{ir} is the weight of dry neat resin specimen before immersion and $W_{wr}(t)$ and $W_{dr}(t)$ are the weight of wet and dried neat resin specimen after immersion for time t. The weight changes of resin part of FRP are evaluated by use of the data of M_g, M_l, M_{gr} and M_{lr}. First, it is assumed that FRP is consisted of matrix resin and fiber as illustrated in Fig.2.10(a), and that the effects of interface between them never appear. In addition, it is assumed that the weight changes of FRP are consisted of the weight changes of only matrix resin and that the weight of fiber never change even after contact with water as illustrated in Fig.2.10(b). Under these assumptions, the net weight gain and the weight loss of resin part of FRP ($M_{gR}(t)$ and $M_{lR}(t)$) are obtained by (see Fig.2.11)

$$M_{gR}(t) = M_{gr}(t) \times (1 - W_f)$$
$$M_{lR}(t) = M_{lr}(t) \times (1 - W_f) \tag{2.21}$$

where W_f is fiber weight fraction in FRP.

Ideally the weight change of composite material should be the sum of the weight changes of each component. Then, eqn(2.21) may be the weight change of ideal FRP. Therefore the weight change mechanism of real FRP can be macroscopically evaluated by comparisons between M_g and M_{gR} and between M_l and M_{lR}. The macroscopic evaluation is essential to understand the outline of the weight change mechanism and to lead to the microscopic evaluation.

2.2.2 Classification of weight change mechanism

Fig.2.12 shows the typical weight change of neat resin due to water immersion. The changes of M_{gR} indicate typical Fickian diffusion and M_{lR} never be caused. On the other hand, the weight change of FRP is very complicated as shown in Fig.2.13. Within a short immersion time, M_g increases linearly against the square root of immersion time and reaches soon the first saturation. After a certain time, however, M_g starts to increase again and such restart time of M_g corresponds to the initiation of M_l. Based on the comparison between Figs.2.12 and 13, the weight change of FRP can be classified into three phases as illustrated in Fig.2.14. In phase I, the weight gain is due to the water mainly absorbed in the resin part, so that M_g reaches the saturation. The changes of M_g and M_{gR} indicate the same tendency since the weight loss also never be caused in FRP. In the following phase II, M_g continuously keeps saturation level and M_l never occurs. Therefore phase I and II are classified by the saturation of M_g (M_{gR}). The increase of M_l accompanied with the second increase of M_g occurs in phase III. As a result, the diffusion coefficient and the saturation level of M_g in phase III differ from those in phase I. Phase II and III are classified by the occurrence of M_l. The periods of phase I, II and III are different by materials and environmental conditions. Accordingly the weight change mechanism of various FRP's can be clarified by the macroscopic evaluation including the proposed phase classification.

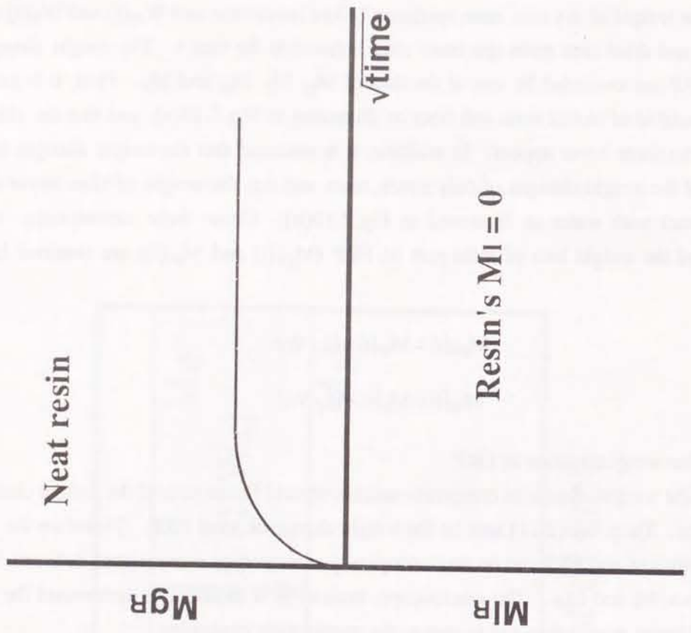

Fig.2.13 Typical weight change of FRP due to water immersion.

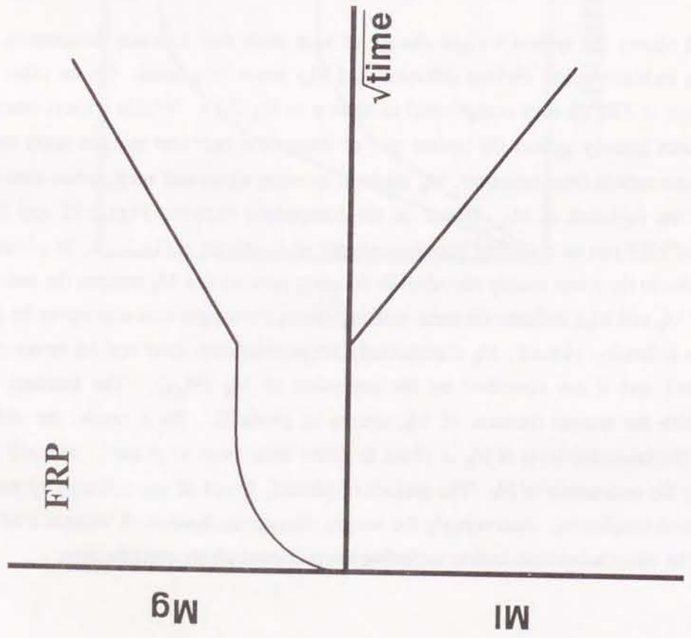

Fig.2.12 Typical weight change of neat resin due to water immersion.

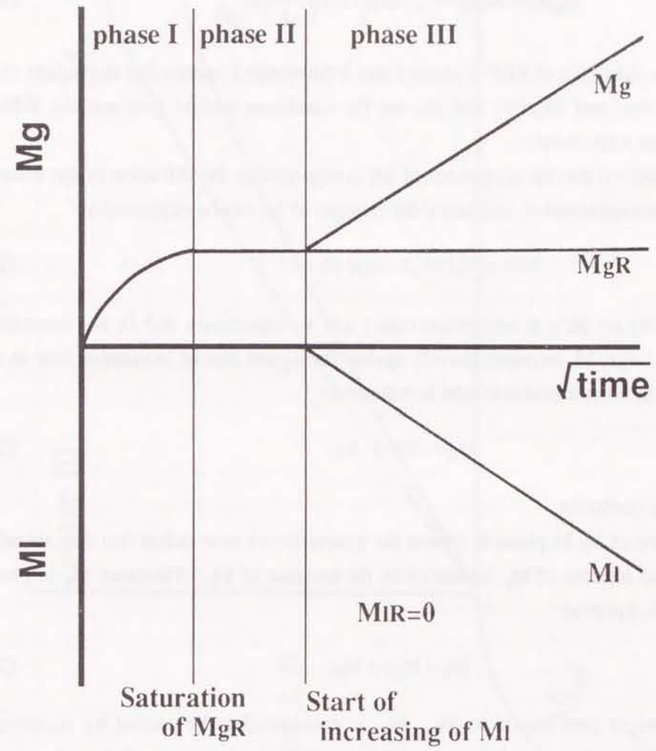

Fig.2.14 Classification into three phases of weight change of FRP.

2.2.3 Formulation of weight change mechanism

In this section, the formulation is attempted for the weight change mechanism proposed above.

The changes of M_g and M_{gR} are the same in phase I and II, and the change of M_g in phase I and II is obtained from the data of M_{gR} and eqn(2.12) is rewritten to

$$M_{gF}(t) = M_{gR}(\infty)\left[1 - \exp\left\{-7.3\left(\frac{D_R\, t}{h^2}\right)^{0.75}\right\}\right] \tag{2.22}$$

where $M_{gF}(t)$ is the weight gain of FRP in phase I and II (subscript F means that the weight change obeys Fickian diffusion) and $M_{gR}(\infty)$ and D_R are the maximum weight gain and the diffusion coefficient in resin part respectively.

It can be considered that the occurrence of M_l is regarded as the diffusion of the dissolved matter into the environmental water, and hence the changes of M_l can be expressed as

$$M_l(t) = M_l(\infty)\left\{1 - \exp(-D_l\, t)^{0.75}\right\} \tag{2.23}$$

where $M_l(t)$ and $M_l(\infty)$ are M_l's at immersion time t and ∞ respectively and D_l is a constant. If $M_l(\infty)$ is remarkably large, M_l increases linearly against the square root of immersion time in short immersion time. M_l in short immersion time is reduced to

$$M_l(t) = D_S\sqrt{t} - M_C \tag{2.24}$$

where D_S and M_C are constants.

The occurrence of M_l in phase III means the generation of new defect that can absorb the water since the second increase of M_g is induced by the increase of M_l. Therefore M_g in phase III is given by the simple equation

$$M_g = M_{gF} + M_{gl} \tag{2.25}$$

where M_{gl} is the weight gain related to M_l. M_{gl} is considered to be caused by replacing the dissolved matter by the environmental water, and this phenomenon is expressed as

$$M_{gl} = M_l \times \frac{\gamma_w}{\gamma_d} \tag{2.26}$$

where γ_w and γ_d are the densities of the water and the dissolved matter. Consequently the changes of M_{gl} indicate the same tendency with those of M_l as shown in Fig.2.15.

Dissolution from FRP into water starts to occur in phase III. The period until reaching phase III is considered to be the time when the dissolved matter starts to diffuse into water, and this time is determined as the "delay time of M_l". The delay time of M_l, t_0, is obtained by substituting M_l=0 for eqn(2.24) and is reduced to

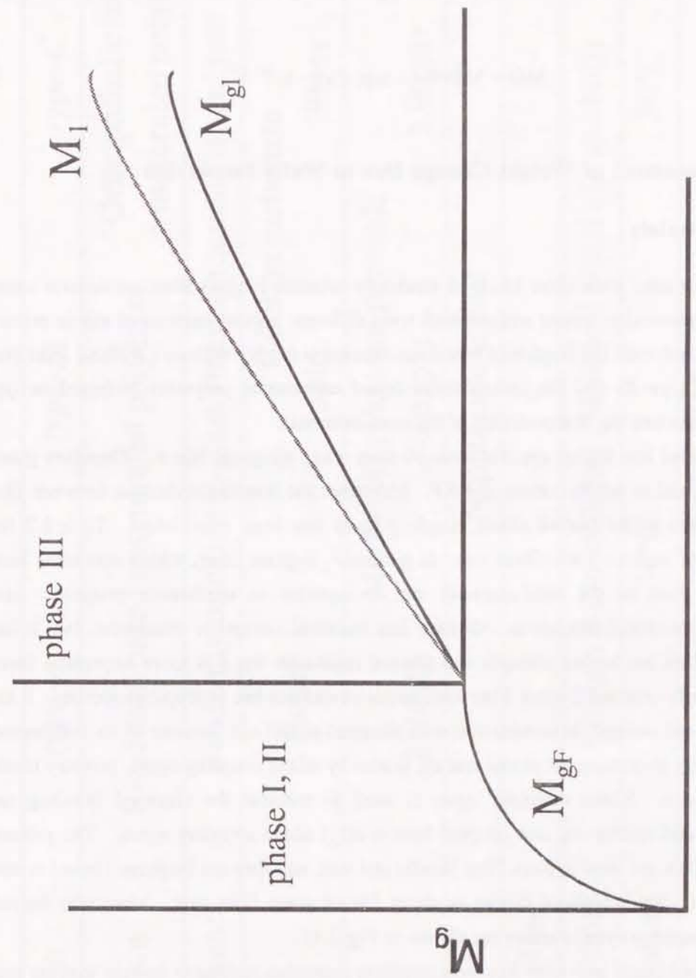

Fig.2.15 Changes of M_l and M_{gl}.

$$t_0 = \left(\frac{Mc_i}{D_S}\right)^2 . \tag{2.27}$$

In other words, the delay time of M_i is determined as the time when the water diffuses into FRP and it produces the dissolved matter. Introducing the delay time of M_i eqn(2.23) is re-expressed as

$$M_i(t) = M_i(\infty)\left[1 - \exp\{-D_i (t - t_0)\}^{0.75}\right]. \tag{2.28}$$

2.3 Measurement of Weight Change Due to Water Immersion

2.3.1 Materials

Materials used were three kinds of randomly oriented E-glass fiber continuous strand mat reinforced unsaturated polyester resins which were different in compositions of matrix resins. The matrix resins used were the bisphenol based unsaturated polyester with and without filler (referred as *type-A* and *type-B*) and the orthophthalic based unsaturated polyester (referred as *type-C*). Table 2.1 summarizes the compositions of the used materials.

Glass fiber has higher specific strength than other inorganic fibers. Therefore glass fiber has ever been used as reinforcement in FRP. Moreover the bonding technique between fiber and matrix resin such as the use of silane coupling agent has been established. Table 2.2 lists the compositions of various glass fibers used in general.[2] E-glass fiber, which was used here, is a popular fiber used as the reinforcement and is superior in mechanical property, corrosion resistance and electrical insulation. C-glass has excellent corrosion resistance, but it has low strength. S-glass has higher strength and thermal resistance but it is more expensive than other glass. Randomly oriented E-glass fiber continuous strand mat has isotropic properties. It also has high modulus and strength in comparison with chopped strand mat because of its continuous long fiber. The fibers in continuous strand mat are coated by silane coupling agent, primary binder and secondary binder. Silane coupling agent is used to enhance the chemical bonding strength between fiber and matrix and that adopted here is acryl silane coupling agent. The primary and secondary binders are used to form fiber bundle and mat, and they are bisphenol based unsaturated polyester resin. The weight of binder is about 3% of glass fiber mat. Molecular formulae of various unsaturated polyester resins are shown in Fig.2.16.

Bisphenol based polyester has most excellent corrosion resistance among various polyester resins since the concentration of ester group, which can hydrolyze easily in water environment, is very low.[100] Orthophthalic based polyester is general purpose polyester resins and can be resisted under water environment below about 60°C. *Type-A* and *type-B* were different in the presence of filler. *Type-B* contained 15phr calcium carbonate as the filler while *type-A* did not. Filler is used to reduce the cost and to modify some properties of FRP. In particular, containing calcium carbonate improves the rigidity, the shading and flow property during compression molding.

Table 2.1 Compositions of used materials.

Specimen	*type-A*	*type-B*	*type-C*
Matrix resin	Bisphenol based unsaturated polyester		Orthophthalic based unsaturated polyester
Reinforcement	Randomly oriented E-glass fiber continuous strand mat		
Filler	None	Calcium carbonate 15phr	Calcium carbonate 30phr
Catalyst	Methyl ethyl ketone peroxide 0.74phr	Methyl ethyl ketone peroxide 0.65phr	Methyl ethyl ketone peroxide 1.00phr
Accelerator	Naphthenic cobalt		
Number of plies	4		
Molding method	Compression molding (Matched metal die method)		
Mold temperature	70°C		80°C
Molding pressure	2MPa		
Molding time	360s		

Table 2.2 Components of various glass fibers.

Component	E-glass	C-glass	S-glass
SiO_2	55.2	65.0	65.0
Al_2O_3	14.8	4.0	25.0
B_2O_3	7.3	5.0	—
MgO	3.3	3.0	10.0
CaO	18.7	14.0	—
Na_2O	0.3	8.5	—
K_2O	0.2	—	—
Fe_2O_3	0.3	0.3	—
F_2	0.3	—	—
Tensile strength (MPa)	3626	3038	4214
Tensile modulus (GPa)	75.46	72.52	86.24

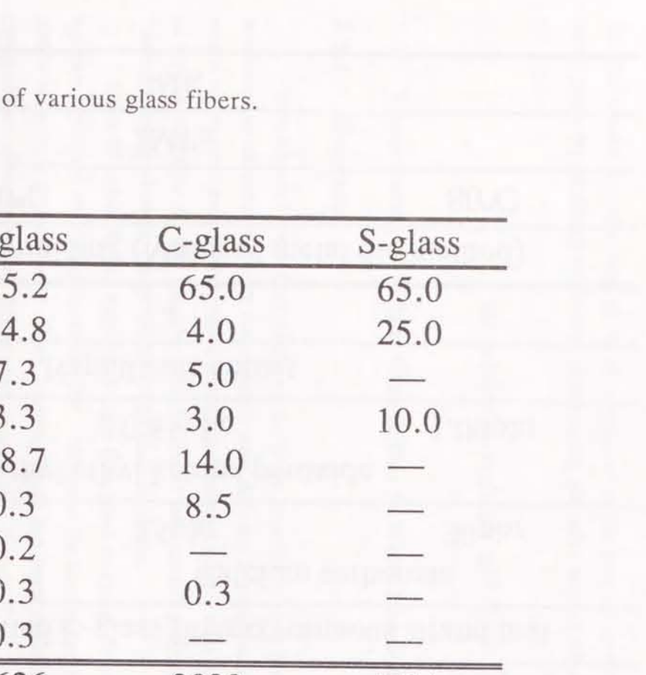

Bisphenol based unsaturated polyester resin

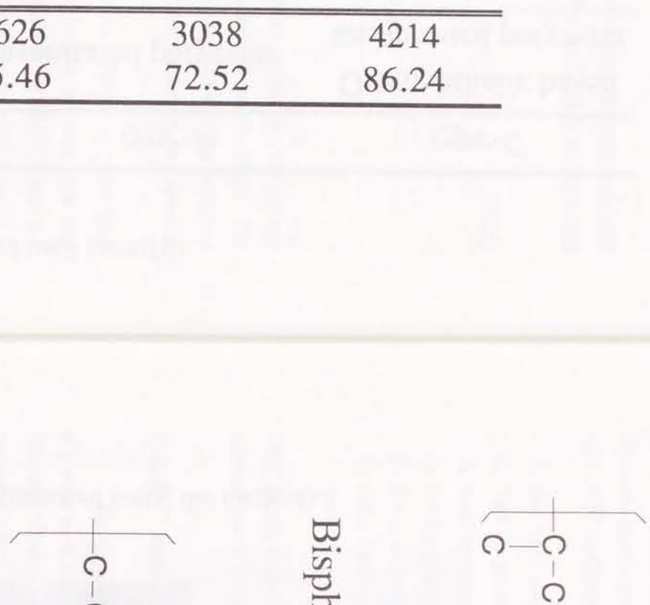

Orthophthalic based unsaturated polyester resin

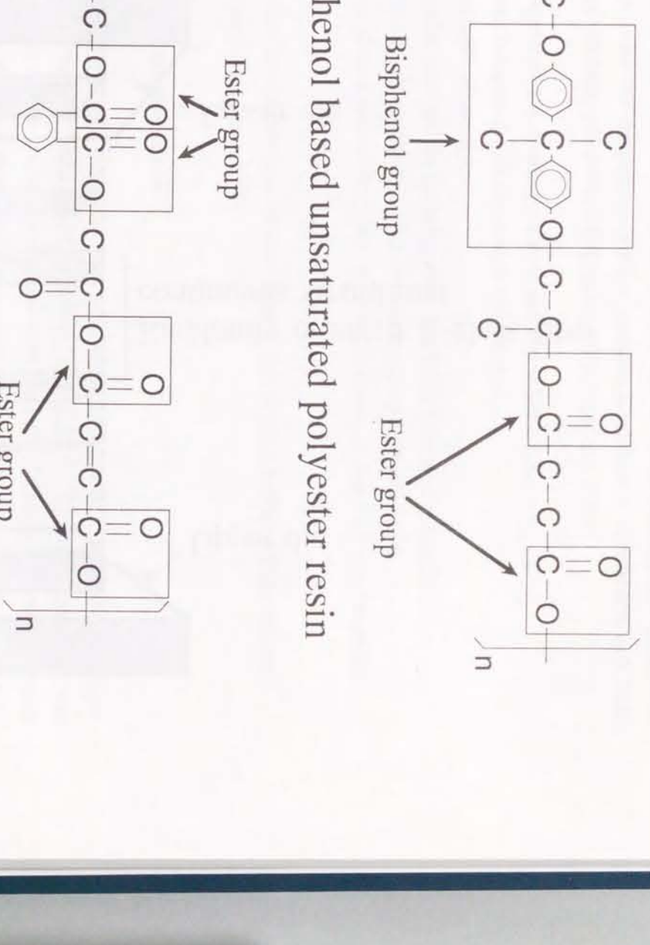

Isophthalic based unsaturated polyester resin

Fig.2.16 Molecular formulae of various unsaturated polyester resins.

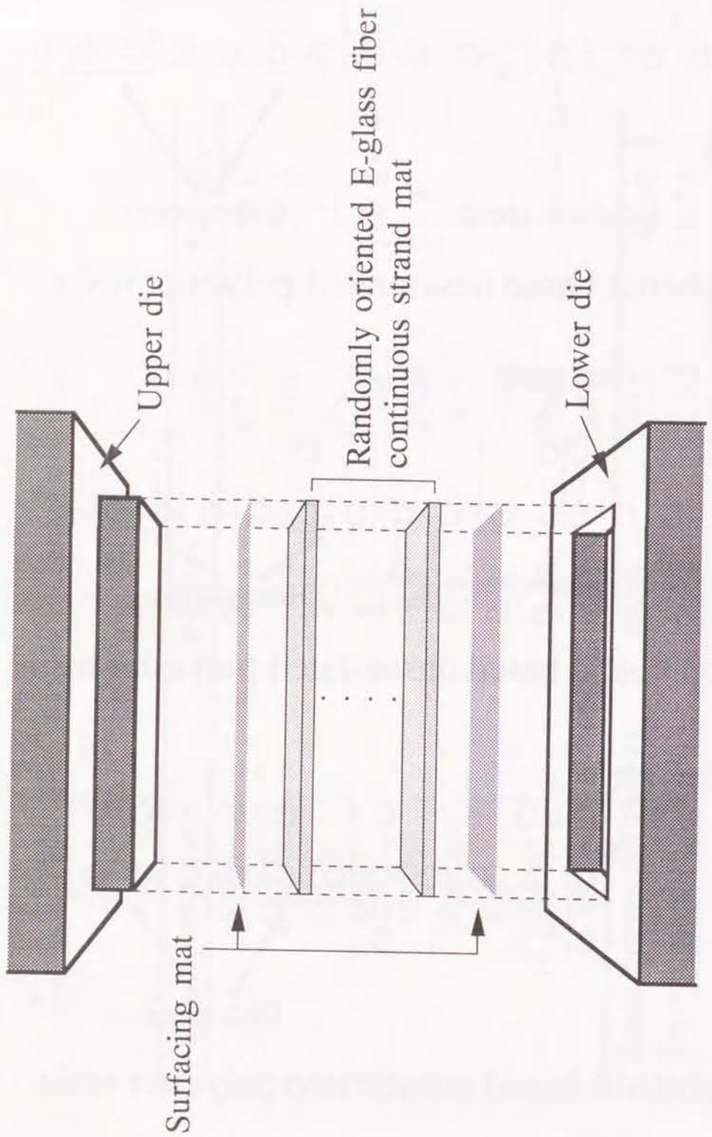

Fig.2.17 Compression molding (matched metal die method).

Using above materials 300mm square panels were fabricated by a compression molding (matched metal die method; MMD). Premix compound is used, and in MMD molding it is possible to fabricate moldings under low temperature and low pressure conditions in comparison with SMC and BMC molding. Molding process by MMD method is summarized below.

1. Set mold temperature and molding pressure as listed in Table 2.1.
2. Mix the premix compound with the catalyst and stir well.
3. Coat the mold with release agent.
4. Set the glass fiber mats and the surfacing mats in mold as illustrated in Fig.2.17.
5. Press at the fixed molding pressure after pouring the compound into mold.
6. After the lapse of the fixed molding time, open the mold and release FRP panel from the mold.

FRP panels were fabricated under the same condition by this molding method. Fiber volume content for all the panels was about 35%.

2.3.2 Experimental procedure

The immersion tests in distilled water were conducted at 60 and 80°C (only 80°C for *type-C*) with temperature controlled water baths as shown in Fig.2.18. Specimen geometry was 50mm × 50mm × 3.8mm and the specimens were cut from the molded panels. Before immersion in water, all specimens were completely dried in a vacuum oven (DP32, Yamato Scientific Co., Ltd.), after which the weight of dry specimen (W_i) was measured. After that specimens were immersed in hot water. The periods of immersion were 3, 5, 10, 30, 100, 300, 1000 and 3000h. After the immersion for the fixed periods, the weight of wet specimen (W_w) was measured. Then the specimens were re-dried in vacuum oven and the weight of re-dried specimen (W_d) was measured. Simultaneously the neat resin specimens were immersed, and the weight changes were evaluated in the same way as those in FRP to clarify the weight change mechanism of FRP. The periods of immersion for neat resin specimens were 3, 10, 30, 100, 300 and 1000h.

The exposure tests in humid air were also conducted for *type-A* and *type-B* in order to discuss the effect of environmental condition on the weight change behavior. The exposure tests were conducted in humid air (80°C in temperature and 95% in humidity) with environmental chamber (IG-46H, Yamato Scientific Co., Ltd.). The weight changes were evaluated in the same way as those in water. The periods of exposure were 3, 5, 10, 30, 50, 100, 500 and 1000h.

2.3.3 Experimental results

Changes of the apparent weight gain, M_a, with the square root of immersion time are shown in Fig.2.19. For short immersion times M_a increased linearly against the square root of immersion time, and kept increasing up to 100h for all the specimens. The variations in M_a, however, were different from typical Fickian diffusion behavior. After 100h, M_a in *type-A* kept

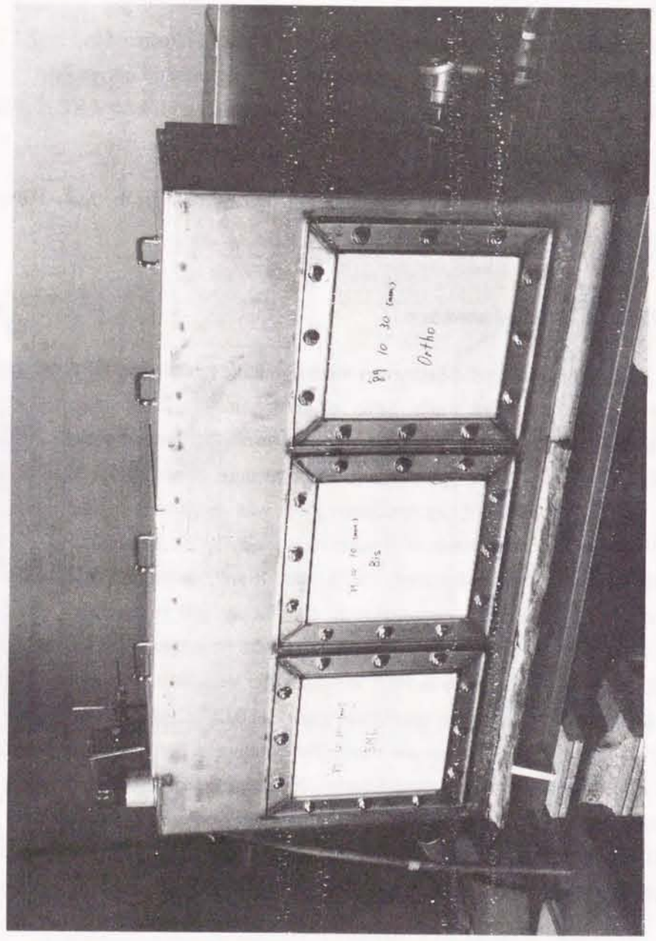

Fig.2.18 Instrument for water immersion.

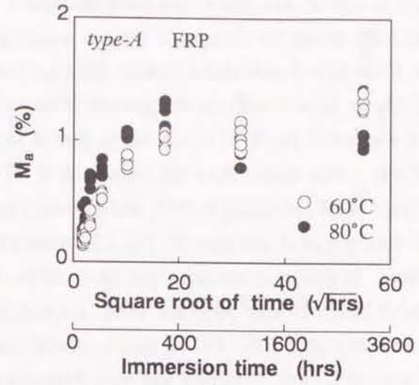

(a)

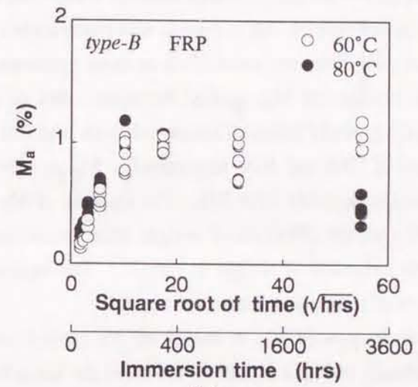

(b)

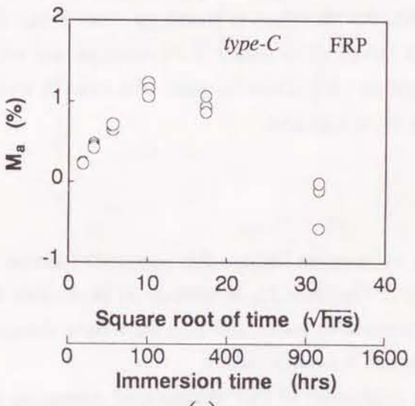

(c)

Fig.2.19 Changes of M_a with the square root of immersion time; (a) *type-A*, (b) *type-B* and (c) *type-C*.

almost constant, while M_a's in *type-B* and *type-C* gradually decreased. In *type-C* M_a at 1000h indicated minus value. Fig.2.20 shows the changes of the net weight gain, M_g, with immersion time. At 80°C M_g for *type-A* and *type-B* indicated a Fickian diffusion before 100h, and after 100h it increased again. At 60°C M_g for *type-A* and *type-B* approached saturation at 300h and after that increased again in the same manner as the 80°C case. M_g in *type-A* indicated the same tendency with *type-B* at 60°C, and it was a little higher than that on *type-B* at 80°C at all immersion times. On the other hand, M_g in *type-C* kept increasing to 300h and gradually approached saturation. M_g was much higher in *type-C* than in *type-A* and *type-B*. Fig.2.21 shows the changes of the weight loss, M_l, with immersion time. In a short immersion time, M_l could be regarded as 0. M_l at 60°C and 80°C in *type-A* and *type-B* increased after 300h and 100h, respectively. In the same manner, M_l in *type-C* increased remarkably after 10h. For all specimens the increases of M_l were linear against the square root of immersion time. In *type-A* and *type-B* the slope of M_l against the square root of immersion time was almost the same, independent of water temperature. The slope of M_l in *type-B* was higher than that of *type-A*. M_l in *type-C* was much higher than in *type-A* and *type-B*, and eventually it reached three times the value of M_l in those materials.

Fig.2.22 shows the changes of M_{gr} against the square root of immersion time. M_{gr} in *type-A* and *type-B* indicated a typical Fickian diffusion behavior and that at 60°C and 80°C almost saturated at immersion times of 100h and 30h, respectively. M_{gr} in *type-C* approached saturation at 30h, however, it increased remarkably after 30h. The changes of M_{lr} with immersion time are shown in Fig.2.23. There was no reduction of weight after immersion in *type-A* and *type-B*, while there was remarkable reduction of weight in *type-C*. The increase of M_{lr} in *type-C* was linear against the square root of immersion time.

Fig.2.24 shows the changes of M_g in humid air for *type-A* and *type-B* compared with those in hot water. The changes of M_g in humid air indicated the same behavior with those in hot water. Changes of M_l in humid with immersion time are shown in Fig.2.25. M_l in *type-A* increased linearly after 100h, but M_l values in humid air were lower than those in water. The changes of M_l in *type-B* in humid air increased in the same manner with those in hot water. In *type-B*, M_l's values in humid air were almost the same with those in water, and the environmental effect on the changes of M_l never appeared.

2.4 Discussion

The changes of M_a are complex because this parameter includes weight gain due to water absorption and weight loss. Therefore M_a is unlikely to be suitable for estimating the weight change behavior of FRP immersed in water, and then the weight change behavior is discussed in detail by the net weight gain and the weight loss.

The weight change mechanism of FRP is discussed comparing the weight change data of FRP and neat resin. The weight change data in Figs.2.20 and 21 were approximated in reference to eqns(2.13) and (2.24). M_{gR} and M_{lR} data obtained from M_{gr} and M_{lr} shown in Figs.2.22 and 23 were approximated in the same manner with M_g and M_l. For *type-A* and *type-B* at 60°C, M_{gR}

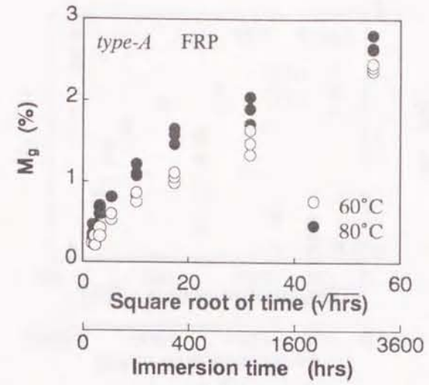

Fig.2.20 Changes of M_g with the square root of immersion time; (a) *type-A*, (b) *type-B* and (c) *type-C*.

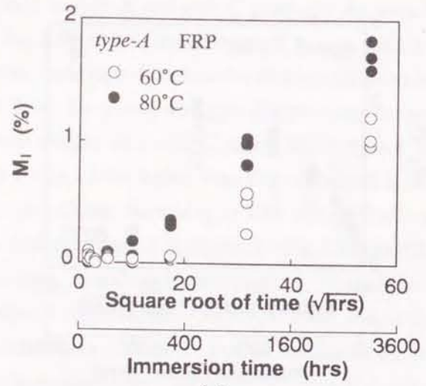

(a)

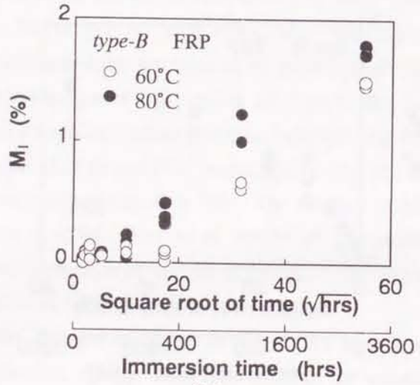

(b)

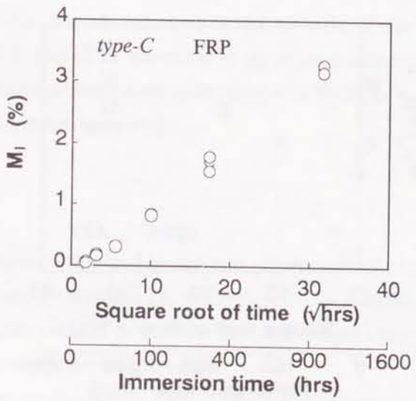

(c)

Fig.2.21 Changes of M_l with the square root of immersion time; (a) *type-A*, (b) *type-B* and (c) *type-C*.

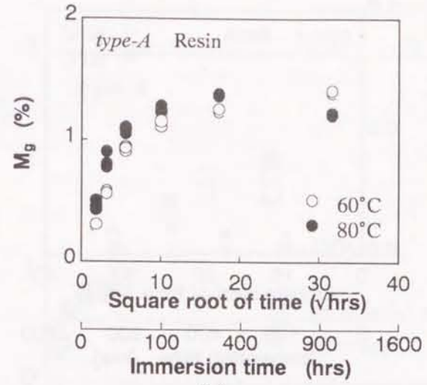

(a)

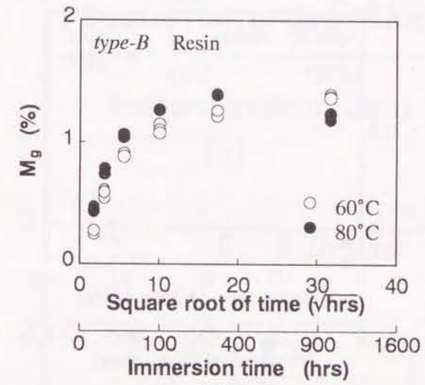

(b)

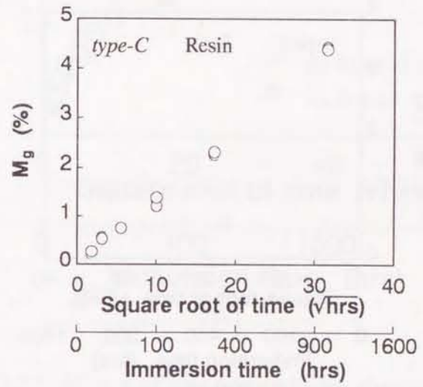

(c)

Fig.2.22 Changes of M_{gr} with the square root of immersion time; (a) *type-A*, (b) *type-B* and (c) *type-C*.

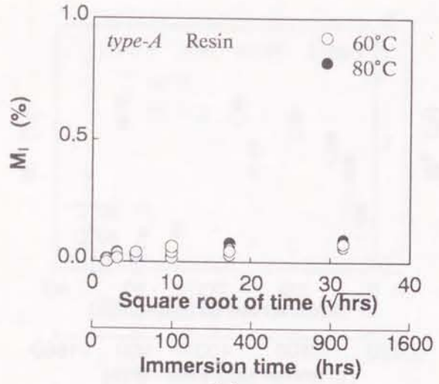

(a)

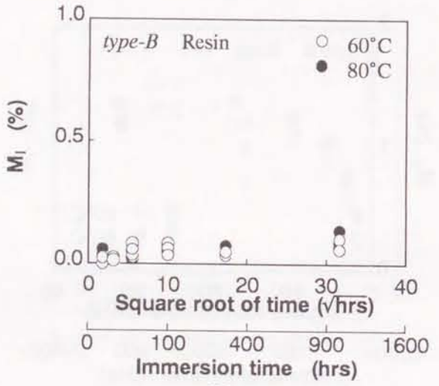

(b)

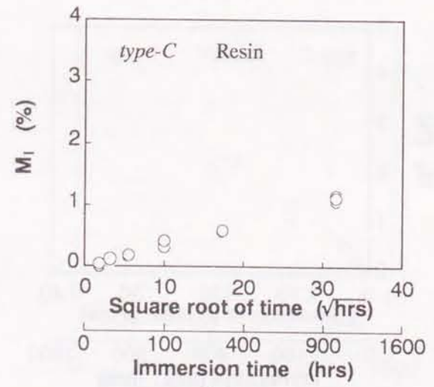

(c)

Fig.2.23 Changes of M_{lr} with the square root of immersion time; (a) *type-A*, (b) *type-B* and (c) *type-C*.

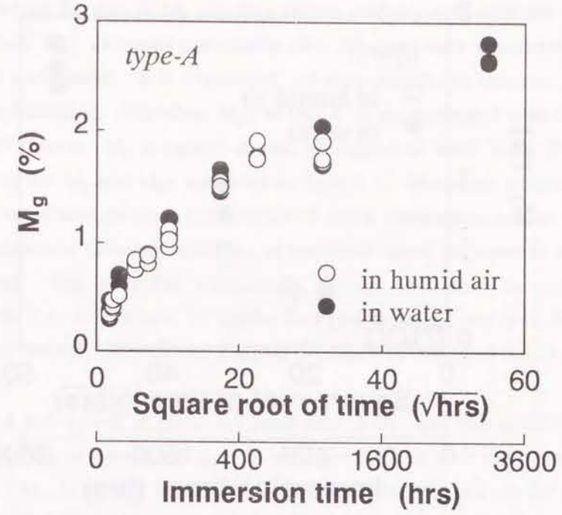

(a)

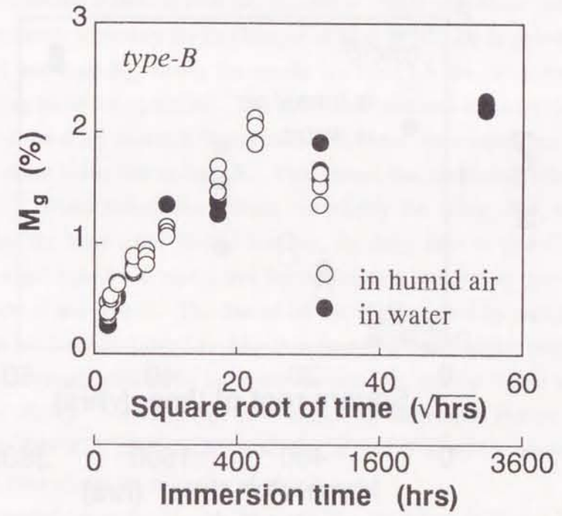

(b)

Fig.2.24 Effect of environment on changes of M_g; (a) *type-A* and (b) *type-B*.

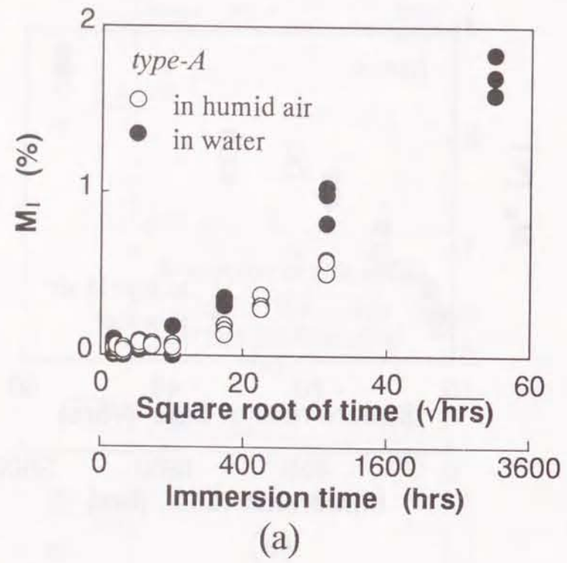

(a)

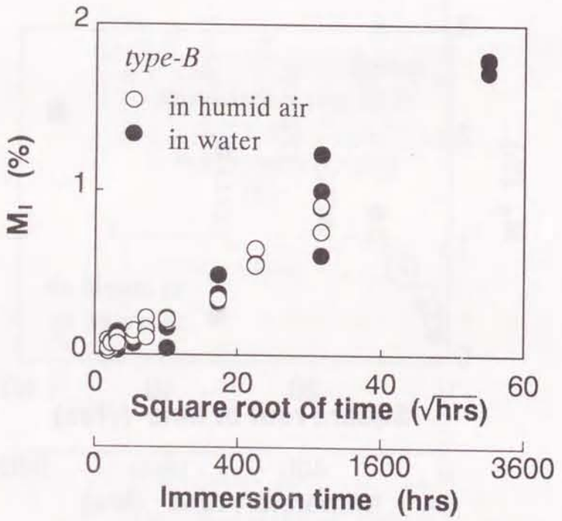

(b)

Fig.2.25 Effect of environment on changes of M_l; (a) *type-A* and (b) *type-B*.

reached saturation at 100h, and M_g did at 300h. At 80°C M_{gR} reached saturation at 30h, and M_g did at 100h. Therefore the data of M_g and M_{gR} before reaching saturation are approximated by eqn(2.13). In *type-C* M_{gR} increased remarkably after 30h, and such phenomenon could not be observed in *type-A* and *type-B*. It is considered that such remarkable increase of M_{gR} in *type-C* was caused by the relaxation. Therefore M_{gR} in *type-C* is approximated until 30h, which is the limit of a Fickian diffusion. M_g in *type-C* is also approximated until 30h. The approximation results by eqn(2.13) for M_g and M_{gR} are listed in Table 2.3. Maximum weight gain ($M_g(\infty)$) in *type-A* and *type-B* are almost the same independent of water temperature and are smaller than that in *type-C*. This means that the water resistance of bisphenol based polyester is superior to that of orthophthalic based. The diffusion coefficients, D, are calculated by eqn(2.15) and are summarized in Table 2.4. D in *type-C* is smaller than that in *type-A* and *type-B*. In comparison between *type-A* and *type-B*, the effect of filler on D cannot be observed but D at 80°C is higher than the 60°C case.

M_l in *type-A* and *type-B* at 60°C increased after 300h, and that at 80°C did after 100h. Therefore the data of M_l in *type-A* and *type-B* are approximated after these immersion times in reference to eqn(2.24). In *type-C* M_l and M_{lR} increased after 3h, and so the approximation is done for the data after 3h. Approximated results for M_l by eqn(2.24) are summarized in Table 2.5. D_S at 80°C in *type-A* is higher than at 60°C, while that at 80°C in *type-B* is lower than at 60°C. The approximation at 60°C is done for the data at 1000h and 3000h only, and so it may be difficult to approximate accurately for the changes of M_l at 60°C. D_S in *type-C* is much higher than that in *type-A* and *type-B*. Using the results in Table 2.5 the delay time of M_l, t_0, is calculated substituting M_l=0 for eqn(2.24). The delay time obtained is summarized in Table 2.6. In *type-A* and *type-B* the delay time at 60°C indicates almost the same value, but the delay time at 80°C in *type-A* is about twice that in *type-B*. This means that containing filler makes easy to dissolve into water. Water temperature affects remarkably the delay time, and higher water temperature shortens the delay time. On the contrary, the delay time in *type-C* is much shorter than those in *type-A* and *type-B*. It means that the degradation progress in *type-C* is very fast in comparison with *type-A* and *type-B*. The data of M_l are approximated by eqn(2.28) substituting t_0, and these results are listed in Table2.7. $M_l(\infty)$ in *type-C* is much higher than those in *type-A* and *type-B*. $M_l(\infty)$ is greatly affected by the water temperature, and the higher water temperature leads to the higher $M_l(\infty)$. $M_l(\infty)$ in *type-A* is almost the same with that in *type-B* at 60°C, however, $M_l(\infty)$ in *type-A* is much higher than that in *type-B* at 80°C. From this result it is considered that the filler affects the reduction of $M_l(\infty)$.

The approximated curves for M_g, M_l, M_{gR} and M_{lR} are drawn in Figs.2.26-30. From the approximated results, the boundary time between phase I and phase II is obtained as the time when $M_{gR}(t)/M_{gR}(\infty)$ reaches 0.999, and the boundary time between phase II and phase III is obtained as the delay time of M_l. These boundaries are also shown in Figs.2.26-30. In section 2.2.1 it was described that the changes of M_g in phase I and phase II were the same with those of M_{gR}. In experimental results, however, M_g indicates higher values than M_{gR}, and the time when M_g reaches saturation is longer than that for M_{gR}. Moreover in *type-C*, phaseII never appears and

Table 2.3 $M_g(\infty)$ and D_a obtained by approximation by eqn(2.13).

Specimen	Water temp.	$M_g(\infty)$ (%)	D_a
type-A (GFRP)	60°C	1.057	0.057
	80°C	1.097	0.132
type-B (GFRP)	60°C	1.057	0.064
	80°C	1.066	0.121
type-C (GFRP)	80°C	1.725	0.136
type-A (Resin)	60°C	0.768	0.122
	80°C	0.758	0.222
type-B (Resin)	60°C	0.768	0.122
	80°C	0.758	0.222
type-C (Resin)	80°C	1.396	0.116

Table 2.4 D obtained by eqn(2.15).

		Diffusion coefficient; D (mm^2/hr)	
		60°C	80°C
type-A	FRP	3.219×10^{-2}	9.670×10^{-2}
	Resin	5.560×10^{-2}	8.622×10^{-2}
type-B	FRP	3.843×10^{-2}	8.841×10^{-2}
	Resin	5.560×10^{-2}	8.622×10^{-2}
type-C	FRP	—	3.622×10^{-2}
	Resin	—	4.375×10^{-2}

Table 2.5 D_s and M_c obtained by eqn(2.24).

Specimen	Water temp.	D_S	M_C
type-A (FRP)	60°C	2.748×10^{-2}	0.433
	80°C	4.038×10^{-2}	0.344
type-B (FRP)	60°C	4.134×10^{-2}	0.660
	80°C	3.685×10^{-2}	0.232
type-C (FRP)	80°C	1.083×10^{-1}	0.214
type-C (Resin)	80°C	3.544×10^{-2}	0.019

Table 2.6 Delay time of M_l obtained by eqn(2.27).

Specimen	Water temperature	Delay time of M_l
type-A (FRP)	60°C	248 h
	80°C	73 h
type-B (FRP)	60°C	255 h
	80°C	40 h
type-C (FRP)	80°C	4 h
type-C (Resin)	80°C	0.3 h

Table 2.7 $M_I(\infty)$, D_I and t_0 obtained by eqn(2.28).

Specimen	Water temp.	$M_I(\infty)$ (%)	D_I	t_0 (hrs)
type-A (FRP)	60°C	1.731	2.34×10^{-3}	248
	80°C	3.361	1.84×10^{-3}	73
type-B (FRP)	60°C	1.606	4.07×10^{-3}	255
	80°C	2.768	2.47×10^{-3}	40
type-C (FRP)	80°C	5.779	2.04×10^{-2}	4
type-C (Resin)	80°C	2.252	2.28×10^{-2}	0.3

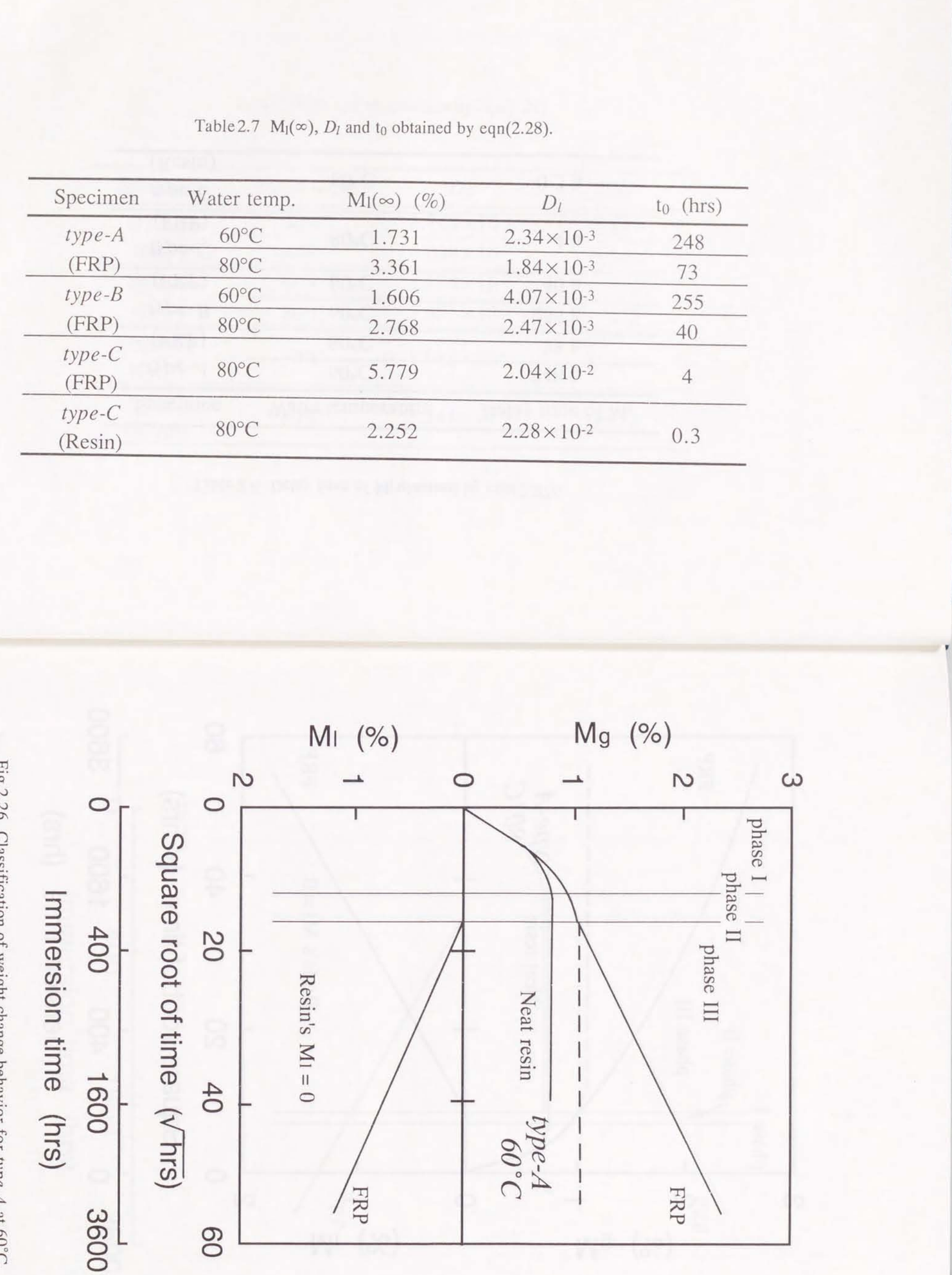

Fig.2.26 Classification of weight change behavior for *type-A* at 60°C.

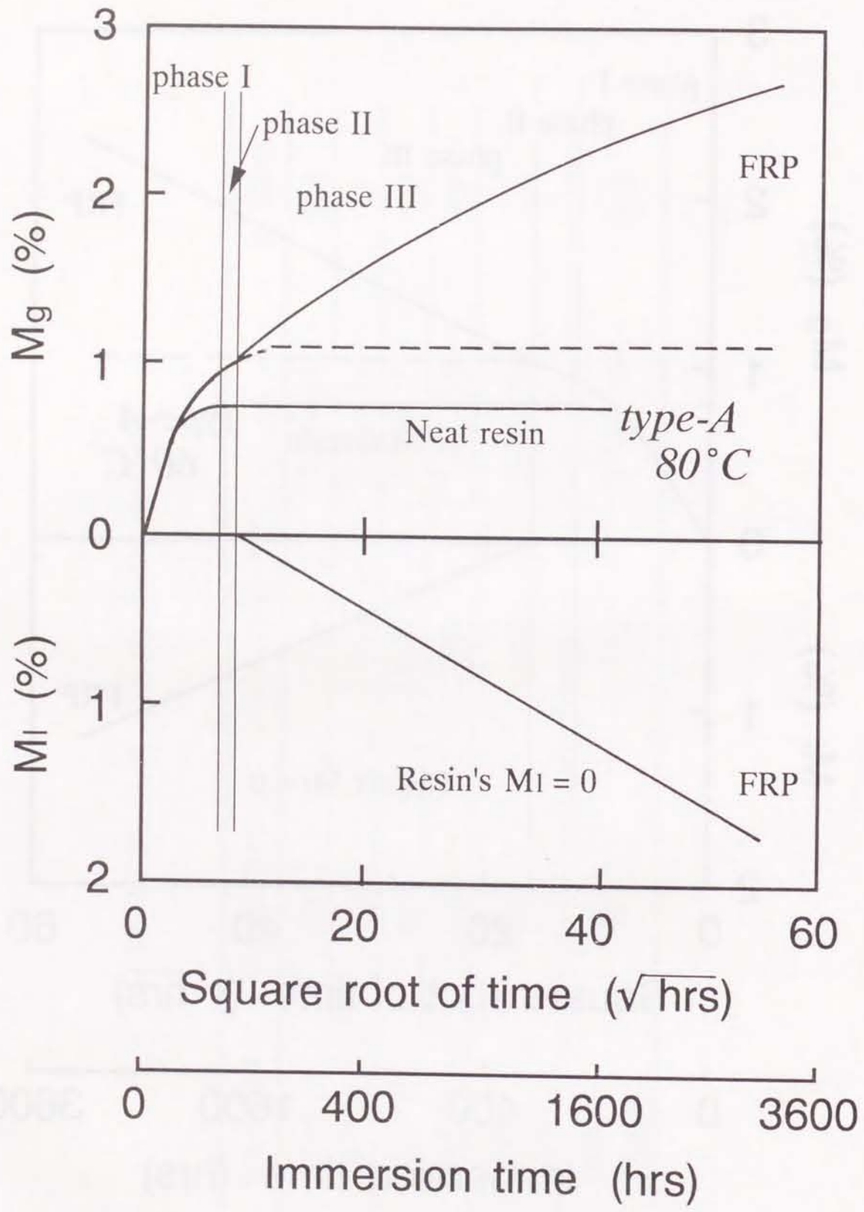

Fig.2.27 Classification of weight change behavior for *type-A* at 80°C.

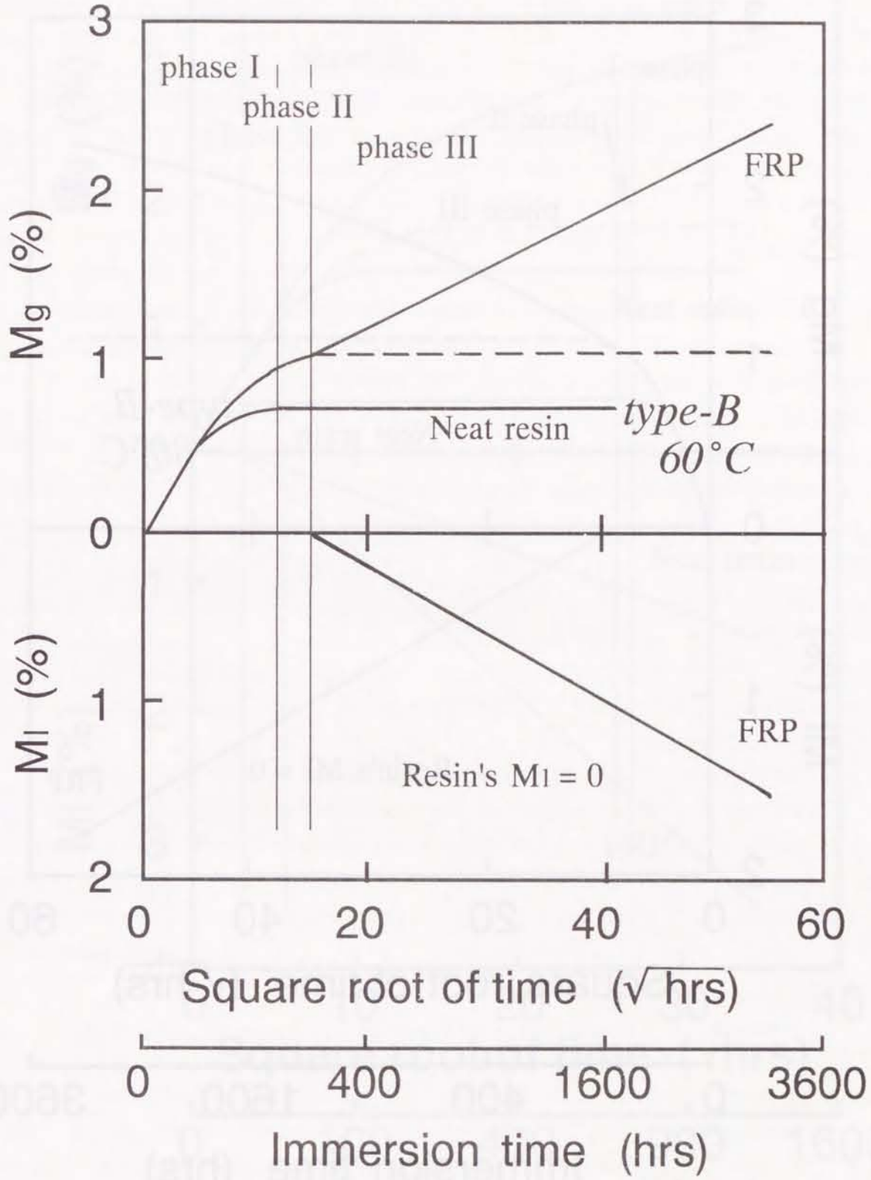

Fig.2.28 Classification of weight change behavior for *type-B* at 60°C.

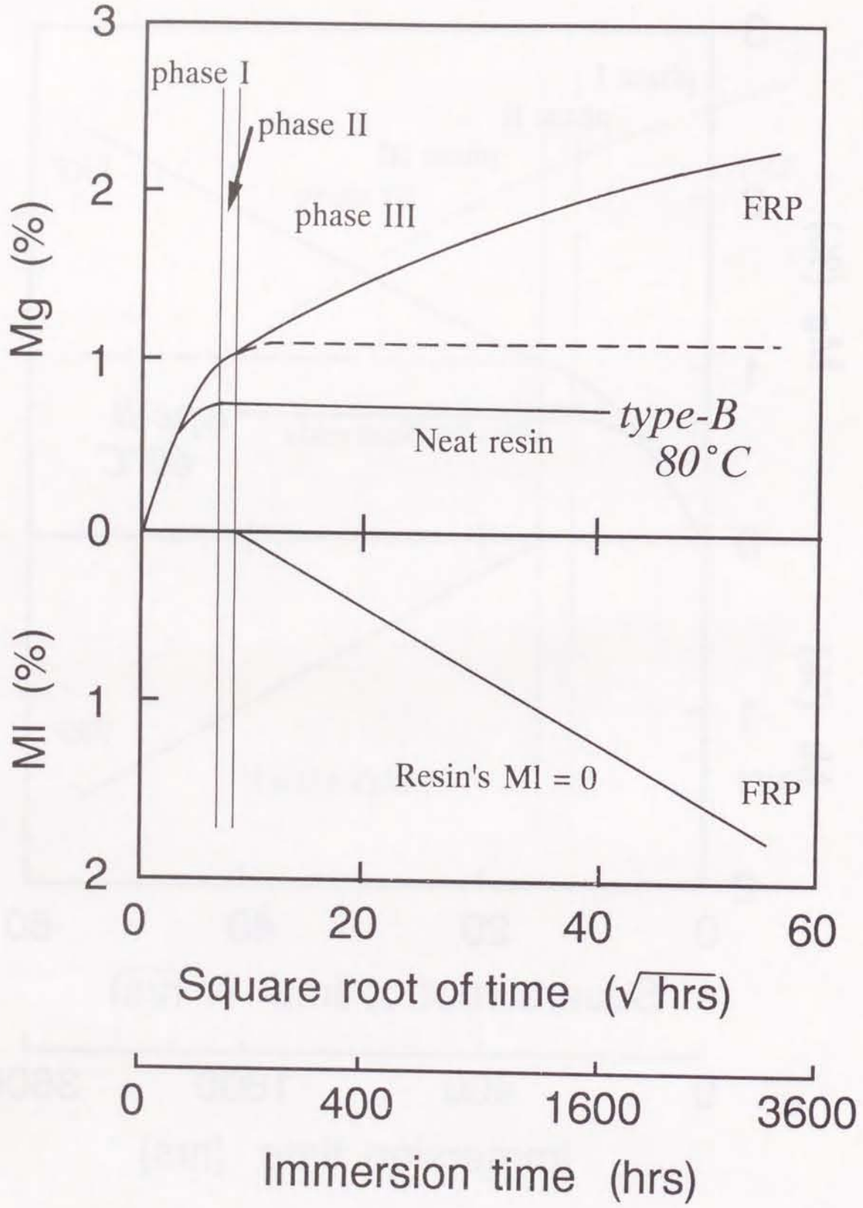

Fig.2.29 Classification of weight change behavior for *type-B* at 80°C.

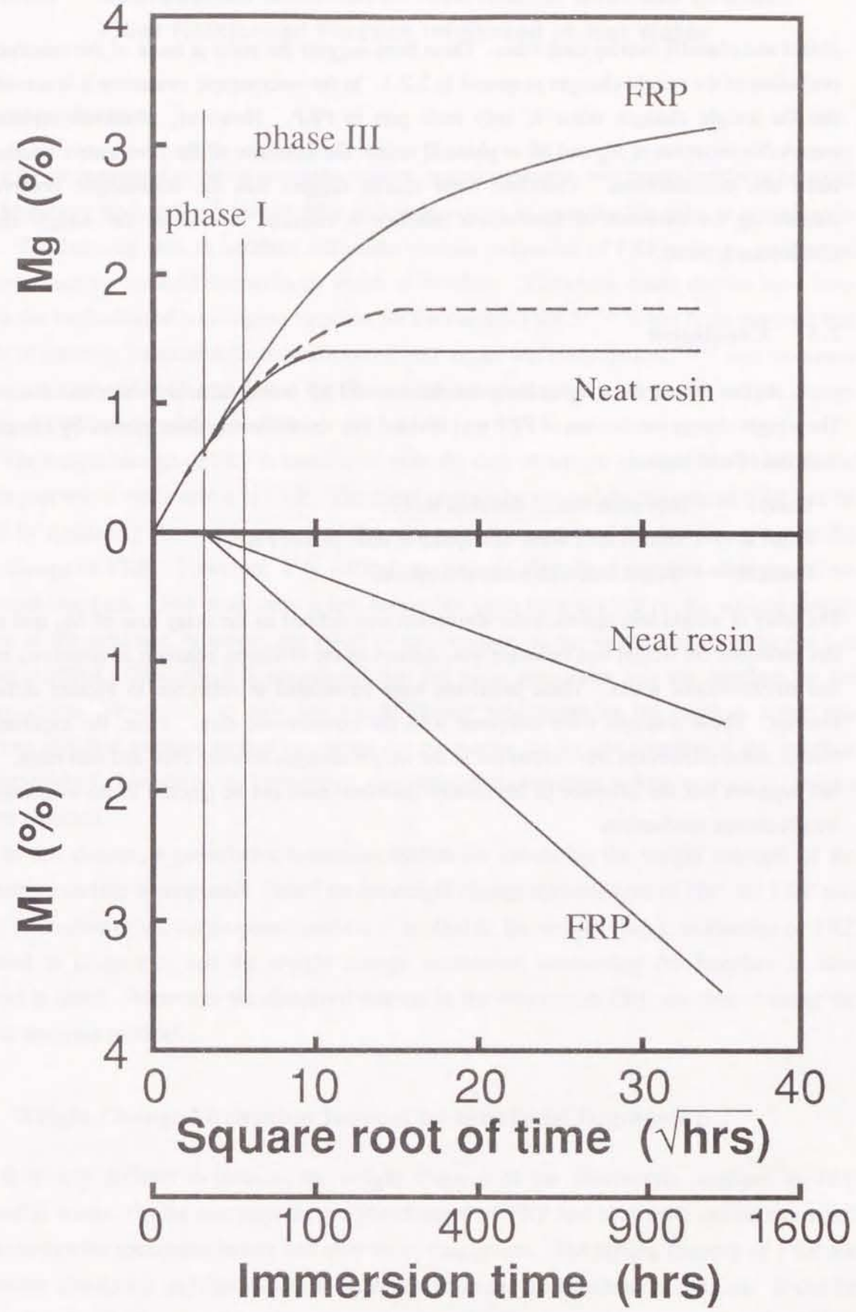

Fig.2.30 Classification of weight change behavior for *type-C* at 80°C.

phaseI and phaseIII overlap each other. These facts suggest the point at issue of the macroscopic evaluation of the weight changes proposed in 2.2.1. In the macroscopic evaluation it is considered that the weight changes occur in only resin part in FRP. However, it cannot explain the remarkable increases of M_g and M_l in phase III unless the influence of the fiber/matrix interface is taken into consideration. Therefore these results suggest that the microscopic observation considering the existence of fiber/matrix interface is essential to evaluate the weight change mechanism in detail.

2.5 Conclusion

In this chapter the weight change mechanism of FRP immersed in hot water was discussed. The weight change mechanism of FRP was divided into the following three phases by comparing with that of neat resin:

Phase I ----- Only resin matrix absorbed water.
Phase II ----- Saturation of water absorption in resin part of FRP.
Phase III ----- Weight loss with water absorption.

The delay of weight loss against water absorption was defined as the delay time of M_l, and using this parameter the weight loss behavior was defined as the diffusion behavior of dissolved matter into environmental water. These behaviors were formulated in reference to Fickian diffusion kinetics. These concepts were compared with the experimental data. From the experimental results, some differences were found out in the weight changes between FRP and neat resin. This fact suggests that the influence of fiber/matrix interface must not be ignored in the evaluation of weight change mechanism.

Chapter 3 Degradation Behavior of Fiber/Matrix Interface of Glass Fiber Reinforced Plastics Immersed in Hot Water

3.1 Introduction

FRP is composed of fibers as reinforcement, resins as matrix, and many interfaces between them. Moreover the interface between filler and resin occurs in case that the filler is contained in matrix. The bonding state at interface influences various properties of FRP such as mechanical properties since the material discontinuity exists at interface. Therefore, many studies have been done for the evaluation of bonding on interface for the various FRP.[44-55] It has been reported that the state of interface influences the degradation of FRP under wet environment,[42,43] and moreover it has been mentioned in Chapter 2 that the fiber/matrix interface greatly affects the weight change behavior of FRP immersed in hot water.

The weight change of FRP is considered to be the sum of weight changes both occurred at the resin part and at the interface in FRP. The effect of resin on the weight changes of FRP can be clarified by measuring the weight change of the neat resin specimen and by comparing that to the weight change of FRP. However, it is difficult to evaluate directly the weight changes of the fiber/matrix interface. Until now, only a few researches have been studied on the weight change behavior of the interface, however, the effect of the interface on the weight change behavior has not been clarified. Generally it is considered that the water penetrates into the interface by the capillary action. However, not only the weight change mechanism by the capillary action has never been clarified, even the evaluation system for measuring the weight changes of the interface is not established. Limited to my knowledge, no quantitative evaluation system on weight changes has been reported.

In this chapter, a quantitative evaluation system for measuring the weight changes of the fiber/matrix interface is proposed. Based on the weight change measurement of both the FRP and the neat resin specimens, the proposed method is applied to the weight change evaluation of FRP mentioned in Chapter 2, and the weight change mechanism concerning the interface is also discussed in detail. Moreover the dissolved matters in the water from FRP are cleared using the chemical analyses method.

3.2 Weight Change Mechanism Induced by Interfacial Degradation

It is very difficult to measure the weight changes of the fiber/matrix interface in FRP immersed in water. On the contrary, the weight changes of FRP and neat resin can be measured easily to weigh the specimens before and after water immersion. The weight changes of FRP are due to water absorption and dissolution of the matrix resin and the fiber/matrix interface. It can be assumed that the fibers never affect the weight changes of FRP. From this assumption, the weight changes of the fiber/matrix interface can be determined by the difference of the weight change data

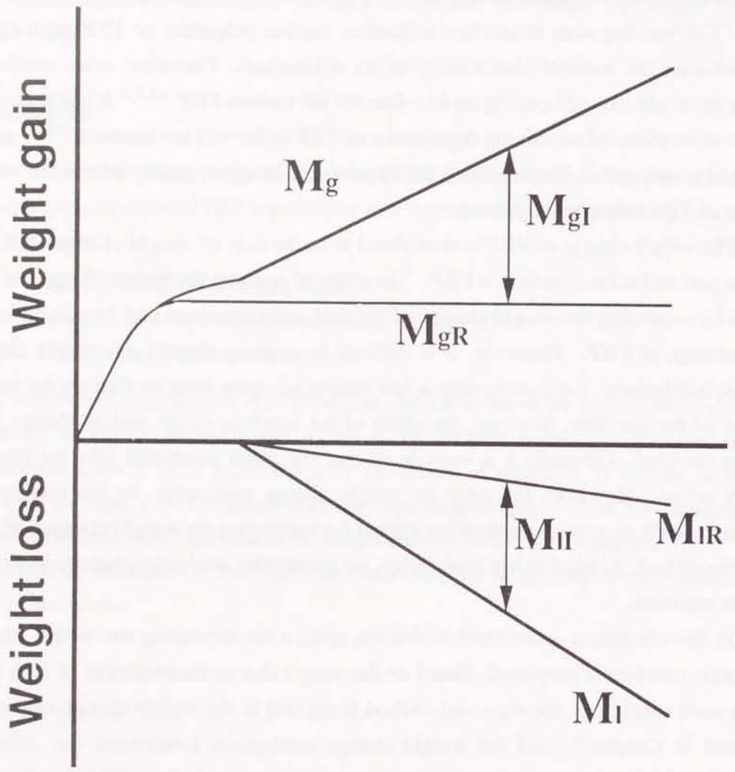

Fig.3.1 Concept of weight changes of fiber/matrix interface (M_{gI} and M_{II}).

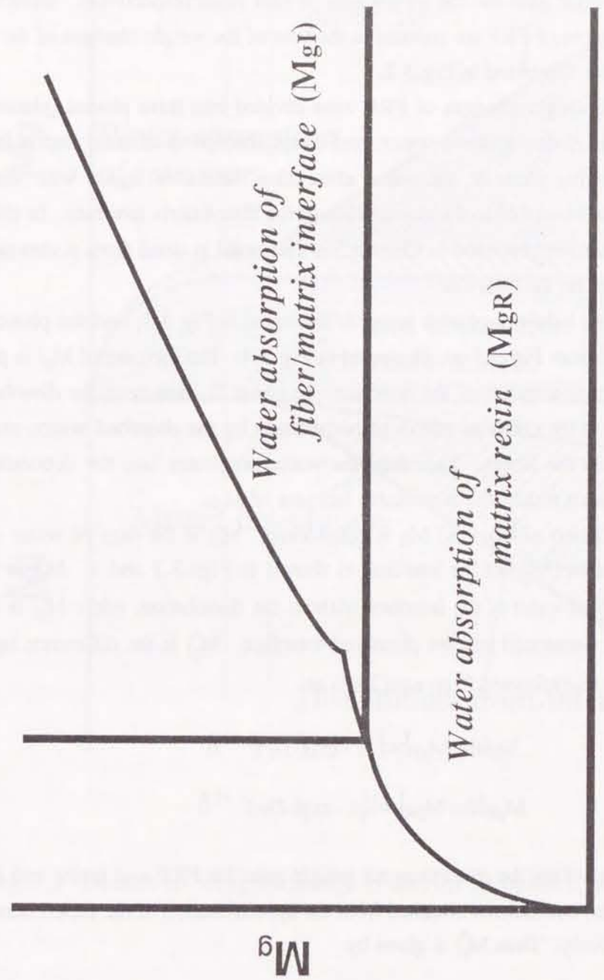

Fig.3.2 Scematic representation and classification of weight gain of FRP.

between the FRP and the resin part of FRP as illustrated in Fig.3.1. The net weight gain of the interface (M_{gI}) and the weight loss of the interface (M_{lI}) are then given by

$$M_{gI}(t) = M_g(t) - M_{gR}(t)$$
$$M_{lI}(t) = M_l(t) - M_{lR}(t) \qquad (3.1)$$

where $M_g(t)$ and $M_l(t)$ are the net weight gain and the weight loss of FRP respectively, and $M_{gR}(t)$ and $M_{lR}(t)$ are the net weight gain and the weight loss of neat resin respectively. Introducing M_{gI} and M_{lI}, the weight changes of FRP are reduced to the sum of the weight changes of the resin part and that of the interface as illustrated in Fig.3.2.

In Chapter 2, the weight changes of FRP were divided into three phases (phases I, II and III). In phase I only resin matrix absorbs water, and water absorption of resin matrix is saturated in phase II. In the following phase III, the water absorption increases again with dissolution, which is considered to be related to the degradation of the fiber/matrix interface. In this chapter, the weight change mechanism proposed in Chapter 2 is discussed in detail from a viewpoint of the weight change evaluation on the interface.

The weight change behavior of each phase is illustrated in Fig.3.3, and the phase divisions of M_{gI} and M_{lI} obtained from Fig.3.3 are illustrated in Fig.3.4. The increase of M_{gI} in phase I and II is caused by the water absorption of the interface. In phase III, however, the dissolution from the interface occurs due to the chemical and/or physical attack by the absorbed water, and then the debondings occur around the fibers. Therefore the water penetrates into the debondings at the fiber/matrix interface which results the remarkable increase of M_{gI}.

Here, the formulation of M_{gI} and M_{lI} is considered. M_{gI} is the sum of water absorption (M_{gI}^{A}) and water penetration (M_{gI}^{P}) of the interface as shown in Figs.3.3 and 4. M_{gI}^{A} is defined as the amount of the absorbed water of the interface without the dissolution, while M_{gI}^{P} is defined as the amount of the water penetrated into the dissolved interface. M_{gI}^{A} is the difference between M_g and M_{gR}, which can be re-expressed from eqn(2.13) as;

$$M_g(t) = M_{gF}(\infty)\left\{1 - \exp(-D_F t^{0.75})\right\}$$
$$M_{gR}(t) = M_{gR}(\infty)\left\{1 - \exp(-D_R t^{0.75})\right\} \qquad (3.2)$$

where $M_{gF}(\infty)$ and $M_{gR}(\infty)$ are the maximum net weight gain for FRP and resin, and D_F and D_R are the apparent diffusion coefficients obtained from the approximation of the experimental data for FRP and resin, respectively. Thus M_{gI}^{A} is given by

$$M_{gI}^{A}(t) = M_{gF}(\infty)\left\{1 - \exp(-D_F t^{0.75})\right\} - M_{gR}(\infty)\left\{1 - \exp(-D_R t^{0.75})\right\} \qquad (3.3)$$

Based on the same conception, M_{lI} is the difference between M_l and M_{lR}, which can be re-expressed from eqn(2.28) as;

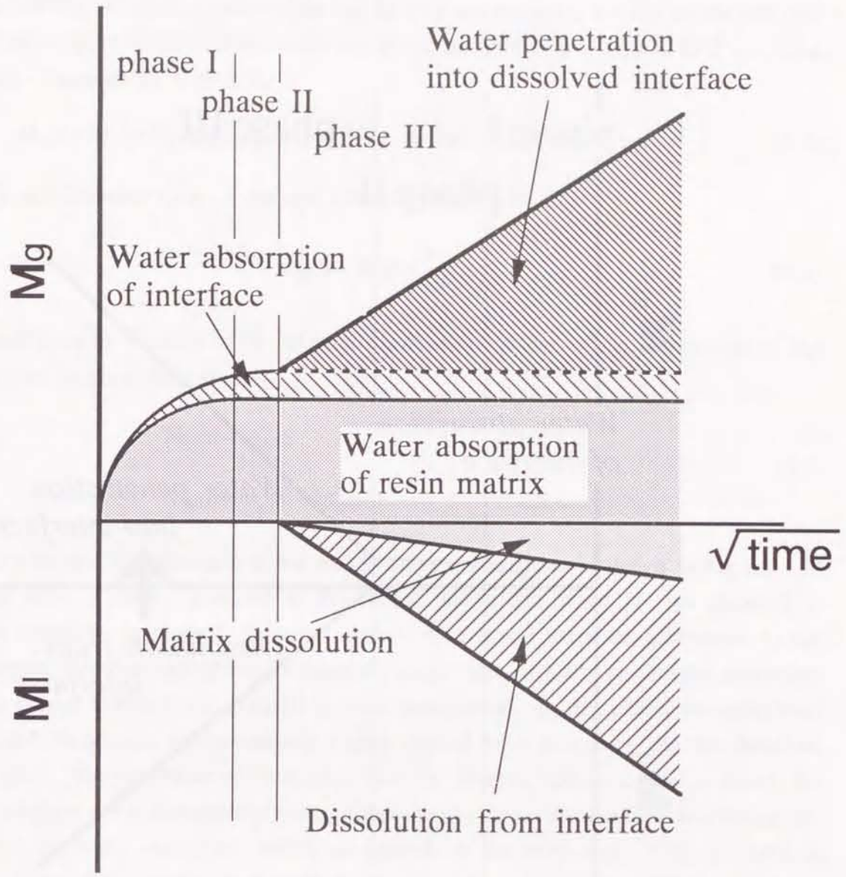

Fig.3.3 Details of weight change behavior in phase I, II and III.

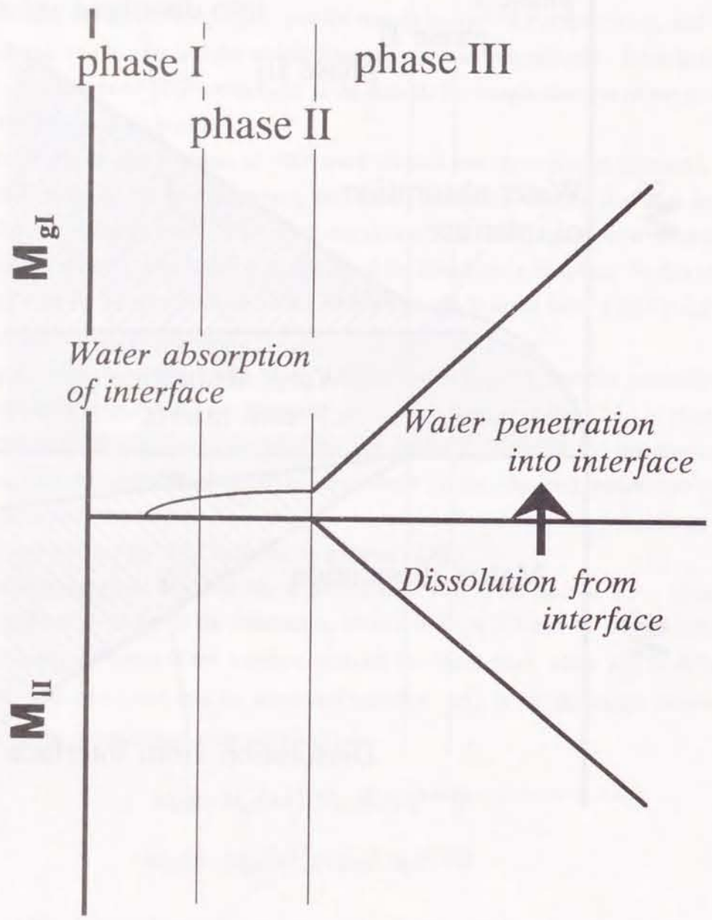

Fig.3.4 Phase divisions of MgI and MII and weight change mechanism of interface.

$$M_{IF}(t) = M_{IF}(\infty)\left[1 - \exp\{-D_{IF}(t - t_{0F})\}^{0.75}\right]$$
$$M_{IR}(t) = M_{IR}(\infty)\left[1 - \exp\{-D_{IR}(t - t_{0R})\}^{0.75}\right] \tag{3.4}$$

where M_{IF} and M_{IR} are the maximum weight loss for FRP and resin, D_{IF} and D_{IR} are the diffusion coefficient for weight loss for FRP and resin, and t_{0F} and t_{0R} are the delay time of FRP and resin, respectively. Therefore M_{II} is given by

$$M_{II}(t) = M_{IF}(\infty)\left[1 - \exp\{-D_{IF}(t - t_{0F})\}^{0.75}\right] - M_{IR}(\infty)\left[1 - \exp\{-D_{IR}(t - t_{0R})\}^{0.75}\right] \tag{3.5}$$

Eqn(3.5) is satisfied when $t \geq t_0$. From eqn(2.26), M_{gI}^P is given by

$$M_{gI}^P(t) = M_{II}(t) \times \frac{\gamma_w}{\gamma_d} \tag{3.6}$$

where γ_w and γ_d are the densities of the water and the dissolved matter. Thus, the changes of M_{gI} with immersion time is expressed as

$$\begin{aligned} M_{gI}(t) &= M_{gI}^{\Lambda}(t) && (t < t_0) \\ M_{gI}(t) &= M_{gI}^{\Lambda}(t) + M_{gI}^P(t) && (t \geq t_0). \end{aligned} \tag{3.7}$$

The schematic representation of the weight change mechanism is shown in Fig.3.5. In phaseI, the water is mainly absorbed in the matrix, and a little water is also absorbed in fiber/matrix interface. In phase II, the water absorption of matrix keeps the saturation. In the interface region, the water absorption continuously occurs and gradually reaches the saturation. The weight change mechanism in phaseIII is more complicated. In this phase, the dissolution from the interface occurs, and immediately a great deal of water penetrates into the dissolved interface region. The occurrence of dissolution from the interface needs the time to absorb the water, to hydrolyze and to dissolve into water. Consequently the dissolution from interface occurs with delay to the water absorption, which corresponds to the delay time of M_I proposed in Chapter 2. The water penetration in phase III is caused by the capillary action, which is different from the water diffusion, through the paths along the fibers, and then M_{gI} increases remarkably. The water penetrating into the interface generates the crack inside the material by the penetrating pressure. Therefore, both M_{gI} and M_{II} keep increasing until the whole of the fiber/matrix interface degrades thoroughly. As a result, the time when M_{gI} reaches the saturation becomes much longer than the time when the water absorption of matrix reaches the saturation. It is considered from these facts that the changes of M_{gI} and M_{II} depend on the amount of the interface region in the material, which affects the weight change kinetics of FRP during long-term immersion.

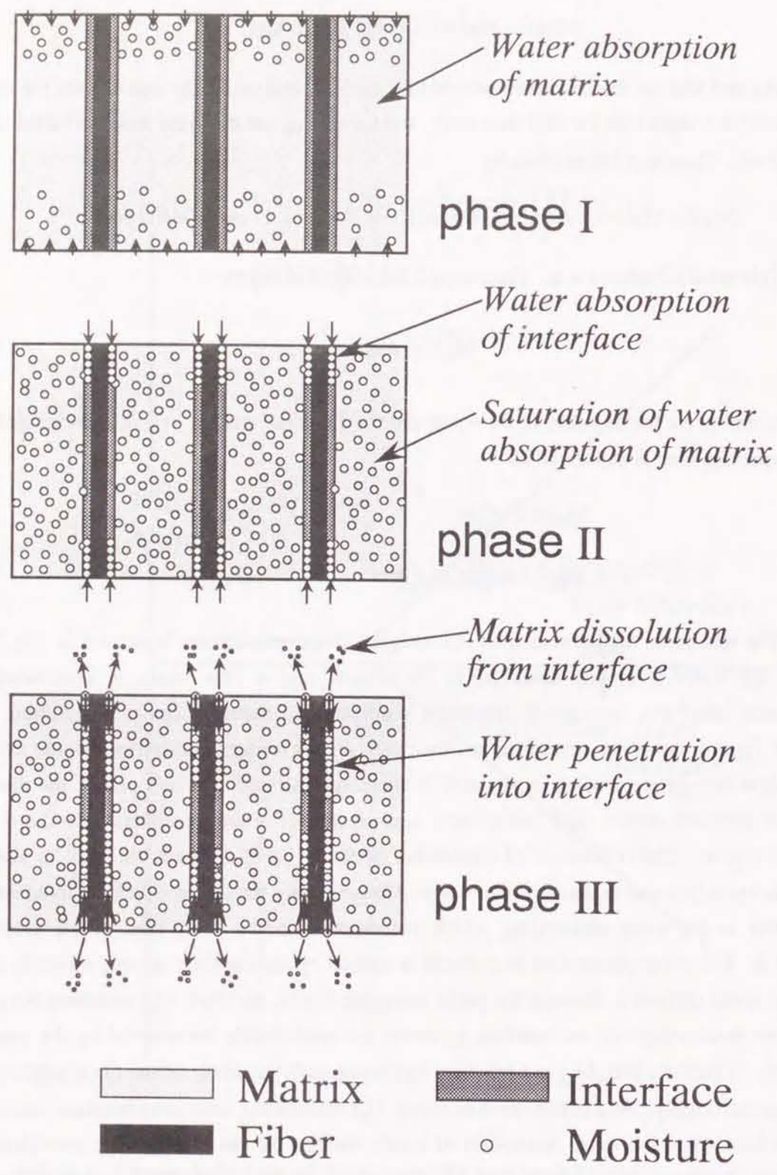

Fig.3.5 Schamatic representation of weight change mechanism of FRP.

3.3 Experiment

3.3.1 Materials

Materials used were three kinds of randomly oriented E-glass fiber continuous strand mat reinforced unsaturated polyester resins, and these were the same to those used in Chapter 2 (*type-A*, *type-B* and *type-C*), that is, *type-A* and *type-B* were the glass-fiber mat reinforced bisphenol based unsaturated polyester without and with filler, and *type-C* was the glass-fiber mat reinforced orthophthalic based unsaturated polyester. 300mm square panels were fabricated from these materials by a compression molding. Fiber volume content for all the panels was about 35%.

3.3.2 Experimental procedure

The water immersion tests were conducted in the same manner with those in Chapter 2 in order to measure the weight changes of FRP and neat resin. The specimens were immersed in distilled water at 60°C (except for *type-C*) and 80°C, and the periods of immersion were 3, 10, 30, 100, 300 and 1000 h. The specimen geometry and the specimen condition before immersion were the same to those described in Chapter 2.

The microscopic observation was done for the cross-section of immersed and original dry FRP's to evaluate the internal degradation by water immersion. In order to facilitate the microscopic observation, the specimens were put by the unsaturated polyester resin in the mold and the surface for observation was polished. Glassy polished surface was observed by an optical microscope.

In order to discuss what matters dissolved into water, the E-glass fiber continuous strand mat used as the reinforcement was immersed in a beaker with hot distilled water at 80°C. The period of immersion was 1000 h. After the immersion, the water in the beaker was evaporated, and the residue was scraped off from the beaker. This residue was analyzed by the Fourier transform infrared spectrometer (FT-IR; Perkin-Elmer 1650). FT-IR analysis was performed for KBr tablet with the residue by the transparent method. The weight loss of the remaining matters was measured using the thermogravimetric analyzer (TG; Perkin-Elmer TGA7). TG analysis for the residue of 6.7mg was done from 30°C to 1000°C at rate of 10°C/min under nitrogen gas . The residue after the TG measurement was analyzed again using the FT-IR as same with the above.

3.3.3 Results and discussion

In this chapter, only the changes of M_{gI} and M_{lI} are presented because the results of M_g, M_l, M_{gR} and M_{lR} were already presented in Chapter 2.

Figs.3.6-8 show the changes of net weight gain of the interface, M_{gI}, with the square root of immersion time. Practically the changes of M_{gI}^A and M_{gI}^P determined in 3.2 must be discussed separately. Since the changes of M_{gI}^A is so small from the obtained experimental data, it is not necessary to discuss the change of M_{gI} by distinguishing it to M_{gI}^A and M_{gI}^P. In *type-A*, M_{gI}

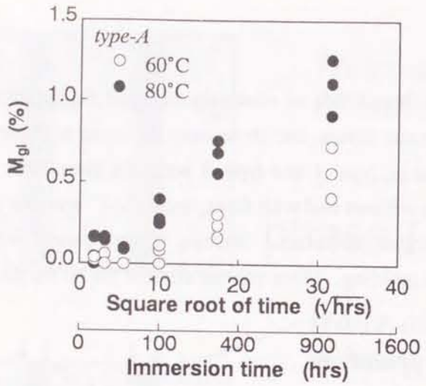

Fig.3.6 Changes of M_{gl} with the square root of immersion time for *type-A*.

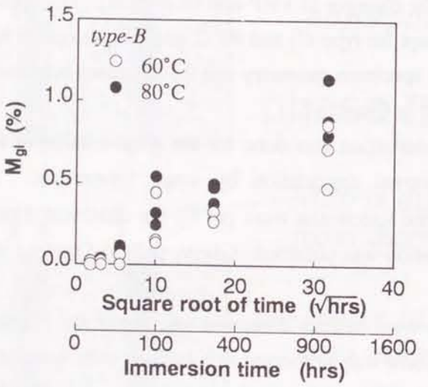

Fig.3.7 Changes of M_{gl} with the square root of immersion time for *type-B*.

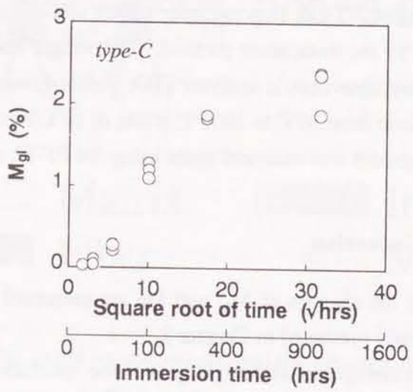

Fig.3.8 Changes of M_{gl} with the square root of immersion time for *type-C*.

Table3.1 Initiation time of M_{gl}.

Specimen	Water temperature	Initiation time of M_{gl}
type-A	60°C	53 h
	80°C	4 h
type-B	60°C	26 h
	80°C	5 h
type-C	80°C	3 h

increased linearly with the square root of immersion time after 100h at 60°C and after 30h at 80°C. The water temperature affected the slope of the increase of M_{gI}, and the slope at 80°C was greater than that at 60°C. M_{gI} in *type-B* started to occur at shorter immersion time than in *type-A*, however, the dependence of the increasing slope on water temperature was less than that in *type-A*. The changes of M_{gI} in *type-C* were quite different from those in *type-A* and *type-B*. M_{gI} in *type-C* increased almost linearly after 10h, however, M_{gI} gradually approached a constant value. Table 3.1 summarizes the time when M_{gI} starts to increase (initiation time of M_{gI}) obtained by the linear approximation of the relation between M_{gI} and the square root of immersion time for each specimen. The initiation time of M_{gI} depends on the used matrix. From these results, the changes of M_{gI} are mainly caused by the water diffusion into the interface. The delay of the initiation time of M_{gI} against M_g is originated from the arrival of the diffusing water to the interface through the matrix.

The change of the weight loss of the interface, M_{II}, is shown in Figs.3.9-11. M_{II} in *type-A* and *type-B* at 60°C increased remarkably after about 300h, and that at 80°C increased linearly with the square root of immersion time after about 100h. M_{II} in *type-C* also increased linearly after about 30h. The occurrence of M_{II} was delayed compared with that of M_{gI}. This means that increase of M_{II} results in the degradation of the fiber/matrix interface due to the hydrolysis caused by the water absorbed in the interface. The chemical reaction such as the hydrolysis spends a certain time, and therefore, the occurrence of M_{II} was delayed compared with that of M_{gI}. The slope of the increase of M_{II} kept almost invariable and was independent of both water temperature and material. Water temperature only affects the time when M_{II} starts to increase. The time when M_{II} starts to increase (initiation time of M_{II}) depends on the used matrix as well as the initiation time of M_{gI}. The initiation time of M_I in *type-C* was much shorter, and the time in *type-B* was a little shorter than that in *type-A*.

The initiation times of M_{gI} and M_{II} in *type-C* is shorter than those in *type-A* and *type-B*. The matrix resin in *type-A* and *type-B* are the same, but different to the filler content. Since some filler is contained in *type-B*, it has both the fiber/matrix interface and the filler/matrix interface. Thus, the amount of the interface in *type-B* is greater than that in *type-A*, and as a result, the initiation times of M_{gI} and M_{II} in *type-B* are shorter than those in *type-A*. Therefore the initiation times of M_{gI} and M_{II} are affected by the used matrix. It can be concluded that the poorer the water resistance of the matrix becomes, the shorter the initiation times of M_{gI} and M_{II} become.

Here, M_{gI} was calculated from the experimental results of M_g, M_{gR}, M_I and M_{IR} by the equations proposed in 3.2. $M_g(\infty)$ and D_a listed in Table 2.3 were substituted for $M_{gF}(\infty)$, $M_{gR}(\infty)$, D_F and D_R in eqn(3.3) and M_{gI}^A was calculated. In the same manner, $M_I(\infty)$, D_I and t_0 listed in Table 2.7 were substituted for $M_{IF}(\infty)$, $M_{IR}(\infty)$, D_{IF}, D_{IR}, t_{0F} and t_{0R} in eqn(3.5) ($M_{IR}(t)=0$ in *type-A* and *type-B*) and M_{II} was calculated. M_{gI}^P could be calculated by eqn(3.6) from the obtained M_{II}. In eqn(3.6) the density of the matrix resin was used as γ_d (γ_d=1.2). From the obtained M_{gI}^A and M_{gI}^P, M_{gI} was calculated by eqn(3.7). The calculated M_{gI} curves are compared with the experimental M_{gI} in Figs.3.12-16. The calculated M_{gI} indicated a few higher value than the experimental one, however, the calculated M_{gI} almost corresponded to the

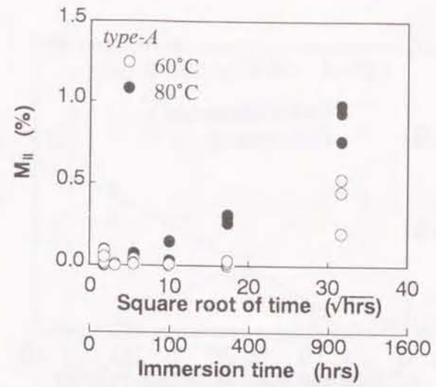

Fig.3.9 Changes of M_{II} with the square root of immersion time for *type-A*.

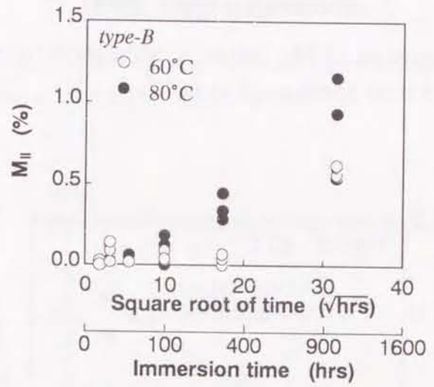

Fig.3.10 Changes of M_{II} with the square root of immersion time for *type-B*.

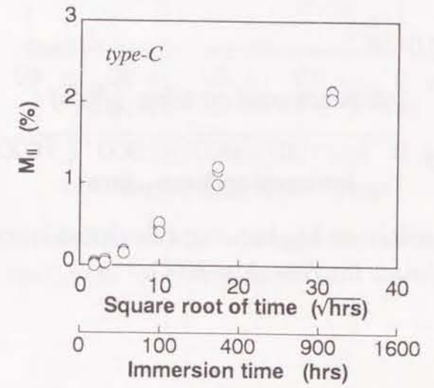

Fig.3.11 Changes of M_{II} with the square root of immersion time for *type-C*.

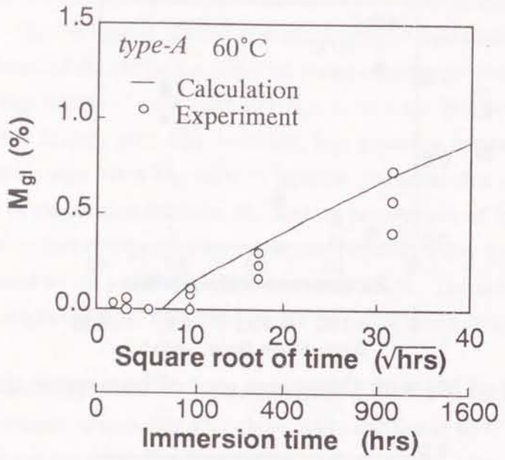

Fig.3.12 Comparison of M_{gl} between calculation by eqn(3.7) and experiment for *type-A* at 60°C.

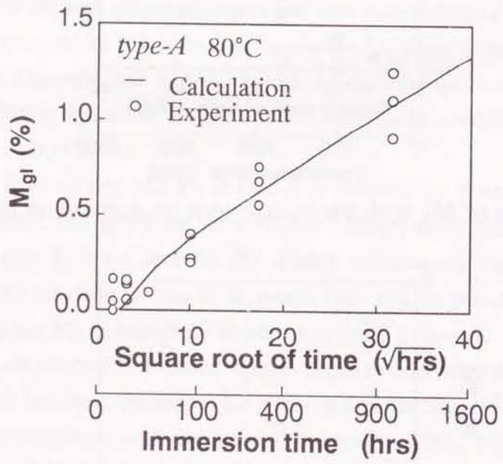

Fig.3.13 Comparison of M_{gl} between calculation by eqn(3.7) and experiment for *type-A* at 80°C.

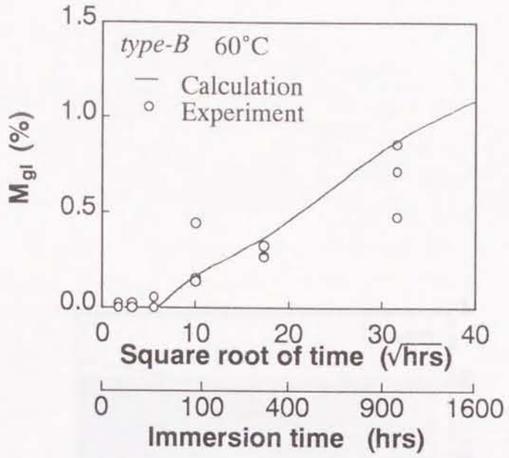

Fig.3.14 Comparison of M_{gl} between calculation by eqn(3.7) and experiment for *type-B* at 60°C.

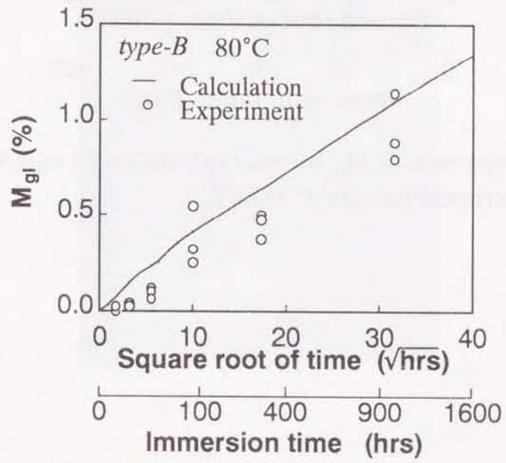

Fig.3.15 Comparison of M_{gl} between calculation by eqn(3.7) and experiment for *type-B* at 80°C.

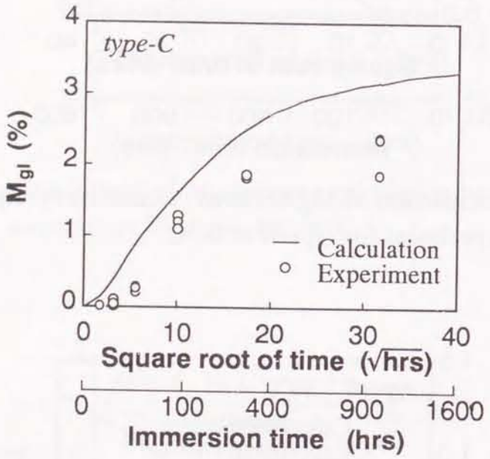

Fig.3.16 Comparison of M_{gl} between calculation by eqn(3.7) and experiment for *type-C* at 80°C.

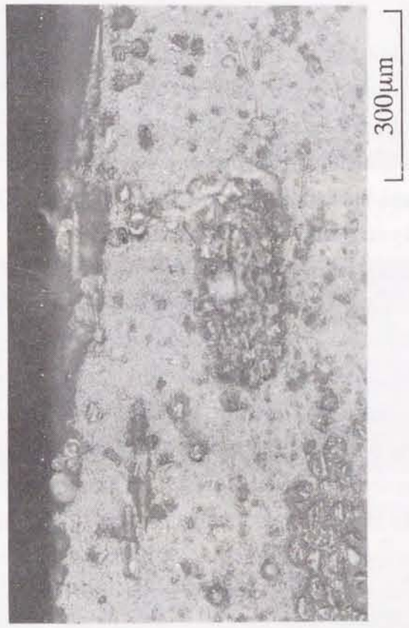

Fig.3.17 Cross-sectional micrograph near the surface of immersed specimen for *type-B*.

experimental M_{gI} except for *type-C*. These results verifies the validity of the weight change mechanism proposed in 3.2. The changes of the calculated M_{gI} of *type-C* agreed to those of the experimental one, however, the calculated M_{gI} was higher than the experimental one. The difference between the calculated and the experimental M_{gI} results in the weight loss due to the material loss from the surface of the specimen as shown in Fig.3.17. A little difference between the calculated and the experimental M_{gI} for *type-A* and *type-B* is also caused by the material loss from the surface. Therefore these results suggest that a greater deal of material is lost in *type-C* than in *type-A* and *type-B*.

Fig.3.18 shows the cross-sectional micrographs of the original dry and immersed specimens for *type-A* and *type-B*. Boundary between fiber and matrix cannot be observed clearly in the original dry specimens. This suggests that fiber and matrix are fully adhered and that debonding between fiber and matrix never occurs. On the other hand, the boundary between fiber and matrix can be observed clearly in the immersed specimens. This indicates that the debonding between fiber and matrix occur by the water absorption and dissolution of the interface. In addition to this, the matrix cracking initiated from the large scale debondings around the fiber bundle can be observed in the cross-section of the immersed *type-B* specimen. It is considered that such matrix cracking is initiated by the pressure coming from the water penetration. These debondings and matrix cracks induce the increase of M_{gI} and M_{II}. Consequently it is concluded that the weight loss is mainly originated from the interface.

Fig.3.19 shows the changes of the microscopic views of the cross-sections for *type-A* and *type-B* specimens at 80°C with the progress of degradation. The debondings around the fiber bundles and inside the fiber bundles cannot be observed in the original dry specimens. It is considered that the black regions in these photos were the voids formed during the molding process. As the immersion time became longer, the circumferences around the fiber bundles and around the fibers inside the fiber bundles appeared clearly. Fig.3.20 is the scanning electron micrographs of the cross-sections shown in Fig.3.19. In the original dry specimen for *type-A*, the voids could be observed in the region surrounded by the fibers, and it was generated by the incomplete impregnation during molding process. At 100h, the debonding appeared between fiber and matrix, however, the degree of the debonding was very small. Such debonding region enlarged with the progress of the degradation. The enlargement of the debonding shown in Fig.3.20 corresponded to the increase of M_{II}. Therefore M_{II} is caused by the dissolution of the matters existing at the interface such as the binder and the silane coupling agent. The water penetrates into the dissolved interface, so that M_{gI} increases. The penetrating water attack the interface, and as a result, the debonding progresses enlarges more and more. Same phenomenon can also be observed also in other material systems. Fig.3.21 shows the scanning electron micrographs of randomly oriented glass-fiber mat reinforced vinylester resin as a function of the immersion time. The debonding between fiber and matrix never appeared until 30h. At 100h small degree of the debonding appeared at a part around the fiber. The debonding spreads around the fiber bundles at 300h, and it enlarges with the progress of the degradation.

type-A, 0hr

type-A, 3000hrs

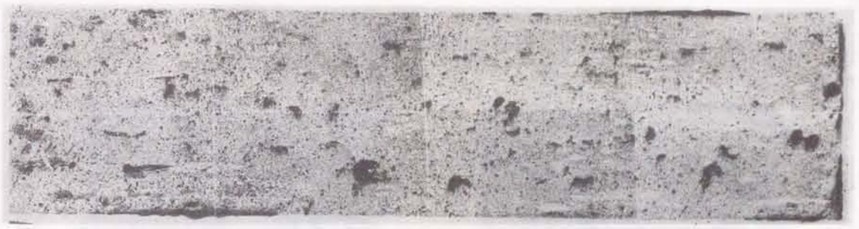

type-B, 0hr

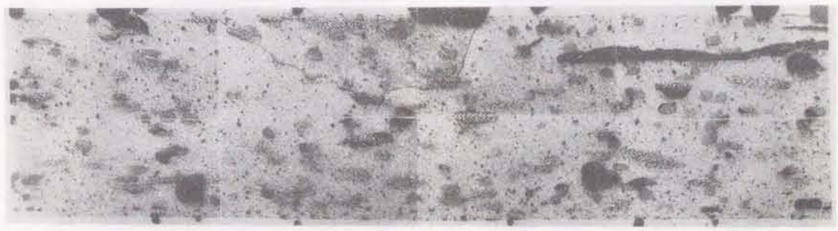

2mm

type-B, 3000hrs

Fig.3.18 Optical micrographs of all over the cross-section of the original dry and immersed specimens for *type-A* and *type-B*.

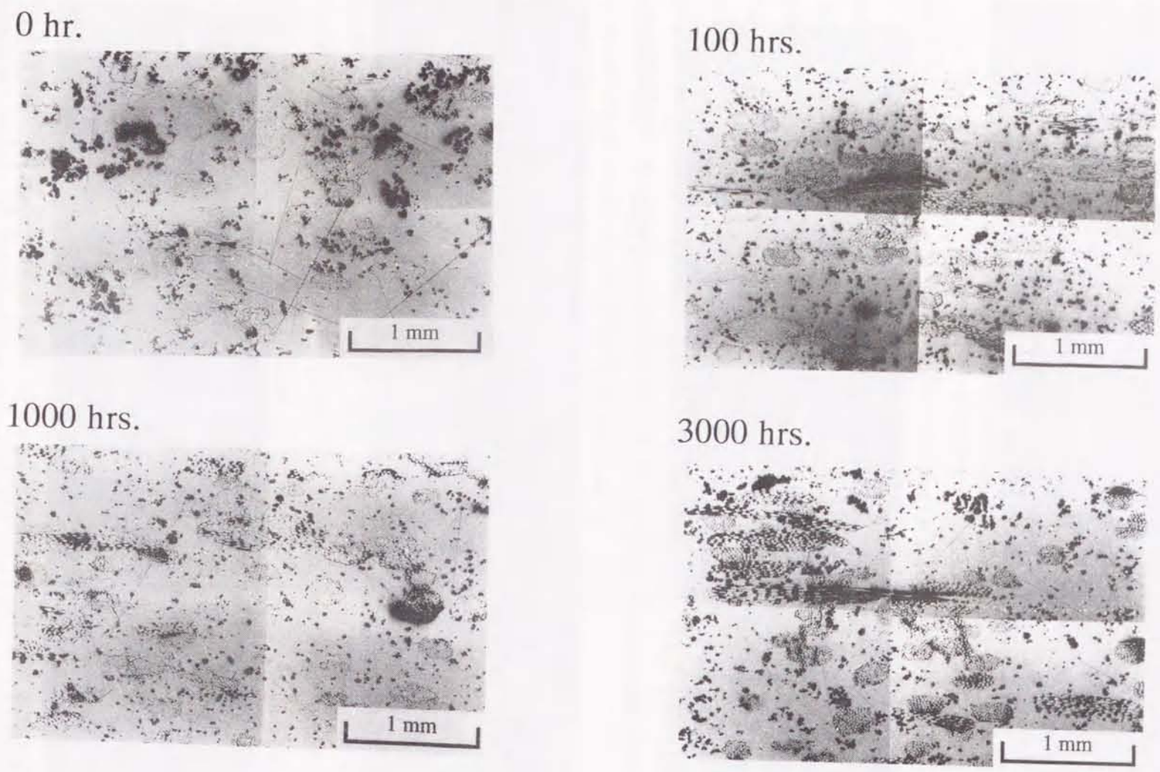

Fig.3.19 Changes of the microscopic views of cross-sections of immersed speciemens at 80°C with progress of degradation; (a) *type-A*.

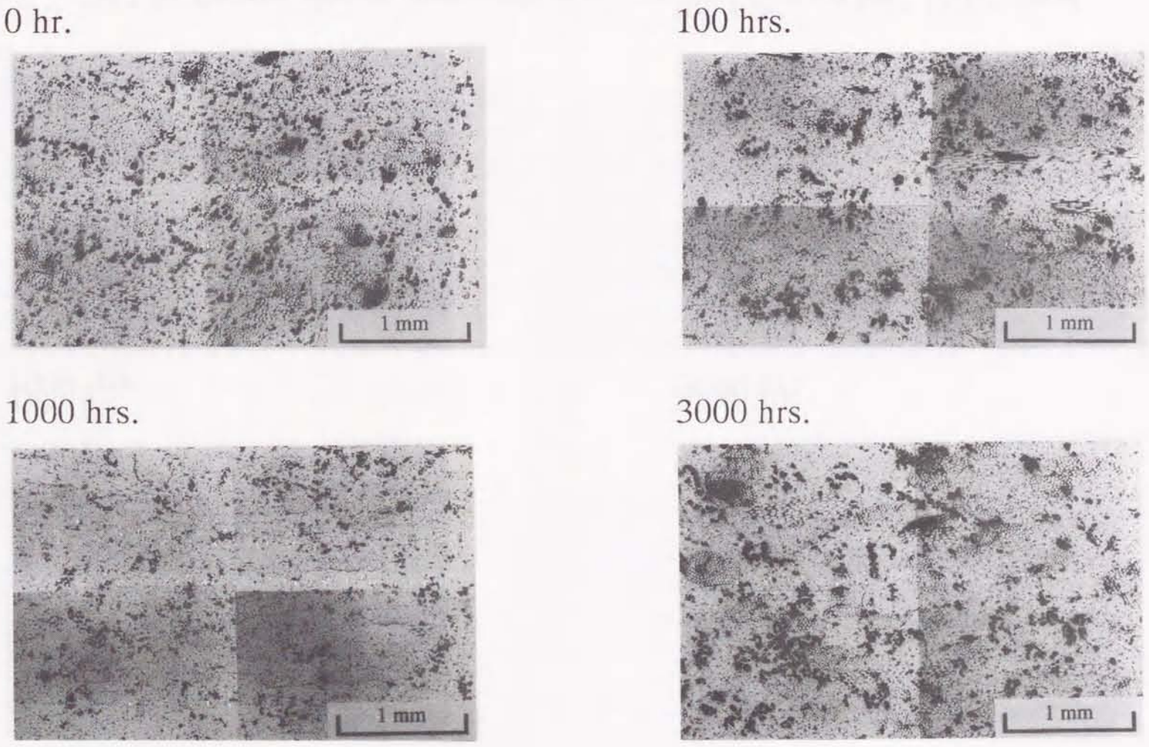

Fig.3.19 Continued; (b) *type-B*.

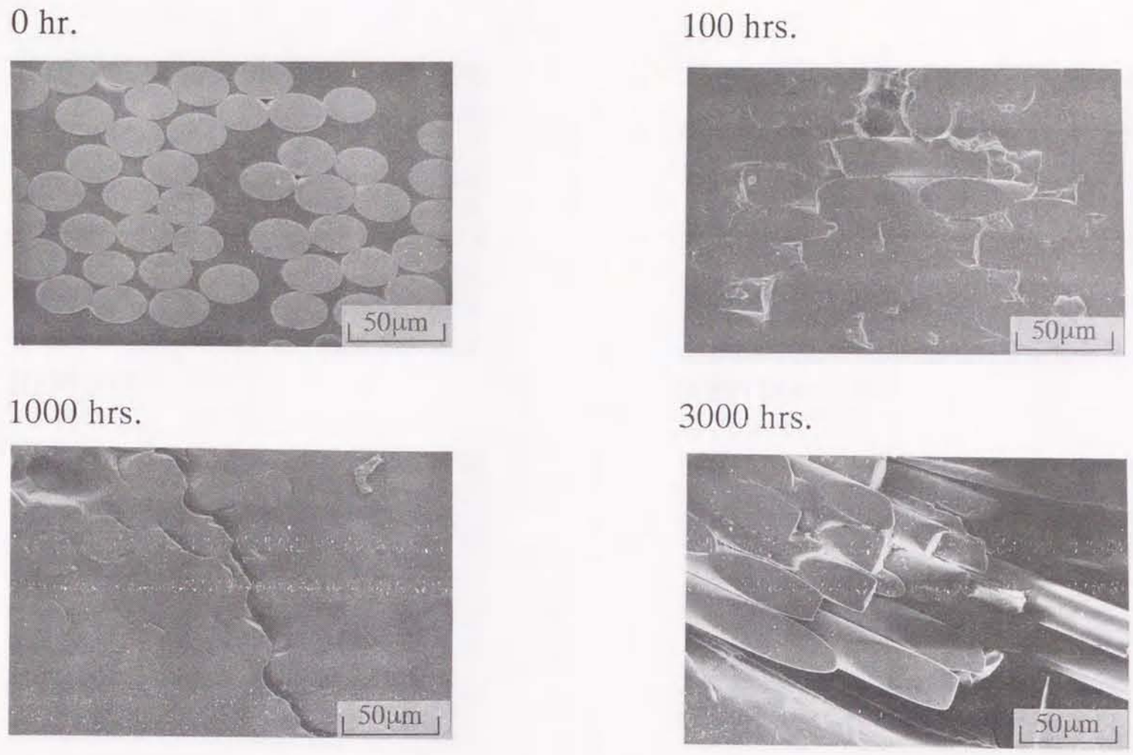

Fig.3.20 Scanning electron micrographs of cross-sections shown in Fig.3.19; (a) *type-A*.

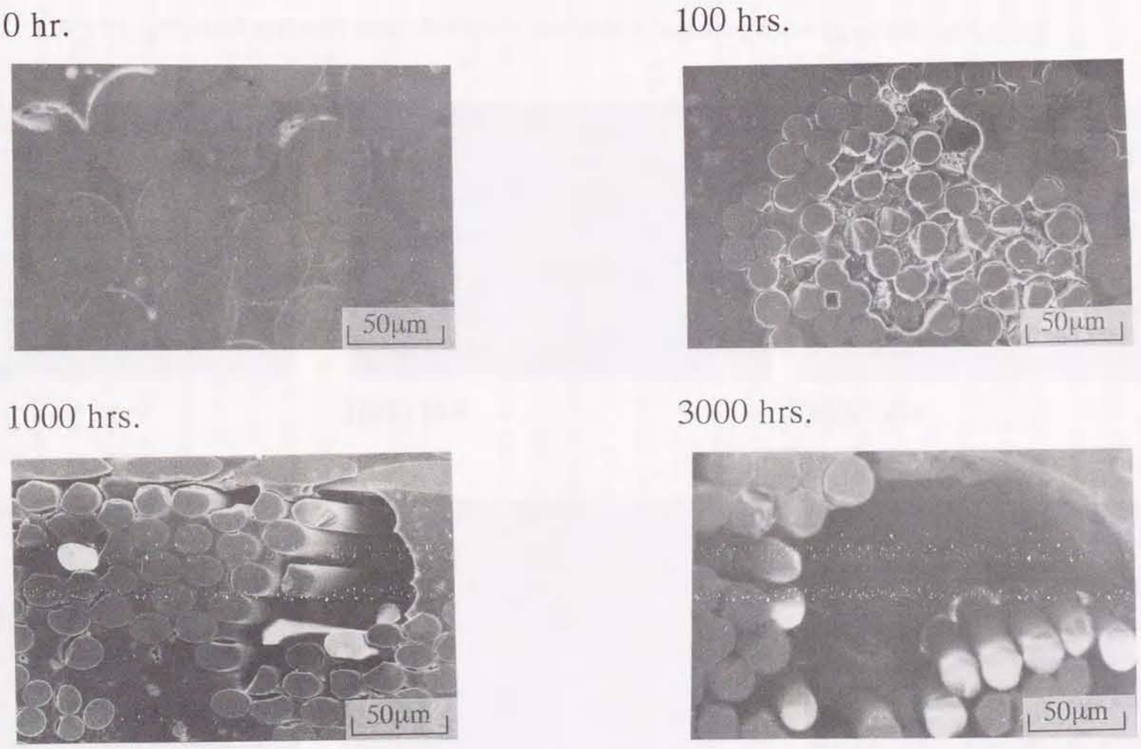

Fig.3.20 Continued; (b) *type-B*.

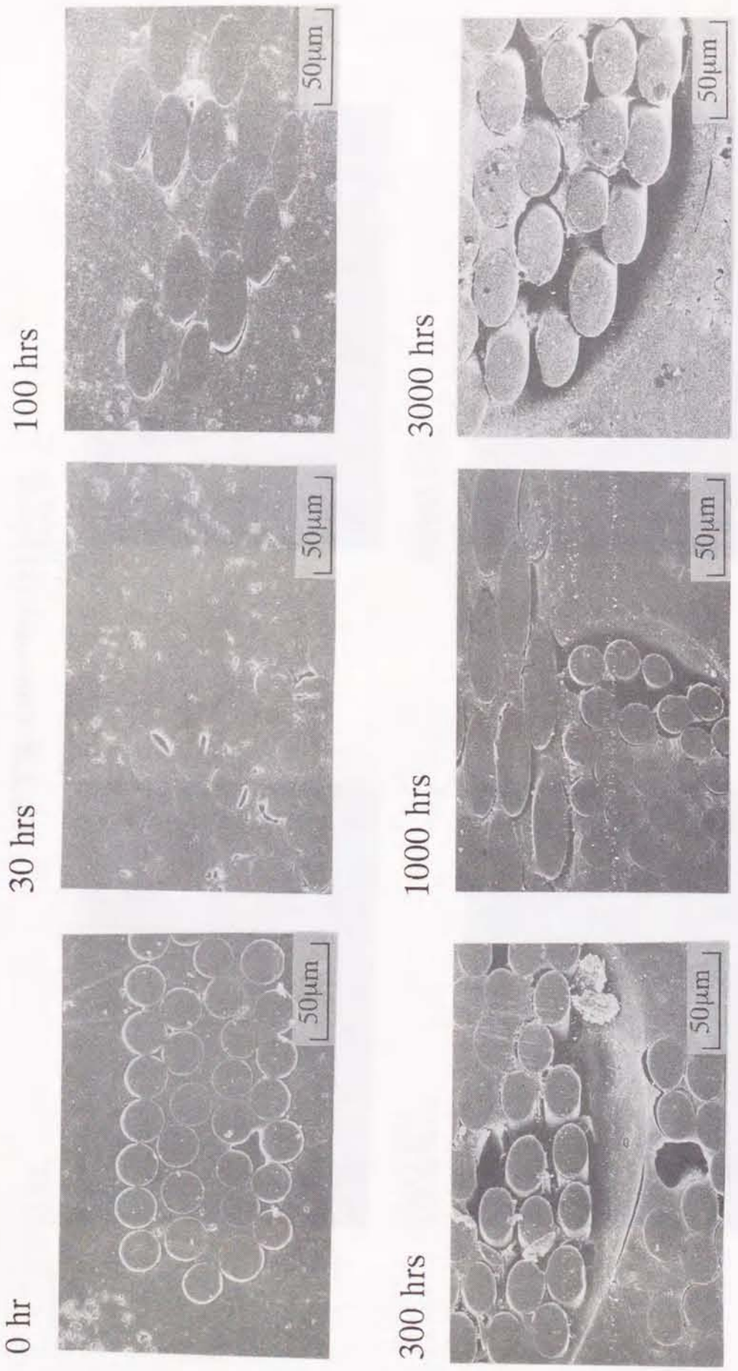

Fig.3.21 Scanning electron micrographs of randomly oriented glass-fiber mat reinforced vinylester resin after water immersion.

Matrix, fiber, silane coupling agent and binder exist in the interfacial region (which may be called as 'interphase'). From the microscopic observation, M_{gI} and M_{lI} is caused by the effect of interface, especially the binder and the silane coupling agent, and therefore M_{gI} and M_{lI} is closely related with the glass fiber mat. It is considered that the dissolved matter from FRP is the same with that from the glass fiber mat. Then, the glass fiber mat was immersed in hot water, and the residue was analyzed by FT-IR and TG. Fig.3.22 shows the IR spectrum of the residue after the immersion test. The absorbance by the ester groups can be observed at about 1730cm^{-1}, and this IR spectrum was similar to the typical spectrum of the unsaturated polyester shown in Fig.3.23. From this result, the main component of the residue after immersion test is unsaturated polyester. Unsaturated polyester was used as the binder in order to form the glass fiber mat, and this adhered on the fiber surface in powder form. The binder in powder form may easily dissolve into water through the fiber/matrix interface than the matrix resin in solid form. Then, the dissolved matter from FRP is considered to be the binder. TG curve for the residue after immersion is shown in Fig.3.24. The weight remarkably decreased over 200°C and reached a constant at about 600°C. The residue after TG measurement was about 35% of the total residue before TG measurement. It is found that 35% of the residue dissolved from glass fiber mat is the inorganic matter and 65% is the binder. Fig.3.25 shows the IR spectrum after TG measurement. The characteristic peak appeared at 1000~1100cm^{-1}, which was the same with the spectrum of SiO_2 shown in Fig.3.26. Consequently the residue after TG measurement is identified with SiO_2 contained in the silane coupling agent as well as in the glass fiber. Then, the dissolved matter from the glass fiber mat is considered to be the silane coupling agent and the glass fiber. From the results of FT-IR and TG analyses, the main matters dissolved from FRP is identified with the binder, the silane coupling agent and the fiber.

3.4 Discussion

The weight changes of FRP are the sum of the weight changes of resin part and interface part as mentioned in 3.2. The weight change of resin part affects the weight change behavior of FRP at relatively shorter immersion time, while that of interface part greatly affects the weight change of FRP at relatively longer immersion time. It was mentioned in 3.3 that the weight changes of the interface became larger as the volume of the interface increased. This suggests that the total amount of the interface affects greatly the weight change behavior of FRP at relatively longer immersion time. Even if the matrix, the reinforcement and the fiber surface treatment are the same, the different thickness of the interface part induces the difference of the weight changes of the interface. If the interface part in FRP is thick as shown in Fig.3.27, the total amount of the interface increases, so that larger M_{gI} and M_{lI} can be obtained.

If the dissolution occurs only from the interface and the amount of the interface is already known, $M_{lI}(\infty)$ can be obtained by multiplying the total amount of the interface by the density of dissolved matter. $M_{gI}(\infty)$ can be obtained by eqn(2.23) and obtained $M_{lI}(\infty)$ value. Moreover, the weight change behavior of FRP during longer immersion can also be predicted. However, the

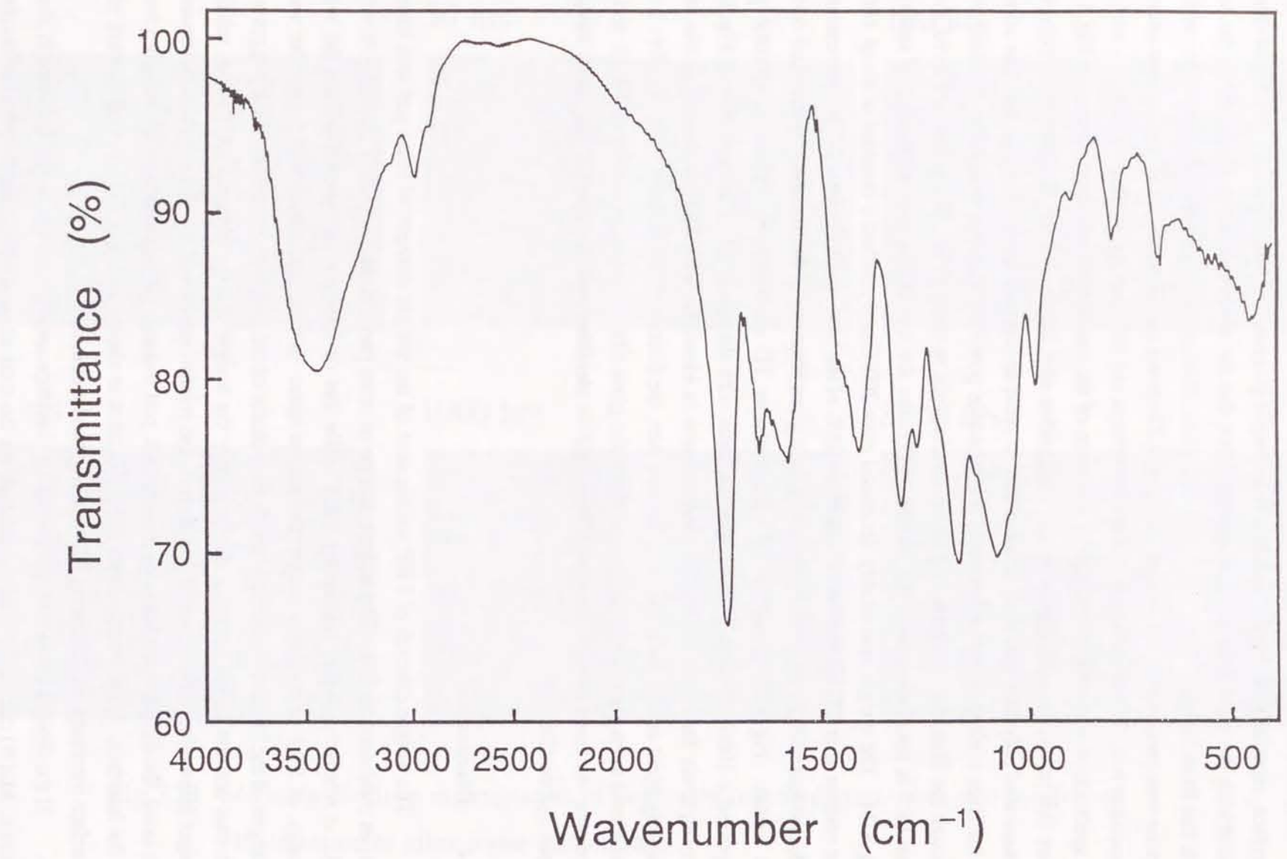

Fig.3.22 IR spectrum of residue after water immersion of glass-fiber mat.

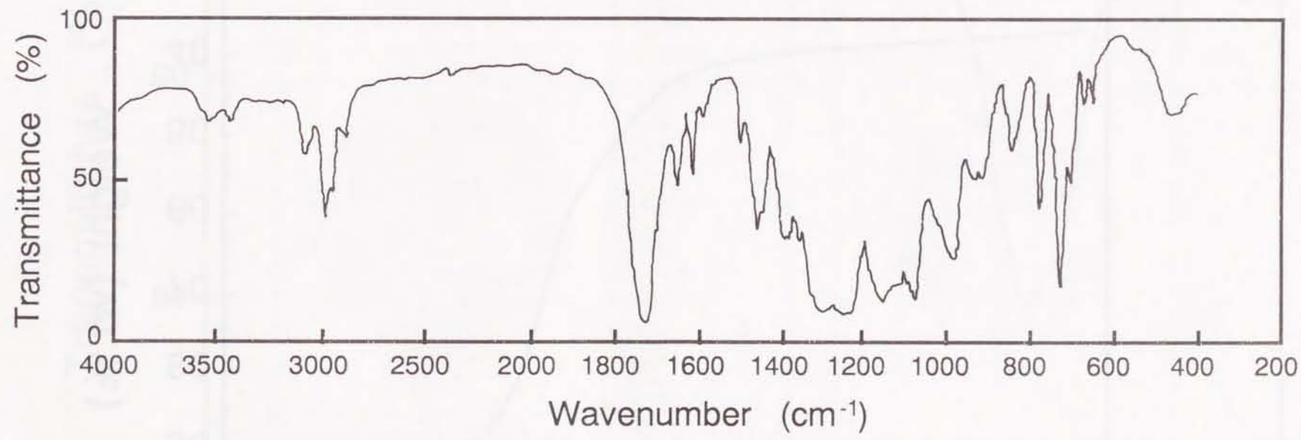

Fig.3.23 Typical IR spectrum of unsaturated polyester resin.

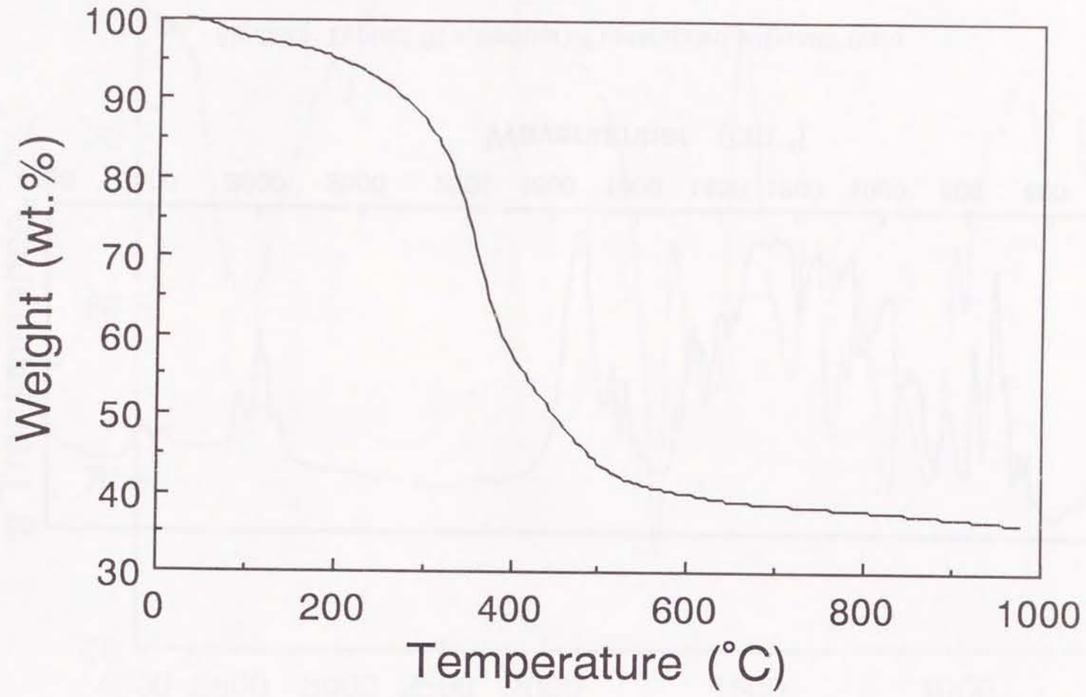

Fig.3.24 TG curve for residue after water immersion of glass-fiber mat.

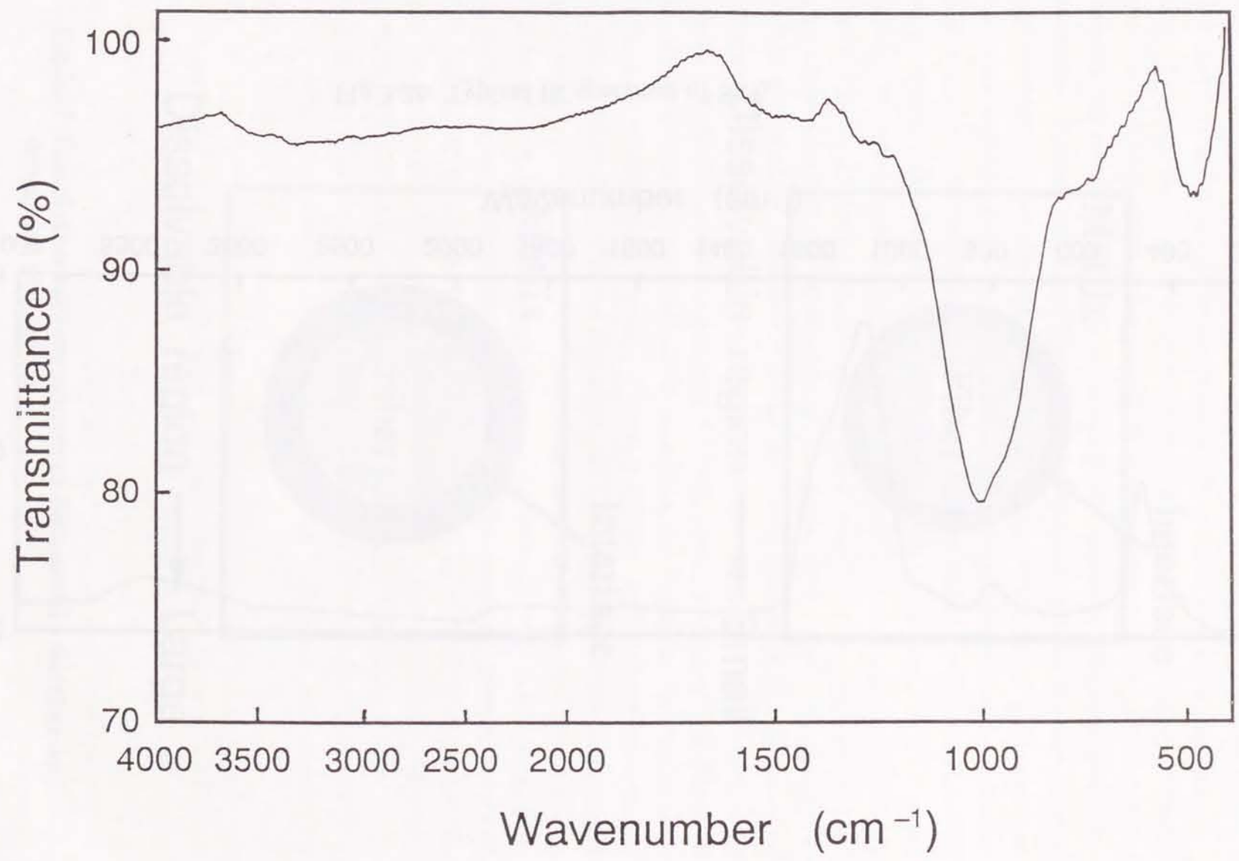

Fig.3.25 IR spectrum after TG measurement for residue.

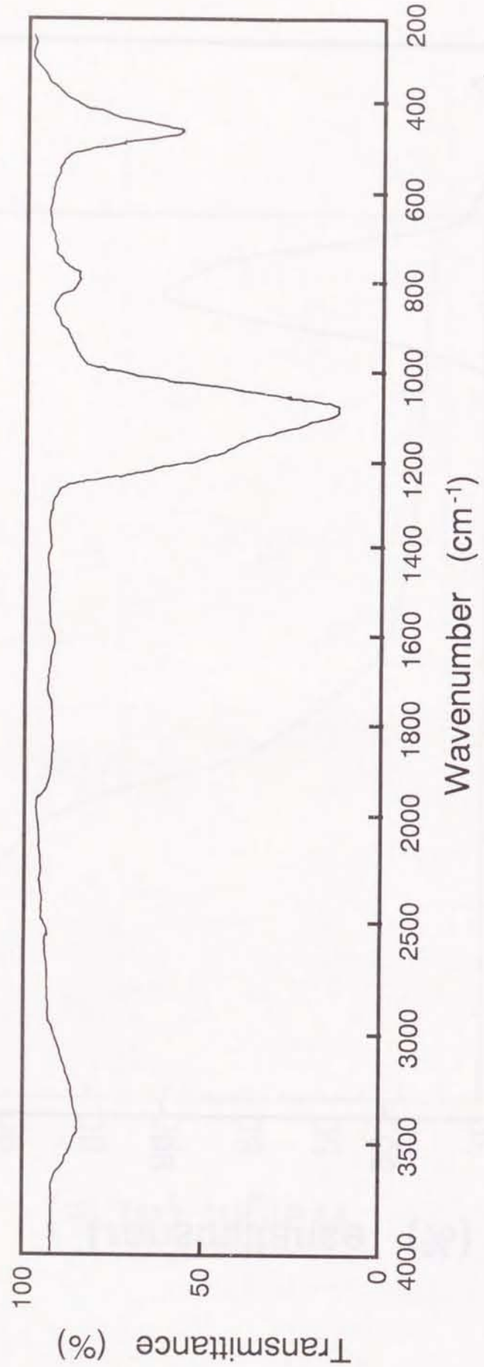

Fig.3.26 Typical IR spectrum of SiO_2.

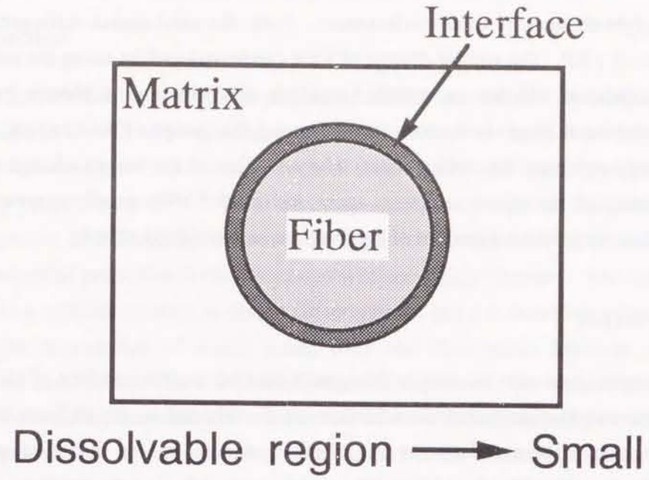

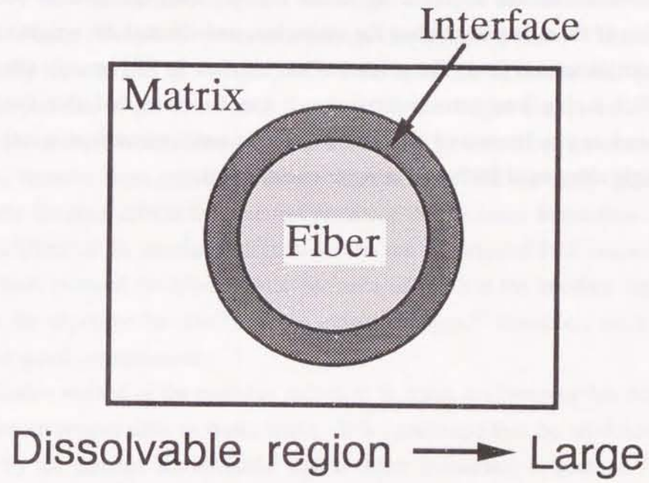

Fig.3.27 Correlation between amount of fiber/matrix interface and dissolution of interface.

material loss near the surface with matrix cracking occurs as shown in Fig.3.17, the prediction of $M_{II}(\infty)$ becomes much complicated.

From the above mentioned results, the design concept of FRP is discussed from the view-point of the weight changes in water environment. First, the used matrix resin greatly affects the weight changes of FRP. The weight change of FRP can be reduced by using the matrix resin with higher water resistance. However, satisfied result is only obtained at shorter immersion time. Little effect is shown at longer immersion time. Second, the design of the interface is important to the weight change at longer immersion time. The reduction of the weight change of FRP can be achieved by using of the silane coupling agent and binder with excellent water resistance in addition to minimizing the total amount of the interface as mentioned above.

3.5 Conclusion

This chapter dealt with the weight changes of the fiber/matrix interface of FRP immersed in hot water. The weight changes of the interface were evaluated as the difference of the weight changes between the FRP and the resin part of FRP. Moreover, the dissolved matter from the interface was analyzed by FT-IR and TG. The weight loss of the interface was originated from the dissolution of the binder, the silane coupling agent and the fiber existing in the interfacial region. The water penetrated into the dissolved interfacial region. Such phenomena occurred after the water absorption of the resin part reached the saturation, and affected the weight change behavior of FRP at longer immersion time. The amount of the interface in FRP greatly affected the weight changes of FRP during long-term immersion. It can be concluded that the design of the fiber/matrix interface (the amount of the interface and the surface treatment agent) is important to reduce the weight changes of FRP used in water environment.

Chapter 4 Elastic Property of Glass Fiber Reinforced Plastics Immersed in Hot Water

4.1 Introduction

It is well known that the mechanical properties of FRP are reduced by long-term exposure in wet environment as a result of weight changes. Many works have been done for the reduction of mechanical properties in wet environment such as static tensile and bending properties, fatigue properties, creep properties, etc.[56-78] Most of these works have reported that the reduction of mechanical properties is induced by the water absorption. Therefore it is considered that the reduction of mechanical properties is closely related with the weight changes. The elastic modulus is an important as a material constant to design the structures, and it is considered that the modulus is reduced by the degradation of matrix resin, fiber and fiber/matrix interface due to water immersion. Shen and Springer have discussed the relation between the weight changes and the tensile moduli,[11] however, the reduction mechanism of the moduli has not been clarified well. Pritchard and Speake have reported the prediction method of the mechanical properties based on the weight changes.[20] In this work, only the effect of the water absorption on the mechanical properties has been discussed. In fact, however, the degradation of the fiber/matrix interface in FRP is caused by the water immersion, and the weight loss due to dissolution as well as the weight gain due to water absorption occurs as mentioned in Chapter 2 and 3. Therefore it is also important to clarify the effect of the weight loss on the reduction of mechanical properties. In Chapter 3, the importance of the fiber/matrix interface on the weight change behavior has been clarified. From this fact, it is considered that the debonding between fiber and matrix causes the loss of the load transfer from matrix to fiber. Therefore, it can be easily guessed that the degradation of the interface affects the modulus reduction due to water immersion. Few works have clarified the effect of the interfacial degradation on the modulus of FRP immersed in water. Vaughan et al. have guessed the effects of the presence of water at the interface on the physical properties from the experimental results of the weight changes,[42] however, such effects have never been investigated experimentally.

The prediction method of the modulus reduction in water environment has been demanded to design the FRP structures such as water tanks. It is considered that the modulus reduction of FRP is caused by the damage accumulation due to water immersion in addition to the rigidity reduction of matrix by the hydrolysis. The mechanical properties of FRP with some internal damages can be estimated by introducing the damage mechanics. In FRP many types of the damages are caused such as matrix cracking, fiber breakage, debonding between fiber and matrix, delamination between laminae, etc. Most of the works for the damage mechanics of FRP have mainly dealt with the effect of the matrix cracking.[101-104] The focus of these works has been to determine the overall elastic and/or thermoelastic properties of FRP containing a specified array of cracks by introducing the micromechanics. These properties are estimated by averaging the local stress and strain fields. In FRP immersed in water, however, the debonding between fiber and

matrix is mainly occurred as mentioned in Chapter 3. Therefore the damages at the fiber/matrix interface must be considered in the damage mechanics for FRP immersed in water. Few works have estimated the mechanical response of FRP with the damages at interface (or interphase).[105] In such work, only the matrix cracking instead of the debonding is considered. The elastic properties of FRP with the debondings at the interface have never been estimated.

The purposes of this chapter are to clarify experimentally the relation between the weight changes and the elastic property and to estimate theoretically the changes of the elastic property due to water immersion. The elastic property is estimated by three point bending of FRP immersed in hot water, and the reduction mechanism of the elastic property is discussed. On the basis of the experimental results, the theoretical estimation method of the elastic modulus of the immersed FRP is established by introducing the damage mechanics.

4.2 Experimental Procedure

Materials used were three kinds of randomly oriented E-glass fiber continuous strand mat reinforced unsaturated polyester resins, and these were the same with those used in Chapter 2 (*type-A*, *type-B* and *type-C*), that is, *type-A* and *type-B* were the glass-fiber mat reinforced bisphenol based unsaturated polyester without and with filler, and *type-C* was the glass-fiber mat reinforced orthophthalic based unsaturated polyester. Using these materials, three kinds of square panels were fabricated by a compression molding. Fiber volume content for all the panels was about 35%.

Water immersion for the bending test specimens was conducted at 80°C with temperature controlled water baths. The periods of immersion were 3, 10, 30, 100, 300, 1000 and 3000 h. The bending elastic moduli were measured by three point loading for the specimens just after the immersion. The geometry of the bending specimen was 80mm × 15mm × 3.8mm. The bending test was performed for 5 specimens on each immersion time at a constant cross-head speed of 2 mm/min with a 60 mm span, at room temperature, using an Instron universal testing machine (type 4206).

4.3 Results and Discussion

4.3.1 Elastic property

Table 4.1 summarizes the bending modulus for each original dry specimen. The elastic modulus of *type-C* were the highest among all the specimens. The modulus of the orthophthalic based polyester resin is higher than that of the bisphenol based. Therefore, this result reflects the bending moduli of the resin matrix. The modulus of *type-B* was higher than that of *type-A*. The filler was effective in improving rigidity.

Fig.4.1 shows the dependence of bending modulus retention on the immersion time. All of the bending test data was presented in this figure. Complicated tendencies were appeared. However, some important aspects could be obtained. The moduli of *type-A* and *type-B* decreased

Table 4.1 Bending modulus of original dry specimens.

	type-A	*type-B*	*type-C*
Bending modulus (GPa)	7.56	8.39	9.51

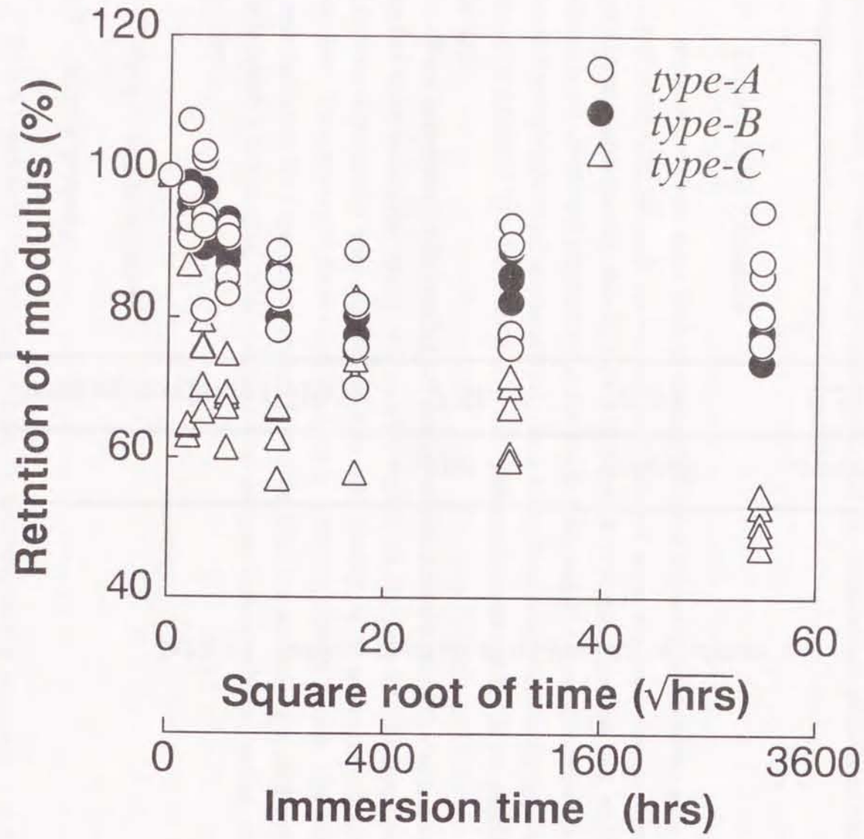

Fig.4.1 Retention of bending modulus as a function of the square root of immersion time.

to 100 h and kept almost constant after 100 h. In *type-C* the modulus decreased rapidly to 10 h and then kept almost constant, however, it decreased again after 3000 h. The constant elastic moduli after water immersion were about 80% of the values for the original dry specimens for *type-A* and *type-B*, and about 65% for *type-C*. The rigidity reduction of *type-C* due to water immersion was remarkable. It is considered that the reduction of modulus is caused by the weight changes such as water absorption, dissolution, etc. In this section, the modulus reduction is discussed with the aid of the weight change data presented in Chapter 2.

First of all, the relation between weight gain, weight loss and elastic properties was examined. Fig.4.2 shows the relation between the bending elastic modulus and the net weight gain (M_g). In this figure the data of *type-C* was plotted for the immersion time from 0 to 1000 h since the weight change data was obtained until 1000 h for *type-C*. The elastic moduli of *type-A* and *type-B* decreased linearly against M_g up to 1% and kept almost constant over 1% of M_g. No difference in the relation between modulus and M_g can be found between *type-A* and *type-B*. In *type-C* the modulus sharply decreased as a result only a little water absorption and after that it kept almost constant. The relation between the bending modulus and the weight loss (M_l) is shown in Fig.4.3. The modulus decreased in a process for which M_l was nearly equal to 0. After M_l started to rise, the modulus kept almost constant. In *type-C* M_l rose immediately after a little water absorption, so that the modulus soon reached a constant value. On the other hand, the changes of the moduli in *type-A* and *type-B* against M_g and M_l indicated the same tendency and the effect of the filler on the modulus reduction could not be found. Fig.4.4 shows the relation between the bending modulus and the weight gain of the interface (M_{gI}). The moduli of *type-A* and *type-B* decreased up to about 0.3% of M_{gI}, after which they kept constant. The effect of the filler never appeared in the relation between the modulus and M_{gI}. The modulus of *type-C* reached a minimum value before the increase of M_{gI}, and it kept a constant after M_{gI} started to increase. The relation between the modulus and the weight loss of the interface (M_{lI}) is shown in Fig.4.5. The moduli for all the specimens decreased and reached minimum values in a process for which M_{lI} was nearly equal to 0. After M_{lI} started to increase, the moduli kept constant values.

4.3.2 Discussion

The reduction of the bending elastic modulus depends on M_g, i.e., the water absorption, and no effect of the increase of M_l on the modulus reduction appeared. It is considered that the phase division discussed in Chapter 2 can be applied to discuss the mechanism of modulus reduction. Then, the dependence of the bending elastic modulus on M_g is divided into phase I, II and III in Figs.4.6-8. The modulus decreases linearly against M_g from phase I through phase II, while it retains a constant in phase III. If the modulus reduction of FRP is caused by only the degradation of matrix, the modulus must decrease only in phase I and must keep a constant in phase II. In fact, however, the modulus also decreases in phase II. Therefore it cannot be concluded that the main cause of the modulus reduction is only the degradation of matrix, and it can be easily supposed that the degradation of the fiber/matrix interface also affects the modulus

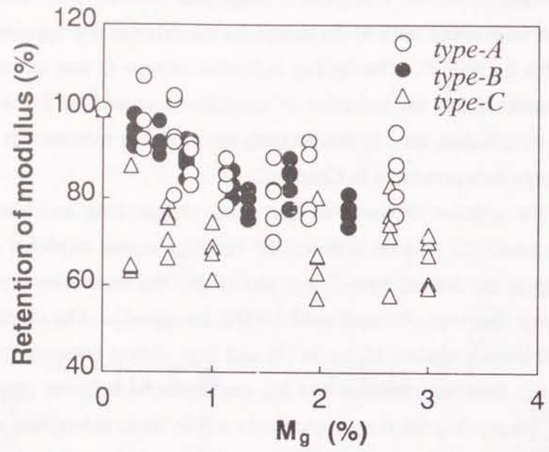

Fig.4.2 Relation between bending modulus and M_g.

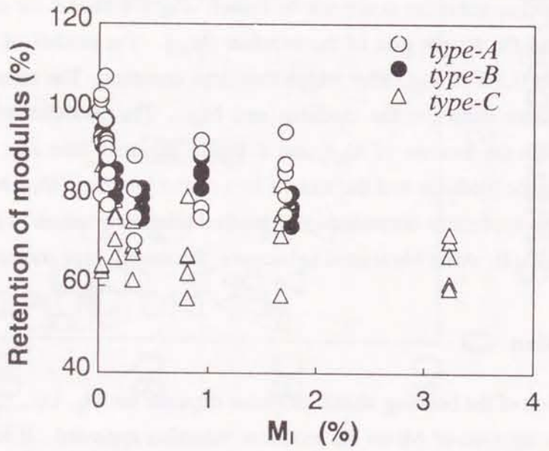

Fig.4.3 Relation between bending modulus and M_I.

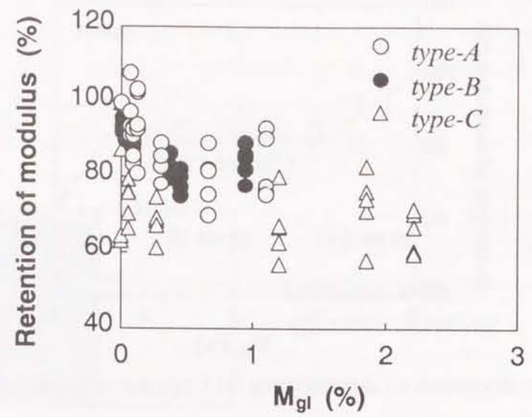

Fig.4.4 Relation between bending modulus and M_{gI}.

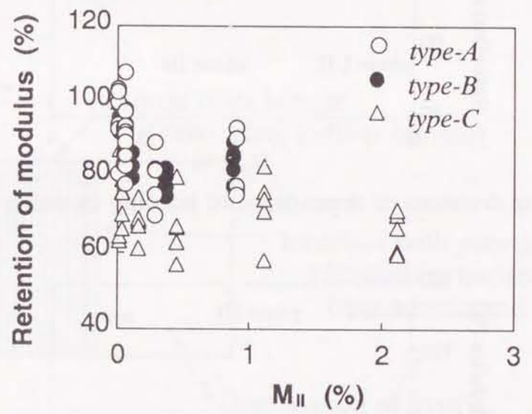

Fig.4.5 Relation between bending modulus and M_{II}.

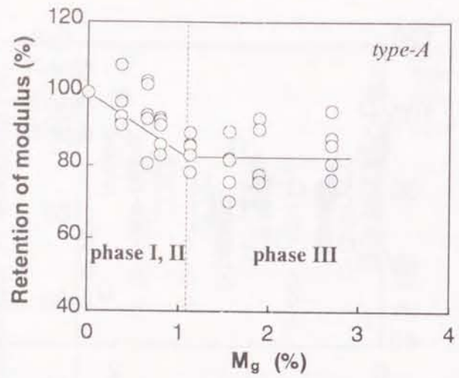

Fig.4.6 Phase divisions of dependence of bending modulus on M_g for *type-A*.

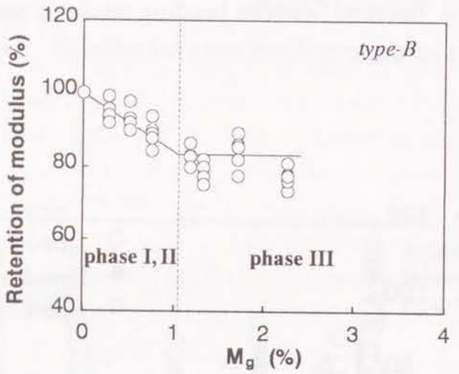

Fig.4.7 Phase divisions of dependence of bending modulus on M_g for *type-B*.

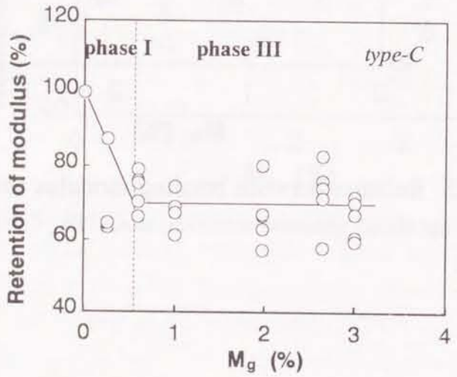

Fig.4.8 Phase divisions of dependence of bending modulus on M_g for *type-C*.

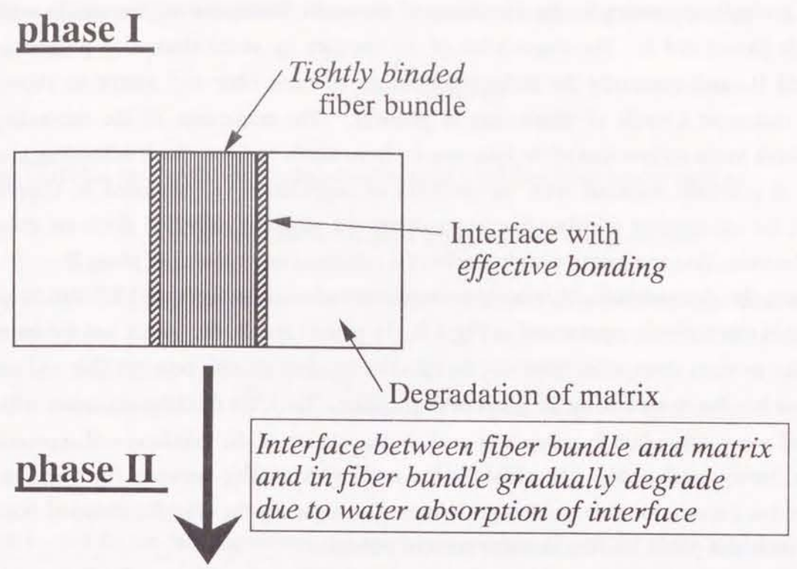

Fig.4.9 Reduction process and mechanism of bending modulus of FRP due to water immersion.

reduction. In phase I, the matrix absorbs the water, and then the modulus of matrix decreases. As mentioned in Chapter 3, the fiber/matrix interface also absorbs the water in phase I and II, and as a result, the applied load cannot be transferred well from matrix to fiber. Therefore the bending modulus gradually decreases by the interaction of the water absorption of the matrix and the interface in phase I and II. The degradation of the interface by water absorption progresses in phaseI and II, and eventually the serious debonding between fiber and matrix as shown in Fig.3.12 occurs as a result of dissolution in phase III. The occurrence of the debonding in phase III leads to the serious loss of the load transfer from matrix to fiber. Such debonding around the fiber is gradually enlarged with the progress of degradation as mentioned in Chapter 3. However, the enlargement of debonding never affects the modulus reduction since the bonding strength between fiber and matrix already reaches the minimum value at start of phase III.

From the above-mentioned results, the modulus reduction process of FRP due to water immersion is schematically represented as Fig.4.9. In phase I and II, the matrix and the interface degrade due to water absorption, however, the effective bonding remains between fiber and matrix and in fiber bundles in spite of the progress of degradation. Then, the modulus decreases with the increase of water absorption in matrix and gradual degradation of the interface, and apparently it decreases linearly against M_g. In phase III, the serious debonding between fiber and matrix occurs, and as a result, the fiber bundles get loosen. Consequently the effective chemical bonding never exists in this phase, and the modulus remains a constant.

4.4 Evaluation of Modulus Reduction Based on Damage Mechanics

4.4.1 Concept of damage mechanics

Usually material accumulates the various internal damages under mechanical loading and/or corrosive environment. When the damage accumulation in the material amounts to the maximum allowable damage, the material properties are led to the minimum value. Therefore the evaluation of the damage accumulation is important to estimate the various properties of the materials. Damage mechanics is established as a mechanics dealing with the damage accumulation and its influence on the various properties of the materials. In the damage mechanics, the damage accumulation in the material, D, is generally expressed as the value from 0 to 1. No damage is expressed as $D = 0$, and the maximum allowable damage is expressed as $D = 1$. When the D value reaches 1, the material property is led to the minimum value. Therefore the definition and the modeling of the damage accumulation are the essential problems in the damage mechanics. Moreover, the influence of the damage accumulation on the material property must be established.

4.4.2 Modeling of internal damage on FRP immersed in hot water

This section deals with the modeling of the randomly oriented FRP immersed in water to predict the elastic modulus. At first, the expression of the modulus of the randomly oriented FRP is considered.

The randomly oriented FRP has elastic properties which are macroscopically isotropic since there is a uniform probability distribution over the entire range of angles from $-\pi/2$ to $+\pi/2$.[2] For long fibers the effect of fiber ends can be neglected in predicting the moduli. Therefore the modulus of randomly oriented FRP, $\bar{E}$, can be obtained by integrating the expression

$$\bar{E} = \frac{2}{\pi}\int_0^{\frac{\pi}{2}} \overline{Q_{11}}(\theta)\, d\theta \tag{4.1}$$

where $\overline{Q_{11}}(\theta)$ is the transformed reduced stiffness of a unidirectional lamina such as

$$\overline{Q_{11}}(\theta) = Q_{11}\cos^4\theta + 2(Q_{12} + 2Q_{66})\cos^2\theta\sin^2\theta + Q_{22}\sin^4\theta. \tag{4.2}$$

In eqn(4.2) Q_{11}, Q_{12}, Q_{22} and Q_{66} are the reduced stiffness of a unidirectional lamina and are given by

$$Q_{11} = \frac{E_1}{1 - \nu_{12}\nu_{21}}, \quad Q_{22} = \frac{E_2}{1 - \nu_{12}\nu_{21}}, \qquad Q_{12} = \frac{\nu_{21}E_1}{1 - \nu_{12}\nu_{21}}, \quad Q_{66} = G_{12} \tag{4.3}$$

where E_1 and E_2 are the longitudinal and transverse moduli, G_{12} is the shear modulus, and ν_{12} and ν_{21} are the Poisson's ratios given by $-\varepsilon_2/\varepsilon_1$ and $-\varepsilon_1/\varepsilon_2$, respectively. On substituting for $\overline{Q_{11}}(\theta)$ from eqn(4.2) in eqn(4.1), $\bar{E}$ is given by

$$\bar{E} = \frac{3(E_1 + E_2) + 2\nu_{21}E_1 + 4G_{12}(1 - \nu_{12}\nu_{21})}{8(1 - \nu_{12}\nu_{21})}. \tag{4.4}$$

Eqn(4.4) is too complicated for most practical case. Therefore, eqn(4.4) is simplified by assuming $\nu_{12}=\nu_{21}=0$ and $G_{12}=E_2/2$, and then eqn(4.4) is reduced to

$$\bar{E} = \frac{3}{8}E_1 + \frac{5}{8}E_2. \tag{4.5}$$

Consequently the modeling for predicting the modulus of randomly oriented FRP is simplified to the modeling for predicting the longitudinal and transverse moduli of a unidirectional lamina.

The longitudinal and transverse moduli of a unidirectional lamina are often obtained by the rule of mixtures such as

$$E_1 = E_f V_f + E_m(1 - V_f), \qquad E_2 = \frac{E_f E_m}{E_f(1 - V_f) + E_m V_f} \tag{4.6}$$

where E_f and E_m are the moduli of fiber and matrix respectively and V_f is the fiber volume fraction. In the rule of mixtures the influence of the fiber/matrix interface on the moduli is neglected, and therefore eqn(4.6) is unsuitable for predicting E_1 and E_2 for the unidirectional

lamina with some damage at fiber/matrix interface. Then, the finite element method (FEM) is adopted here for predicting E_1 and E_2 because the complicated material system can be easily expressed by dividing the material into the finite elements with different material properties.

The finite element modeling is done for a unit cell of the unidirectional lamina which contains only one fiber. Fig.4.10 represents the finite element models of the unidirectional lamina adopted here. The individual models were adopted for the analyses of the longitudinal and the transverse moduli, respectively. These models were consisted of the elements of matrix, fiber and interface. The fiber diameter was 20μm and the fiber volume fraction was 20%. The thickness of the interface was determined as 4μm, which was the maximum thickness of debonding of the degraded FRP obtained by the microscopic observation of the cross-section. The model for E_1 (Fig.4.10(a)) was divided by the two-dimensional plane stress triangle elements, while that for E_2 (Fig.4.10(b)) was divided by the two-dimensional plane strain triangle elements. The applied material constants are summarized in Table 4.2. Here, the damage was expressed by debonding at the fiber/matrix interface. The modulus of damaged element was reduced from 5GPa to 1MPa. The boundary conditions at the analyses are shown in Fig.4.11. The constrained uniform displacements were applied to the nodes at the one side of the models, and the reaction forces at each node were obtained. The elastic moduli were calculated from the applied displacement and the reaction forces.

The effect of damage progress at the interface on the modulus is discussed. It is considered that the damage starts to progress from the fiber surface and that the damage thickness becomes greater with the degradation progress. Then, the effect of the damage thickness on the modulus should be clarified. Fig.4.12 shows the relation between elastic moduli (E_1, E_2 and $\bar{F}$) and the damage thickness. It was assumed as illustrated in Fig.4.13 that the damage occurred in the circumference of the fiber and that the damage only thickened with the degradation. E_1 kept almost constant in spite of the damage of the interface, and it was little affected by the damage. On the other hand, E_2 was remarkably reduced with the increase of the damage thickness. Consequently, the changes of $\bar{F}$ calculated by eqn(4.5) from E_1 and E_2 indicated the same tendency with that of E_2. Therefore, only the effect of E_2 on $\bar{F}$ is discussed hereinafter.

Practically, the debonding around the fiber occurs locally as illustrated in Fig.4.14, which is verified by the microscopic observation of the cross-section of the degraded FRP. Accordingly the results in Fig.4.12 can be regarded as the minimum moduli under each damage thickness. The localized debonding in Fig.4.14 progresses along the fiber surface, and the angle of debonding gradually becomes wider with the degradation.

Here, it is assumed that the damage (debonding) with constant thickness progresses along the fiber surface as illustrated by the allows in Fig.4.14. Under this assumption, the changes of E_2 with the damage progress were analyzed, and the changes of $\bar{F}$ was obtained from this result. The damage angles around the fiber were 45°, 135°, 225°, 315° and 360° (complete debonding) as illustrated in Fig.4.15. Fig.4.16 shows the dependence of the retention of $\bar{F}$ on the damage thickness as a function of the damage angle, and Fig.4.17 shows the dependence of the retention of $\bar{F}$ on the damage angle as a function of the damage thickness. $\bar{F}$ decreased with the increase of

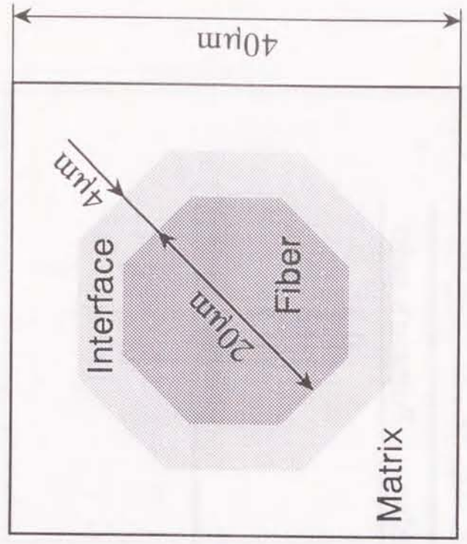

(b)

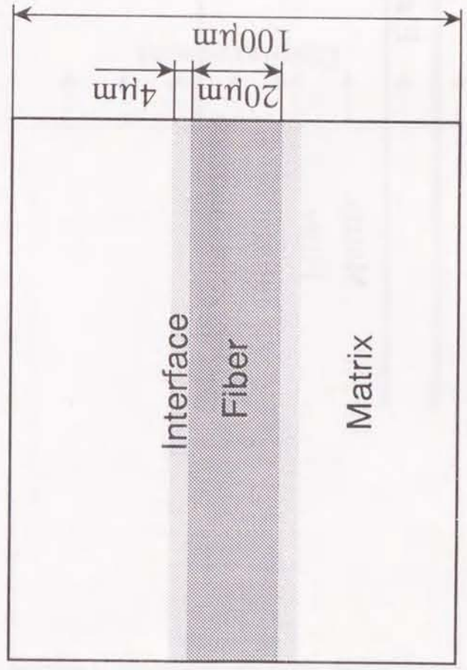

(a)

Fig.4.10 Finite element models of unidirectional lamina for analyses of (a) longitudinal modulus and (b) transverse modulus.

Table 4.2 Material constants for finite element analyses.

	Elastic modulus	Poisson's ratio
Matrix	5 GPa	0.3
Fiber	76 GPa	0.3
Interface	5 GPa	0.3
Degraded interface	1 MPa	0.3

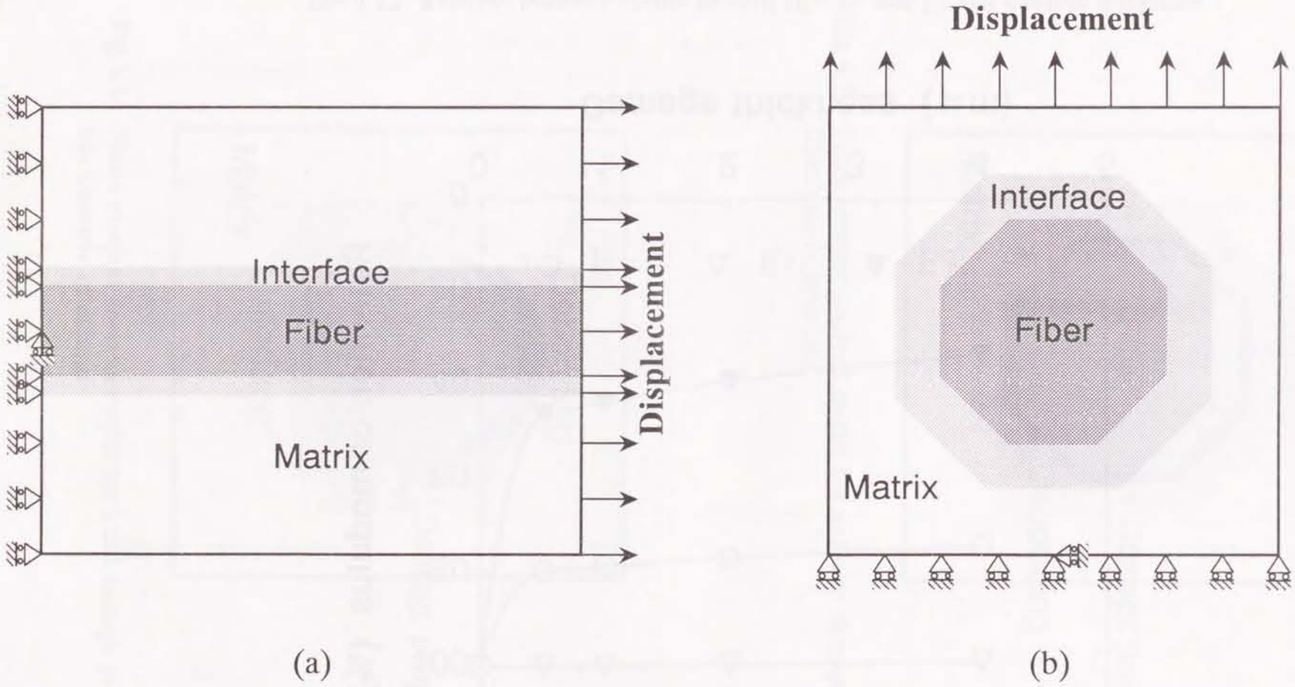

Fig.4.11 Boundary conditions for finite element analyses of (a) longitudinal modulus and (b) transverse modulus.

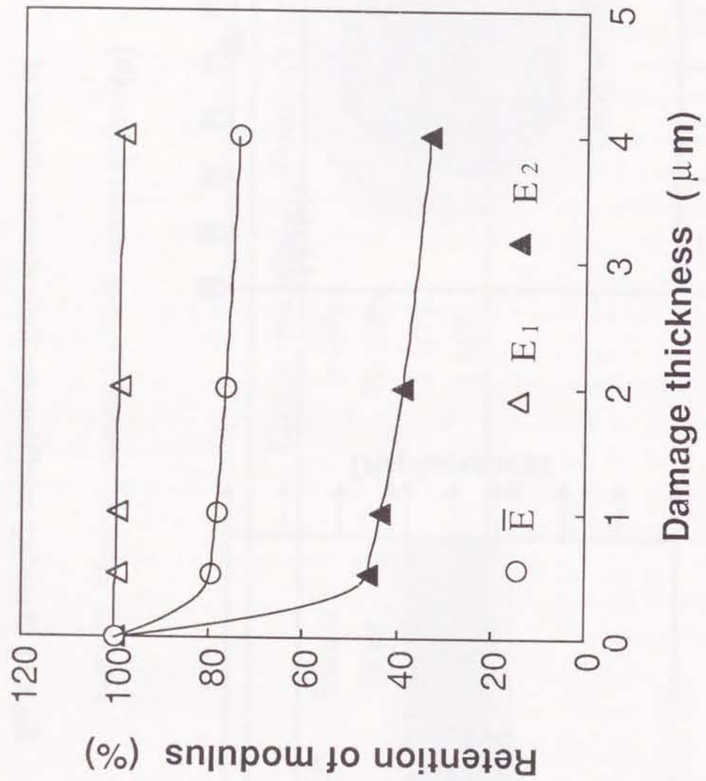

Fig.4.12 Relation between elastic moduli (E_1, E_2 and $\bar{E}$) and damage thickness.

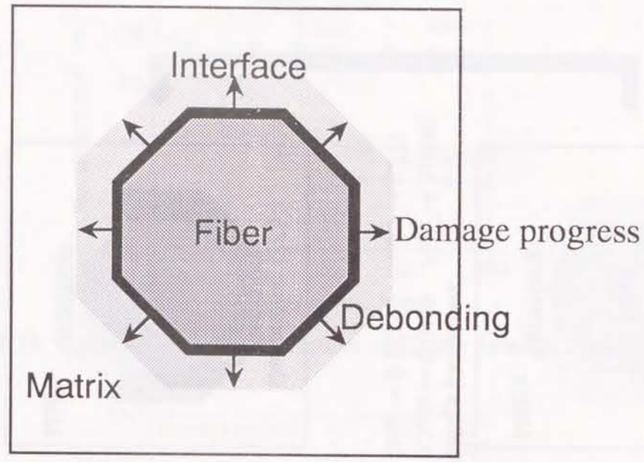

Fig.4.13 Finite element analysis model for uniform damage progress at fiber/matrix interface.

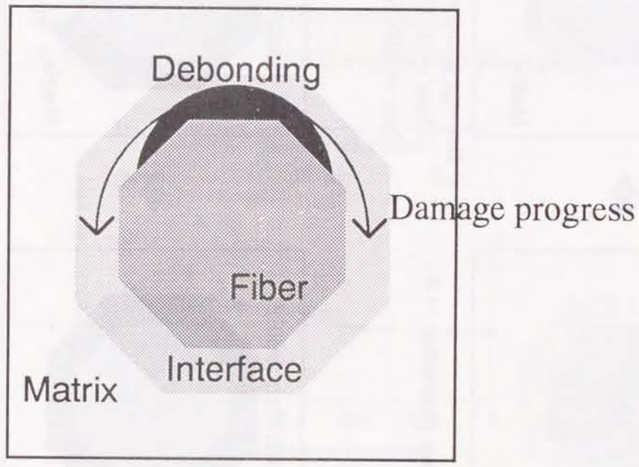

Fig.4.14 Finite element analysis model for local damage progress at fiber/matrix interface.

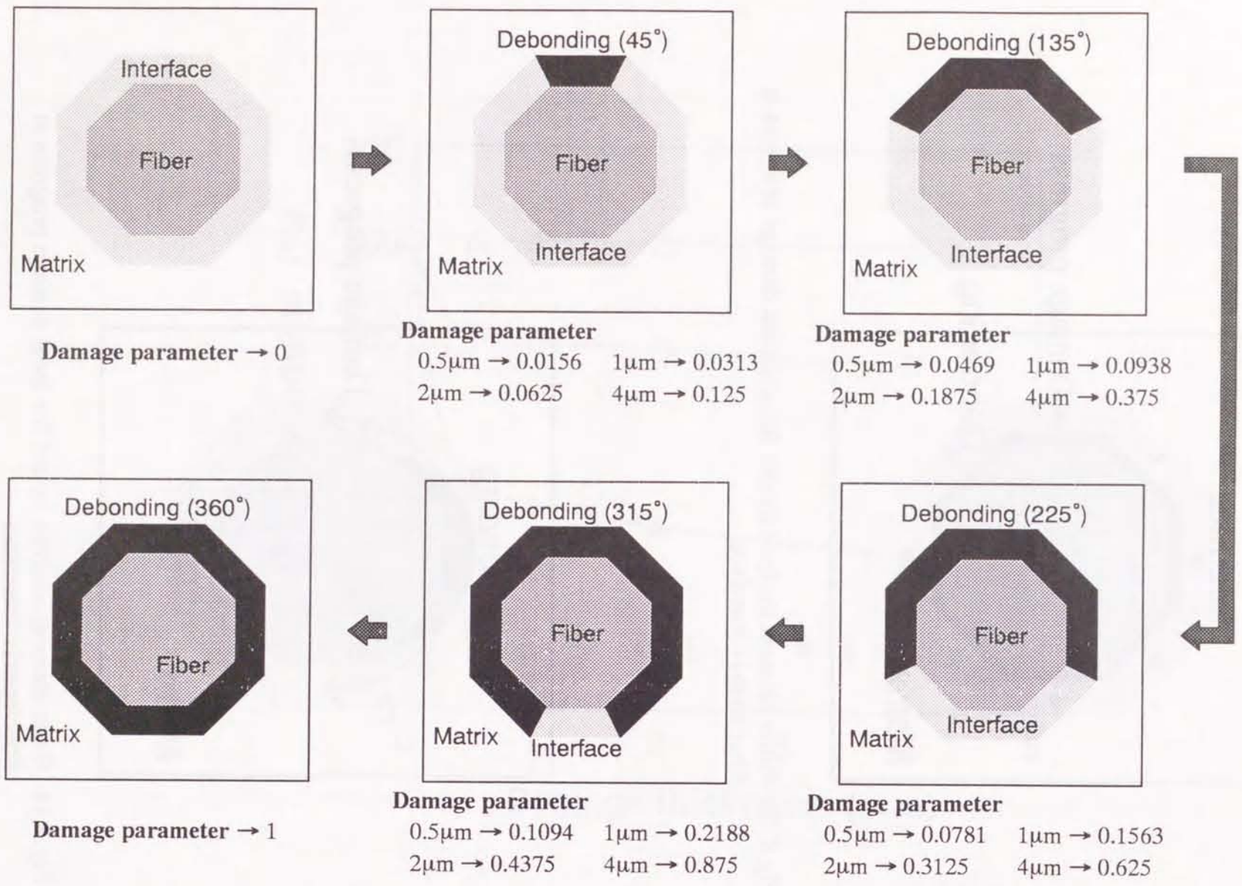

Fig.4.15 Patterns of damage progress at fiber/matrix interface and their damage parameters for finite element analyses.

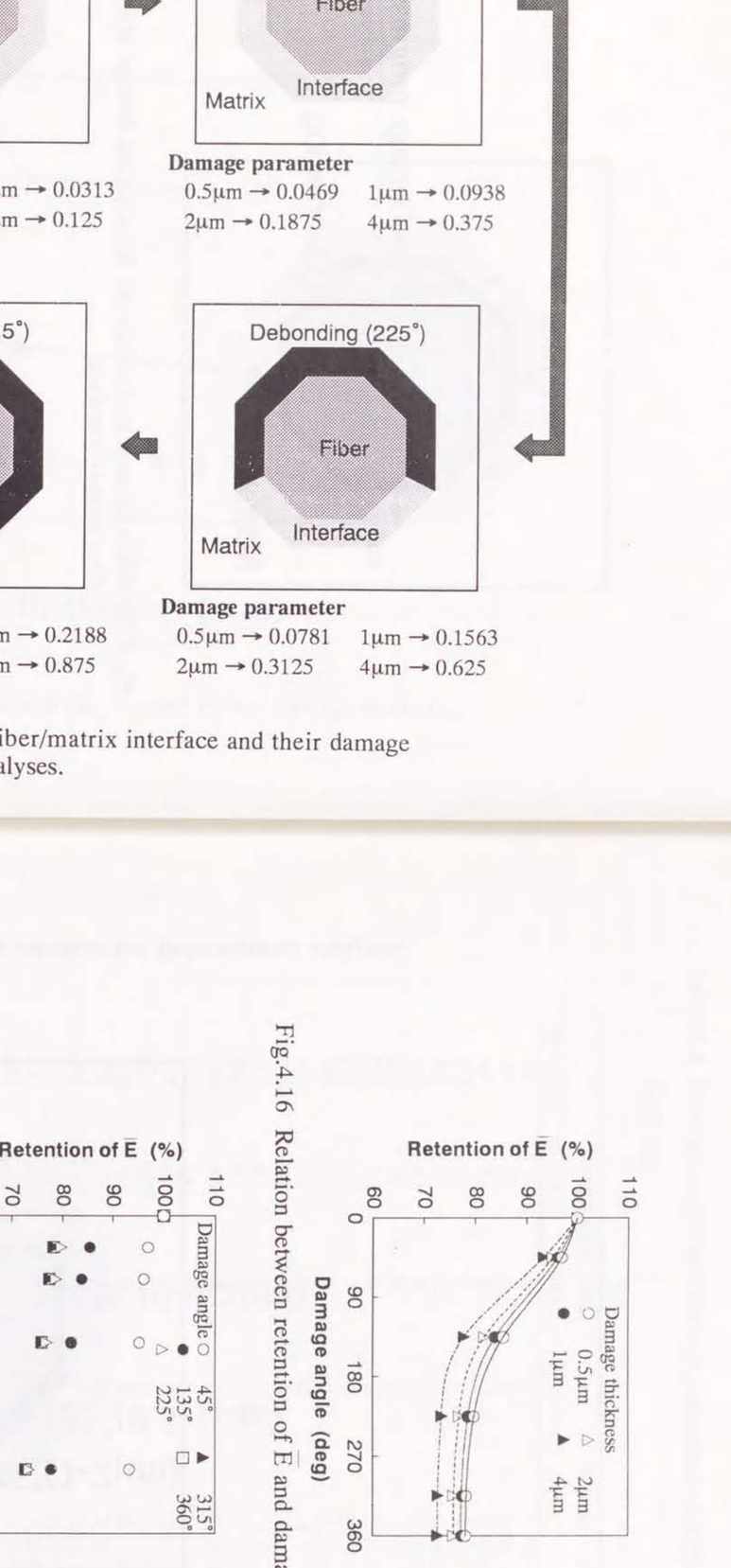

Fig.4.16 Relation between retention of $\bar{E}$ and damage angle.

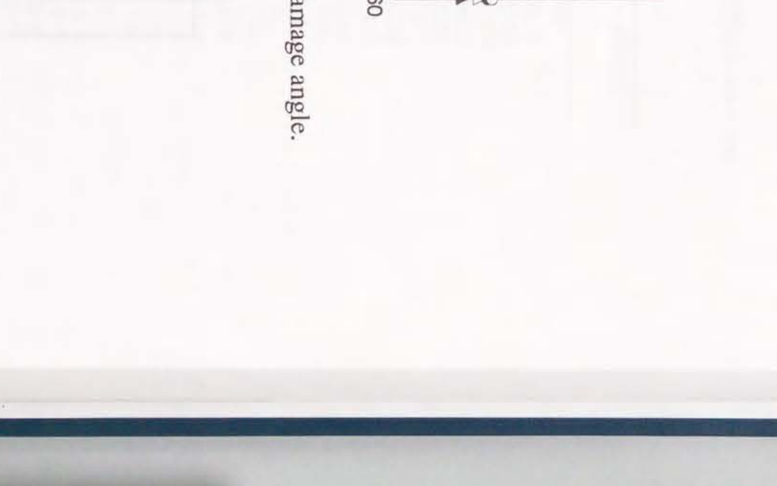

Fig.4.17 Relation between retention of $\bar{E}$ and damage thickness.

Fig.4.18 Relation between retention of $\bar{E}$ and damage parameter.

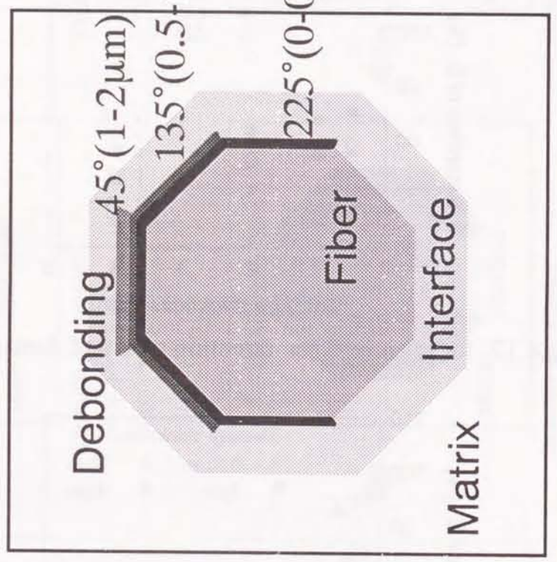

Fig.4.19 Damage pattern at fiber/matrix interface for finite element analyses.

Table 4.3 Damage angles and damage parameters for finite element analyses.

Damage angle (deg)				Damage parameter
0-0.5μm	0.5-1μm	1-2μm	2-4μm	
0	0	0	0	0
45	0	0	0	0.0156
45	45	0	0	0.0313
135	0	0	0	0.0469
45	45	45	0	0.0625
135	45	0	0	0.0625
225	0	0	0	.0781
225	45	0	0	0.0938
135	135	0	0	0.0938
315	0	0	0	0.1094
45	45	45	45	0.125
225	135	0	0	0.125
315	45	0	0	0.125
360	0	0	0	0.125
360	45	0	0	0.1406
225	135	45	0	0.1563
315	135	0	0	0.1563
225	225	0	0	0.1563
360	135	0	0	0.1719
135	135	135	0	0.1875
315	225	0	0	0.1875
315	135	45	0	0.1875
360	225	0	0	0.2031
360	135	45	0	0.2031
315	225	45	0	0.2188
315	315	0	0	0.2188
360	315	0	0	0.2344
360	225	45	0	0.2344
135	135	135	45	0.25
360	360	0	0	0.25
360	315	45	0	0.2656
315	225	135	0	0.2813
360	225	135	0	0.2969
225	225	225	0	0.3125
360	315	135	0	0.3281
135	135	135	135	0.375
225	225	225	45	0.375
360	315	225	0	0.3906
315	315	315	0	0.4375
225	225	225	135	0.5
315	315	315	45	0.5
360	360	360	0	0.5
360	360	360	45	0.5
360	360	360	45	0.5625
225	225	225	225	0.625
315	315	315	135	0.625
360	360	360	135	0.6875
315	315	315	225	0.75
360	360	360	225	0.8125
315	315	315	315	0.875
360	360	360	315	0.9375
360	360	360	360	1

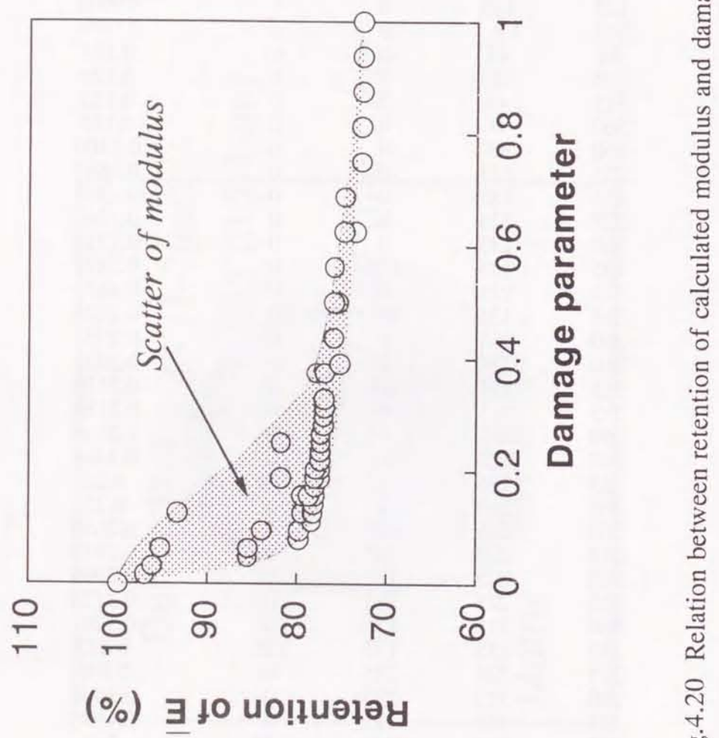

Fig.4.20 Relation between retention of calculated modulus and damage parameter.

the damage angle, and it decreased little at the damage angles over about 180°. Even if the damage thickness was different, the differences between each $\bar{E}$ were very few. Therefore the damage thickness little affects the reduction of $\bar{E}$, on the other hand, the damage angle greatly affects the reduction of $\bar{E}$. The damage parameter (P) was defined as the ratio of the damage area to the total area of the interface, that is;

$$P = \frac{h}{4} \times \frac{\theta}{360} \tag{4.7}$$

where h is the damage thickness and θ is the damage angle. For example, when the damage thickness was 1μm and the damage angle was 135°, the damage parameter was obtained by

$$P = \frac{1}{4} \times \frac{135}{360} = 0.09375. \tag{4.8}$$

In Fig.4.15 the damage parameters of each case are indicated. Fig.4.18 shows the relation between the retention of $\bar{E}$ and the damage parameter. Even if the damage parameter is the same, the reduction of $\bar{E}$ was different according to the damage thickness.

The effect of the damage patterns on the modulus is discussed. Fig.4.19 shows the damage pattern adopted here. It is assumed from the microscopic observation of cross-section that the angle of the outer damage is shallower than that of the inner damage. Based on this assumption, $\bar{E}$ of FRP with damage at the interface listed in Table 4.3 was calcuiated. Table 4.3 also lists the damage parameter of each damage at the interface. The relation between the calculated $\bar{E}$ and the damage parameter is shown in Fig.4.20. $\bar{E}$ was scattered broadly up to the damage parameter of 0.4, however, it was almost the same over 0.4. In the experimental result, the scatter of modulus was very remarkable. Therefore it is considered that the scatter of modulus is caused by the influence of damage pattern at the interface.

4.4.3 Evaluation of modulus reduction on FRP immersed in hot water

In Chapter 3, it has been clarified that the weight loss of the fiber/matrix interface (M_{II}) is mainly caused by the dissolution of the interface. As a result of the dissolution, the debonding occurs at the interface. Therefore the changes of the weight loss can represent the damage accumulation at the fiber/matrix interface. In *type-A*, M_{II} was equal to M_I since the dissolution of the resin never occurred. Then, M_I can represent the damage accumulation in *type-A*. Here, the evaluation of the modulus in *type-A* is discussed.

As mentioned in Chapter 2, the changes of M_I have been considered to be a kind of the Fickian diffusion behavior since M_I increases linearly against the square root of immersion time. Accordingly the degree of the weight loss ($M_I/M_I(\infty)$) in the material can be calculated by using D_I proposed in Chapter 2 as diffusion coefficient. D_I at 80°C in *type-A* was 1.84×10^{-3} mm^2/h as listed in Table 2.7. Here, the finite element analysis was used and the half-thick FRP panel was divided into 8 layers in thick direction. Each layer was divided by the triangular elements as shown in Fig.4.21. The boundary conditions for analysis are also shown in Fig.4.21. 100%

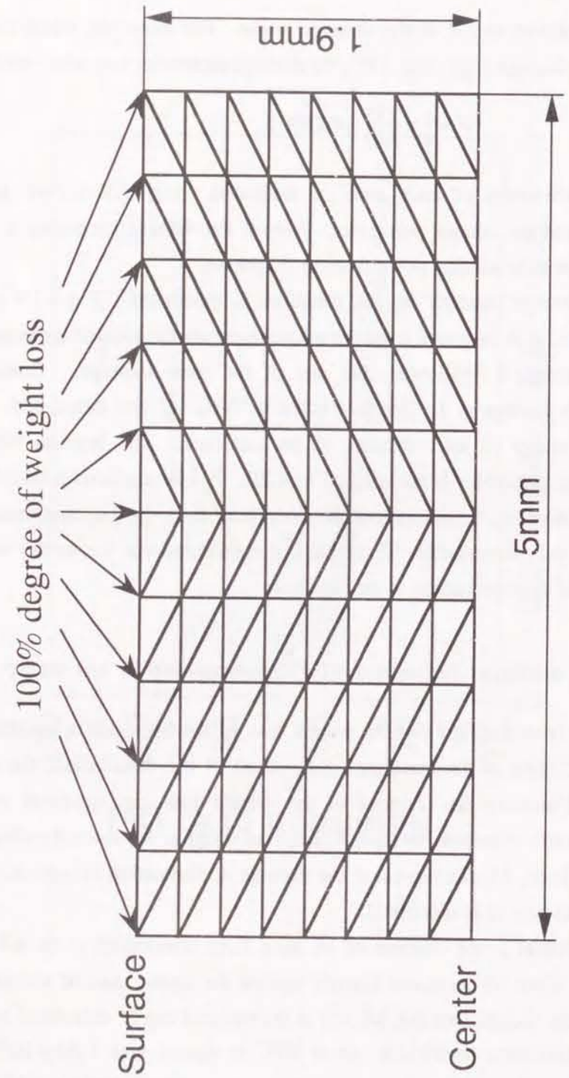

Fig.4.21 Finite element division and boundary conditions for weight loss analyses.

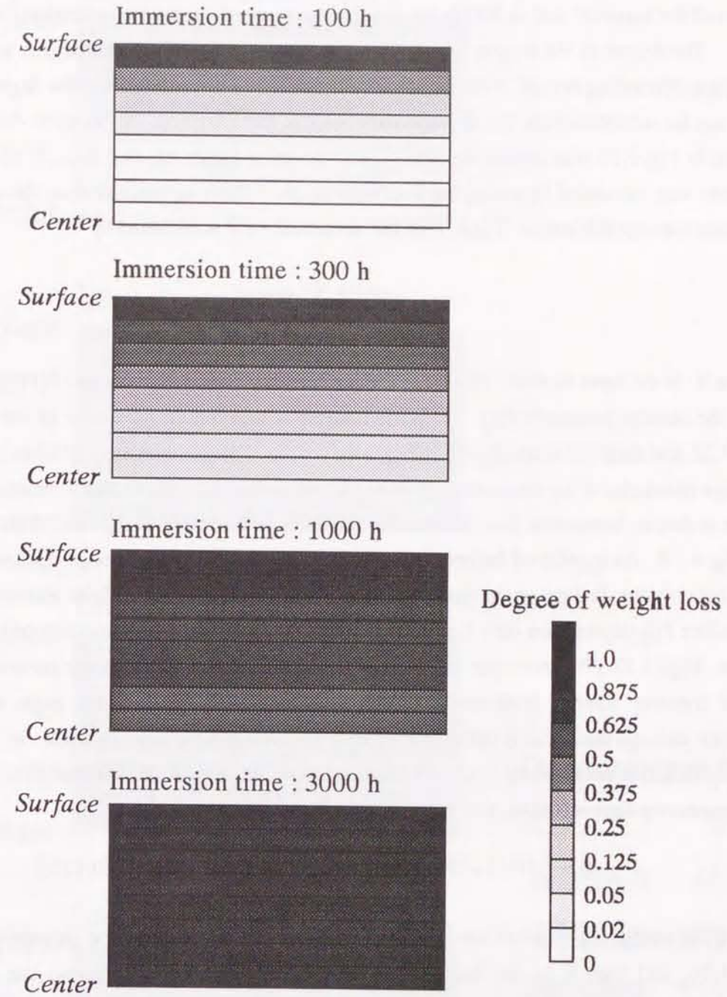

Fig.4.22 Degree distribution of weight loss calculated by finite element analyses.

degree was applied to the nodes at the surface of the material. The degree distributions of the weight loss at 100, 300, 1000 and 3000 h were calculated. The obtained degree distributions are represented in Fig.4.22. The degree of the weight loss became greater toward the surface from the center of the material, and at 3000h the weight loss reached almost the saturation.

The degree of the weight loss is the value from 0 to 1. When the degree is equal to 1, the complete debonding occurs at the interface. Therefore it is considered that the degree of the weight loss can be substituted for the damage parameter at the interface. $\overline{F}$ on each damage parameter shown in Fig.4.18 was applied to each layers shown in Fig.4.22, and then, $\overline{F}$ of FRP immersed in water was calculated by averaging $\overline{F}$ of each layers. This was calculated on the condition of the constant damage thickness. Thus, $\overline{F}$ of the immersed FRP is obtained by

$$\overline{E} = \frac{1}{8}\sum_{i=1}^{8} \overline{E}(P(i)) \tag{4.9}$$

where 'i' is the layer number, P(i) is the damage parameter at 'i'th layer and $\overline{F}(P(i))$ is the modulus with the damage parameter P(i). $\overline{F}(P(i))$ is obeyed by the damage parameter of the layer shown in Fig.4.22 and their value are shown in Fig.4.18. If the damage thickness is thinner, the maximum damage parameter at the constant damage thickness is smaller. Therefore $\overline{F}$ reaches the minimum value at shorter immersion time in case that the damage thickness is thinner. This can be verified by Fig.4.18. As mentioned before, however, it is assumed that the damage thickness is a constant and that only the damage angle changes due to water immersion in the finite element analysis here. Therefore P(i) depends on only the damage angle, so that $\overline{F}(P(i))$ also depends on only the damage angle. Figs.4.23-26 summarize the damage angle obtained by the damage parameter in Fig.4.22 under constant damage thickness at each immersion time. The damage angle of each layer at constant damage thickness is obtained by Fig.4.15 from the damage parameter in Fig.4.22. As a result, $\overline{F}(P(i))$ is obtained by Fig.4.16. For example, in case of the damage thickness = 4μm and the immersion time = 1000 h, $\overline{F}$ is expressed by eqn(4.9) as

$$\overline{E} = \frac{1}{8}\left\{\overline{E}(1) + \overline{E}(0.875) + 2\overline{E}(0.625) + 2\overline{E}(0.375) + 2\overline{E}(0.125)\right\} \tag{4.10}$$

$\overline{F}(P(i))$ in eqn(4.10) is substituted for $\overline{F}$ in Fig.4.16 on the basis of the damage angle shown in Fig.4.26, and then $\overline{F}$ of the immersed FRP is obtained. Fig.4.27 shows the changes of the retention of the calculated $\overline{F}$ on each damage thickness against the square root of immersion time. The experimental $\overline{F}$ is also shown in Fig.4.27. $\overline{F}$ in the damage thickness of 4μm decreased until 1000 h, and after which it reached a constant value of about 80% in the retention. On the other hand, $\overline{F}$ in the damage thickness of 0.5μm reached almost constant at 300 h. The changes of the calculated $\overline{F}$ were almost the same tendency with those of the experimental $\overline{F}$. Therefore the calculated results verify that the reduction of the elastic modulus due to water immersion is caused by the debonding between fiber and matrix. In Fig.4.27 the scatter of the experimental $\overline{F}$ was remarkable. In this figure the scatter of the calculated $\overline{F}$ also appeared due to the difference of the

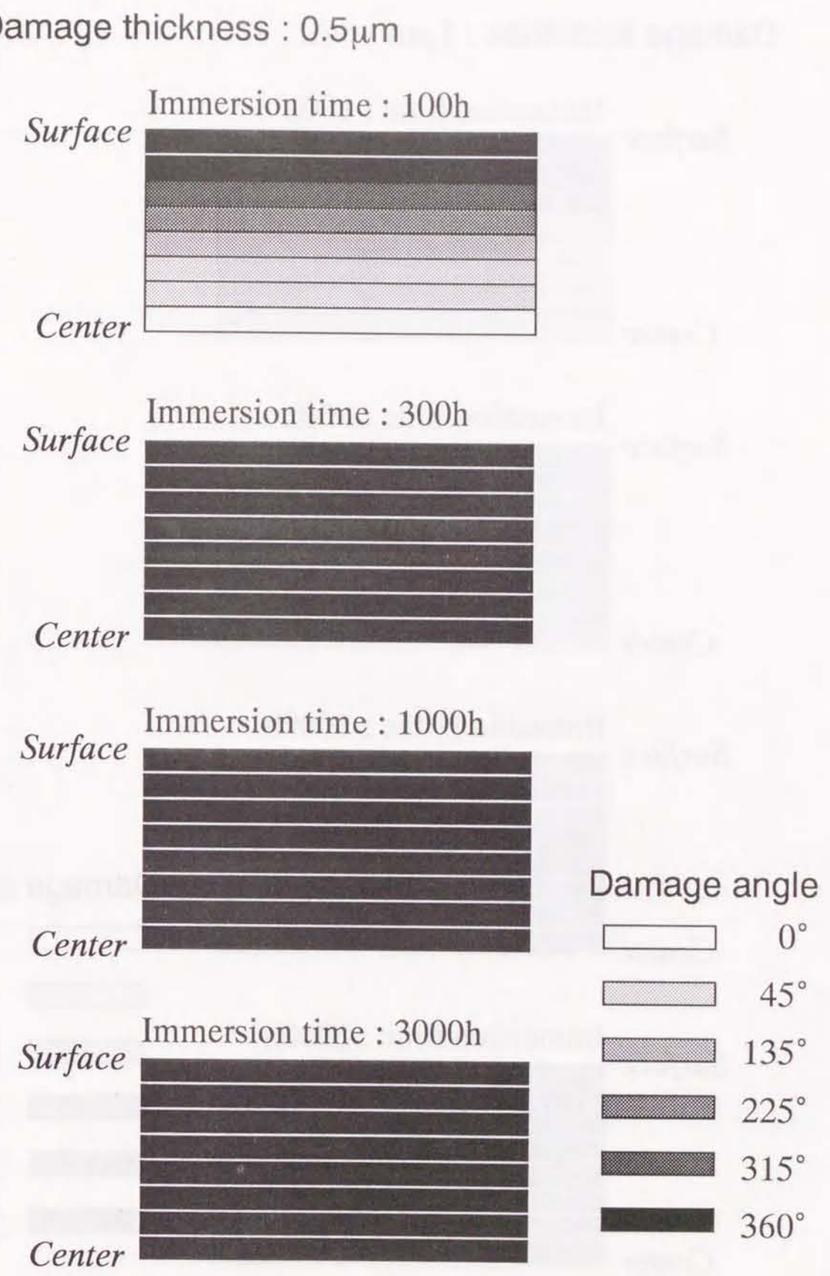

Fig.4.23 Damage angle obtained from damage parameter at constant damage thickness of 0.5μm.

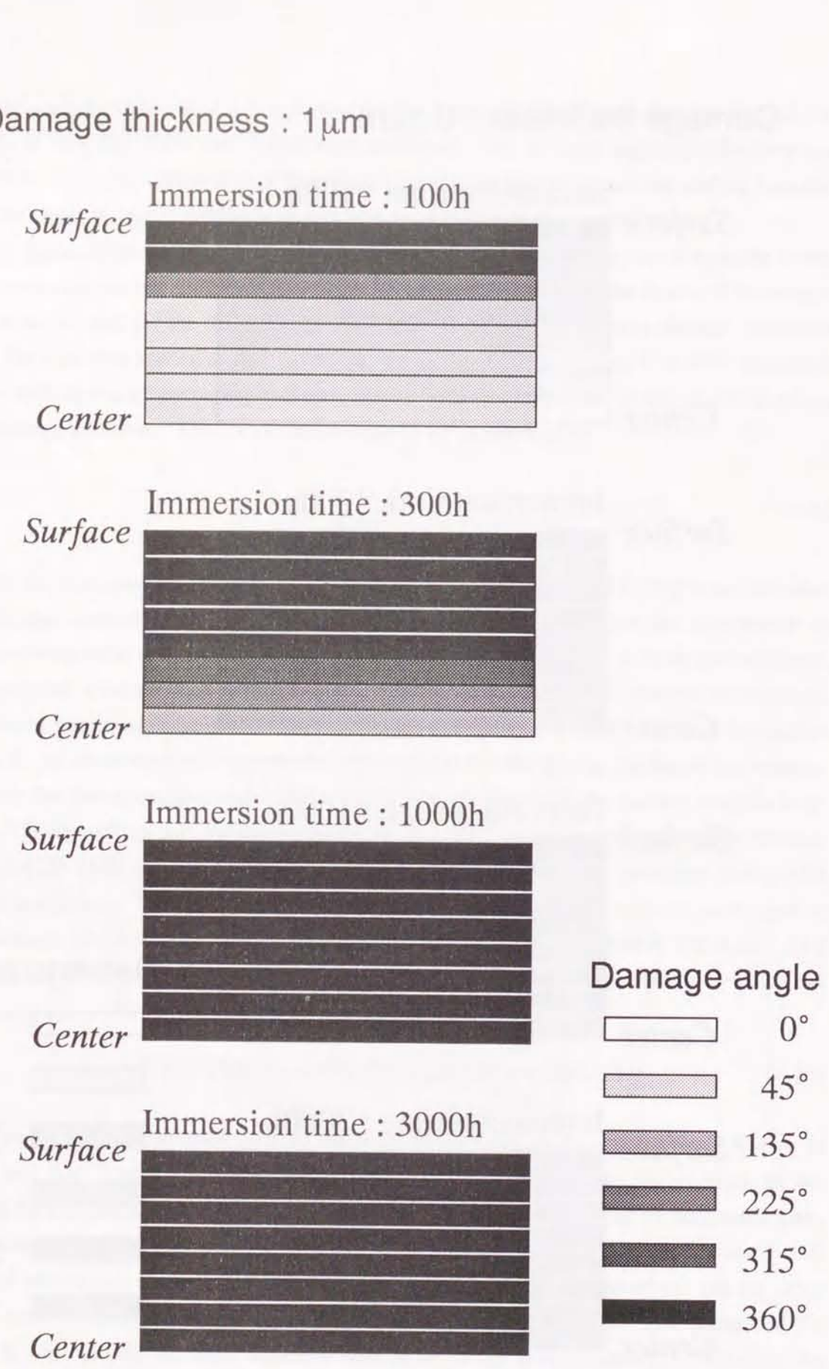

Fig.4.24 Damage angle obtained from damage parameter at constant damage thickness of 1μm.

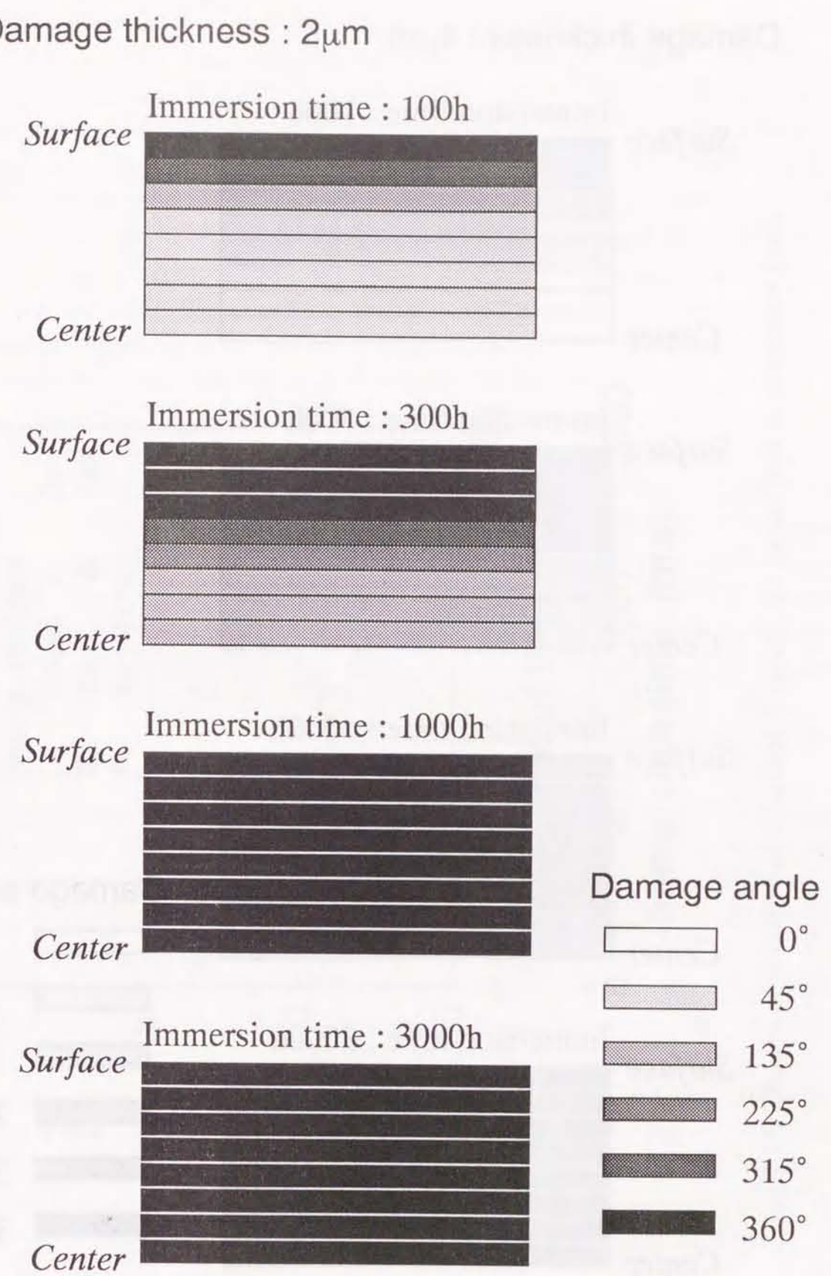

Fig.4.25 Damage angle obtained from damage parameter at constant damage thickness of 2μm.

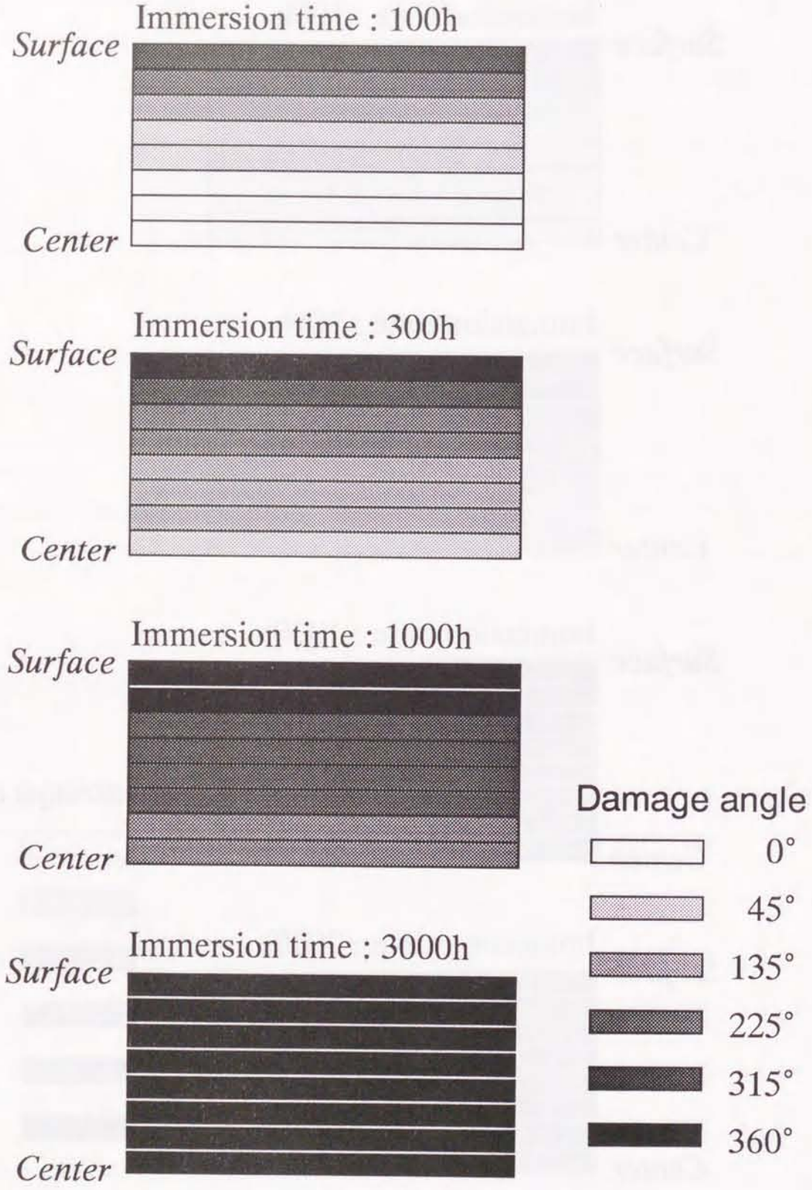

Fig.4.26 Damage angle obtained from damage parameter at constant damage thickness of 4μm.

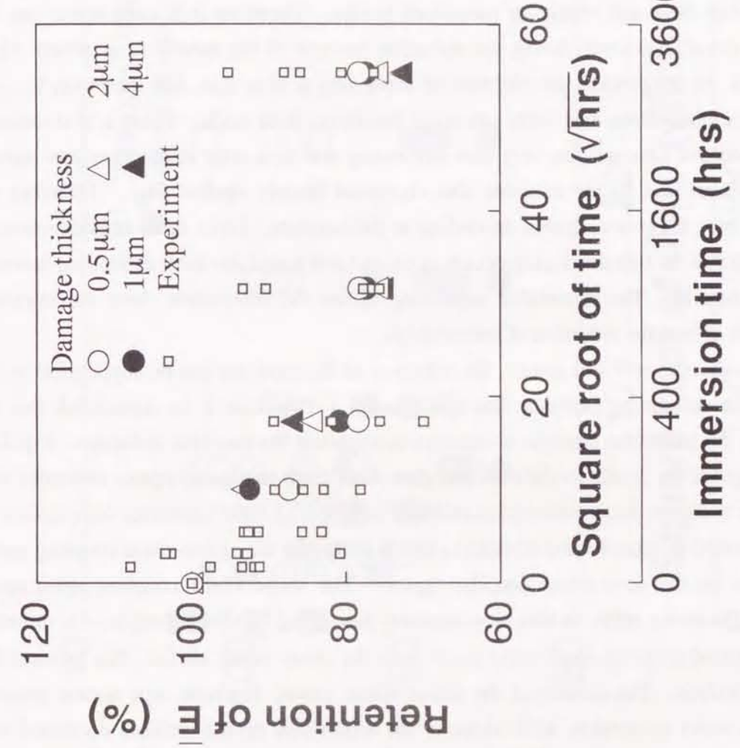

Fig.4.27 Changes of retention of calculated $\bar{E}$ against the square root of immersion time.

damage thickness. From this result, it is considered that the scatter of the experimental $\bar{E}$ is mainly caused by the difference of the thickness of each debonding at the interface.

The experimental $\bar{E}$ reached a constant at about 30 h, whereas the calculated $\bar{E}$ reached at 300 h in the damage thickness of 0.5μm, which is the thinnest damage thickness in the calculation. This difference between them seems to be caused due to the damage thickness. The damage dealt here was the thickness over 0.5μm. In fact, however, the damage with the thickness below 0.5μm should also occur between fiber and matrix. In such case the damage parameter becomes smaller than those dealt here. If the damage is thinner, $\bar{E}$ can be reduced in shorter immersion time. Such influence of the damage thickness may appear as the difference of the changes of $\bar{E}$ between the experiment and the calculation. As shown in Fig.4.3, the increase of M_l seems not to affect the reduction of the modulus. However, the reduction of the modulus is affected by the debonding between fiber and matrix as mentioned before. Therefore it is considered that the debonding has already occurred during the reduction process of the modulus, in which M_l is almost equal to 0. In this process the thickness of debonding is very thin, and therefore, the path through which the dissolution into water can occur has never been made. Then, it is considered that M_l hardly occurs although the very thin debonding due to a little dissolution has already occurred. In phase I and II, the modulus also decreased linearly against M_{gI}. Therefore the increase of M_{gI} may suggest such thin debonding at the interface. From these considerations, it can be concluded that the thin debonding occurs in phase I and II and that such debonding becomes remarkable in phase III. The remarkable debonding causes the dissolution from the interface, however, it never affects the reduction of the modulus.

From the above-mentioned results, the reduction of the modulus can be suppressed by the prevention of the debonding between fiber and matrix. Therefore it is considered that the improvement of the interfacial strength is effective to suppress the modulus reduction. Fig.4.28 shows the changes of the tensile modulus of the glass-fiber cloth reinforced epoxy laminates with different surface treatment due to water immersion. The fibers of these laminates were treated by only the silane coupling agent (without binder). One is treated by the amino-silane coupling agent, and the other is by the acryl-silane coupling agent. The amino-silane coupling agent reacts chemically with the epoxy resin, so that, this laminates has strong bonded interface. On the other hand, the acryl-silane coupling agent never reacts with the epoxy resin, so that, this laminate has poor bonded interface. The moduli of the amino-silane treated laminate kept almost constant regardless of the water immersion, while those of the acryl-silane treated laminate decreased with the water immersion. These results reflect only the effect of the silane coupling treatment. Therefore, this clarifies that the choice of the appropriate and the simple surface treatment of the fiber is important to suppress the modulus reduction due to the water immersion.

4.6 Conclusion

This chapter dealt with the elastic property of FRP immersed in hot water. The reduction mechanism of the elastic modulus was discussed from the relation between the weight changes and

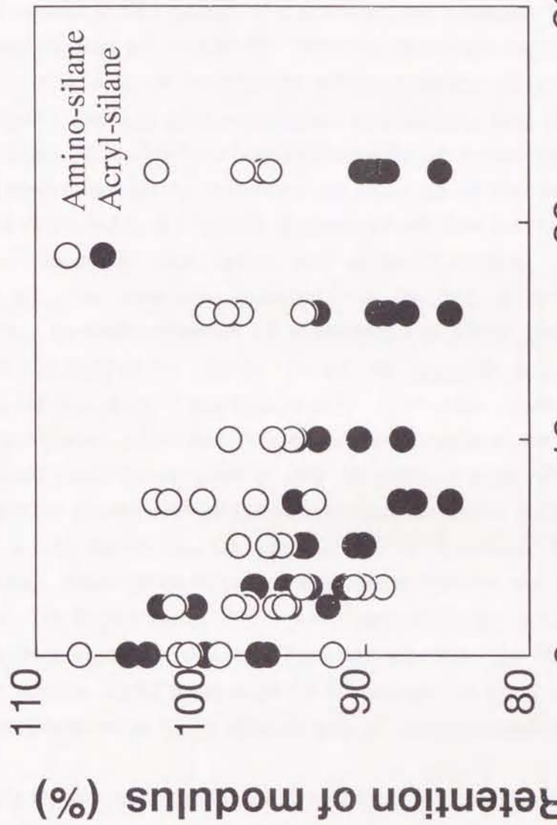

Fig.4.28 Changes of tensile modulus of glass-fiber cloth/epoxy laminates with different surface treatment of fiber due to water immersion.

the modulus. Moreover, the estimation method of the modulus introducing the damage mechanics was proposed, and this was applied to the estimation of the elastic modulus of FRP immersed in water. The elastic modulus decreased linearly against the weight gain due to water absorption (M_g), and it was not affected macroscopically by the weight loss (M_l) during the modulus reduction process (phase I and II). From the experimental results, it was supposed that the main cause of the modulus reduction was the degradation of the interface between fiber bundle and matrix and in fiber bundle. The effect of the interfacial damage on the modulus was discussed by the estimation method introducing the damage mechanics, and it was verified that the main cause of the modulus reduction of FRP immersed in water was the debonding between fiber and matrix.

Chapter 5 Fracture Mechanism of Glass Fiber Reinforced Plastics Immersed in Hot Water

5.1 Introduction

Fracture phenomena of fiber reinforced plastics (FRP) are complex since it is the composite consisted of the matrix resin and the fiber. Therefore both matrix cracking and fiber breakage occur during fracture. In addition, friction and debonding at the fiber/matrix interface may also occur. During fracture, such processes occur simultaneously and compete. The failure of FRP is often dominated by the fracture process. Crack growth and fracture mode of FRP have become a subject of attention to FRP research in recent years, and a common relation between crack growth rate and applied stress has clarified.[106] However, the fracture mechanism and its process of FRP has never been detailed, and the influence of them on the strength has never discussed well.

Acoustic emission (AE) measurement is a useful method for evaluation of the fracture process. Many AE studies have been conducted for the estimation of the fracture mechanism of FRP and relationship between fracture and AE characteristics have been studied.[107-110] Generally cumulative events and peak amplitude of enveloped AE have been used as parameters for fracture evaluation. Especially microfracture, such as matrix cracking, fiber breakage, debonding at interface, etc., has often been classified with the help of peak amplitude and amplitude distribution. Berthelot performed AE measurement of CFRP laminates with various stacking sequences and clarified the relation between AE amplitude and fracture mechanisms.[111,112] However, Faudree, et al.[113] and Kau, et al.[114] reported that amplitude distribution was different for some composites, which were differed only in fiber surface treatment. Therefore it is difficult to divide clearly each fracture mode by only AE amplitude since AE source and its characteristics are different due to used materials (matrix, reinforcement, filler, etc.).

It is well known that the strength of FRP is reduced by usage in wet and water environment. Therefore the life-time predictions of FRP are required for the safety of the FRP structures. The degradation of FRP in a wet environment has been studied and weight changes and reduction in mechanical properties have been reported. The AE technique has been used for life-time prediction of FRP water tanks.[115,116] Structural safety of water tanks has been evaluated by Felicity ratio based on Kaiser effect in spite of incomplete understanding of AE characteristics on FRP.

This chapter deals with the changes of the fracture mechanisms and the strength and AE characteristics of randomly oriented FRP panels in hot water environment. FRP panels are immersed at 80 °C. Bending test and AE measurement are subsequently performed. Fracture process is clarified roughly by the relation between the weight changes and the strength. The relation between AE characteristics and fracture process under bending load is discussed through microscopic observation of cross-section. Moreover the estimation method of fracture mechanisms by AE characteristics is suggested.

5.2 Experimental Procedure

5.2.1 Bending test

Materials used were three kinds of randomly oriented E-glass fiber continuous strand mat reinforced unsaturated polyester resins, and these were the same with those used in Chapter 2 (*type-A*, *type-B* and *type-C*), that is, *type-A* and *type-B* were the glass-fiber mat reinforced bisphenol based unsaturated polyester without and with filler, and *type-C* was the glass-fiber mat reinforced orthophthalic based unsaturated polyester. Using these materials, three kinds of 300mm square panels were fabricated by a compression molding. Fiber volume content for all the panels was about 35%.

Water immersion for the bending test specimens was conducted at 80°C with temperature controlled water baths. The periods of immersion were 3, 10, 30, 100, 300, 1000 and 3000 h. The bending strength was measured by three point loading system for the specimens just after the immersion. The geometry of the bending specimen was 80mm × 15mm × 3.8mm. The bending test was performed for 5 specimens on each immersion time at a constant cross-head speed of 2 mm/min with a 60 mm span, at room temperature, using an Instron universal testing machine (type 4206).

The microscopic observation was done for the cross-section of the specimens after the loading until 20%, 40%, 60%, 80% and 100% of the static strength to clarify the fracture process. In order to facilitate the microscopic observation, the specimens were put by the epoxy resin in the mold and the observed surface was polished. Glassy polished surface was observed by an optical microscope (PME3, Olympus Co., Ltd.) and by a scanning electron micrograph (SEM; JSM-5200, JEOL Ltd.).

5.2.2 Acoustic emission measurement

Type-A and *type-B* specimens were used for the AE measurement during the bending test.

Water immersion for the AE measurement specimens was conducted at 80°C with temperature controlled water baths. The periods of immersion were 100, 1000 and 3000 h. The geometry of the specimen was 80mm × 15mm × 3.8mm. The three point bending was performed at constant cross-head speed of 2mm/min with 60mm span. Fig.5.1 illustrates AE system used in this work. The AE measurement and analysis were conducted using the 3000 SPARTAN acoustic emission analyzer (Physical Acoustic Corporation). Fixed gains of preamplifier and mainamplifier were 40dB and 20dB respectively, and the system threshold level was fixed at 40dB. The dead-time, rise-time out and rearm time were 50 μsec, 20 μsec and 50 μsec, respectively. AE transducer with a resonant frequency of 150 kHz (R-15, Physical Acoustic Corporation) was attached on the specimen as illustrated in Fig.5.2. The AE hits detected over the threshold level were analyzed.

Kaiser test was performed by three point bending for only *type-A* specimen. Kaiser test is an evaluation method of the material soundness using Kaiser effect. Kaiser effect is the phenomenon that AE wave never be detected during loading process until the load applied before,

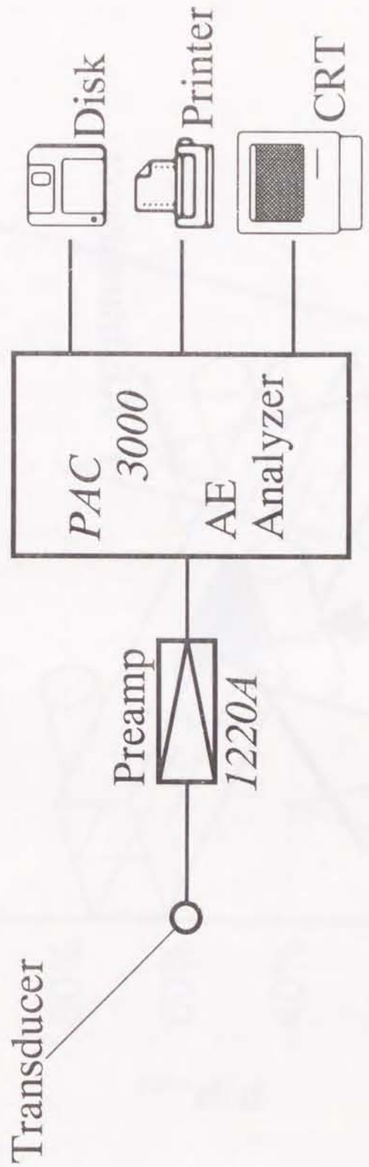

Fig.5.1 Acoustic emission measuring system.

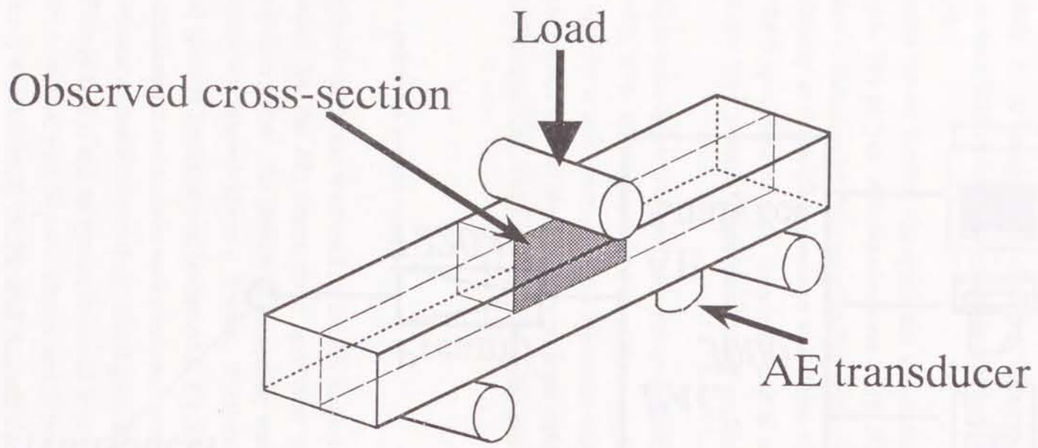

Fig.5.2 Bending test with AE measurement and cross-section observed by microscope.

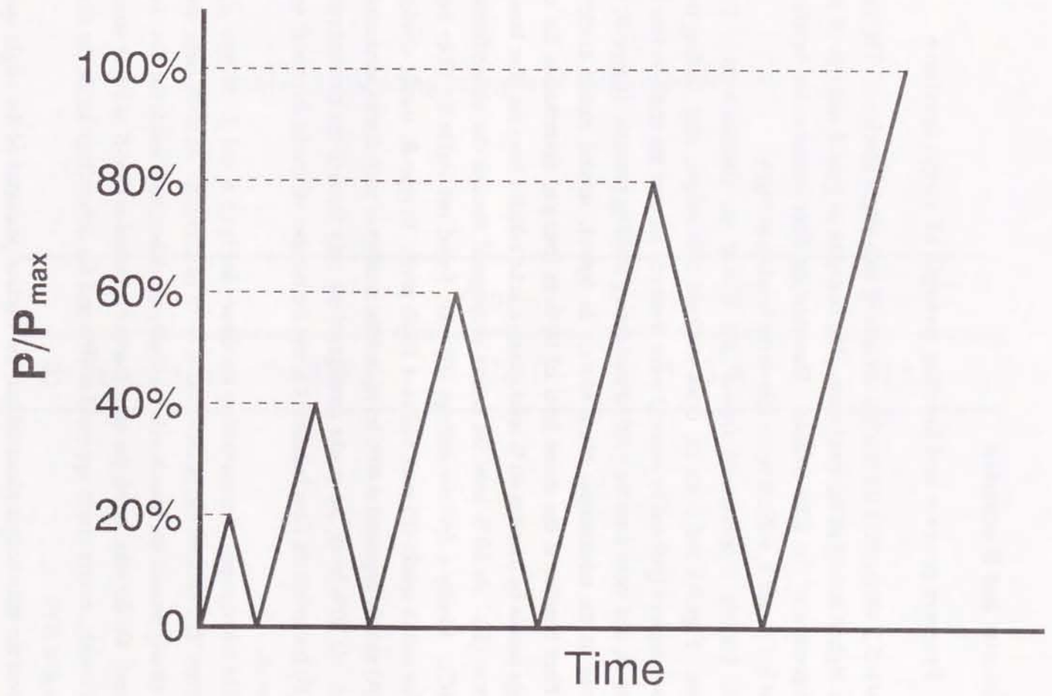

Fig.5.3 Load history in Kaiser test.

and it was found out by Kaiser. In case that Kaiser effect is satisfied, AE wave never be detected also during unloading process. Using Kaiser effect the material soundness in FRP tank/vessel has been evaluated. In Kaiser test, the stepped loading-unloading to 20%, 40%, 60%, 80% and 100% of the static strength was repeated as illustrated in Fig.5.3 at constant cross-head speed of 2mm/min with 60mm span.

5.3 Results and Discussion

5.3.1 Fracture process and bending strength of virgin specimen

Table 5.1 summarizes the bending strength of each virgin specimen. The strength of *type-C* was the highest among all the specimens. The strengths of *type-A* and *type-B* were almost the same independent of the filler content. Therefore the filler improves the bending modulus as mentioned in Chapter 3, while it never affects the bending strength.

The fracture processes of *type-A* and *type-B* are discussed from the microscopic observation. Figs.5.4 and 5 are the cross-sectional micrographs after loading until each stress level. Black regions (pointed by arrows) were observed all over the cross section both in *type-A* and in *type-B*, and these were the void formed during molding process. In *type-B*, the filler could be observed as the microscopic black spots. In *type-A*, several matrix cracks (A) appeared between fiber bundles at the stress level of 60 % in strength, nevertheless the cracks and the debondings cannot be found at 40 % level. Such cracks initiated from the fiber bundles as pointed by the arrow (B). At 80 % level the cracks propagated through the circumference of the fiber bundles (C). Finally a few debondings (D) were found out inside the fiber bundles, and the progressive matrix cracks (E) were visible at 100% level. In *type-B*, matrix cracks between fiber bundles (A) already appeared at 40% level, and the number of such cracks increased remarkably at 60% level. At 80% level, the cracks propagated not only through the circumference of the fiber bundles (B) but inside the fiber bundles (C), and the number of cracks in *type-B* was greater than that in *type-A*.

SEM micrographs of cross section are shown in Figs.5.6 and 7. In *type-A*, matrix cracks initiated from fiber bundles can be observed at 60 % of strength. At 80 % large scale debondings appeared clearly around the fiber bundles. Finally the debondings inside the fiber bundles can also be observed. On the other hand, the same fracture occurred in *type-B* at lower stress level than in *type-A*. Namely, matrix cracks appeared at 40% and the debondings inside the fiber bundles can be observed at 80%.

From the microscopic observations, the fracture processes of the virgin specimens can be expressed as illustrated in Fig.5.8. At first the debondings appear around the fiber bundles, and immediately matrix cracks propagate from the debondings around the fiber bundles. These cracks progress further independent of the loading direction. As the applied stress increases, the debondings also appear inside the fiber bundles. Consequently the fracture process was dominated by the matrix cracks and the debondings around the fiber bundles. The filler reduces only the stress at initiation of each fracture, and never affect the fracture modes.

Table 5.1 Bending strength of virgin specimens.

	type-A	*type-B*	*type-C*
Bending strength (MPa)	174.0	173.5	215.6

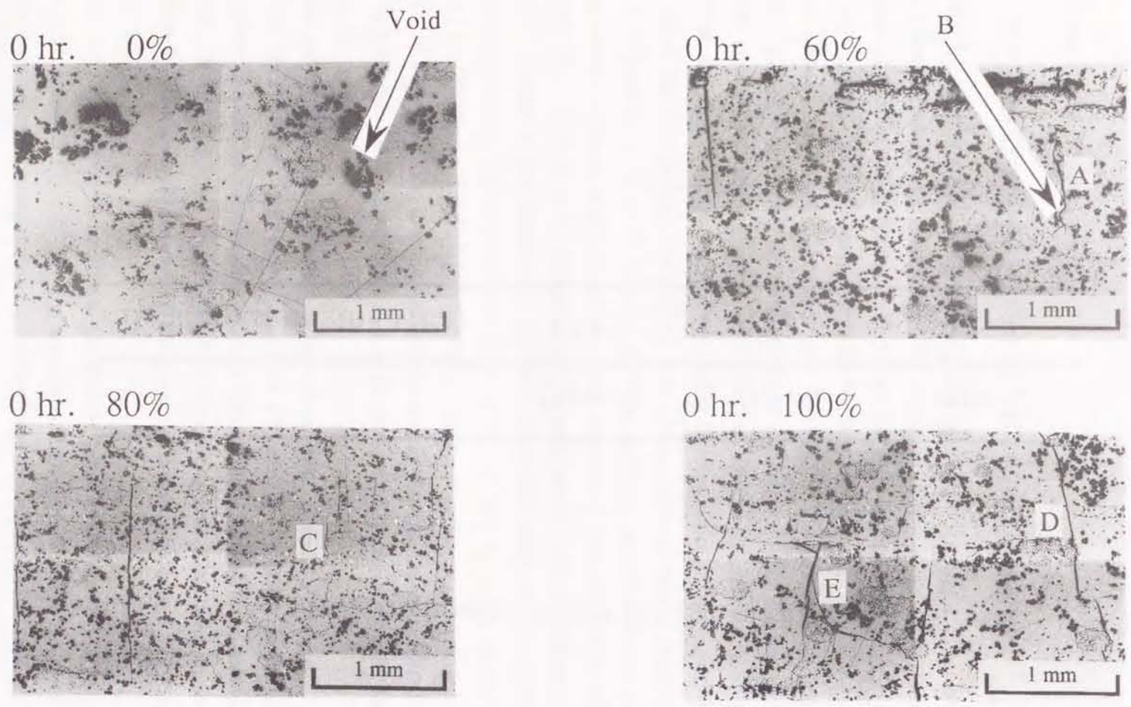

Fig.5.4 Cross-sectional micrographs for virgin *type-A* specimen at fixed stress level.

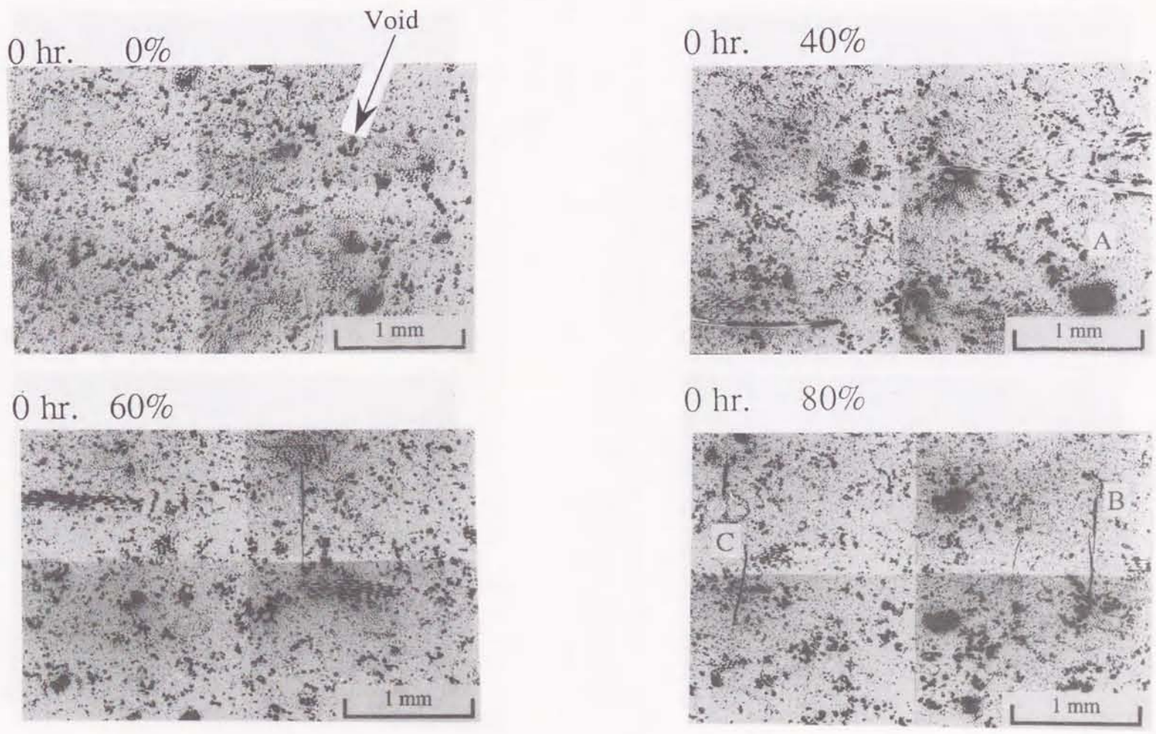

Fig.5.5 Cross-sectional micrographs for virgin *type-B* specimen at fixed stress level.

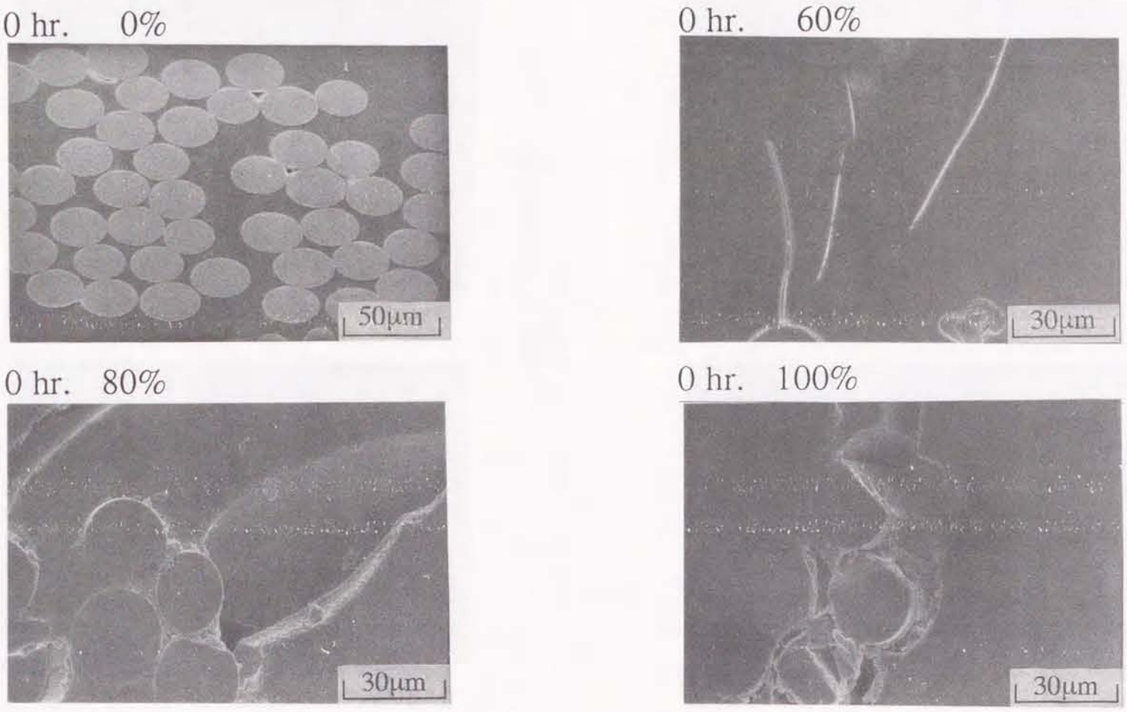

Fig.5.6 Scanning electron micrographs of cross-section for virgin *type-A* specimen at fixed stress level.

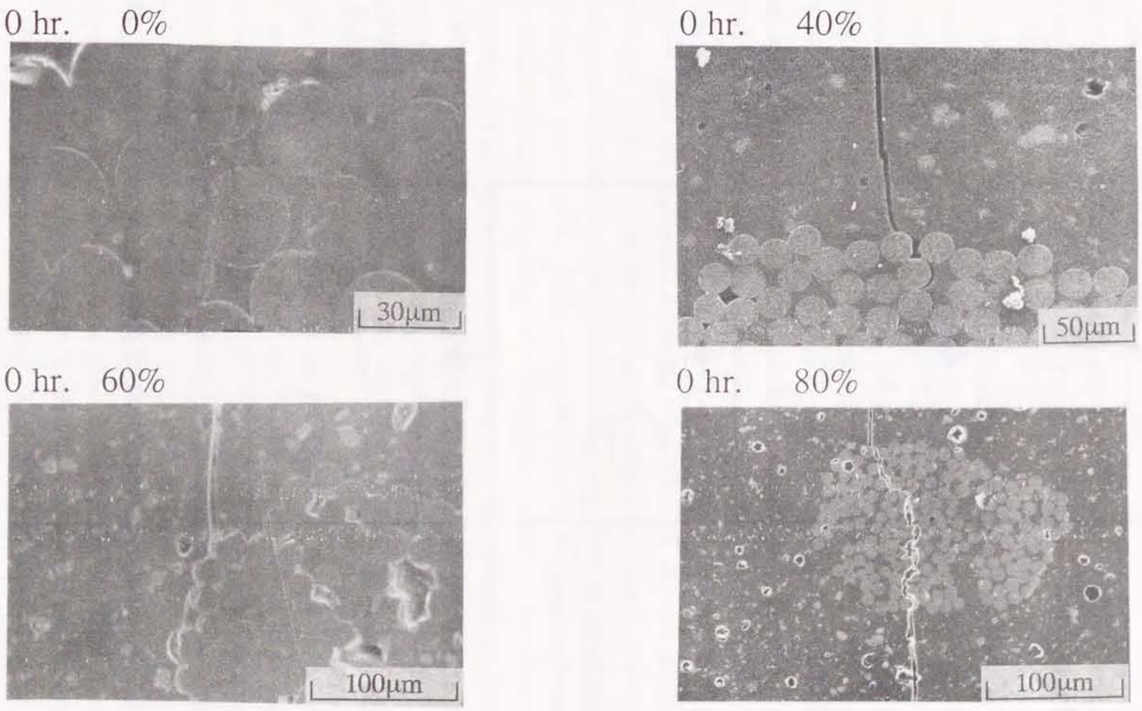

Fig.5.7 Scanning electron micrographs of cross-section for virgin *type-B* specimen at fixed stress level.

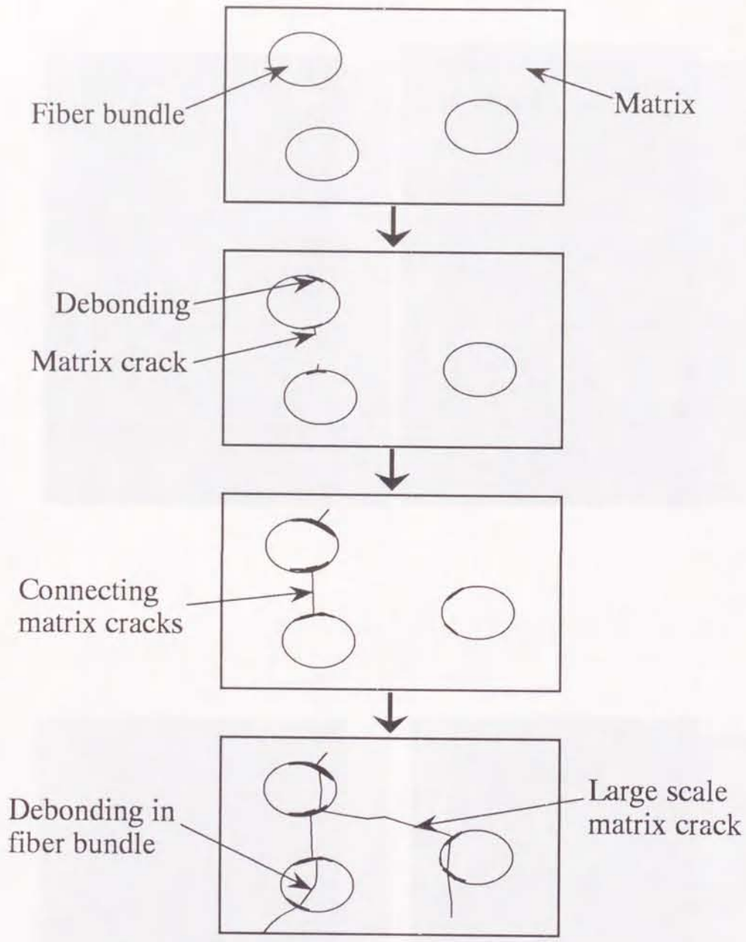

Fig.5.8 Schematic representation of fracture process for virgin specimen under bending load.

5.3.2 Relation between weight changes and bending strength of immersed specimen

Fig.5.9 shows the dependence of bending strength retention on the immersion time. The strength of *type-C* decreased remarkably than those in *type-A* and *type-B*. The strength of *type-C* decreased at about 60% retention until 100h, however, after 100h it decreased gradually. The strength reduction of *type-A* and *type-B* indicated almost the same tendency. These strengths decreased at about 80% up to 30h, and after that the gradual reduction of the strength was caused continuously. It has been considered in previous section that the strength reduction as well as the modulus reduction is closely related to the weight changes. Therefore the relation between the bending strength and the weight changes is discussed below. The relation between the strength and the net weight gain (M_g) is shown in Fig.5.10. The strength decreased almost linearly against M_g, and the relation between the strength and M_g indicated almost the same tendency independent of the materials. It is thought that the greater strength reduction of *type-C* in comparison with *type-A* and *type-B* (as shown in Fig.5.9) is caused by the greater water absorption. Fig.5.11 shows the relation between the bending strength and the weight loss (M_l). The strength decreased while M_l remained nearly equal to 0. After M_l started increasing, the strength of *type-A* and *type-B* reduced almost linearly against M_l, while the modulus kept constant as shown in Fig.4.3. The strength of *type-C* gradually approached a constant value when M_l exceeded 2% in spite of a further large increase in M_l. The increase of M_l greatly affected the strength reduction, while it affected little the modulus reduction. Fig.5.12 shows the relation between the bending strength and the net weight gain of the interface (M_{gI}). In this figure the data for the immersion time from 0 to 1000h was plotted since the data of M_{gI} was obtained until 1000h. The strength decreased linearly against M_{gI}, and the relation between the strength and M_{gI} indicated the same tendency independent of the used matrix. The relation between the bending strength and M_{II} is shown in Fig.5.13. The strength also decreased linearly against M_{II}, however, *type-C* indicated the greater strength reduction than *type-A* and *type-B*. The strength reduction of *type-A* and *type-B* against M_{II} indicated the same tendency.

In order to discuss the mechanism of the strength reduction, the phase divisions discussed in Chapter 2 are applied as same manner with Chapter 4. The dependence of the bending strength on M_g is divided into phase I, II and III in Figs.5.14-16. The strength decreases linearly against M_g from phase I through phase II, and such tendency is the same with the modulus reduction. Therefore it is considered that the main cause of the strength reduction from phase I through phase II is both the degradation of matrix and the gradual degradation of the interface (very thin debonding between fiber and matrix). Also in phase III, the strength decreased linearly against M_g, however, the slope of the strength reduction in phase III was different from that from phase I through II. Therefore it is supposed that the main cause of the strength reduction in phase III is different from that from phase I through II. In phase III, the remarkable debondings appear, and therefore it is considered that the debondings induce the strength reduction. The slope of the strength reduction against M_g in *type-A* and *type-B* was the same in each phase, and the strength reduction in phase III was greater than from phase I through II. However, the slope of the strength

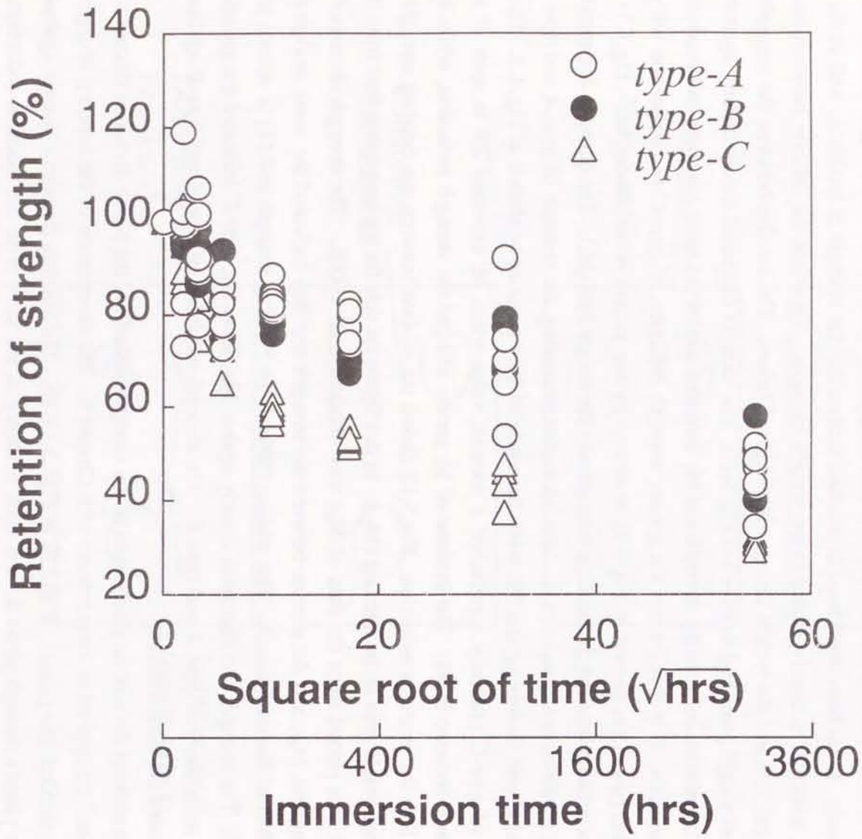

Fig.5.9 Retention of bending strength as a function of the square root of immersion time.

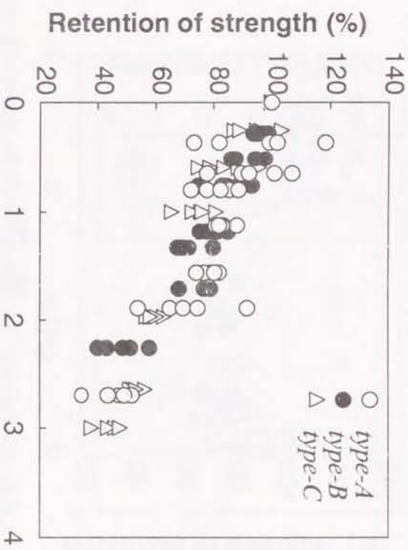

Fig.5.10 Relation between bending strength and M_g.

Fig.5.11 Relation between bending strength and M_I.

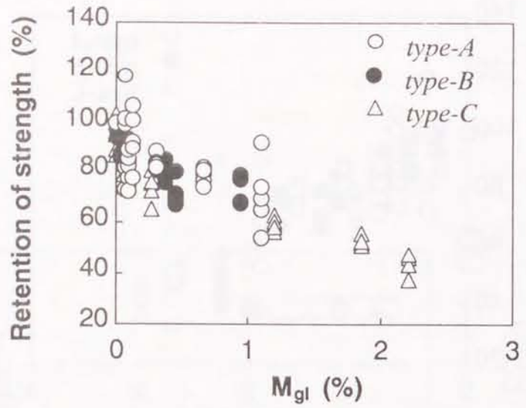

Fig.5.12 Relation between bending strength and M_{gI}.

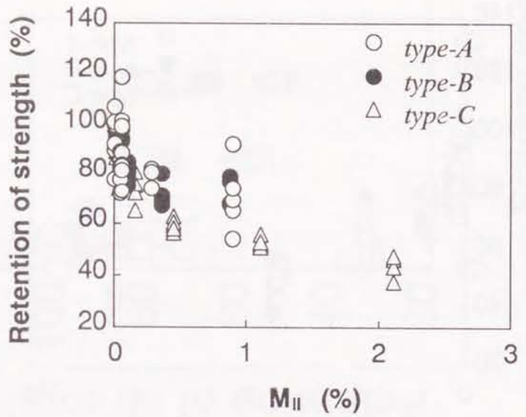

Fig.5.13 Relation between bending strength and M_{II}.

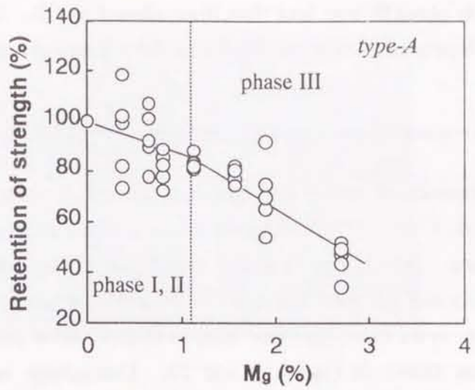

Fig.5.14 Phase divisions of dependence of bending modulus on M_g for *type-A*.

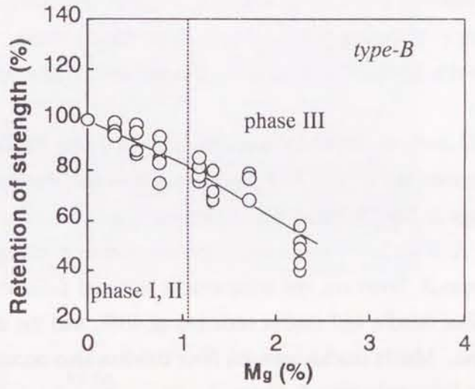

Fig.5.15 Phase divisions of dependence of bending modulus on M_g for *type-B*.

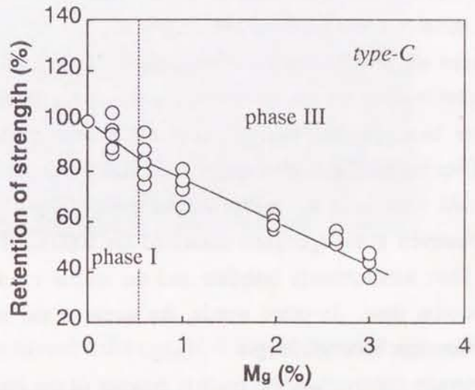

Fig.5.16 Phase divisions of dependence of bending modulus on M_g for *type-C*.

reduction in *type-C* was quite different from those in *type-A* and *type-B*. In *type-C* the strength reduction against M_g in phase III was less than from phase I and II. It is considered that this difference in the slope is originated from the difference of the sensitivity to the debonding.

5.3.3 Fracture process of immersed specimen

The fracture processes of *type-A* and *type-B* immersed in water are discussed from the microscopic observation. Figs.5.17 and 18 are the cross-sectional micrographs of specimens just after the water immersion. Both in *type-A* and in *type-B*, the circumference of the fiber bundles could be observed clearly and the black spots, which is considered to be voids, gradually spread all over the cross-section as the immersion time became longer. SEM photos of the cross-section in Figs.5.17 and 18 are shown in Figs.5.19 and 20. Debondings around the fiber bundles increased as immersion time became longer. Such debondings could not be observed on the virgin specimen. The debondings inside the fiber bundles could also be observed at 1000 h. After 1000 h the amount of matrices and binders adhering on fiber decreased and the surface of each fiber was made smooth ('A' in Fig.5.19). From these observations, it is considered that the interfacial strength between fiber and matrix and between fiber bundle and matrix reduced due to water immersion.

Figs.5.21 and 22 show the cross-sectional micrographs after the fixed load for *type-A* and *type-B* specimens immersed for 100h. In *type-A*, matrix cracks between fiber bundles can be observed and debondings at fiber bundle/matrix interface appeared connecting with matrix cracks at stress level of 40%. At 60 % level matrix cracks propagated with enlarging both in length and in width directions. In *type-B*, however, the microcracks initiated from the fiber bundles and the debondings between fiber bundle and matrix occurred at 40%, and the debonding enlarged with increase of applied stress. Matrix cracks between fiber bundles also occurred in *type-B* as well as in *type-A*. At 100h, the fracture in *type-B* occurred at lower stress level than in *type-A*. Figs.5.23 and 24 show the cross-sectional micrographs after loading for the specimens immersed for 1000h. Both in *type-A* and in *type-B*, the debonding inside the fiber bundles and the matrix cracks initiated from the fiber bundles could be observed at 20% stress level, and such debondings and cracks enlarged and spread all over the cross-section at 40%. Figs.5.25 and 26 show the cross-sectional micrographs after loading for the specimens immersed for 3000h. At 20% stress level, the debondings at fiber bundle/matrix interface and the matrix cracks propagated from the debondings inside the fiber bundles, and grew larger scale than those at 20 % level of the specimen immersed for 1000 h. At 40 % level the matrix cracks connected with other cracks, and such phenomena cannot be observed in the specimen immersed for 1000 h. Therefore it is considered that the debondings at fiber bundle/matrix interface and the matrix cracks occur at lower stress level with longer immersion time. In other words, the stress at the initiation of this fracture decreases as the immersion time becomes longer.

From the microscopic observation, the fracture process of the immersed specimen can be expressed as shown in Fig.5.27 and the stress level at each fracture initiation is summarized in

100 hrs. 0%

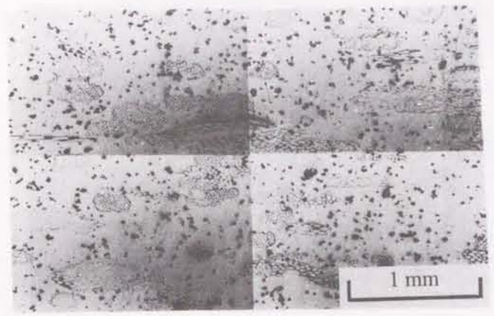

1000 hrs. 0%

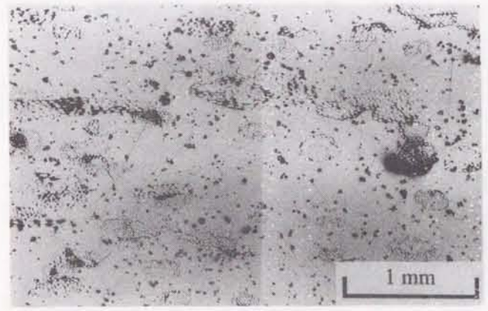

3000 hrs. 0%

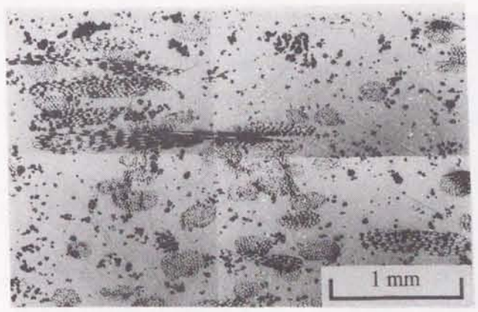

Fig.5.17 Cross-sectional micrographs for immersed *type-A* specimen before loading.

100 hrs. 0%

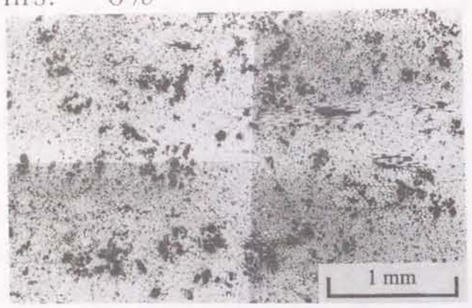

1000 hrs. 0%

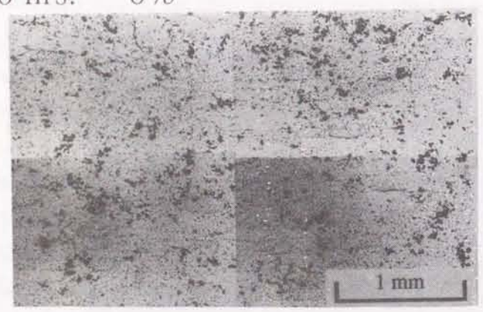

3000 hrs. 0%

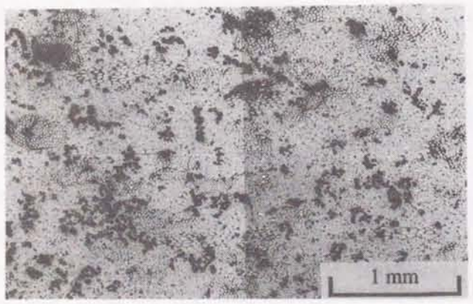

Fig.5.18 Cross-sectional micrographs for immersed *type-B* specimen before loading.

100 hrs. 0%

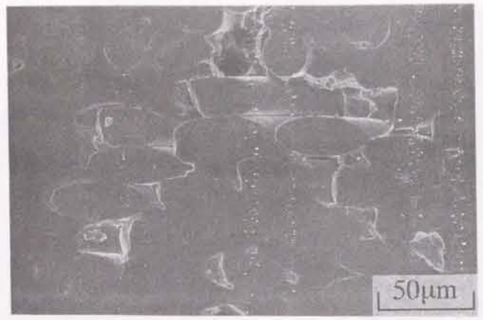

1000 hrs. 0%

3000 hrs. 0%

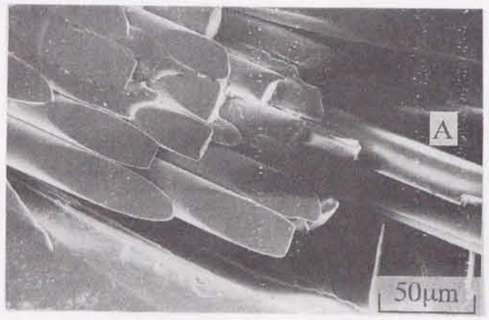

Fig.5.19 Scanning electron micrographs of cross-section for immersed *type-A* specimen before loading.

100 hrs. 0%

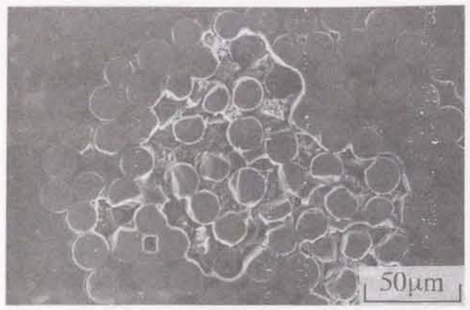

1000 hrs. 0%

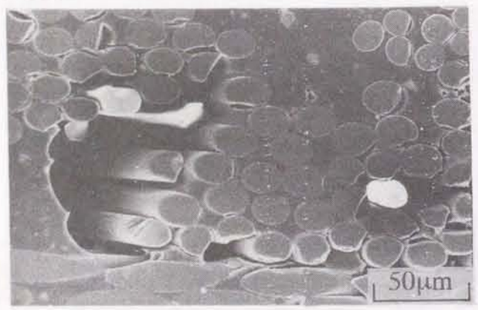

3000 hrs. 0%

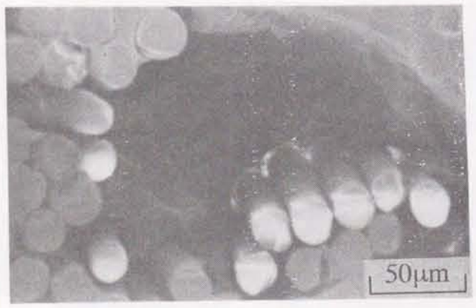

Fig.5.20 Scanning electron micrographs of cross-section for immersed *type-B* specimen before loading.

100 hr. 40%

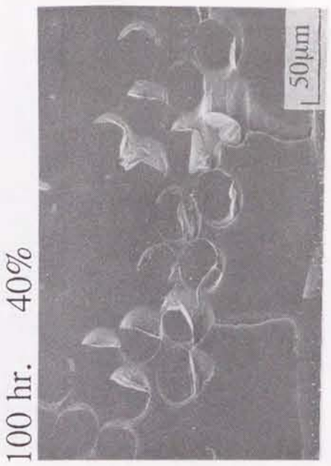

100 hr. 60%

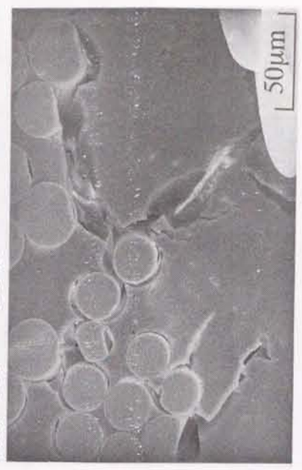

100 hr. 40%

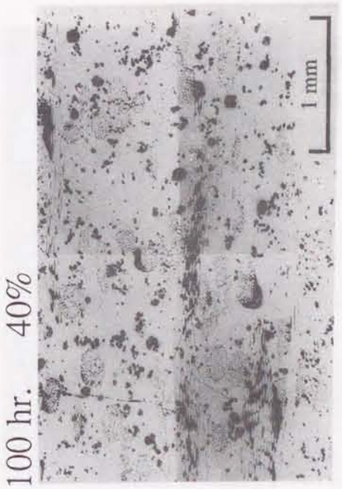

100 hr. 60%

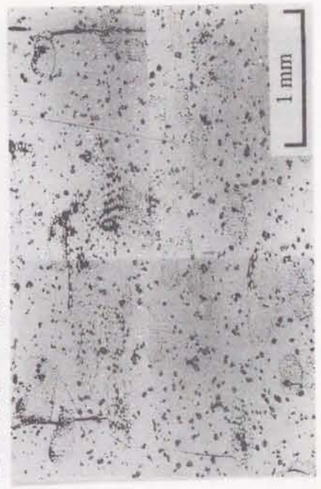

Fig.5.21 Cross-sectional micrographs for immersed *type-A* specimen at fixed stress level (immersion time: 100h).

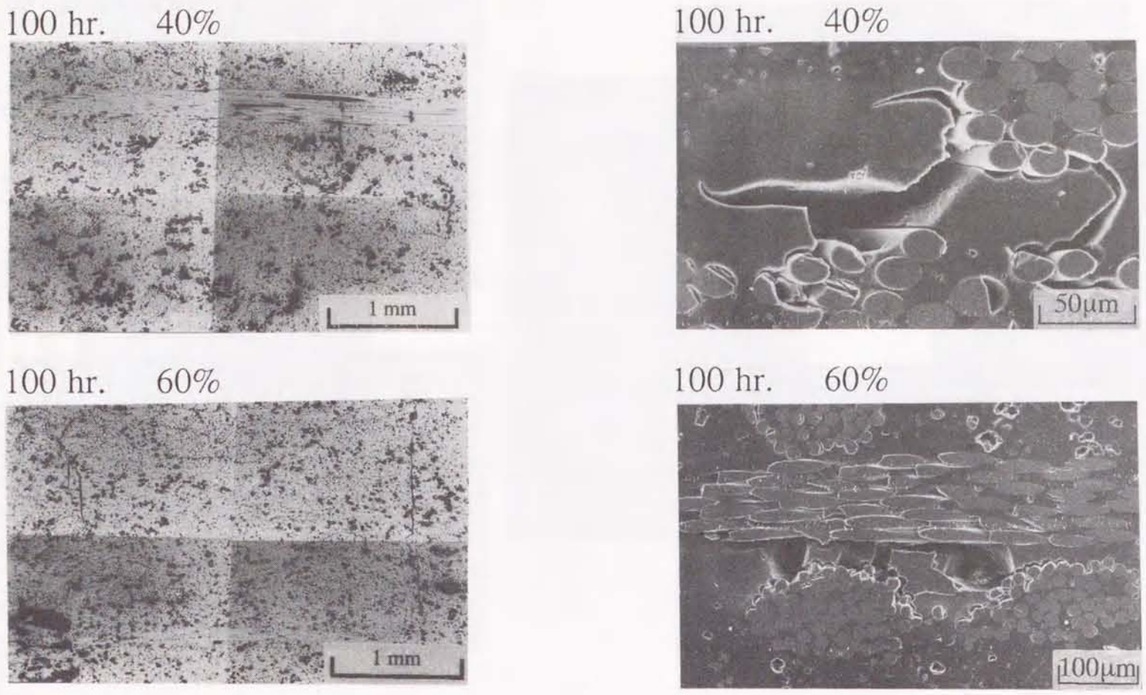

Fig.5.22 Cross-sectional micrographs for immersed *type-B* specimen at fixed stress level (immersion time: 100h).

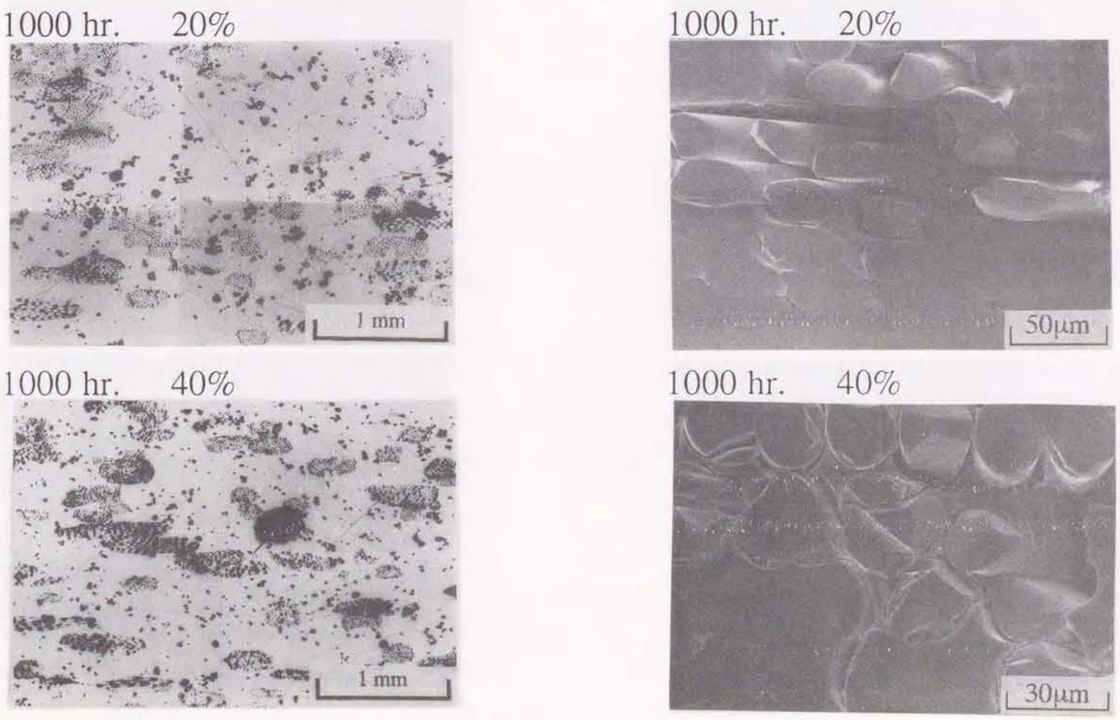

Fig.5.23 Cross-sectional micrographs for immersed *type-A* specimen at fixed stress level (immersion time: 1000h).

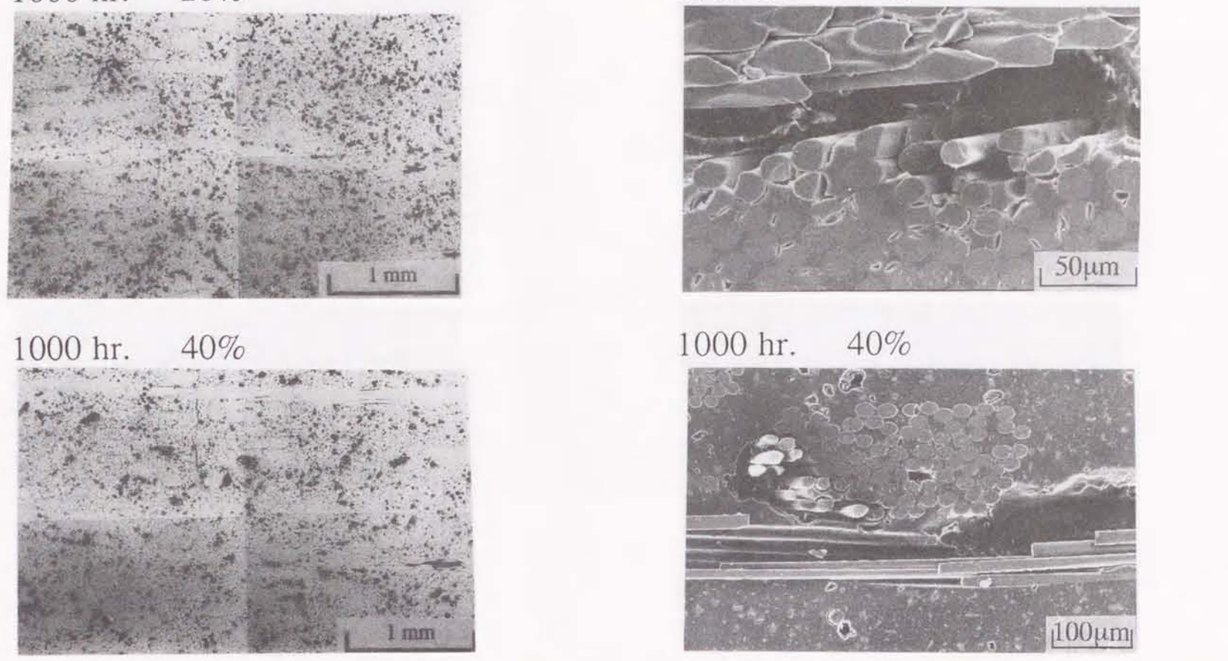

Fig.5.24 Cross-sectional micrographs for immersed *type-B* specimen at fixed stress level (immersion time: 1000h).

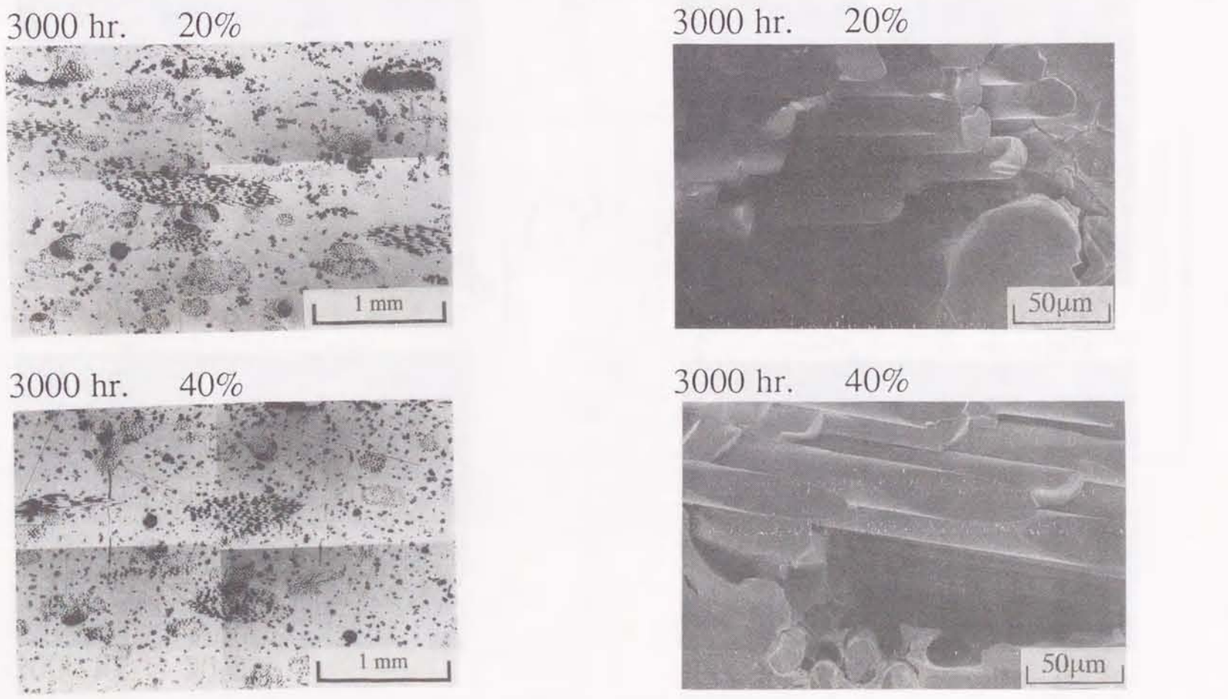

Fig.5.25 Cross-sectional micrographs for immersed *type-A* specimen at fixed stress level (immersion time: 3000h).

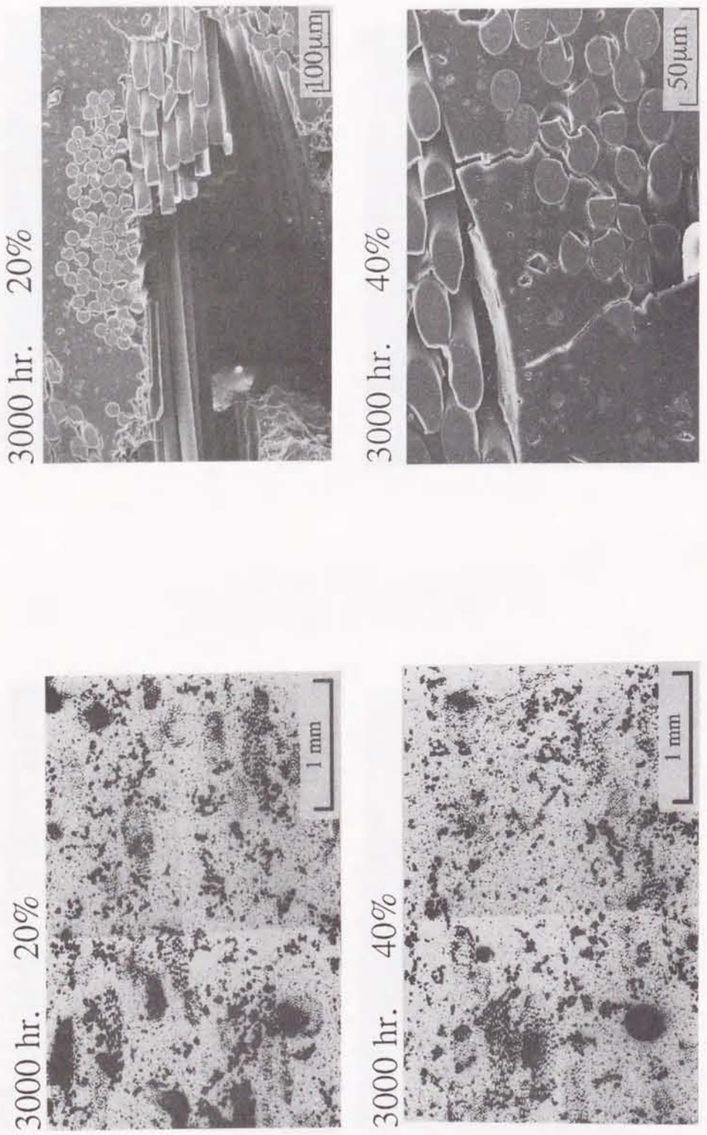

Fig.5.26 Cross-sectional micrographs for immersed *type-B* specimen at fixed stress level (immersion time : 3000h).

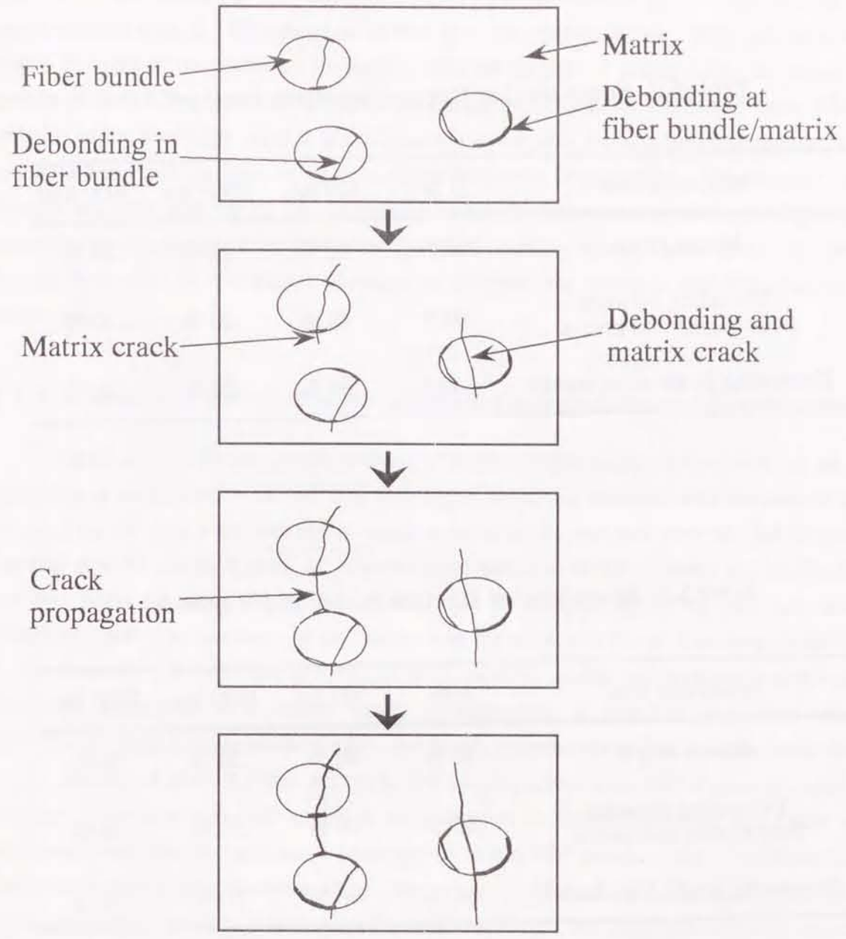

Fig.5.27 Schematic representation of fracture process for immersed specimen under bending load.

Table 5.2 Stress level at fracture initiation for *type-A*.

Immersion time	0 hr	100 hrs	1000 hrs	3000 hrs
Matrix crack	60 %	40 %	20 %	20 %
Debonding between fiber bundle and matrix	60 %	40 %	20 %	20 %
Debonding inside fiber bundle	100 %	60 %	20 %	20 %

Table 5.3 Stress level at fracture initiation for *type-B*.

Immersion time	0 hr	100 hrs	1000 hrs	3000 hrs
Matrix crack	40 %	40 %	20 %	20 %
Debonding between fiber bundle and matrix	40 %	40 %	20 %	20 %
Debonding inside fiber bundle	80 %	60 %	20 %	20 %

Tables 5.2 and 3 for the virgin and the immersed specimens. Water absorption due to immersion induces the strength reduction at fiber/matrix interface, and as a result, the debondings inside the fiber bundles occur. The stress level at the initiation of the debonding inside the fiber bundles decreases as the immersion time becomes longer. The debondings grow larger and the matrix cracks initiated from the debondings occur with applying bending stress. With increasing applied stress, the scale of the cracks grows larger, while the number of cracks never increases. Such fracture process in the immersed specimen is different from that in the virgin specimen. The crack initiation in the virgin specimen is the debondings at the fiber bundles/matrix interface, whereas that in the immersed specimen is the debondings inside the fiber bundles. Therefore the bending strength is greatly affected by the degradation inside the fiber bundles and such degradation is caused by the dissolution of the binder and the silane coupling agent. Consequently the design of the interface must be considered carefully to suppress the strength reduction due to water immersion.

5.3.4 Relation between acoustic emission characteristics and fracture process

Figs.5.28 and 29 display the changes of amplitude distribution histograms for the virgin specimens at each stress level. AE hits with higher amplitude occurred with increase of applied stress. Few AE hits were detected at stress level of 20 %, and hits with 40 ~ 60 dB gradually occurred at 40 %. At 60 % level, AE hits with amplitude over 60 dB occurred and the distribution had two peaks (at about 45 dB and 75 dB). At stress level of 80 %, total hits increased remarkably, however, the shape of distribution was the same with that at stress level of 60 %.

Generally AE amplitude has been divided into low, middle and high range amplitude and they have corresponded to matrix cracking, debonding at interface and fiber breakage, respectively. Main fracture mode of FRP used in this chapter was matrix cracking since the fiber volume fraction of used FRP was extremely low in comparison with that of generally used FRP. However, many hits with high amplitude were detected for this material, and as a result, above-mentioned classifications have never been applied to this FRP panel. From the detailed fracture observation, catastrophic fracture such as a large scale matrix cracking corresponds to AE hits with high amplitude. Therefore it is supposed in this chapter that AE amplitude indicates the scale of fracture. However, the relation between fracture and AE signal could not be clarified by only amplitude. AE energy in addition to amplitude was introduced as AE parameter. It is considered that AE energy signifies the essential energy needed to induce the final failure. In this chapter AE hits were divided into three regions by amplitude; 40~50 dB, 50~70 dB and 70~100 dB.

Changes of cumulative AE energy for the virgin specimens at each stress level are shown in Figs.5.30 and 31. AE energy of the hits with 70~100 dB started increasing at stress level of 40 %. This phenomenon corresponds to the occurrence of cracks as shown in Figs.5.4 and 5. The slope of cumulative energy curve gradually increased as stress increasing. On the other hand, AE hits with 70~100 dB started increasing at stress level of 20% in *type-B*, and the total cumulative energy in *type-B* was greater than in *type-A*. This corresponds to that the fracture in

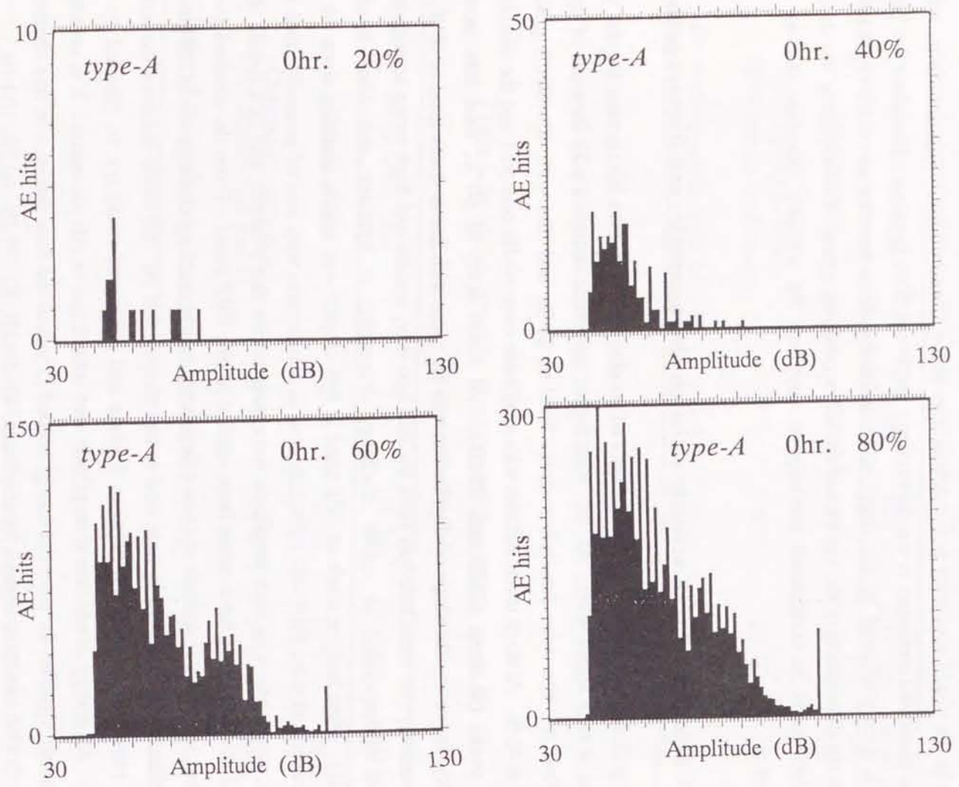

Fig.5.28 Changes of amplitude distribution histograms for virgin *type-A* specimen with increase of stress.

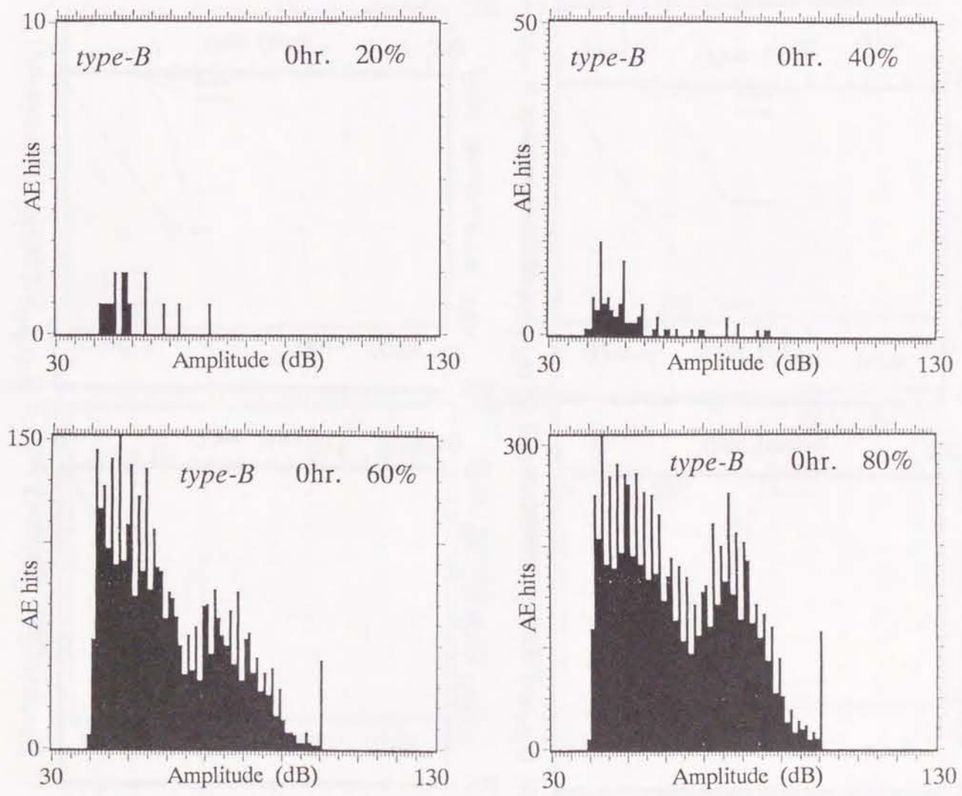

Fig.5.29 Changes of amplitude distribution histograms for virgin *type-B* specimen with increase of stress.

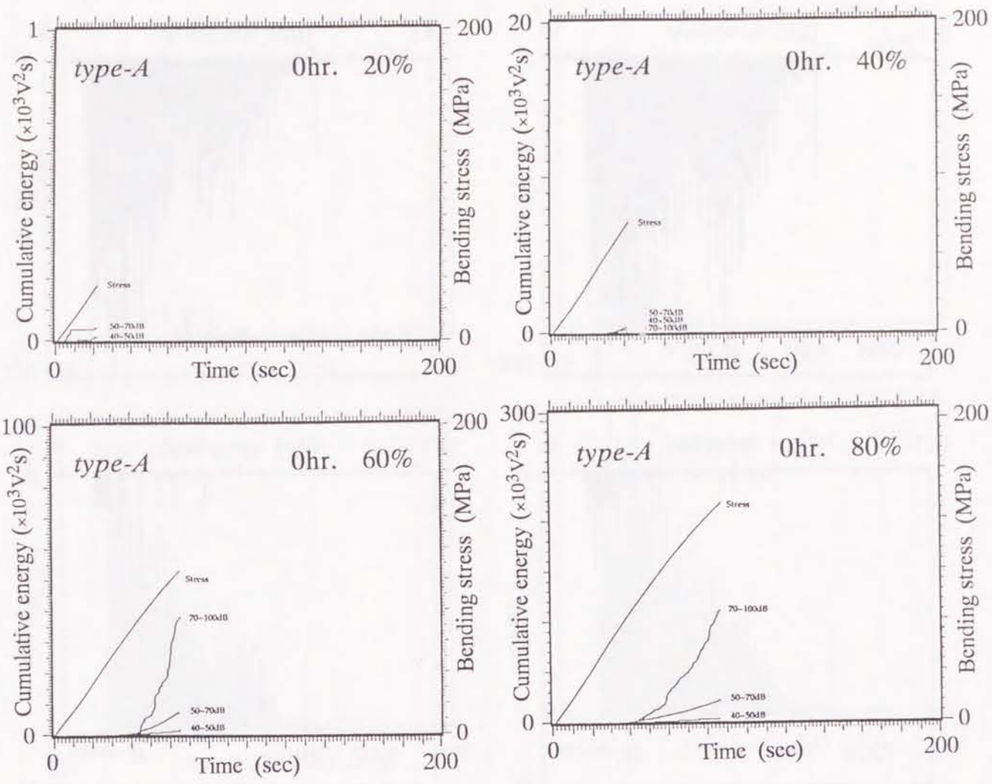

Fig.5.30 Changes of cumulative AE energy for virgin *type-A* specimen with increase of stress.

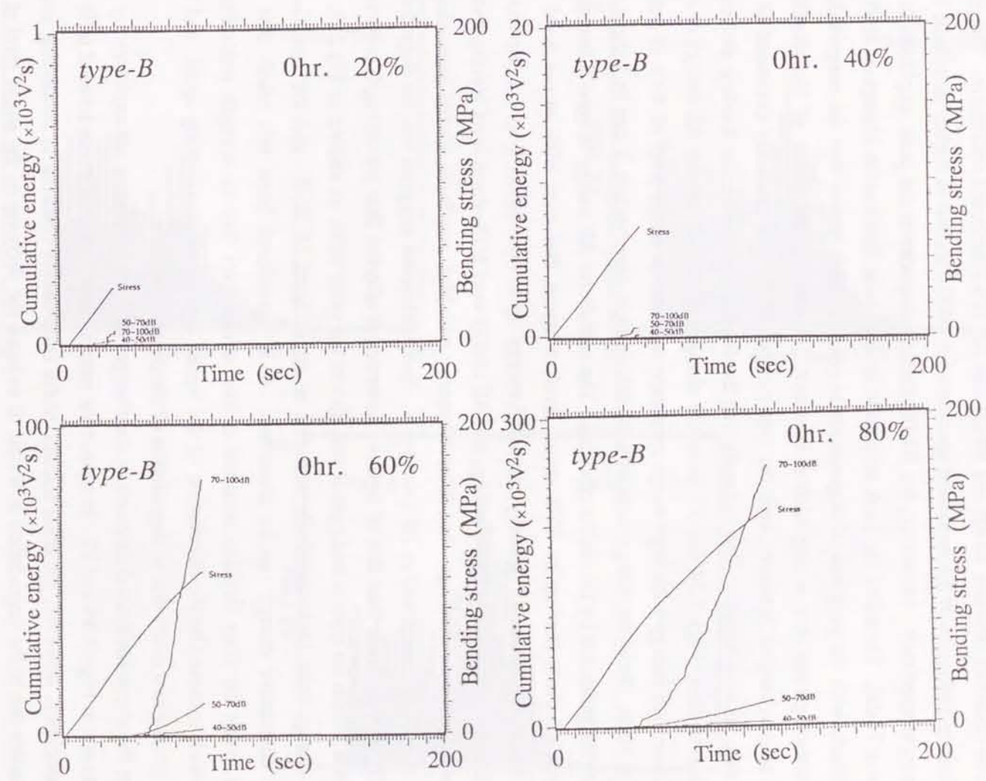

Fig.5.31 Changes of cumulative AE energy for virgin *type-B* specimen with increase of stress.

type-B initiated at lower stress level than in *type-A*. From these results, it is considered that the AE energy signifies the scale of fracture and that the cumulative AE energy signifies the progress of the fracture. Therefore the fracture process can be estimated with AE energy.

Figs.5.32 and 33 show the AE amplitude distributions at stress level of 80% for each immersion time. In the virgin specimen for *type-A*, two peaks could be observed at 45 dB and 72 dB and the main peak was 45 dB as shown in Fig.5.28. At 100 h, however, the remarkable peak cannot be observed between 40 dB and 80 dB and AE hits distributed uniformly. The main peak amplitude in histogram of the immersed specimen for 1000 h shifted to higher amplitude than that of the virgin specimen. Moreover, for 3000h immersed specimen the peak amplitude in the histogram was 73 dB. Therefore the peak amplitude in amplitude distribution histogram shifts to higher amplitude with the progress of degradation in *type-A*. This means that the magnitude of fracture becomes greater due to degradation in water. In *type-B*, the shape of the amplitude distribution never changed, however, only the total number of AE hits gradually decreased as the immersion time became longer. This suggests that the fracture caused by the loading decreased due to the degradation. Figs.5.34 and 35 show the changes of the cumulative AE energy at each immersion time. AE energy with high range amplitude occurred at stress level of 40% in *type-A* immersed for 100h. From the comparison with the microscopic observation, it can be judged that these AE hits are generated by the matrix cracking. The cumulative AE energy in *type-B* immersed for 100h was relatively low up to 60% stress level, whereas that over 60% stress level the cumulative AE energy increased radically. Low AE energy up to 60% stress level corresponds to the generation of microcracks and debonding, and AE energy over 60% stress level corresponds to the enlargement of the debondings. At 1000h AE energy with high amplitude started increasing at stress level of 30% in *type-A* and of 20% in *type-B*. Such difference suggests that the degradation progress of *type-B* is faster than that of *type-A*, however, it affected little the strength reduction. The strength at 1000h for *type-A* and *type-B* was almost the same value as shown in Fig.5.9. At 3000 h AE energy with high amplitude occurred at stress level of 20 %, and the remarkable increase of cumulative energy can be observed. It is considered from this result that the debondings inside the fiber bundles occurred at low stress level due to strength reduction at interface, which is caused by the dissolution of the binder and the silane coupling agent, and that the fracture propagated easily due to degradation of matrix and interface.

From the above-mentioned discussion, the changes of fracture process are explained by AE energy as shown in Figs.5.36 and 37. In *type-A* the matrix cracks occur at stress level of 60% for the virgin specimen, however, the main fracture shifts from matrix cracking to debonding inside the fiber bundles due to the degradation in water. It induces the decrease of the stress level at the initiation of AE with high amplitude and the increase of the accumulation rate of AE energy. In *type-B* the matrix cracks occur at stress level of 40% for the virgin specimen and the changes of the main fracture appear as well as *type-A*. The changes of the accumulation rate of AE energy due to degradation are remarkable in *type-B*.

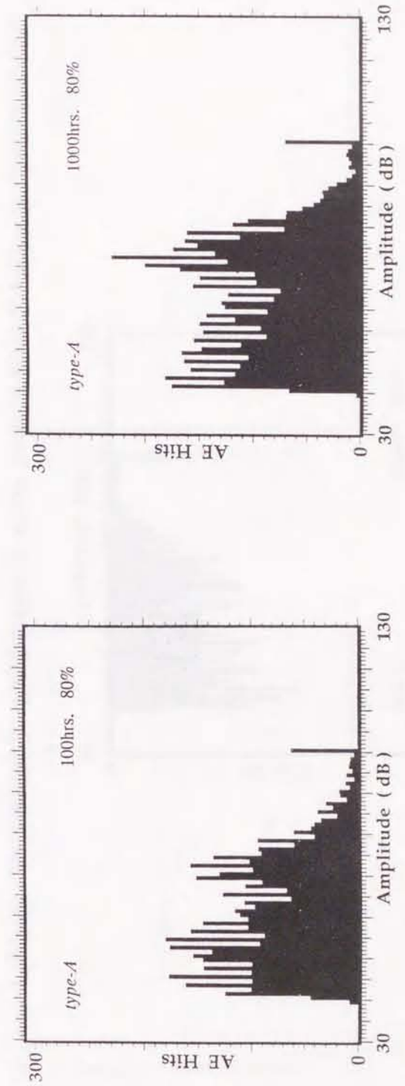

Fig.5.32 AE amplitude distributions at stress level of 80% for *type-A* specimen.

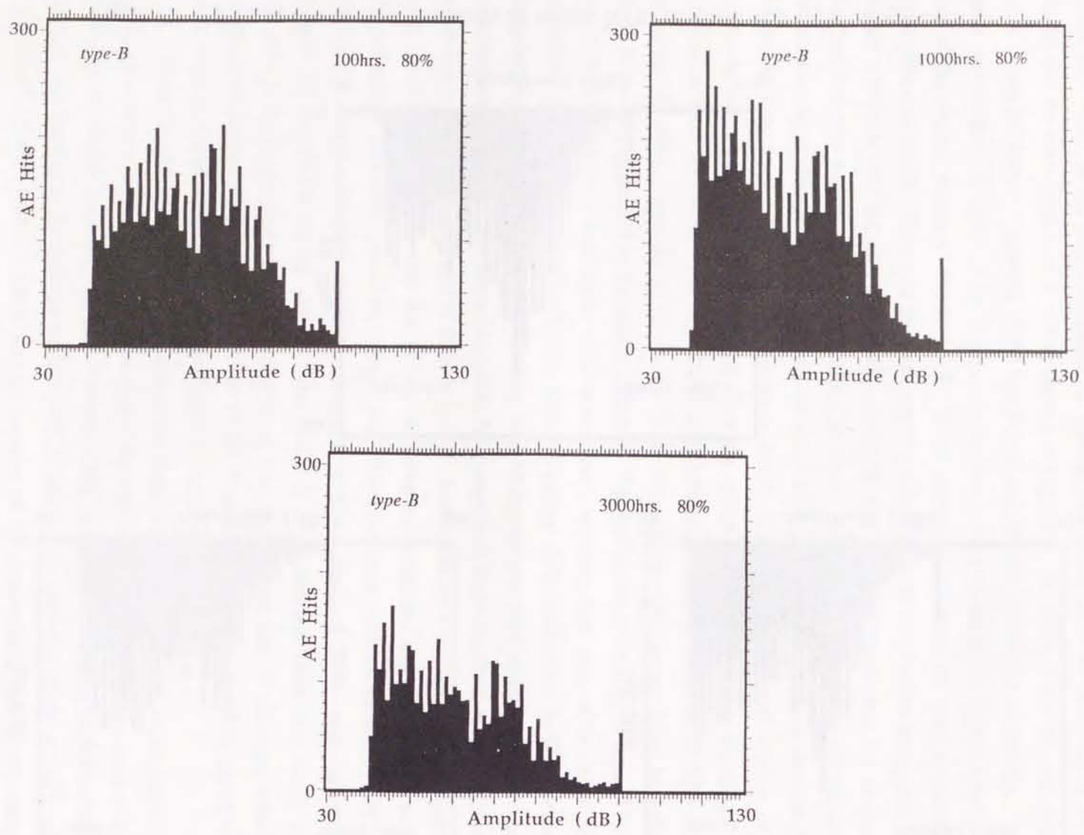

Fig.5.33 AE amplitude distributions at stress level of 80% for *type-B* specimen.

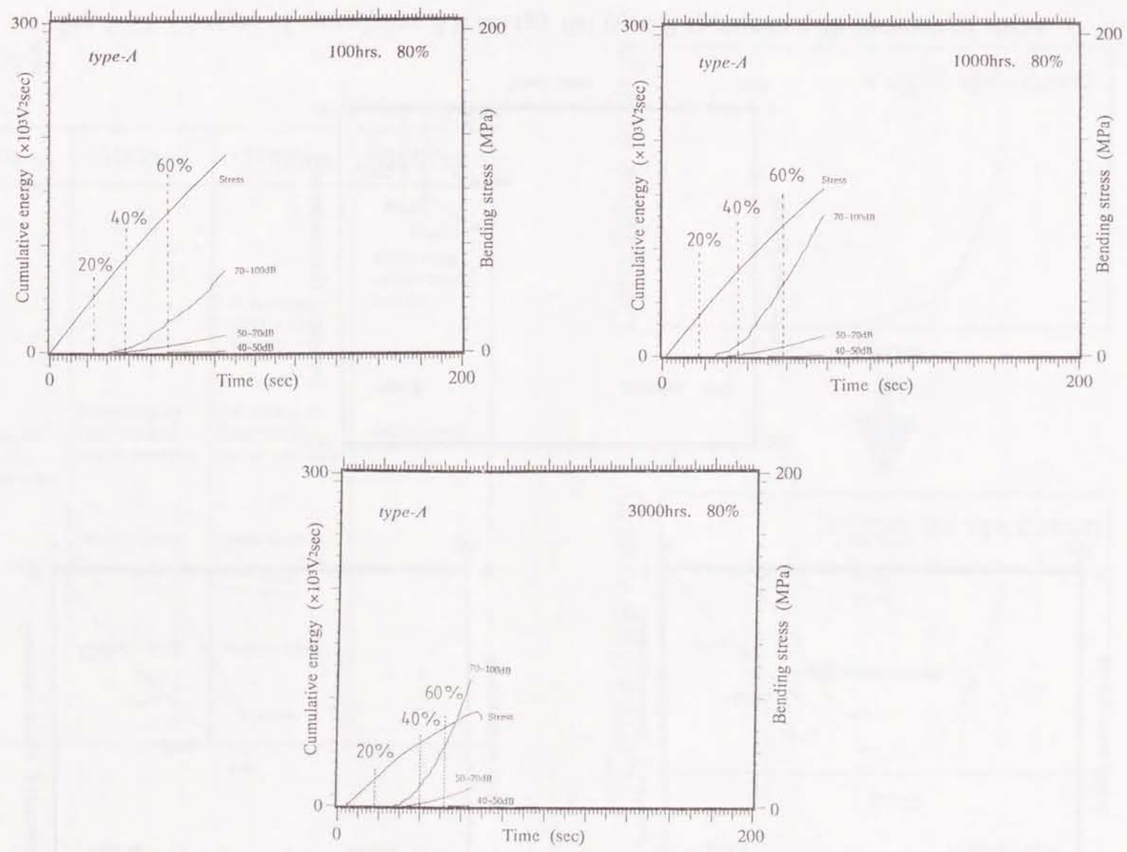

Fig.5.34 Changes of cumulative AE energy for *type-A* specimen with increase of stress.

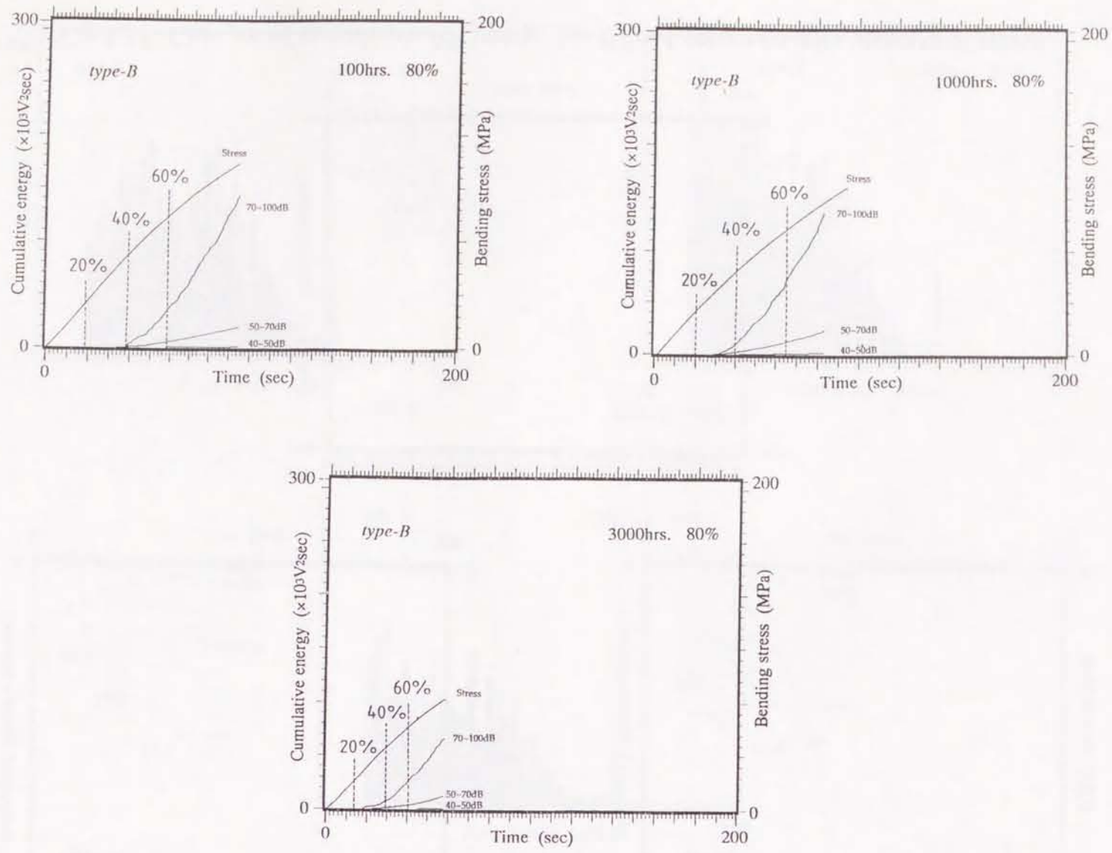

Fig.5.35 Changes of cumulative AE energy for *type-B* specimen with increase of stress.

type-A

	0hr.	100hrs.	1000hrs.	3000hrs.
0 %			debonding within fiber bundle	debonding within fiber bundle
≀	debonding of fiber bundle/ matrix interface matrix crack	debonding of fiber bundle/ matrix interface & matrix crack	debonding of fiber bundle/ matrix interface & matrix crack	matrix crack
80 %		matrix crack	matrix crack	

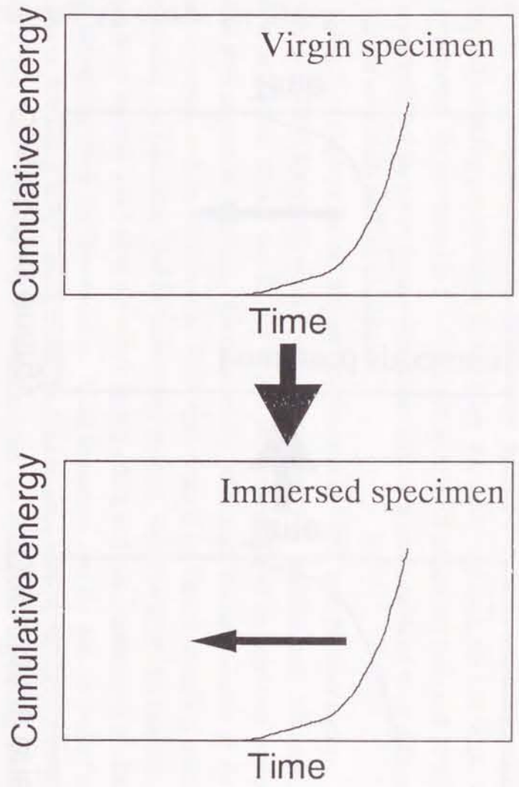

Fig.5.36 Explanation of fracture process by introducing AE energy for *type-A*.

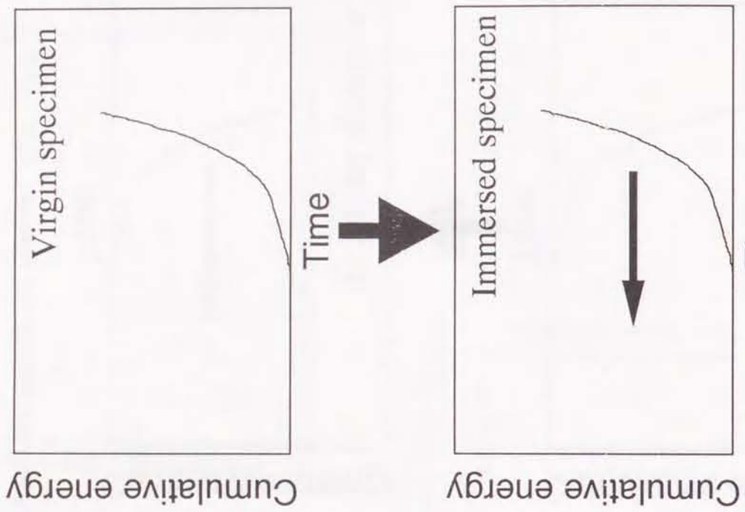

Fig.5.37 Explanation of fracture process by introducing AE energy for *type-B*.

type-B

	0hr.	100hrs.	1000hrs.	3000hrs.
0 %			debonding within fiber bundle	debonding within fiber bundle
~	debonding of fiber bundle/ matrix interface	debonding of fiber bundle/ matrix interface	debonding of fiber bundle/ matrix interface	matrix crack
	matrix crack	& matrix crack	& matrix crack	
80 %		matrix crack	matrix crack	

5.3.5 Kaiser effect on FRP immersed in hot water

Fig.5.38 displays the AE hits and amplitude with the load history. In the virgin specimen, Kaiser effect was satisfied until stress level of 80%. In the immersed specimen, however, Kaiser effect was never satisfied and many AE hits were detected even in the unloading process. In the loading and unloading process when Kaiser effect was never satisfied, AE hits below 70dB were mainly detected. As mentioned in 5.3.4, AE hits over 70dB affects the failure of FRP. Therefore it is considered that the stress levels when Kaiser effect was never satisfied were different, in case that AE hits over 70dB are only discussed.

Fig.5.39 displays the AE hits and amplitude over 70dB with the load history. In case of AE hits over 70dB Kaiser effect up to 80% stress level was satisfied until 30h, that is, Kaiser effect is satisfied in phase I and II. Up to 30h the nonlinearlity of the load-time curves to stress level of 80% cannot be observed. On the contrary, after 100h the nonlinearlity of the load-time curves appeared, and the AE hits over 70dB were detected during the unloading process. From these results, it is considered that the catastrophic fracture, which produces the modulus reduction, occurs in the material which does not satisfy Kaiser effect, and this phenomenon is closely related to the debonding inside the fiber bundles. Until immersion time for 30h (in phase I and II), the remarkable debonding never occurs inside the fiber bundles because the water absorption of the interface is a little. Therefore, it is considered that the remarkable debonding inside the fiber bundles never exists before loading. Over immersion time for 30h (in phase III), the remarkable debonding appears inside the fiber bundles, and eventually such material cannot satisfy Kaiser effect. Then, it can be estimate the degradation inside the fiber bundles by the Kaiser test dealt with the AE hits over 70dB, and further the soundness of the material can be also evaluated by this Kaiser test.

5.4 Conclusion

This chapter dealt with the bending strength and the fracture mechanism of the randomly oriented FRP immersed in hot water. The reduction behavior of the bending strength was discussed from the relation between the weight changes and the strength. The fracture mechanism was investigated by the microscopic observations of the cross-section and the acoustic emission characteristics. Fracture initiation was the debonding between fiber bundle and matrix in the virgin specimen, while it was the debonding inside the fiber bundles in the immersed specimen. The strength reduction due to water immersion was caused both by the degradation of the matrix and by the gradual degradation of the fiber/matrix interface from phase I through phase II. In phase III the strength was reduced by the debondings between fiber bundle and matrix and inside the fiber bundles. The changes of the cumulative AE energy indicated the remarkable increase with the fracture mode change. The magnitude of the fracture could be estimated by both AE amplitude and AE energy. It was clarified that this method could be applied to the estimation of the fracture mode changes of FRP due to immersion in water. Moreover it was clarified that the degradation inside the fiber bundles could be estimated by Kaiser test with AE hits over 70dB.

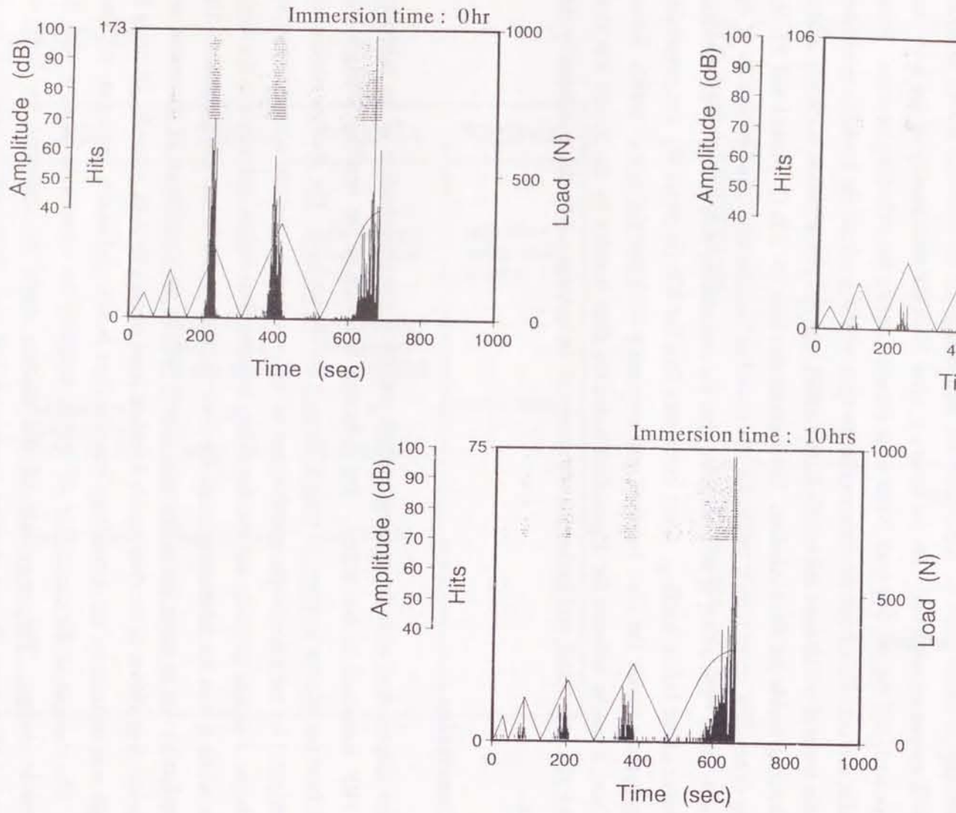

Fig.5.39 Detected AE hits and their amplitude with load history in the range from 70dB to 100dB.

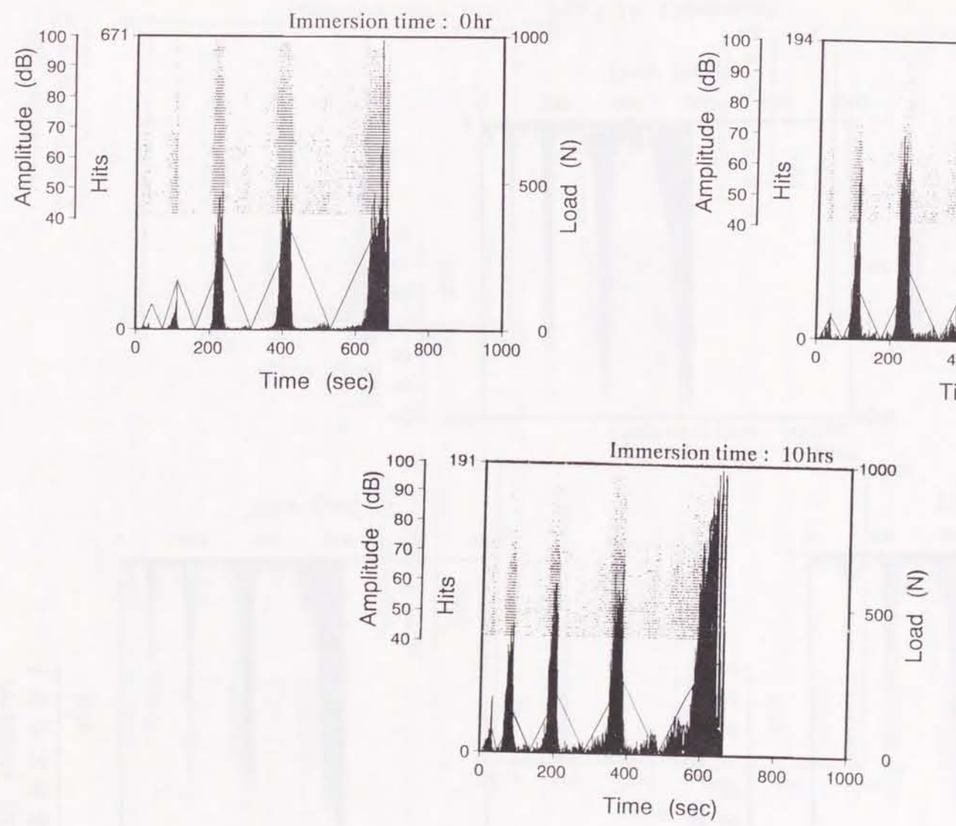

Fig.5.38 Detected AE hits and their amplitude with load history.

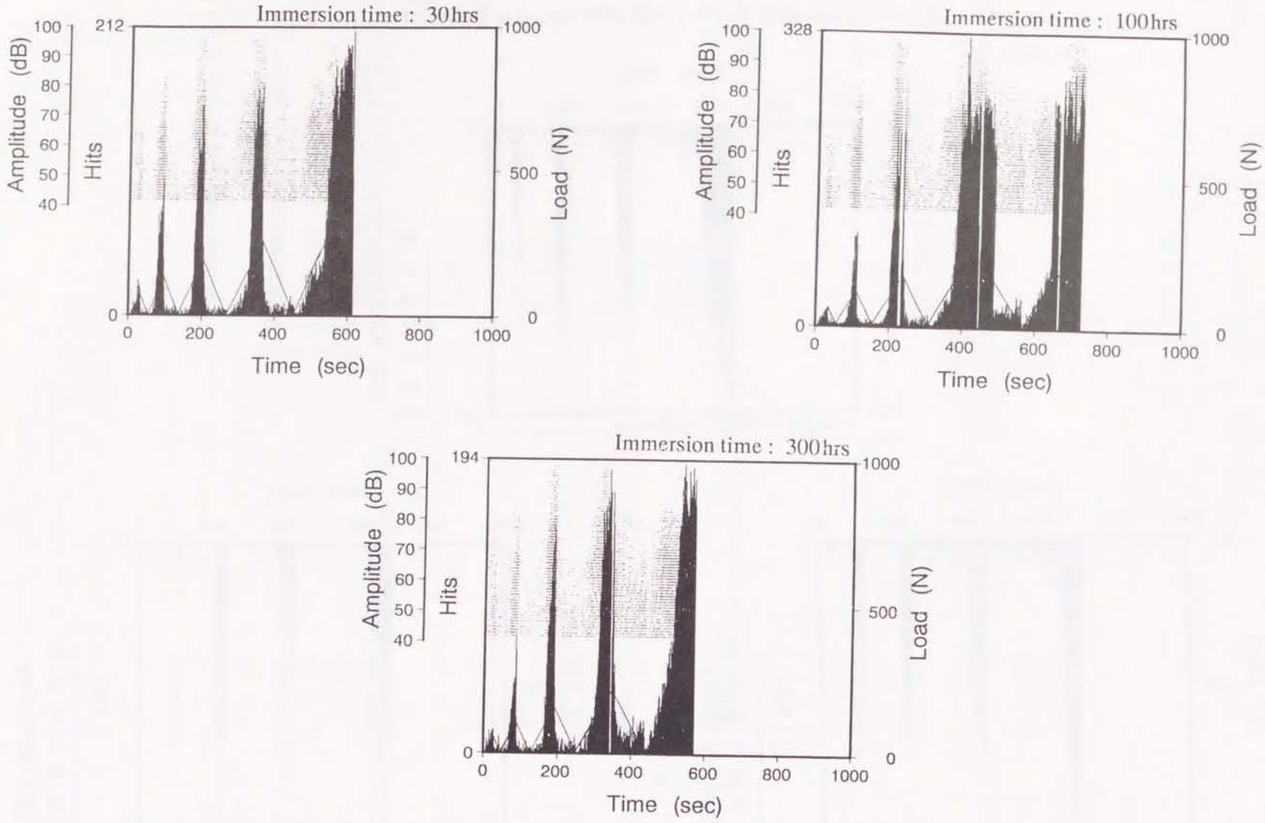

Fig.5.38 Continued.

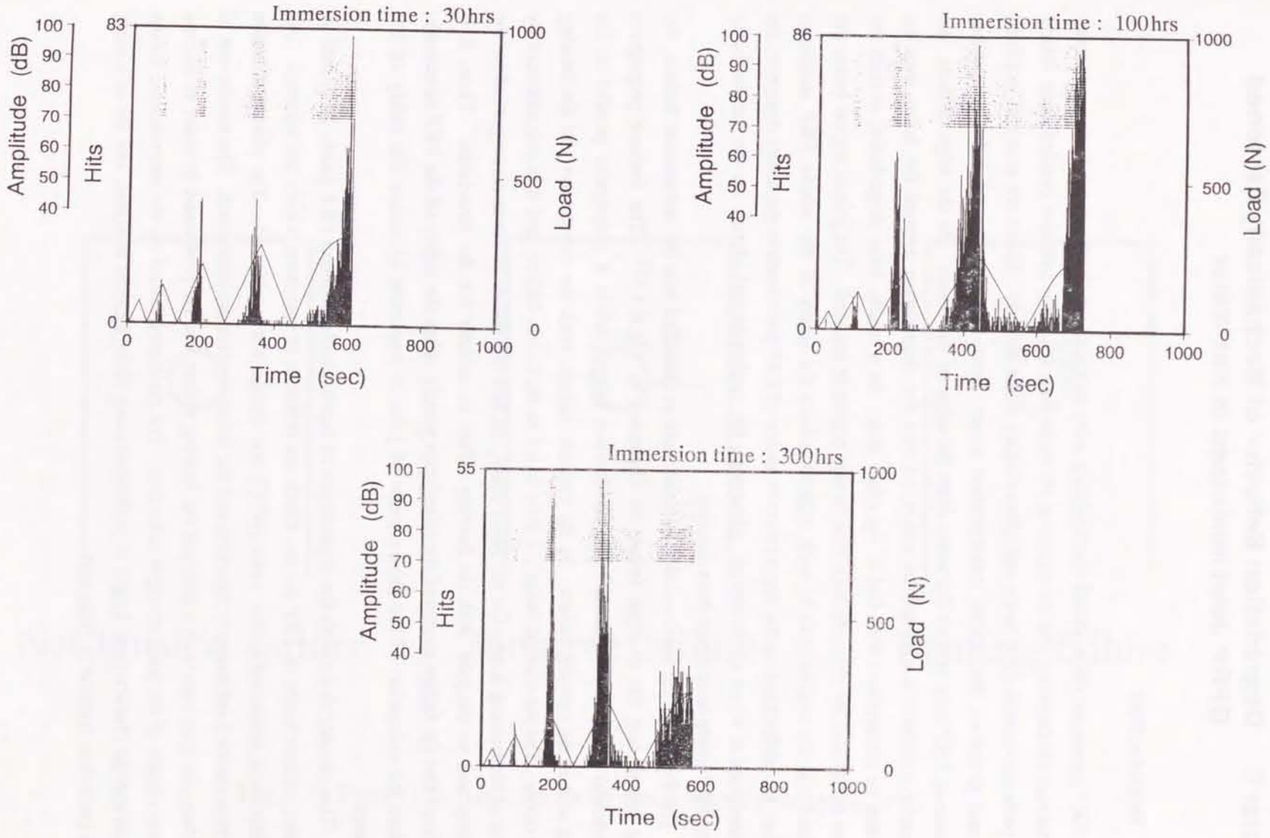

Fig.5.39 Continued.

Chapter 6 Degradation Behavior of Mechanically Fastened GFRP Joint Immersed in Hot Water

6.1 Introduction

FRP panels are often joined mechanically with another parts in the case of usage as water tanks because the handling and the repairing are easier than those for adhesive bonded joint. Many joined parts can exist in FRP tanks and often contact water directly. Holes are required in joined parts, and therefore, the stress concentration arises from the existence of hole. In water environment, FRP may absorb the water from the edge of the holes. At the edge of hole, the fiber/matrix interface is exposed to water, so that the degradation around the holes may be accelerated in comparison with that of the other area. As a result, local degradation around the hole can occur and the strength reduction in this region is induced. The joined region bears the local load and the degradation in such regions affects the safety of the whole FRP structure. Therefore the understanding the degradation behavior of FRP joint leads to the safety design of the FRP structures in water environment. However, the environmental effects on the mechanically fastened FRP joints have never been detailed.

The failure of the mechanically fastened joint is classified into the net-tension failure, the bearing failure and the multiple failure as illustrated in Fig.6.1.[117] The fracture propagates perpendicular to the loading axis in the net-tension failure, while it propagates parallel to the loading axis in the bearing failure. In the multiple failure, both the net-tension and the bearing failure occur. The net-tension failure of joint is led to the brittle failure, and it is accompanied by the drop of the bearing load. On the other hand, the bearing failure is never accompanied by the load drop and so the joint with the bearing failure is suitable for the structures. Then, it is considered that the failure modes of the joined part greatly affect the safety of the FRP structures. Therefore the estimation of the failure mode of joint is important to assure the safety of the structures.

This chapter deals with the degradation of mechanically fastened FRP joints immersed in hot water. Three kinds of FRP joints, which are different in specimen width, are adopted. All the joints were immersed in hot water (80°C) and tensile test performed. The effects of water immersion on the joint strength reduction and the failure modes are discussed. The tensile test of the rectangular specimen with a hole and the bearing failure test are performed in order to discuss the main causes of the joint strength reduction. The prediction based on the macroscopic failure criterion and the characteristic length is performed using finite element analysis, and the efficiency of this prediction method is discussed.

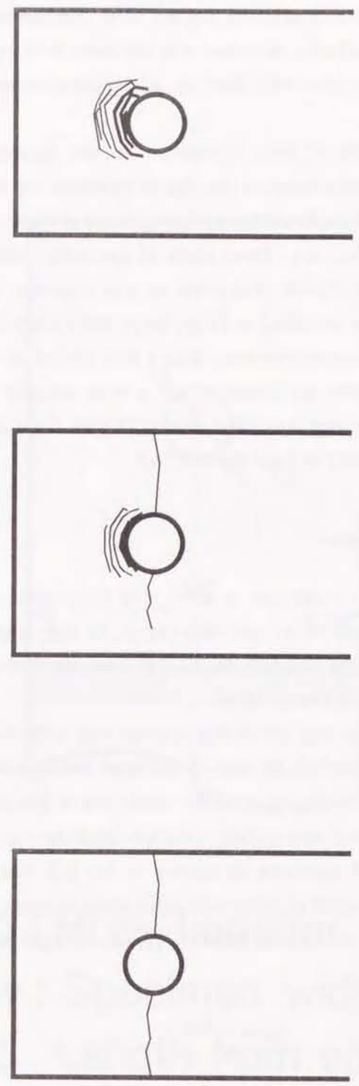

Fig.6.1 Typical failure modes of mechanically fastened joint.

6.2 Joint Strength and Fracture Mode

6.2.1 Material

Material used was the randomly oriented E-glass fiber continuous strand mat reinforced orthophthalic based unsaturated polyester resin and was the same with *type-C* used in Chapter2. Using this material square panels were fabricated by a compression molding method. Fiber volume content was about 35%.

Fig.6.2 shows the geometry of joint specimen. In this figure, d, w and e are hole diameter, specimen width and distance between the edge of specimen and the center of hole (called as edge distance), respectively. The hole diameter, d, was fixed at 6 mm and e was also fixed at 18 mm (three times of hole diameter; 3e). Three kinds of specimen width were adopted; 18 mm (three times of hole diameter; 3w), 30 mm (five times of hole diameter; 5w) and 42 mm (seven times of hole diameter; 7w). These are called as 3w3e, 5w3e and 7w3e joints for short. Figs.6.3 and 4 show the geometry of rectangular specimen with a hole (called as notched specimen) and bearing test specimen. Also in these specimens w and e were selected as the multiple of hole diameter as same manner with the joint specimen, that is, e was fixed at 18mm (3e) and three kinds of w were 18mm (3w), 30mm (5w) and 42mm (7w).

6.2.2 Experimental procedure

Water immersion tests were conducted at 80 °C with temperature controlled water baths. Before immersion test, the free-edges of the specimen except for hole edge were coated with heat resistant resin in order to prevent the moisture penetration from the free-edges. The periods of immersion were fixed at 3, 10, 30, 100 and 300 h.

Tensile test of joint specimen after immersion in water was performed with double lap joint at constant cross-head speed of 1mm/min by Instron universal testing machine (type 4206) under room temperature. Fig.6.5 illustrates the set-up of the tensile test of double lap joint. Diameter of steel pin was fixed at 6mm. The load was applied to the specimen through a steel pin.

Tensile test of the notched specimen as shown in Fig.6.3 was performed after water immersion at constant cross-head speed of 2mm/min under room temperature in order to compare the strength of joint showing the net-tension failure. Tensile strength of the notched specimen (σ_{nt}) is obtained by

$$\sigma_{nt} = \frac{P_{nt}}{(w - d) \cdot t} \tag{6.1}$$

where P_{nt} is the maximum load, w is the width, d is the hole diameter and t is the thickness of the notched specimen.

Moreover the bearing test method was devised in order to compare the bearing strength of the joint showing the bearing failure. A compression load was applied to the specimen with half-circular notch by the compression jig as shown in Fig.6.6. Bearing test was performed at constant

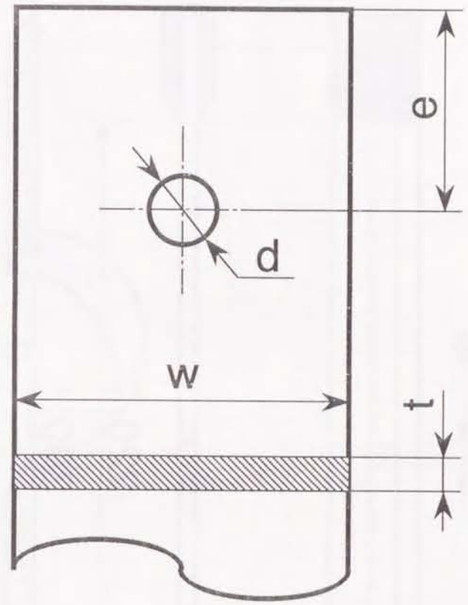

d : Hole diameter
w : Specimen width
e : Length from edge to center of hole

Fig.6.2 Geometry of joint specimen.

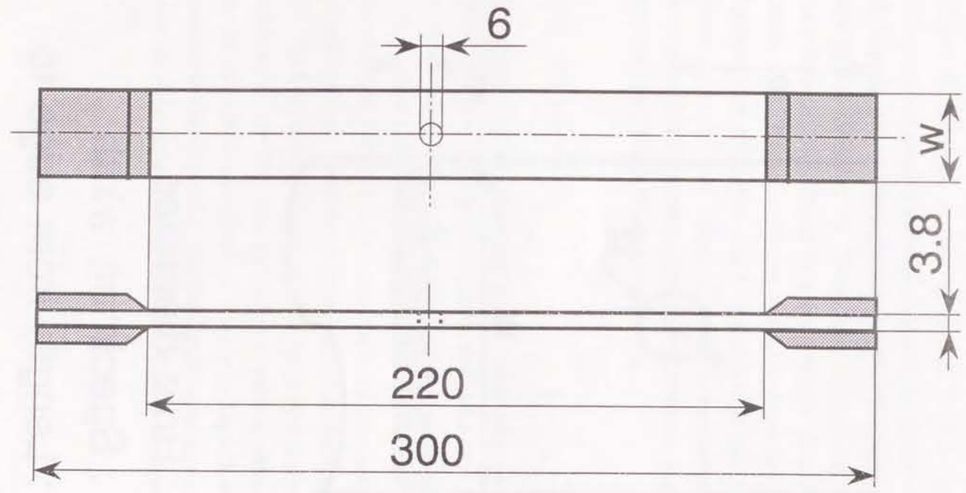

Fig.6.3 Geometry of notched specimen.

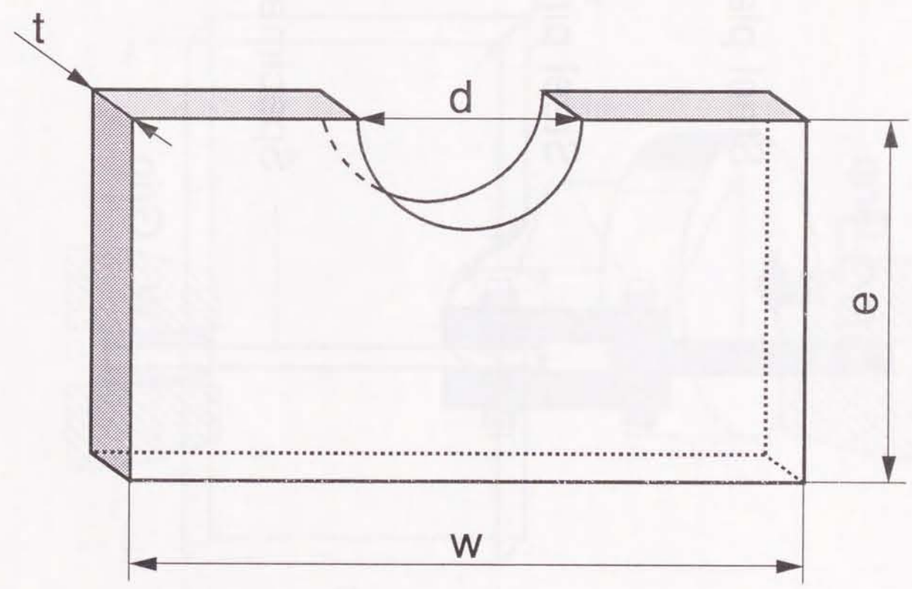

Fig.6.4 Geometry of bearing test specimen.

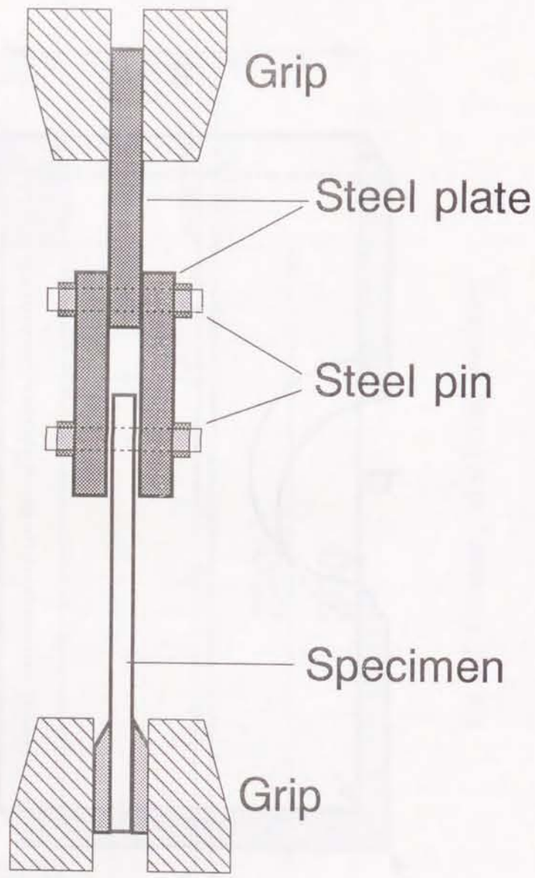

Fig.6.5 Set-up of tensile test of double lap joint.

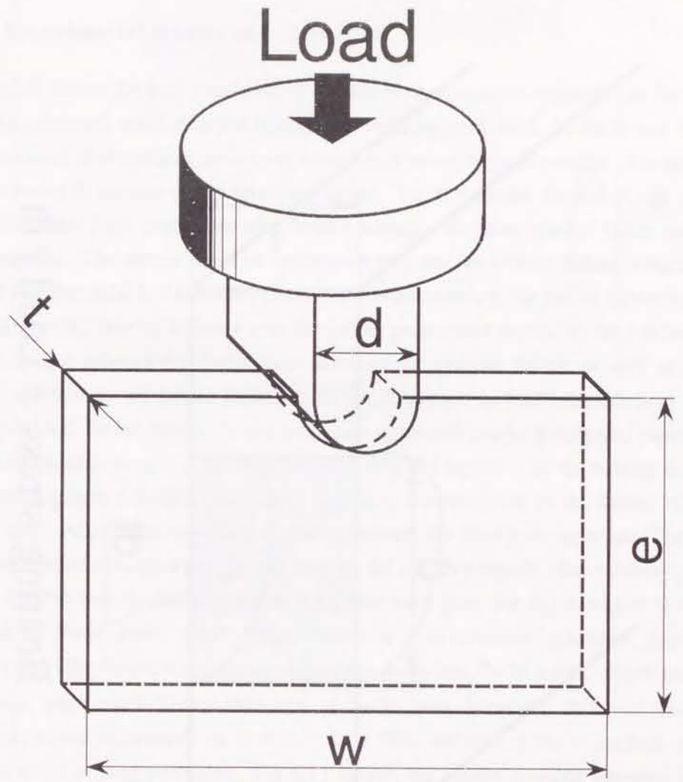

Fig.6.6 Bearing test.

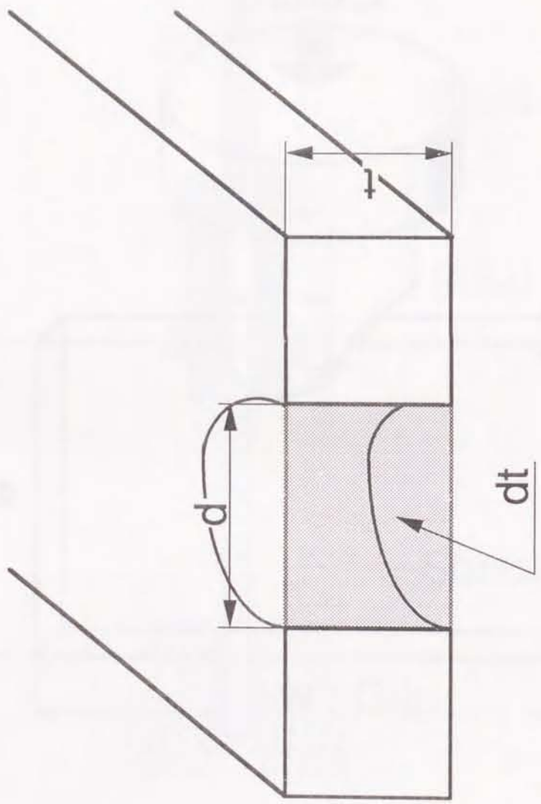

Bearing stress = Load / dt

Fig.6.7 Calculation of bearing strength.

cross-head speed of 0.1 mm/min under room temperature. As illustrated in Fig.6.7, bearing strength (σ_b) is obtained by

$$\sigma_b = \frac{P_b}{d \cdot t} \tag{6.2}$$

where P_b is the maximum load in bearing test, d is the notch diameter and t is the thickness.

6.2.3 Experimental results and discussion

Fig.6.8 shows the load-displacement curves of the original dry joints. In 3w3e joint the load linearly increased, and it dropped rapidly after reaching peak load. In 5w3e and 7w3e joints, the load decreased after reaching peak load, however, it never dropped rapidly. The peak loads of joints increased with increase of the specimen width. Fig.6.9 shows the soft X-ray photographs of typical fractured joint specimens after tensile testing. In these photos black area indicates fractured regions. The failure mode of 3w3e joint was the net-tension failure where the failure propagated perpendicular to the loading direction. On the contrary, the failure modes of 5w3e and 7w3e joints were the bearing failure where the failure propagated parallel to the loading direction. In addition, a few original dry 5w3e joint indicated the multiple failure as well as the bearing failure. The difference in failure mode led to the difference in load - displacement curve after reaching peak load. In net-tension failure mode, the generated cracks propagated rapidly in width direction with the fiber breakage, and then the load dropped rapidly. In the bearing failure mode, the progressive failure occurred, and a little load drop occurred due to the failure of the matrix around the hole. After the failure of the matrix, however, the fiber existing around the hole could bear the load applied through a pin, so that the load did not drop rapidly after reaching peak load.

Fig.6.10 shows the changes of failure load for each joint due to immersion in water. The failure load of 3w3e joint, which failure mode was net-tension, gradually decreased with immersion time. The failure loads of the original dry 5w3e and 7w3e joints, which failure modes were bearing, were much higher than that of 3w3e joint, however, those of the immersed specimens decreased remarkably up to 30 h. After 30 h, the failure loads reached almost same value independent of joint geometry. Fig.6.11 shows the tensile strength retention of the joint specimens and the smooth specimens. The changes of the joint strength of 3w3e indicated the same tendency with those of the smooth specimens. This is related to the net-tension failure mode of 3w3e joints. The strength reduction was remarkable in 5w3e and 7w3e joints. Thus the joint with bearing failure mode is greatly affected by the immersion in water. Fig.6.12 summarizes the failure modes of the immersed joints. In 3w3e joint, the fracture tended to progress also in parallel to the loading direction with immersion time, and the failure mode changed from the net-tension to the multiple failure. The failure modes of 5w3e and 7w3e joints were the bearing failure both before and after immersion, and the fractured region was spread out as the immersion time was longer.

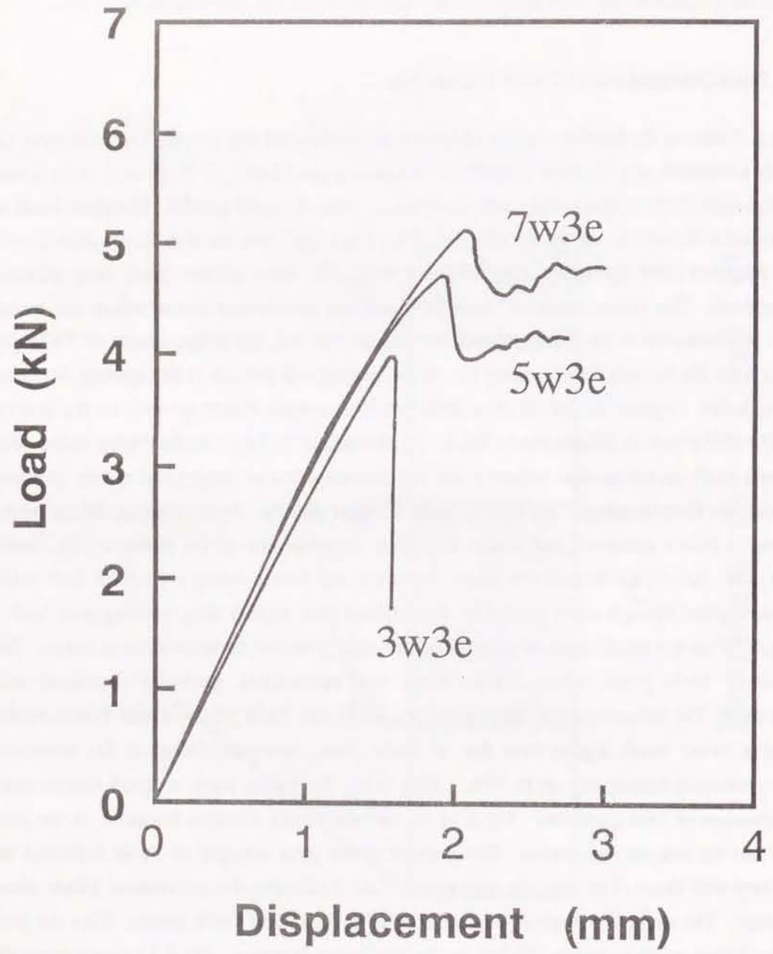

Fig.6.8 Comparison of load-displacement curves for virgin joints in tensile test.

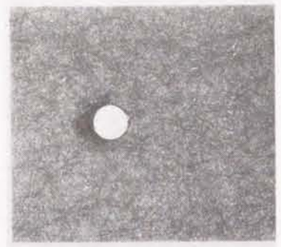

7w3e
Bearing failure

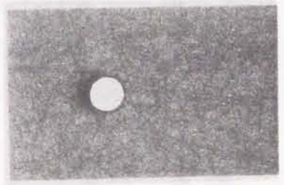

5w3e
Bearing failure

3w3e
Net-tension Failure

Fig.6.9 Soft X-ray photographs of typical fractured virgin joints in tensile test.

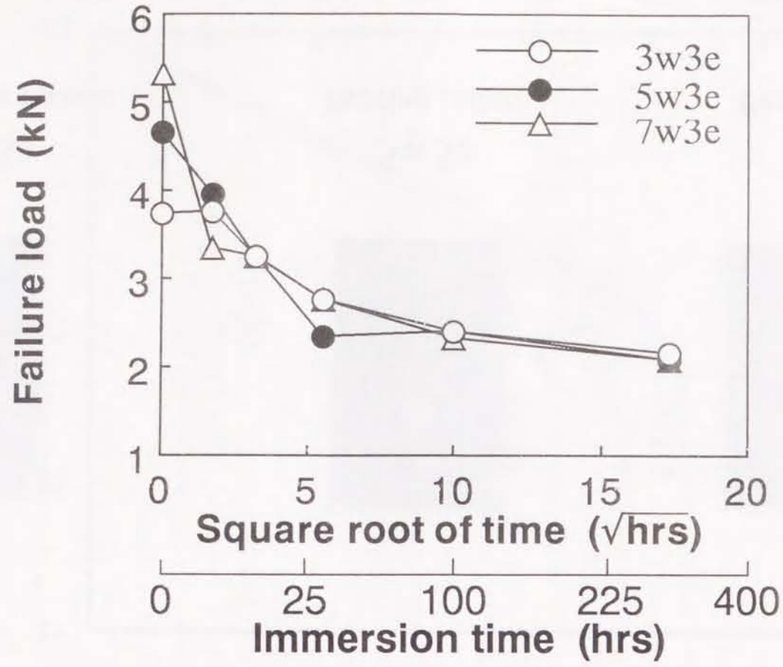

Fig.6.10 Changes of failure load in tensile test for joints due to water immersion.

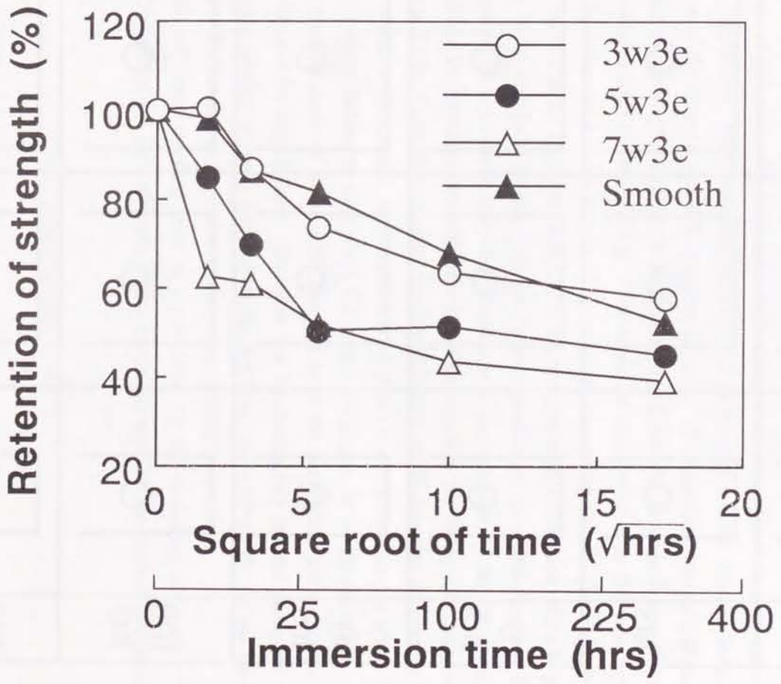

Fig.6.11 Retention of tensile strength for joints and smooth specimens.

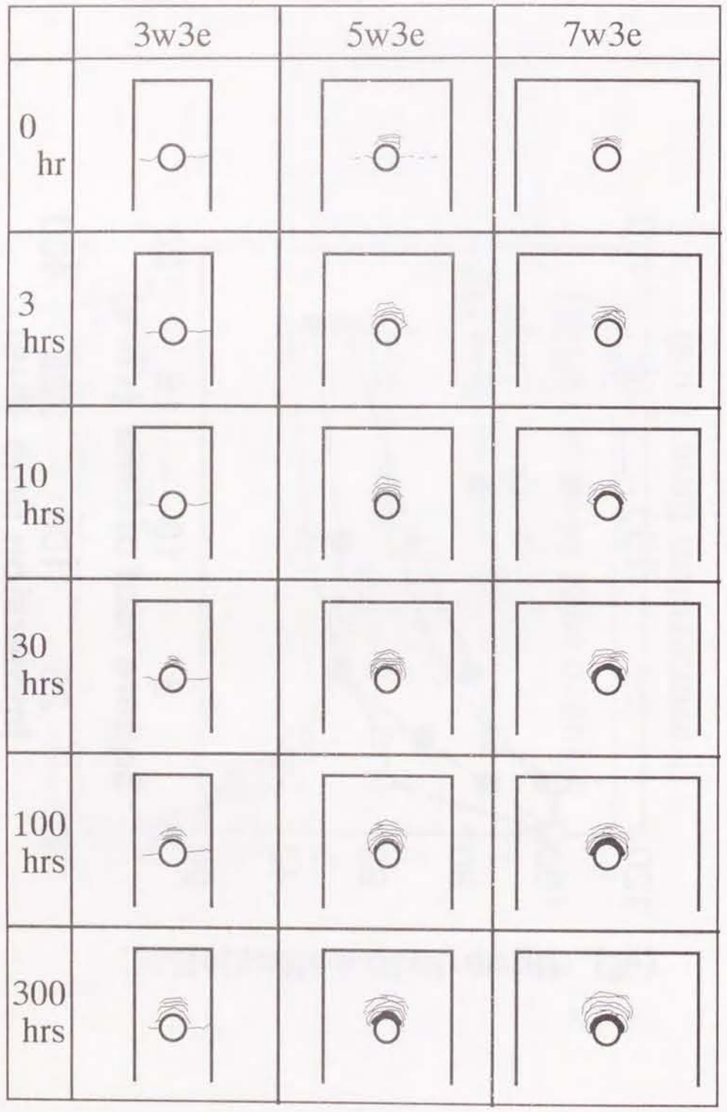

Fig.6.12 Failure mode changes for joints due to water immersion.

It can be considered that the changes of the fracture mode due to water immersion are related to the water absorption around the hole. Then, the moisture concentration distribution around the hole was calculated by the finite element analysis of diffusion. The weight gain data shown in Fig.2.19 was used to obtain the diffusion coefficient. The weight gain data were approximated by eqn(2.13) without phase division in order to obtain the overall water absorption behavior, and the maximum water absorption was obtained. The maximum water absorption ($M_g(\infty)$) obtained was 3.385%. From the approximated curve and the maximum water absorption, the diffusion coefficient was calculated by eqn(2.15). The obtained diffusion coefficient was $0.92\times10^{-2}mm^2/h$. Using the diffusion coefficient the moisture content was analyzed by the two dimensional finite element analysis of diffusion. Fig.6.13 is the finite element divisions for each joint specimen and the boundary conditions. 100% moisture was applied to the nodes at the edge of hole, and the initial condition of the material was 0% moisture content. The analytical moisture concentration distributions for each joint geometry are illustrated in Figs.6.14-16. In these figures the moisture concentration is expressed by $M_g/M_g(\infty)$). The moisture distribution was the same up to 30 h immersion independent of joint geometry. The moisture absorption around the hole progressed concentrically up to 30h for all joints. After 30 h, the concentration distribution of 3w3e joint was different from 5w3e and 7w3e joints. The moisture concentration in width direction for 3w3e joint became greater than for 5w3e and 7w3e joints due to the existence of the free-edge near the hole, and similarly the moisture concentration in width direction for 5w3e joint became greater than for 7w3e at 300h. From these results, the degradation in width direction progresses faster as the specimen width is narrower. It is considered that the water absorption in width direction affects the net-tension failure of joint since the cracks propagate in width direction. In fact, however, the fracture mode of 3w3e joint changed from the net-tension failure to the multiple (both net-tension and bearing) failure. Therefore this result suggests that the absorbed moisture greatly affects the bearing strength than the tensile strength. As a result, the failure mode of all joints changed to the bearing or the multiple failure due to water immersion.

The joint efficiency is often used as a parameter for the designing of joints. The joint efficiency is the ratio of the joint strength to the tensile strength of the smooth specimen and is given by

$$\text{Joint efficiency} = \frac{P_{max}}{\sigma_0 \cdot w \cdot t} \tag{6.3}$$

where P_{max} is the maximum load of joint, σ_0 is the tensile strength of the smooth specimen, w and t are the width and the thickness of the joint. Fig.6.17 shows the changes of the joint efficiency of each joint due to water immersion. The joint efficiency decreased with increase of the specimen width. In 3w3e joints the joint efficiency kept about 0.6 even after the water immersion. On the other hand, the joint efficiencies of 5w3e and 7w3e joints, which failure mode was the bearing failure, decreased up to 30h, and after that they kept almost constant. This result suggests that the bearing strength of joints shows the greater reduction than the tensile strength. Therefore the

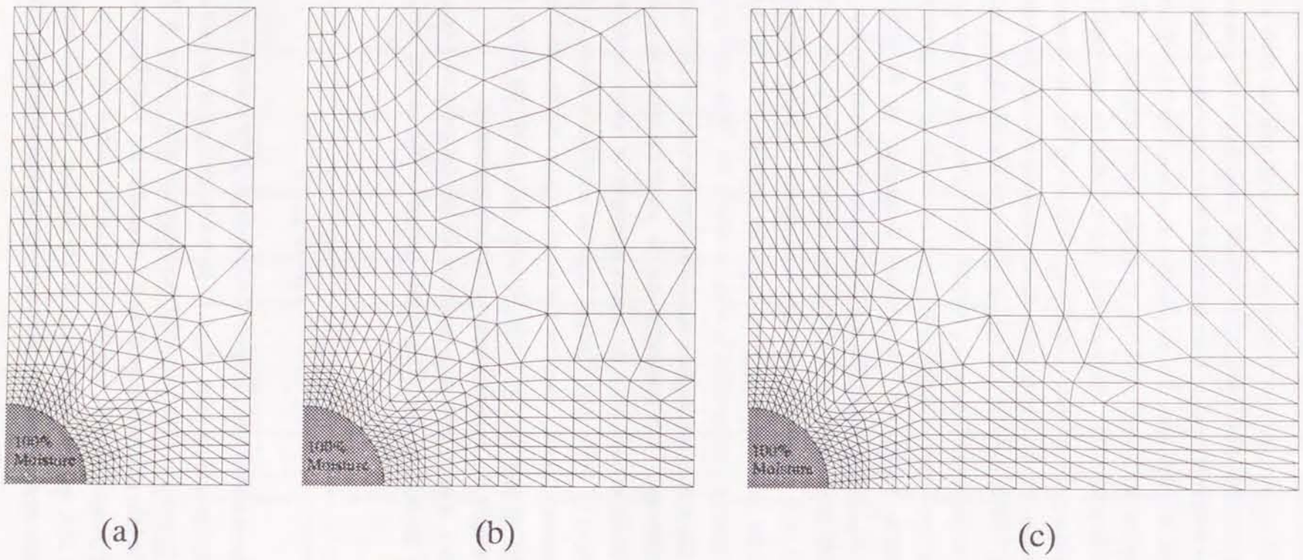

Fig.6.13 Finite element divisions and boundary conditions for moisture diffusion analyses; (a) 3w3e joint, (b) 5w3e joint and (c) 7w3e joint.

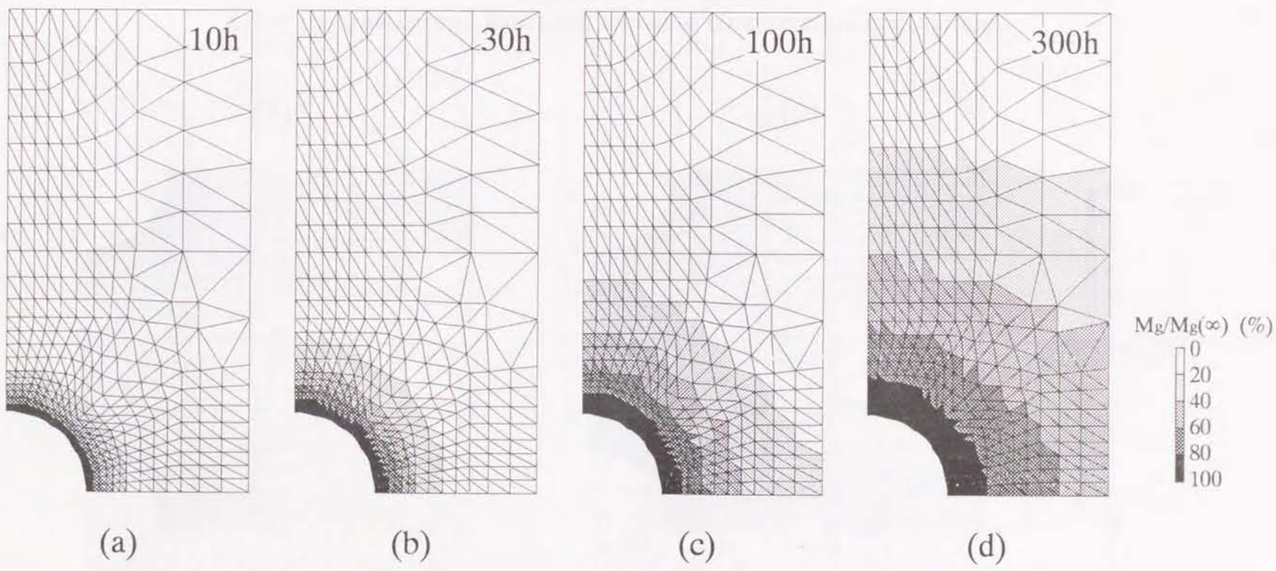

Fig.6.14 Analytically generated moisture concentration distribution for 3w3e joint; (a) 10h, (b) 30h, (c) 100h and (d) 300h.

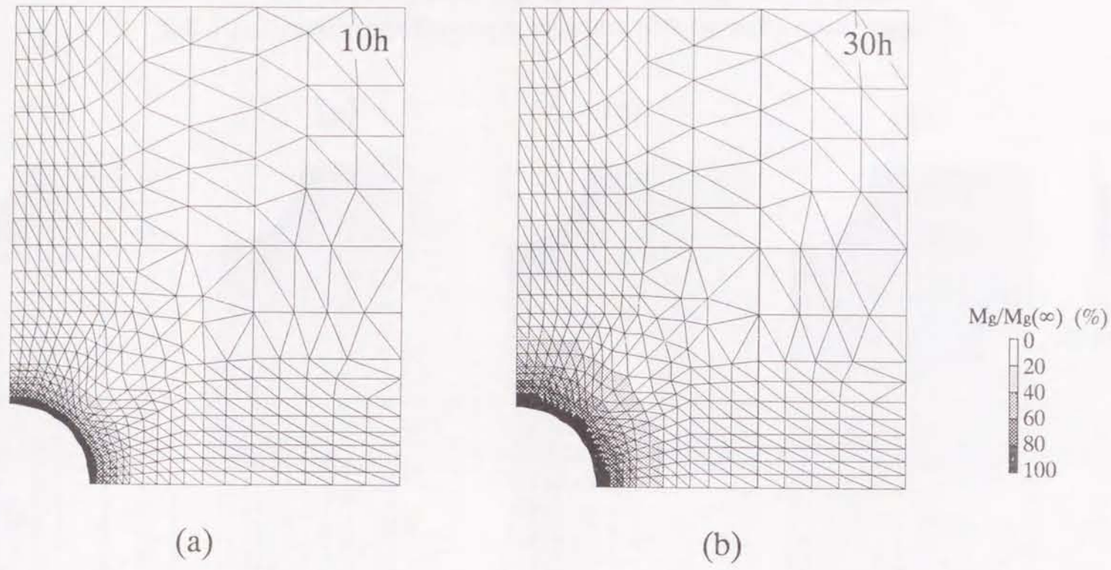

Fig.6.15 Analytically generated moisture concentration distribution for 5w3e joint; (a) 10h and (b) 30h.

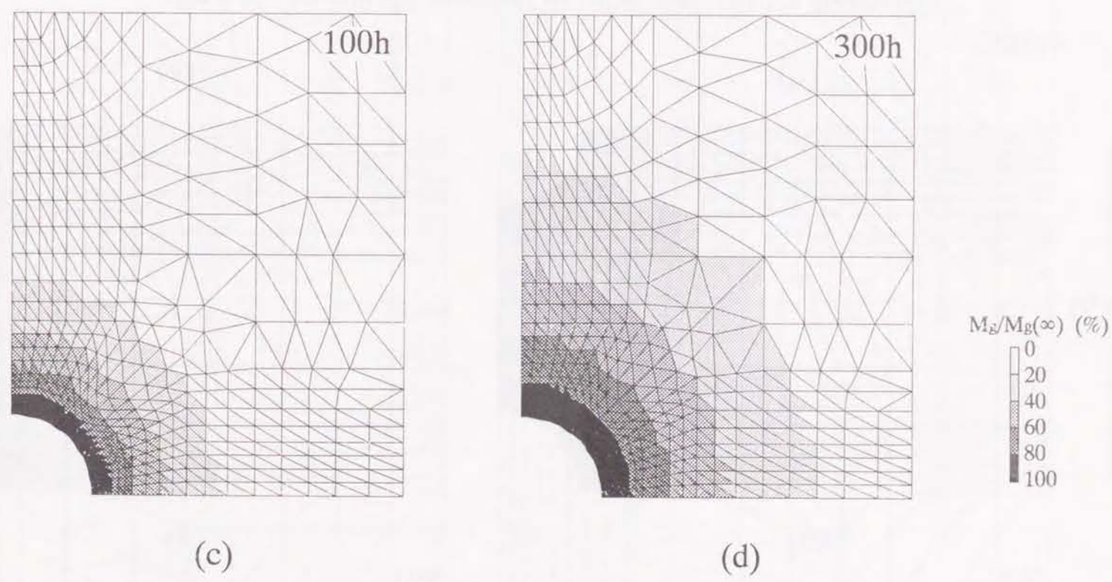

Fig.6.15 Continued; (c) 100h and (d) 300h.

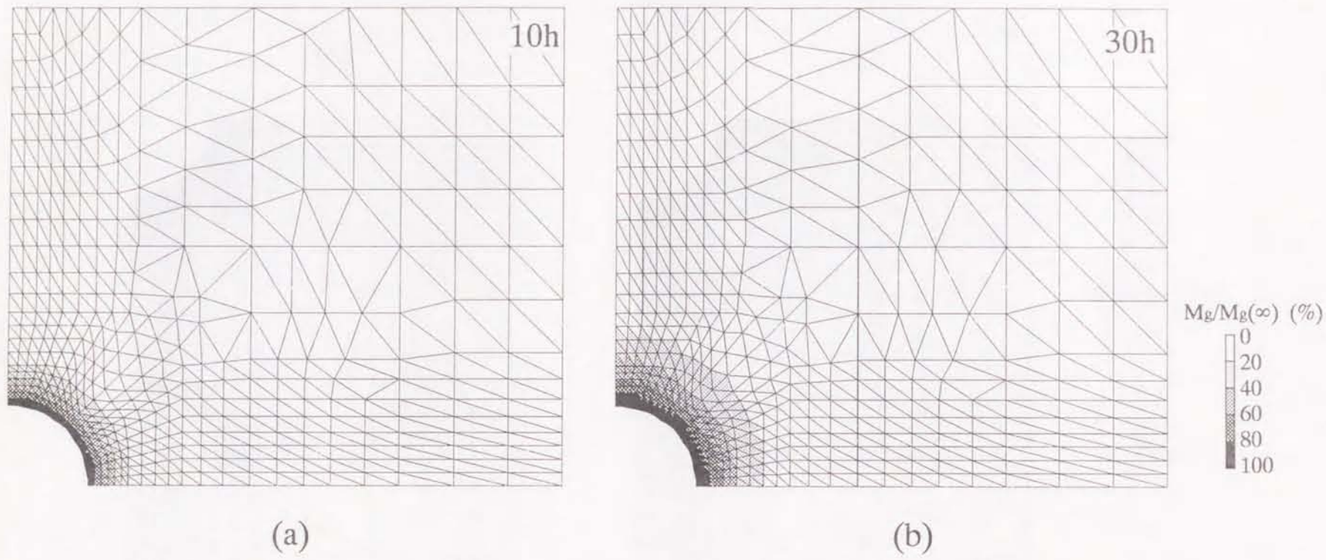

Fig.6.16 Analytically generated moisture concentration distribution for 7w3e joint; (a) 10h and (b) 30h.

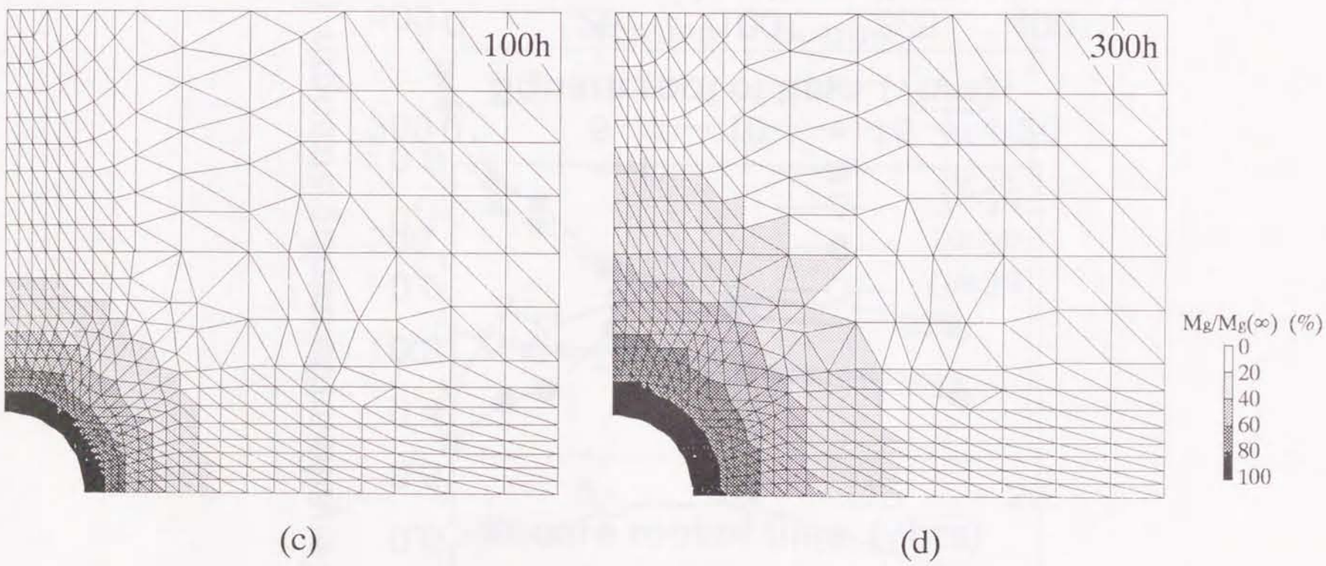

Fig.6.16 Continued; (c) 100h and (d) 300h.

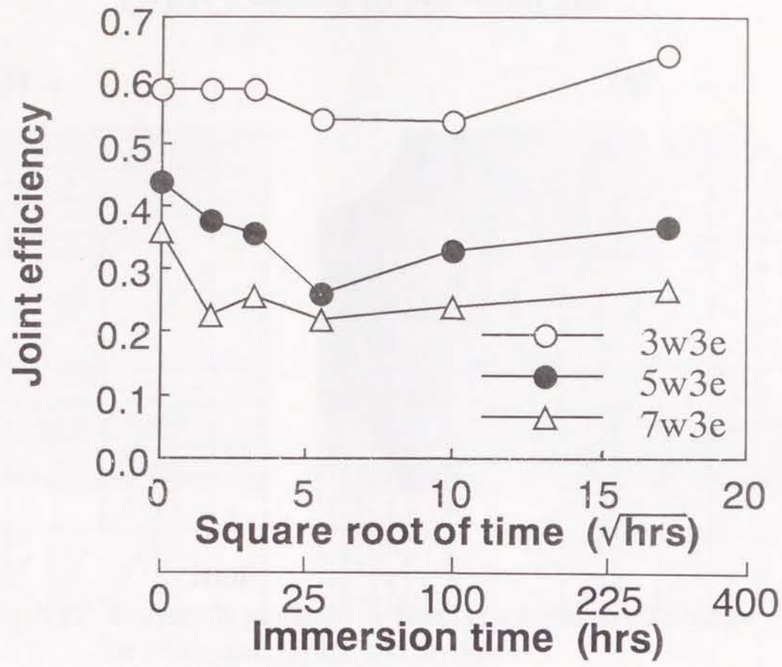

Fig.6.17 Changes of joint efficiency due to water immersion.

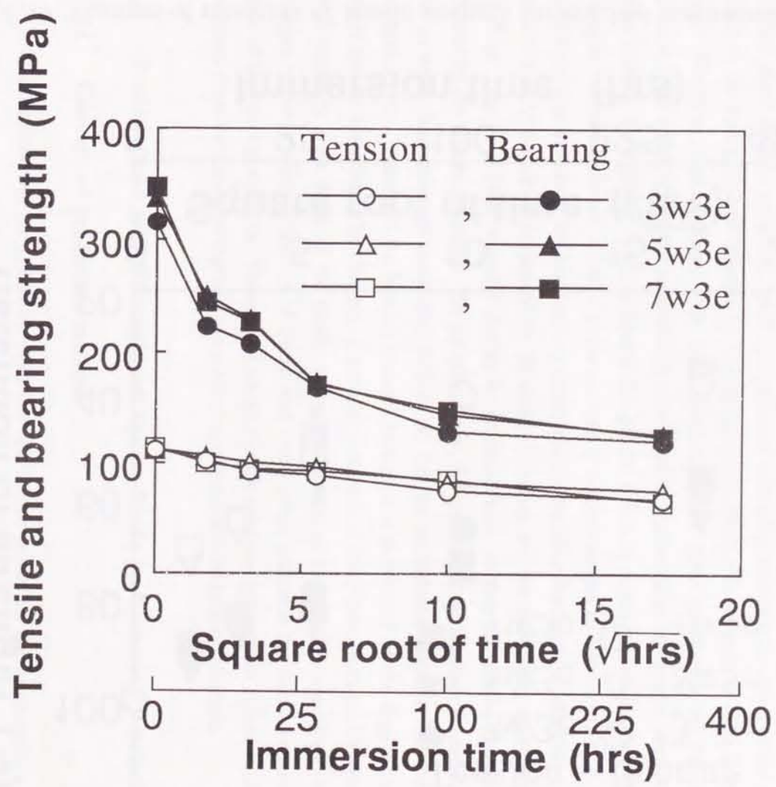

Fig.6.18 Changes of tensile strength for notched specimen and of bearing strength against the square root of immersion time.

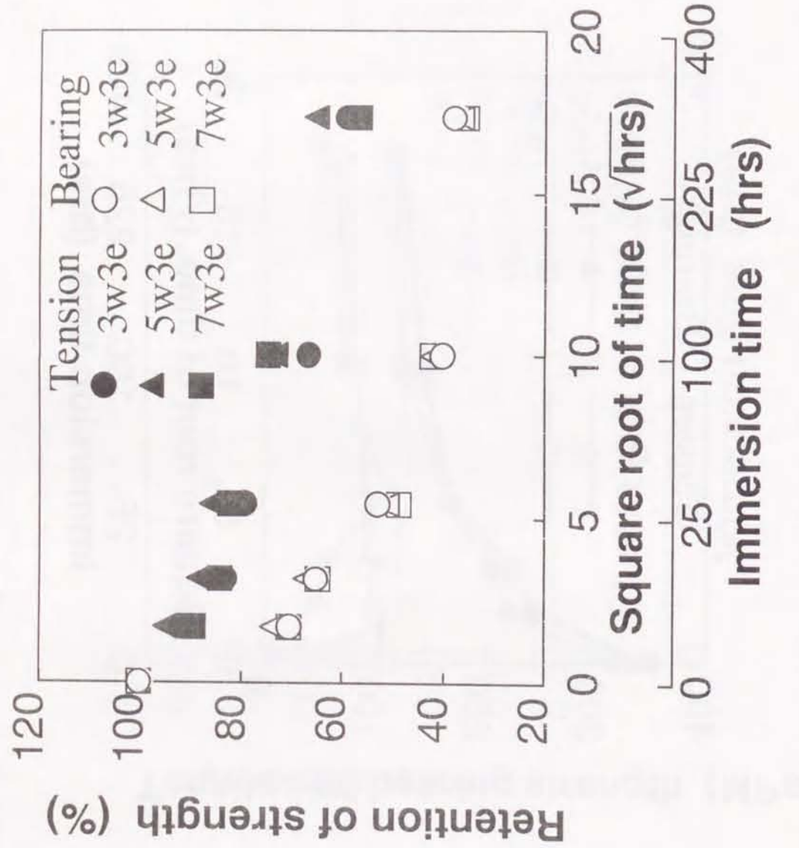

Fig.6.19 Changes of retention of tensile strength for notched specimen and of bearing strength against the square root of immersion time.

changes of the bearing strength due to water immersion must be considered to design the joint structures.

Fig.6.18 shows the changes of the tensile strength of the notched specimen and the bearing strength as a function of the immersion time. The bearing strength of the original dry specimen was much higher than the tensile strength of the original dry specimen, however, the bearing strength decreased due to water absorption and it gradually approaches the tensile strength. Fig.6.19 shows the changes of the retention of the tensile strength and the bearing strength. The tensile strength decreased almost linearly against the square root of immersion time, and it reached to 60% in retention at 300h. On the other hand, the bearing strength decreased until 100h, and it reached about 40 % in retention. Both in tensile and in bearing strength, the effect of the specimen width on the strength never appeared. The moisture absorbed area around the hole, especially in width direction, was different with joint geometry after 100h as shown in Figs.6.14-16. However, the difference of the moisture absorbed area little affected on the tensile strength. From these results, the bearing strength shows the greater effect of water immersion that the tensile strength. These results are reflected in the changes of fracture modes as shown in Fig.6.12. It is considered that the tensile failure is mainly dominated by the fiber breakage, while it is considered that the bearing failure is dominated by the matrix cracking and the debonding at the fiber/matrix interface. The fiber little degrades due to water immersion, so that the tensile strength is little affected by the water immersion. On the other hand, the matrix and the interface degrade seriously due to water immersion as mentioned before, so that the remarkable reduction of the bearing strength occurs. Therefore the bearing strength reduction is dominated by the degradation of the matrix and the interface. The changes of strength reduction of 3w3e joint in Fig.6.10 indicated the same tendency with those of the tensile strength retention of the notched specimen, while the changes of the strength reduction of 5w3e and 7w3e joints indicated the same tendencies with those of the bearing strength. Therefore it seems that the joint strength and its failure mode can be predicted from the tensile strength of the notched specimen and the bearing strength.

6.3 Prediction of Joint Strength and Failure Mode by Numerical Analysis

6.3.1 Concept of prediction method

The prediction of the failure strength and the failure mode for the mechanically fastened FRP joints has been performed by comparing the stress distribution in the material with the basic strength data.[118] In such prediction, the failure has been defined by introducing the failure criteria such as the maximum stress criterion, Hoffman criterion, Tsai-Wu criterion, etc. By these criteria the fracture region at applying a certain stress can be only obtained, and another failure criterion (final failure criterion) must be needed to define the final failure of joint. Generally it can be considered that the final failure of joint is caused when the fracture region reaches the allowable limit of the material. Therefore the final failure of joint is often defined by the length of the fracture region from the edge of hole, and this length is defined as the "characteristic length". Chang et al.[87-89] and Wilson et al.[90] have predicted the strength of the mechanically fastened joint

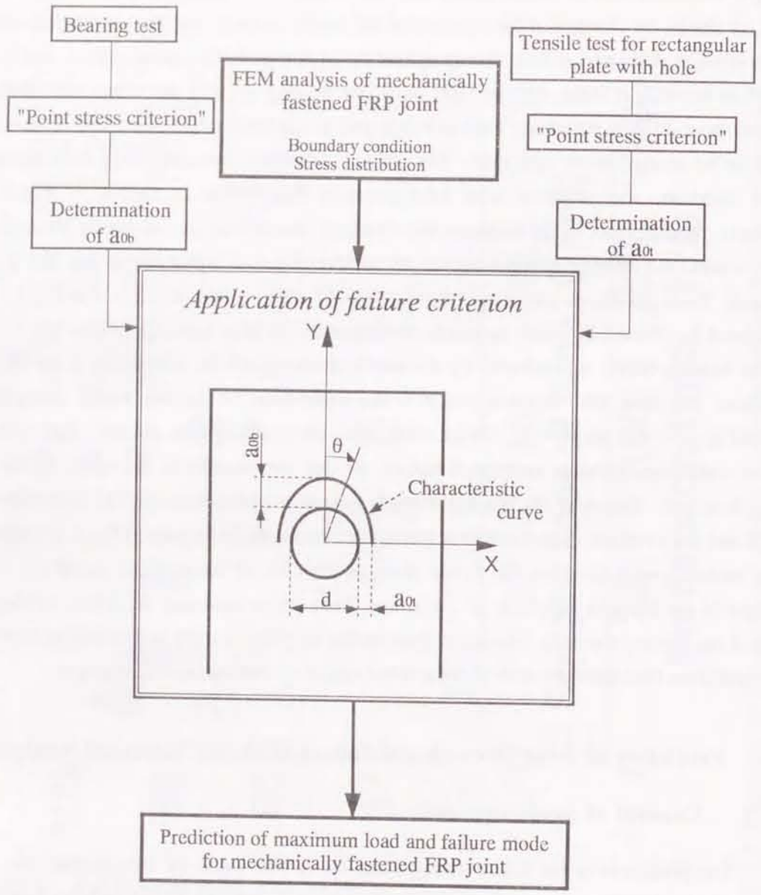

Fig.6.20 Flow chart of strength and failure mode analyses of joint.

by combination of the failure criterion and the characteristic length. Chang et al. have adopted the combined failure criterion with Yamada-Sun criterion and the characteristic length obtained by the average stress criterion, while Wilson et al. have adopted Tsai-Wu criterion and the characteristic length obtained by the point stress criterion. The average stress criterion and the point stress criterion had been proposed by Whitney and Nuismer.[119] The average stress criterion defines the final failure by that the average tensile stress from the edge of hole to a certain point reaches the tensile strength, while the point stress criterion defines it by that the tensile stress at a certain point far from the edge of hole reaches the tensile strength.

Based on these works, the predictions of the joint strength and its failure mode were performed by introducing the macroscopic failure criterion and the characteristic lengths in this study. Fig.6.20 is the flow chart of the strength and failure mode analyses of joint in this study. First of all, the characteristic lengths in tension (a_{0t}) and in bearing (a_{0b}) are obtained by applying the point stress criterion on the basis of the experimental results of the tensile test and the bearing test. The stress distribution of joint is analyzed by the finite element analysis, and the stress on the characteristic curve obtained from a_{0t} and a_{0b} is applied to the failure criterion, and then, the failure load and the failure mode are predicted. This prediction method needs the experimental results both of the tensile test of the notched specimen and of the bearing test, and the finite element analytical results of the notched specimen, the bearing test specimen and the joint specimen.

6.3.2 Finite element modeling and analysis

i) Finite element analysis of joint

Fig.6.21 shows the finite element divisions of each joint specimen. In consideration of the symmetry, half of the joint in width direction was divided by the two-dimensional plane stress triangle elements. Fig.6.22 summarizes the boundary conditions for analysis. The truss elements were adopted instead of the pin, and the load was applied to the node at the center of the hole. The finite element analysis code used here was the structural analysis program, SAP V-2. Isotropic material constants as listed in Table 6.1 were adopted at each immersion time. The material constant of iron (Elastic modulus; 210GPa) was applied as the constant of truss element.

ii) Definition of characteristic length

Fig.6.23 schematically illustrates the concept of the point stress criterion to the tensile failure. In the point stress criterion to the tensile failure, it is regarded as the final failure when the tensile stress at length a_{0t} from the edge of the hole reaches the tensile strength, and a_{0t} is defined as the characteristic length in tension. a_{0t} is determined by the tensile stress distribution of the notched specimen at maximum load obtained by the experiment. The stress distribution was calculated by the finite element analysis. Finite element divisions and the boundary conditions of the notched specimen are shown in Fig.6.24. Half of the notched specimen in width direction was divided by the two-dimensional plane stress triangle elements. The fixed displacements were

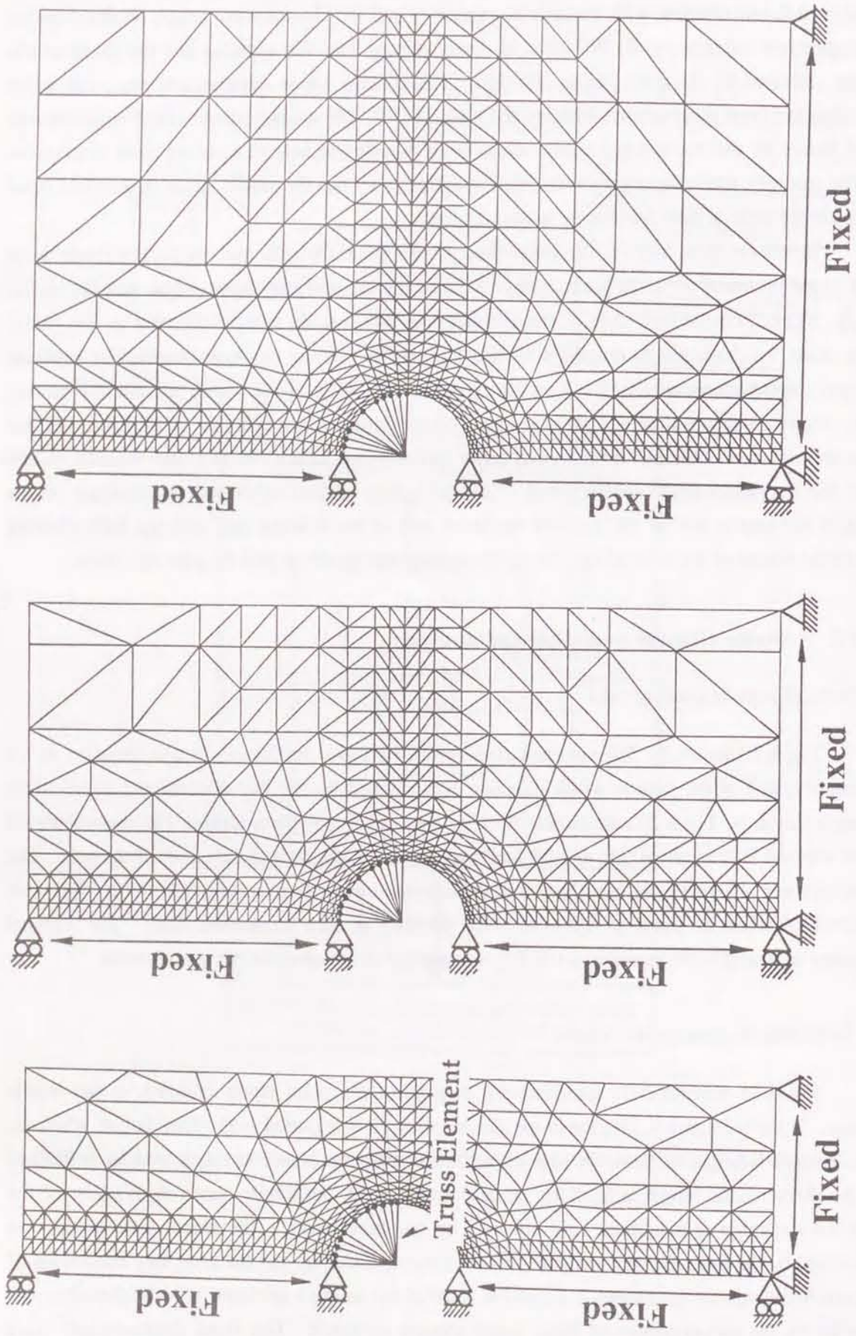

Fig.6.21 Finite element divisions of joint specimens

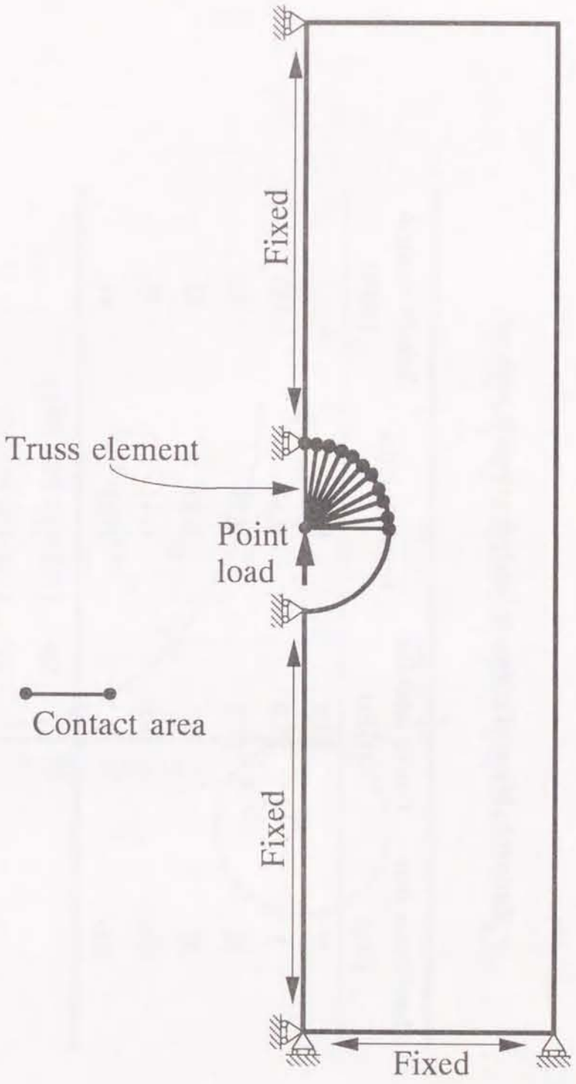

Fig.6.22 Boundary conditions for finite element analysis of joint.

Table 6.1 Material constants for finite element analyses.

Immersion time (hrs)	Tensile modulus (GPa)	Poisson's ratio	Tensile strength (MPa)
0	12.4	0.35	116
3	12.0	0.34	113
10	10.7	0.35	100
30	9.1	0.39	93
100	8.0	0.41	79
300	7.7	0.35	61

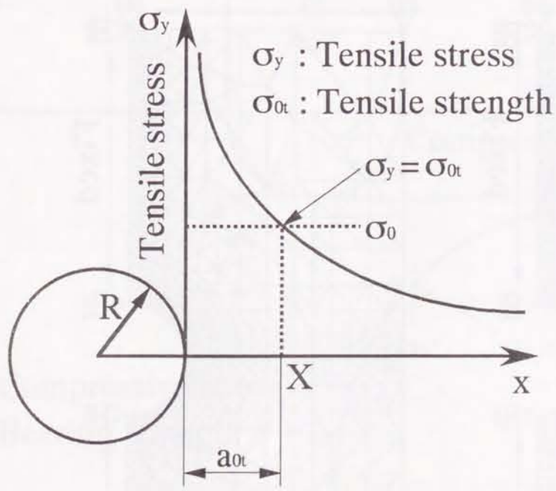

Characteristic length in tension (a_{0t}) = X–R

Fig.6.23 Concept of point stress criterion to tensile failure.

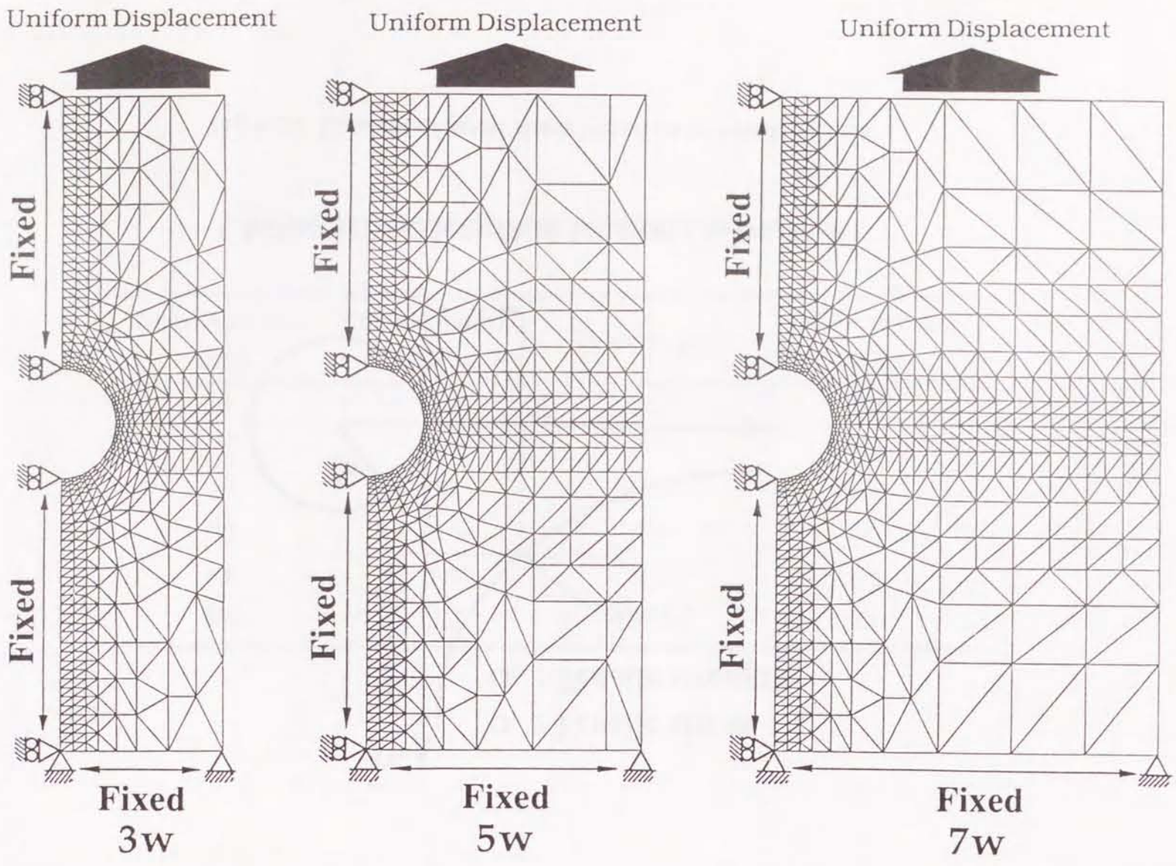

Fig.6.24 Finite element divisions and boundary conditions for finite element analyses of notched specimen

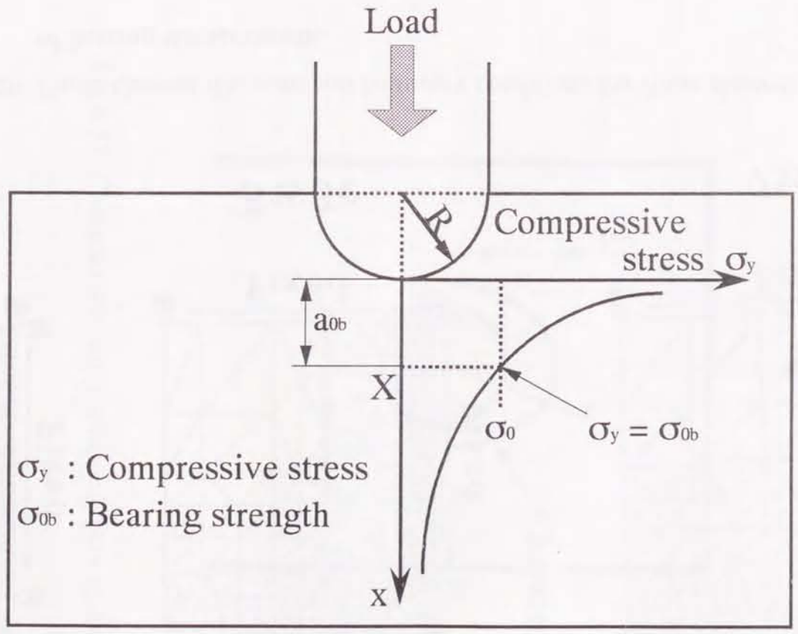

Fig.6.25 Concept of point stress criterion to bearing failure.

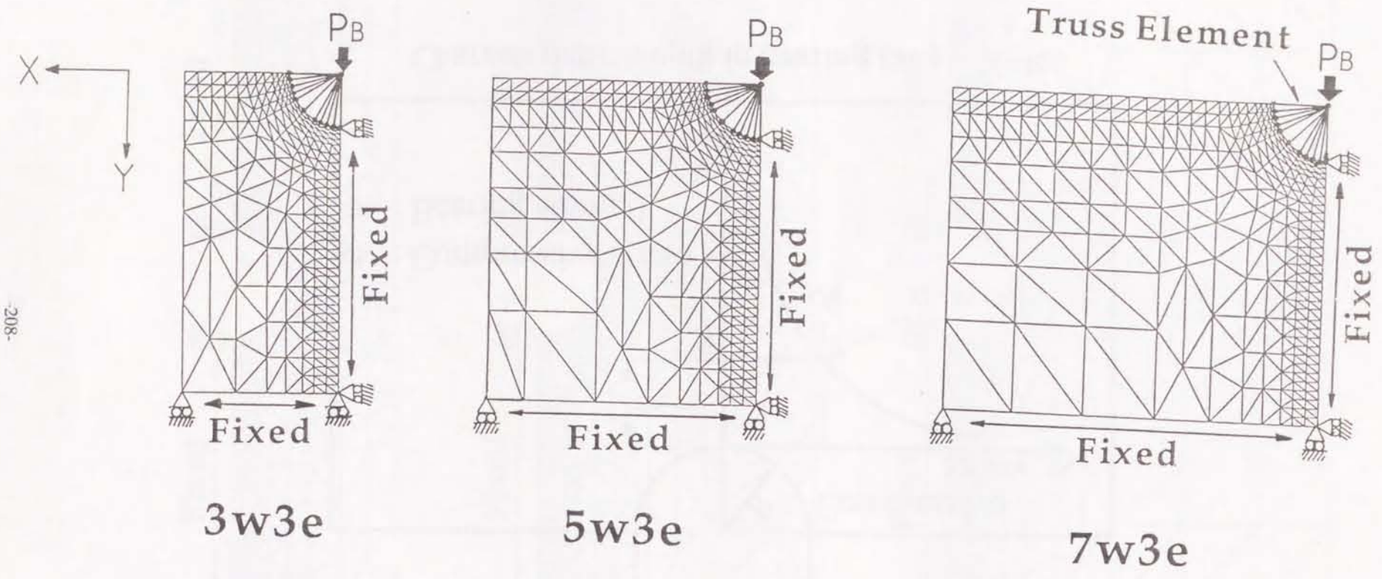

Fig.6.26 Finite element divisions and boundary conditions for finite element analyses of bearing test specimens.

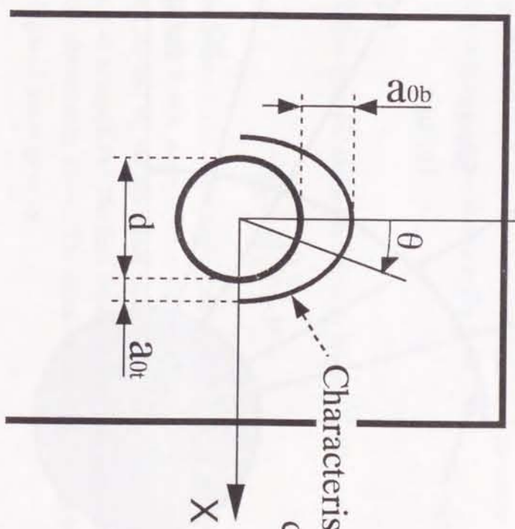

Fig.6.27 Characteristic curve obtained from a_{0t} and a_{0b}.

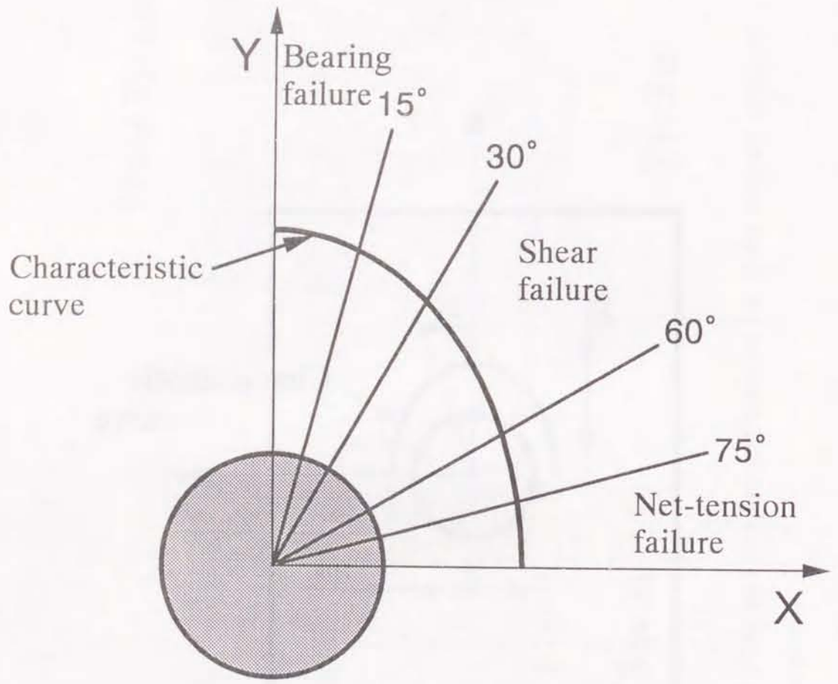

Fig.6.28 Definition of joint failure mode in prediction.

applied to the nodes at the upper edge and the total reaction force at their nodes was the failure load of the notched specimen (P_{nt}). The applied loads P_{nt} were obtained by the experimental data shown in Fig.6.18.

Generally the point stress criterion has been applied to the tensile and the compressive test results. In this study this criterion is also applied to the bearing test results. Fig.6.25 schematically illustrates the concept of the point stress criterion to the bearing failure. From the compressive stress distribution calculated by the finite element analysis and the bearing strength, the characteristic length in bearing (a_{0b}) is determined by the same manner with the determination of a_{0t}. Fig.6.26 shows the finite element divisions and the boundary conditions of the bearing test specimens. Half of the bearing test specimen was divided by the two-dimensional plane stress triangle elements, and the pin was substituted for the truss elements. In the analysis, the failure load in the bearing test (P_b) was applied to the node at the center of the notch. The applied loads P_b were obtained by the experimental data shown in Fig.6.18.

iii) Failure criterion

Macroscopic failure criterion adopted in this study is given by[120]

$$\left(\frac{\sigma_{x_1}}{X}\right)^2 + \left(\frac{\sigma_{y_1}}{X}\right)^2 = F^2 \tag{6.4}$$

where σ_x is the stress perpendicular to the loading direction and σ_y is the stress parallel to the loading direction. X is the tensile strength when σ_x and σ_y are the plus value, while it is the bearing strength when σ_x and σ_y are the minus value. Generally it was determined that the fracture occurs when F=1 in eqn(6.4). The final failure of joint was judged by the macroscopic failure criterion and the characteristic curve. The characteristic curve ($r_c(\theta)$) is obtained from a_{0t} and a_{0b} as shown in Fig.6.27 and is given by

$$r_c(\theta) = \frac{d}{2} + a_{0t} + (a_{0b} - a_{0t})\cos\theta \tag{6.5}$$

where d is the hole diameter. It was assumed that the joint fails when F value in eqn(6.4) reaches 1 on the characteristic curve. The failure mode was judged by the angle between the loading axis and the fractured point on the characteristic curve. The definition of the failure mode is illustrated in Fig.6.28. The bearing failure occurs in case that the point where F value reaches 1 is located from 0° to 15° to the loading direction, while the net-tension failure occurs in case that such point is located from 75° to 90°.

6.3.3 Predicted results and discussion

Table 6.2, Figs.6.29 and 30 show a_{0t} and a_{0b} obtained by the finite element analysis. a_{0b} kept almost constant value and was little affected by the water immersion. On the other hand, a_{0t} became longer as the immersion time became longer. The changes of a_{0t} due to water immersion

Table 6.2 a_{0t} and a_{0b} obtained by finite element analyses.

Immersion time	3w3e		5w3e		7w3e	
(hrs)	a_{0t} (mm)	a_{0b} (mm)	a_{0t} (mm)	a_{0b} (mm)	a_{0t} (mm)	a_{0b} (mm)
0	1.75	0.87	2.13	0.64	2.53	0.60
3	1.51	0.87	2.70	0.57	2.64	0.57
10	1.69	0.87	3.50	0.59	3.54	0.57
30	1.75	0.87	4.24	0.57	4.64	0.57
100	1.81	0.90	4.64	0.60	5.55	0.57
300	2.83	0.87	5.17	0.57	7.39	0.57

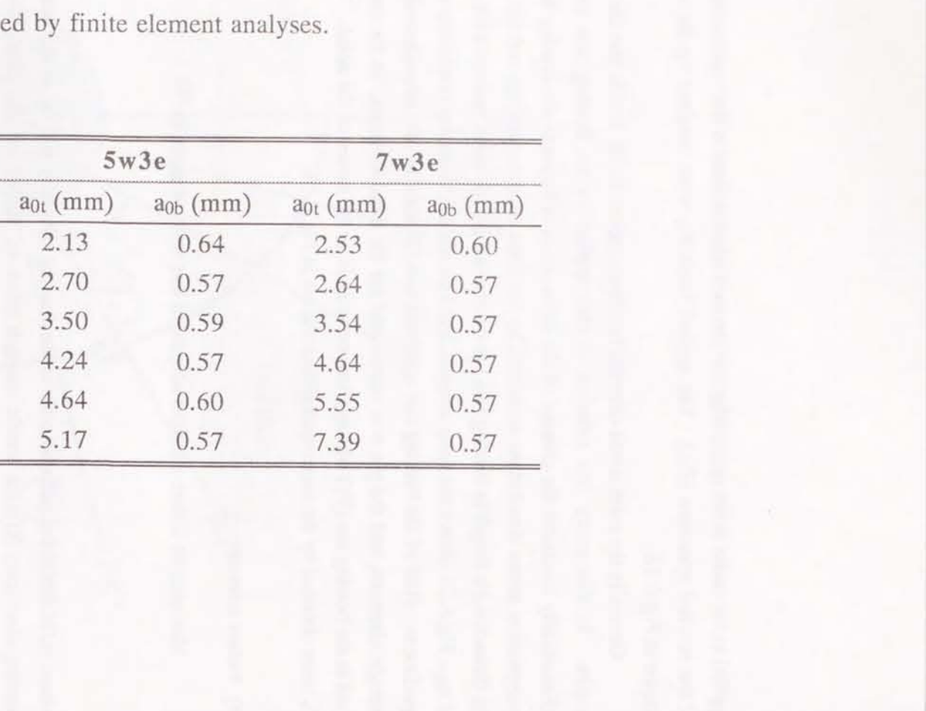

Fig.6.29 Changes of a_{0t} obtained by finite element analysis against the square root of immersion time.

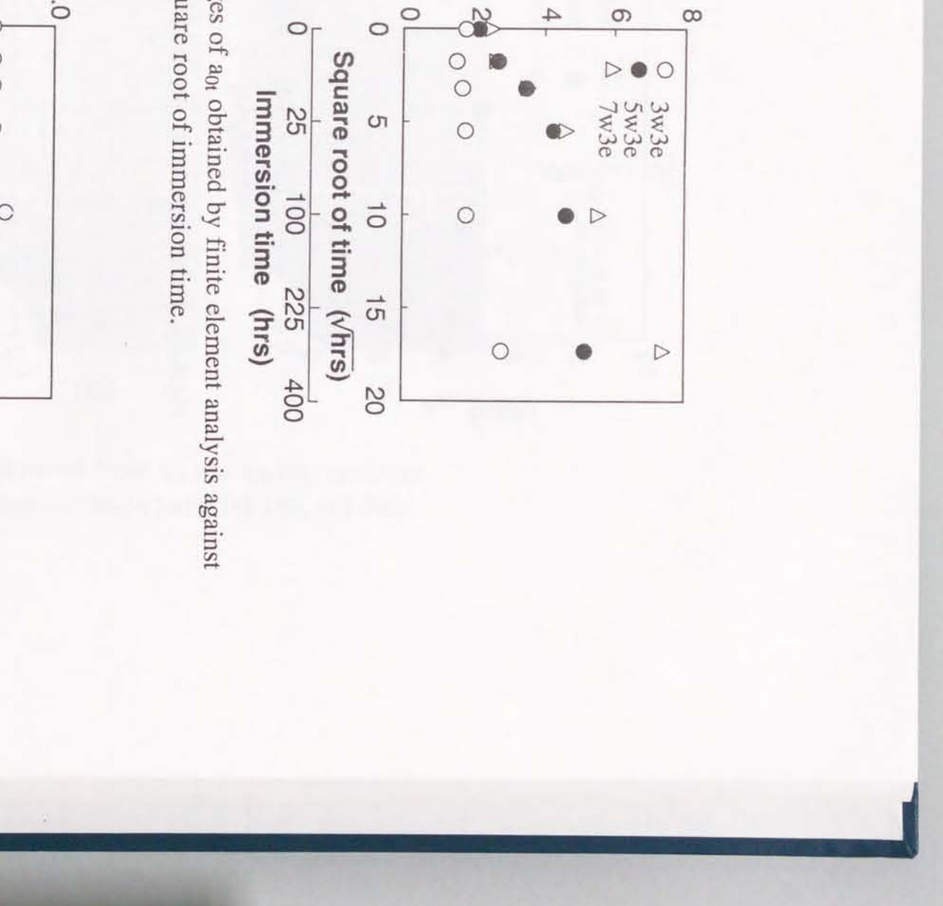

Fig.6.30 Changes of a_{0b} obtained by finite element analysis against the square root of immersion time.

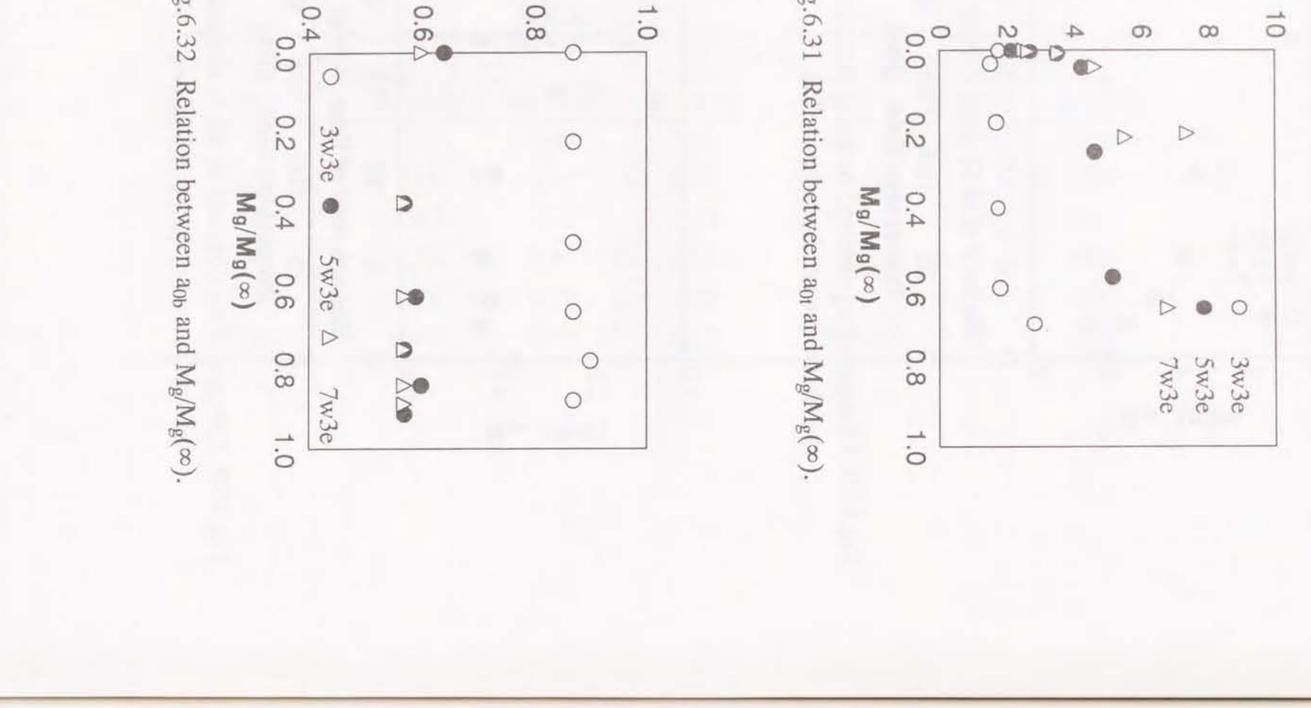

Fig.6.31 Relation between a_{0t} and $M_g/M_g(\infty)$.

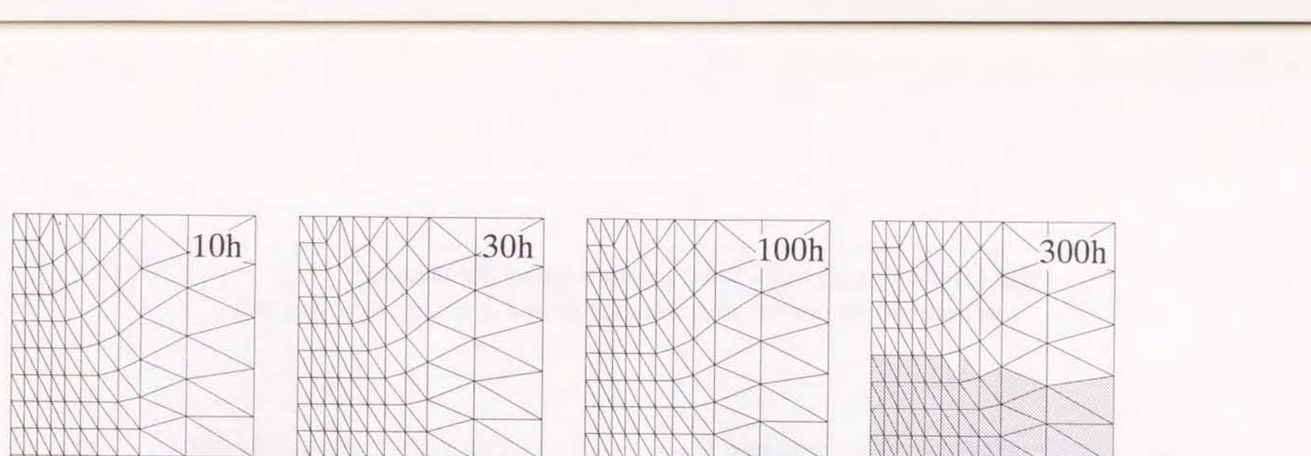

Fig.6.32 Relation between a_{0b} and $M_g/M_g(\infty)$.

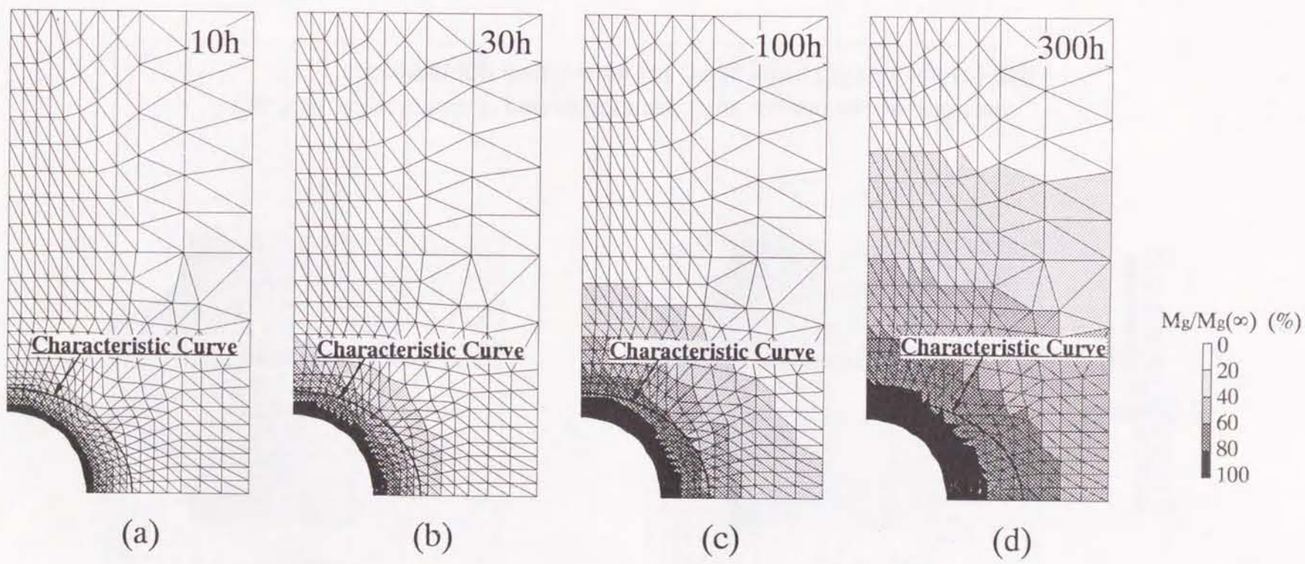

Fig.6.33 Characteristic curves obtained from a_{0t} and a_{0b} on moisture concentration distribution for 3w3e joint; (a) 10h, (b) 30h, (c) 100h and (d) 300h.

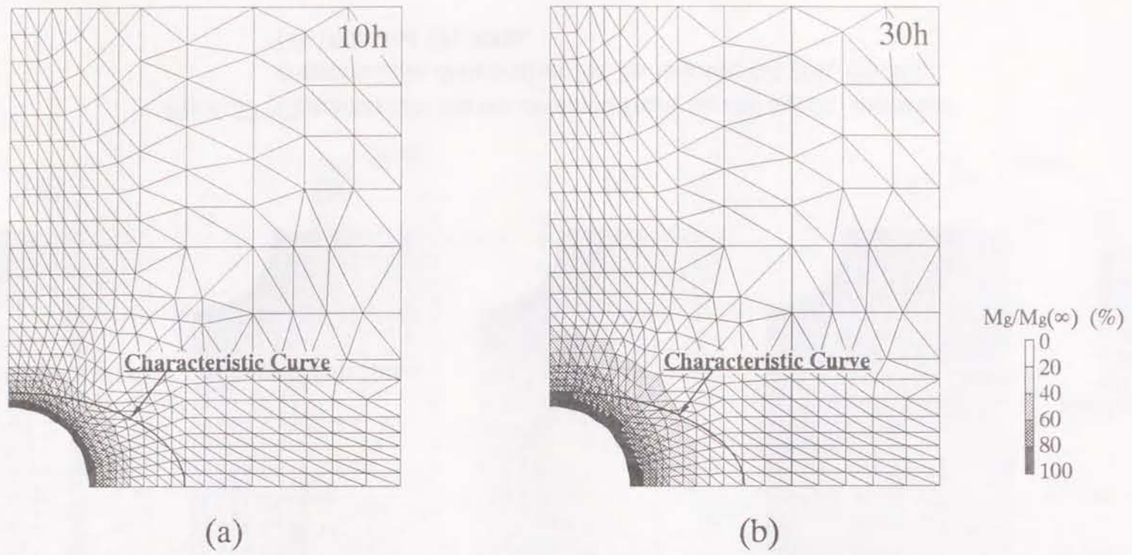

Fig.6.34 Characteristic curves obtained from a_{0t} and a_{0b} on moisture concentration distribution for 5w3e joint; (a) 10h and (b) 30h.

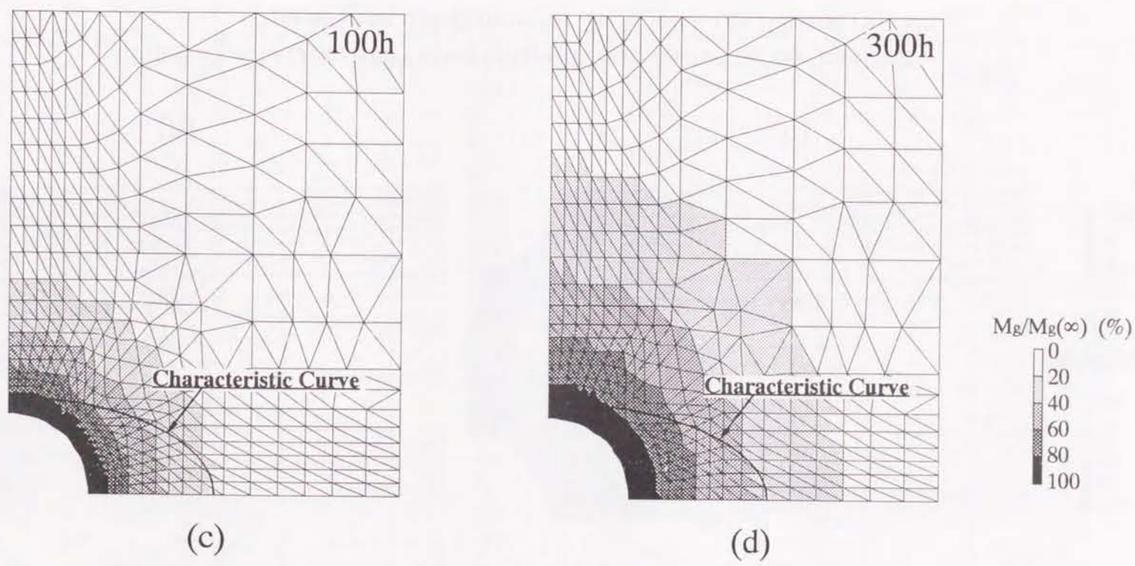

Fig.6.34 Continued; (c) 100h and (d) 300h.

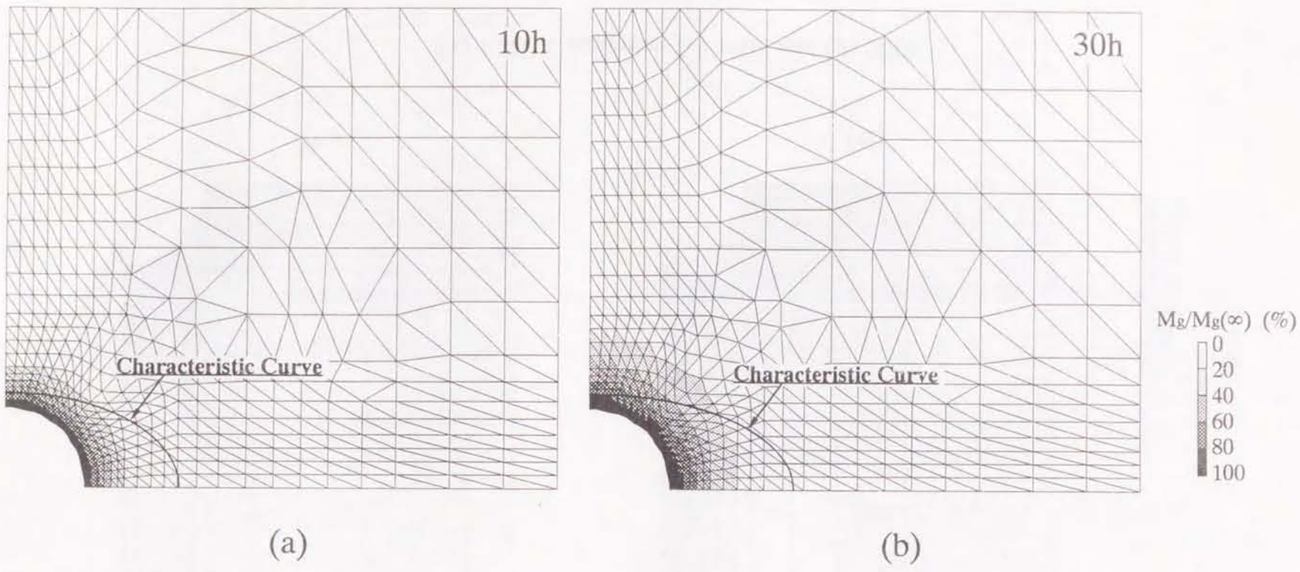

Fig.6.35 Characteristic curves obtained from a_{0t} and a_{0b} on moisture concentration distribution for 7w3e joint; (a) 10h and (b) 30h.

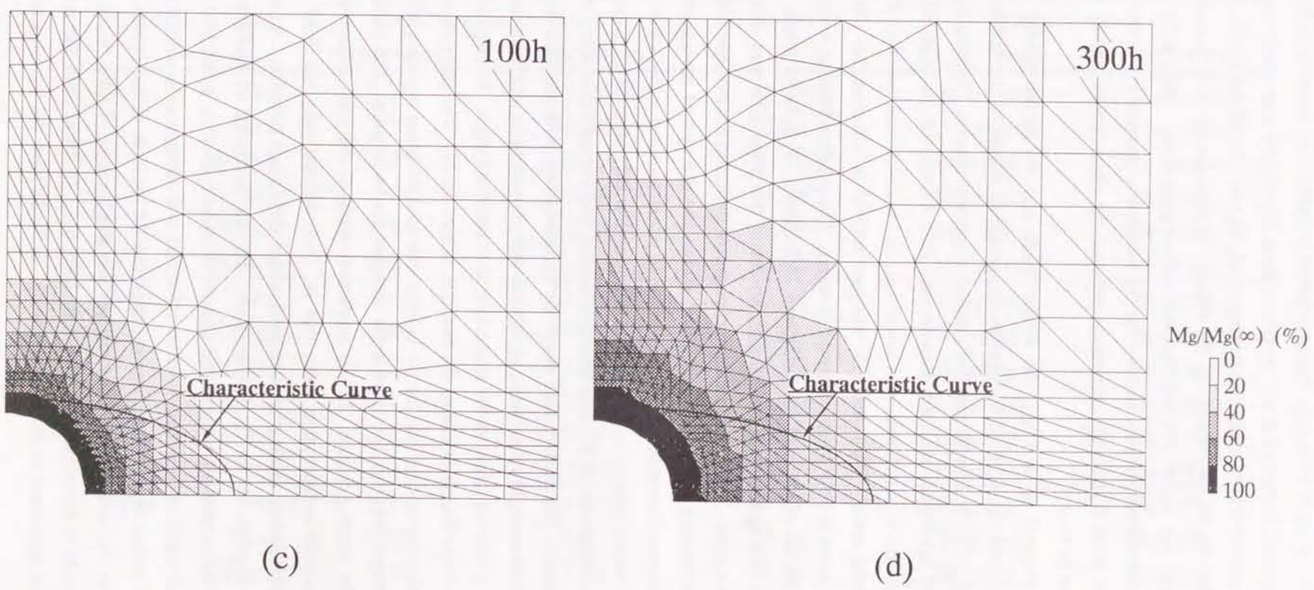

Fig.6.35 Continued; (c) 100h and (d) 300h.

became greater as the specimen width was wider. Figs.6.31 and 32 show the relation between a_{0t}, a_{0b} and $M_g/M_g(\infty)$ at these points. a_{0b} kept constant value and was never affected by the water absorption. a_{0t} in 3w3e joint kept almost constant in spite of the increase of $M_g/M_g(\infty)$. a_{0t} in 5w3e and 7w3e joints increased at the process which $M_g/M_g(\infty)$ was nearly equal to 0. In 5w3e joint a_{0t} kept almost constant after increasing of $M_g/M_g(\infty)$. In all the joints, the correlation between a_{0t}, a_{0b} and $M_g/M_g(\infty)$ could not be found. Consequently it is considered that the characteristic lengths are never affected by the water absorption. Figs.6.33-35 show the characteristic curves obtained from a_{0t} and a_{0b} on the moisture concentration distributions at each immersion time. In these figures the correlation between the characteristic curves and the water absorption could not be found.

Using the obtained a_{0t} and a_{0b}, the failure loads and the failure modes of joint were predicted. Table 6.3 and Figs6.36-38 summarize the predicted results of the maximum loads and the failure modes of joints in comparison with the experimental results. The predicted maximum loads showed good agreement with the experimental data except for *5w3e* at 30 h. The joint strength for *5w3e* at 30 h in experiment was lower than that at 100 h, and therefore it is considered to be an experimental error. This strength analysis method is effective for the mechanically fastened randomly oriented FRP joint immersed in water. The predicted failure mode also showed good agreement with the experiment for 5w3e and 7w3e joints. For 3w3e joints, the predicted *failure mode up to 10 h agreed with experiment, however, that after 30 h was different between* prediction and experiment. The failure mode in experiment indicated the multiple failure while that in prediction did the bearing failure. Figs.6.39-41 shows the changes of maximum F value both in tension and in compression sides due to immersion in water for each joints. For 3w3e joint, F value came to 1 in tension side up to 10 h and in compression side after 30 h, respectively. After 30 h, however, the difference in F value between tension and compression was very small, and therefore the net-tension failure may also occur easily combining with the bearing failure. For 5w3e joint, the difference in F value between tension and compression side was small in original dry specimen, and it became larger as the immersion time became longer. In original dry specimen of 5w3e joint, a few specimens indicated the multiple failure mode. The changes of maximum F value in tension and compression side for 7w3e joint indicated the same tendency with 5w3e joint, however, the difference between them was larger than that for 5w3e joint. The failure mode of all 7w3e joints was the bearing failure. In this prediction method, the joint failure was judged by only F = 1 in tension or compression side, that is, F=1 defined only the final failure mode. Therefore the multiple failure mode cannot be predicted in this failure criterion. As a result, a little misunderstanding might be led for the failure mode. For the prediction of multiple failure mode, the difference of F value between tension and compression side must be taken into consideration. Consequently the changes of maximum F value in tension and compression sides are important to predict the detailed failure mode. Here, it is assumed that the multiple failure occurs in case that F value exceeds 0.9 in one side when F value reaches 1 in another side. Under this assumption, the predicted failure mode is reevaluated as shown in Table 6.4. In 3w3e joint the predicted failure mode showed good agreement with the experiment. In 5w3e joint the reevaluated failure mode

Table 6.3 Predicted and experimental results for joint strength and failure modes.

Immersion time		Maximum load (kN)		% of error	Failure mode	
		Experiment	Prediction		Experiment	Prediction
3w3e	0 hr.	3.70	3.75	-1.35	Net-tension	Net-tension
	3 hrs.	3.71	3.40	8.36	Net-tension	Net-tension
	10 hrs.	3.21	3.23	-0.56	Net-tension	Net-tension
	30 hrs.	2.74	2.86	-4.38	Multiple	Bearing
	100 hrs.	2.34	2.33	0.43	Multiple	Bearing
	300 hrs.	2.14	2.13	0.42	Multiple	Bearing
5w3e	0 hr.	4.58	4.75	-3.71	Bearing	Bearing
	3 hrs.	3.89	3.70	4.88	Bearing	Bearing
	10 hrs.	3.22	3.25	-0.93	Bearing	Bearing
	30 hrs.	2.13	2.70	-26.76	Bearing	Bearing
	100 hrs.	2.32	2.40	-3.45	Bearing	Bearing
	300 hrs.	2.07	2.05	0.97	Bearing	Bearing
7w3e	0 hr.	5.21	4.85	6.91	Bearing	Bearing
	3 hrs.	3.30	3.55	-7.85	Bearing	Bearing
	10 hrs.	3.23	3.24	-0.31	Bearing	Bearing
	30 hrs.	2.53	2.62	-3.56	Bearing	Bearing
	100 hrs.	2.38	2.35	1.26	Bearing	Bearing
	300 hrs.	2.09	1.90	-9.10	Bearing	Bearing

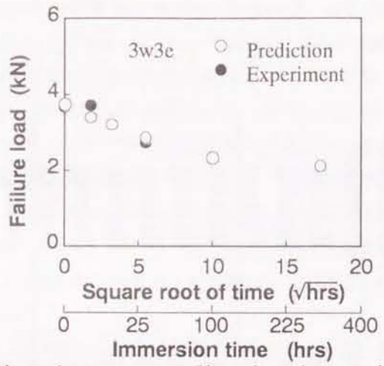

Fig.6.36 Comparison between predicted and experimental failure loads for 3w3e joint.

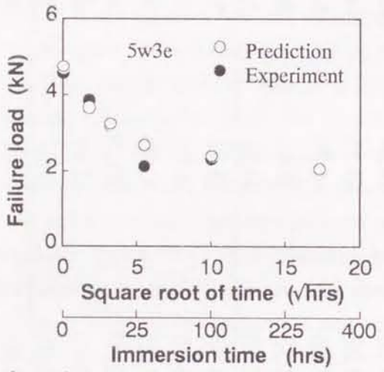

Fig.6.37 Comparison between predicted and experimental failure loads for 5w3e joint.

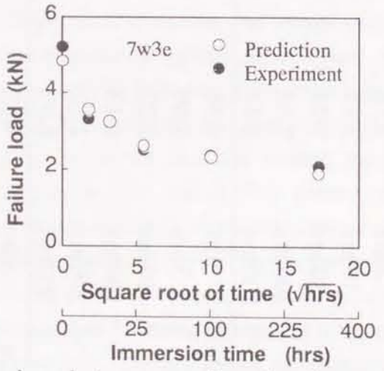

Fig.6.38 Comparison between predicted and experimental failure loads for 7w3e joint.

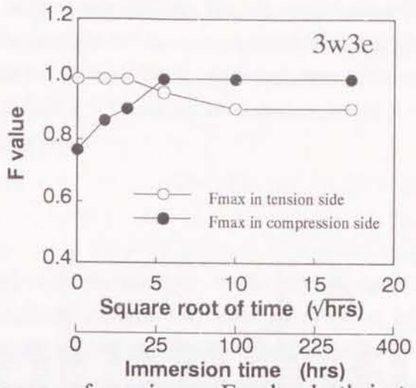

Fig.6.39 Changes of maximum F value both in tension and in compression sides due to water immersion for 3w3e joint.

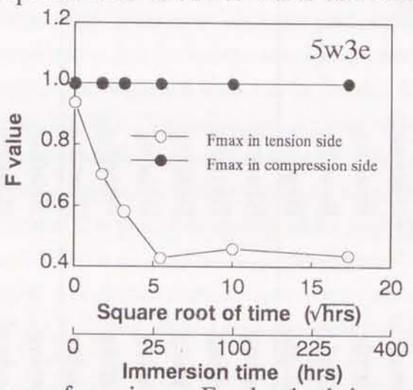

Fig.6.40 Changes of maximum F value both in tension and in compression sides due to water immersion for 5w3e joint.

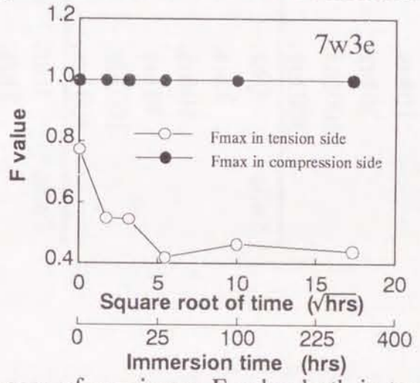

Fig.6.41 Changes of maximum F value both in tension and in compression sides due to water immersion for 7w3e joint.

Table 6.4 Comparison between re-evaluated prediction and experiment for failure modes.

Immersion time		Failure mode		
		Experiment	Prediction (F=1)	Prediction (F>0.9)
3w3e	0 hr.	Net-tension	Net-tension	Net-tension
	3 hrs.	Net-tension	Net-tension	Net-tension
	10 hrs.	Net-tension	Net-tension	Net-tension
	30 hrs.	Multiple	Bearing	Multiple
	100 hrs.	Multiple	Bearing	Multiple
	300 hrs.	Multiple	Bearing	Multiple
5w3e	0 hr.	Bearing	Bearing	Multiple
	3 hrs.	Bearing	Bearing	Bearing
	10 hrs.	Bearing	Bearing	Bearing
	30 hrs.	Bearing	Bearing	Bearing
	100 hrs.	Bearing	Bearing	Bearing
	300 hrs.	Bearing	Bearing	Bearing
7w3e	0 hr.	Bearing	Bearing	Bearing
	3 hrs.	Bearing	Bearing	Bearing
	10 hrs.	Bearing	Bearing	Bearing
	30 hrs.	Bearing	Bearing	Bearing
	100 hrs.	Bearing	Bearing	Bearing
	300 hrs.	Bearing	Bearing	Bearing

was the multiple failure, and this was different from the experimental failure mode on the table. In 5w3e joint, however, the multiple failure also occurred in the original dry joint as mentioned before. Consequently the reevaluated failure mode corresponded completely to the experimental failure mode as listed in Table 6.4. Therefore the consideration of F value is important to predict correctly the failure mode of joint.

6.4 Conclusion

This chapter dealt with the changes of the strength and the failure modes of the mechanically fastened randomly oriented FRP joint immersed in hot water. The degradation behavior of the joint was discussed from the experimental results of the tensile test of the notched specimen and the bearing test. Moreover the joint strength and the failure mode were predicted by the finite element analysis and the experimental results. The joint strength with bearing failure decreased remarkably due to water immersion, while the joint strength with net-tension failure decreased a little due to water immersion. This difference was caused by the remarkable reduction of the bearing property, and it was originated from that the bearing failure was dominated by the fracture of the matrix and the interface. The matrix and the interface were greatly affected by the water immersion, and as a result, all the joints eventually come to fail in the bearing failure mode. Therefore the changes of the bearing property in joint must be considered for the structural design with mechanical fastened joints. The prediction method of the joint strength and the failure mode of the FRP joint was proposed and it was applied to the prediction of the degradation behavior of FRP joint immersed in water. The predicted results showed good agreement with the experimental results and it was verified the proposed method could be applied to the design of the structures under water environment.

Chapter 7 Degradation Behavior of Glass Fiber Reinforced Thermoplastics Immersed in Hot Water

7.1 Introduction

Plastics are generally classified into thermosettings and thermoplastics in point of the thermal properties. In the past years the thermosettings have been mainly employed as the matrix resin for FRP. In recent years, however, thermoplastics have gotten attention in points of the improvement of the productivity and the ease of recycling and reuse. In thermoplastic composites the short fibers have been used as the reinforcement. However, the long fiber reinforced thermoplastics have been demanded for the application to the structural materials. Stampable sheet is a kind of the long fiber reinforced thermoplastics, and it consists of the randomly oriented continuous fiber mat and the thermoplastics. Stampable sheet has spread as the parts of the automobile. Generally the thermoplastics have more excellent chemical resistance than the thermosettings. Therefore the thermoplastic composites can be used as the structural material under various environments. However, the degradation behavior of thermoplastic composites under various environments has never been studied in detail.

This chapter deals with the degradation behavior of randomly oriented glass-fiber continuous mat reinforced polypropylene immersed in hot water. The degradation behavior was evaluated by the weight changes, the bending properties and the joint properties. The changes of these properties are discussed by introducing the evaluation method mentioned in Chapter 2 to Chapter 6.

7.2 Material

Material used in this chapter was glass-fiber mat reinforced thermoplastic composite known as "stampable sheet" (X-Sheet, Idemitsu NSG Co., Ltd., Japan). Matrix was polypropylene (PP) and reinforcement was randomly oriented E-glass fiber continuous strand mat. The thickness of this sheet was 3.8 mm. Using these materials, the square-shaped panels were fabricated by a compression molding method and specimens were cut out from these panels.

Fig.7.1 shows the molecular formula of polypropylene. Polypropylene is the linear polymer and is synthesized from ethylene. Polypropylene is a low cost material and has excellent moldability and chemical resistance, however, it is inferior to the other engineering plastics in thermal resistance. Then, the thermal resistance of polypropylene is improved by blending the inorganic filler, fiber reinforcing, etc.

Stampable sheet is consisted of thermoplastics and randomly oriented glass fiber mat, and is manufactured by pressing after impregnating the continuous strand mat with the matrix resin. The molding process (stamping molding) of X-sheet is summarized as follows;

1. Heat the blank X-sheet at 350°C by heater.
2. Charge the heated sheet into the mold which is set at 50°C.

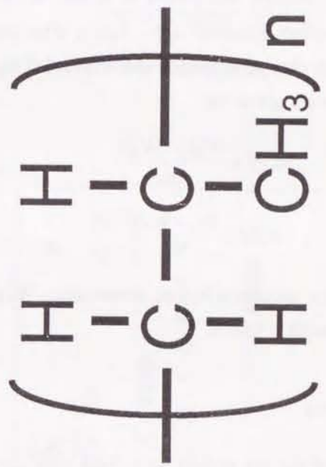

Fig.7.1 Molecular formula of polypropylene.

3. Press the sheet at 14.7MPa for 30 seconds by a compression molding machine, after that cooling the sheet.
4. Release the sheet from the mold.

The specimen panel was molded by charging the blank sheet in the whole of the mold. The geometry of molded panel was 300mm × 300mm × 3.8mm. Fiber volume content of this panel was about 40%.

7.3 Weight Change

7.3.1 Experimental procedure

In order to measure the weight changes, the water immersion was conducted in distilled water at 60°C and 80°C with a temperature controlled water bath. The immersion times were fixed to 3, 5, 10, 30, 50, 100, 300, 500, 1000 and 3000h. The specimen geometry of weight change measurement was 50mm × 50mm. Before immersion in water, all specimens were completely dried in a vacuum oven (DP32, Yamato Scientific Co., Ltd.), after that all the specimens were immersed in hot water. The weight change behavior was evaluated by the net weight gain (M_g) and the weight loss (M_l) and these were given by

$$M_g(t) = \frac{W_w(t) - W_d(t)}{W_o}$$
$$M_l(t) = \frac{W_o - W_d(t)}{W_o} \qquad (7.1)$$

where W_o was the weight of the dry specimen before immersion, $W_w(t)$ and $W_d(t)$ were the wet and the re-dried specimen after immersion time t.

7.3.2 Results and discussion

Fig.7.2 shows the changes of the net weight gain (M_g) with the square root of immersion time. M_g at 60 °C was lower than that at 80 °C before 100 h, however, it was a little higher after 300 h. The changes of M_g both at 60 °C and at 80 °C indicated typical Fickian diffusion behavior before 300h, after which M_g at 80°C slightly increased again. It is supposed that such diffusion behavior is due to the occurrence of the weight loss. Fig.7.3 shows the changes of the weight loss (M_l) with the square root of immersion time. M_l both at 60 °C and at 80 °C increased and the slope of the M_l's curves gradually decreased. M_l at 80 °C indicated higher value than at 60 °C at all immersion time. The water temperature affected the changes of M_l rather than that of M_g. The changes of M_l are very similar to the typical Fickian diffusion curve. Therefore the weight loss behavior may be considered to be the diffusion of the dissolved matrix into water. Fig.7.4 shows the cross-sectional micrographs of the original dry specimen and the specimens immersed for 10, 100, 1000 and 3000 h. In this material the glass fiber mats exist only near the surface, and only the matrix resin exists in the central part of the material. The effective bonding at the fiber/matrix

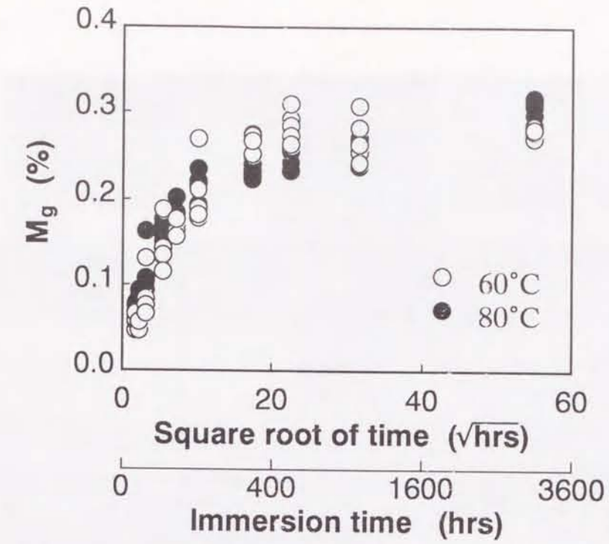

Fig.7.2 Changes of M_g with the square root of immersion time.

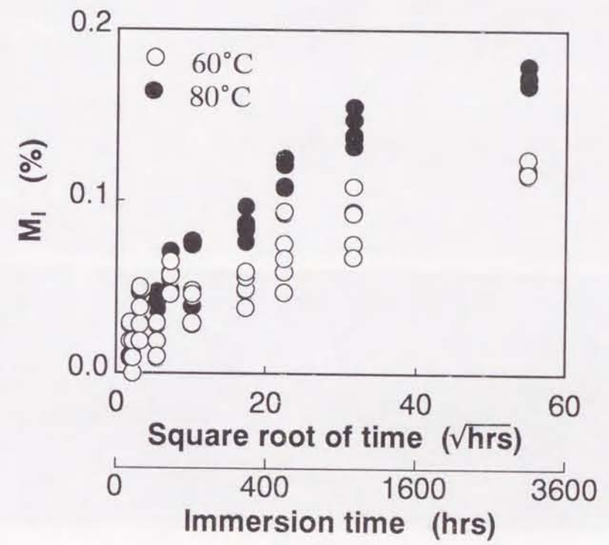

Fig.7.3 Changes of M_l with the square root of immersion time.

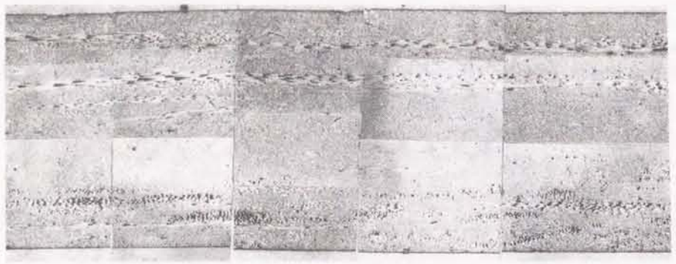

(a)

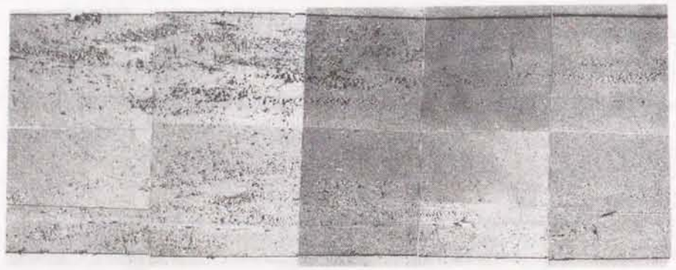

(b)

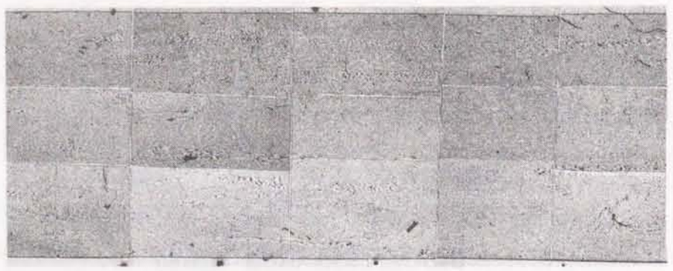

(c) 2mm

Fig.7.4 Cross-sectional micrographs of the specimens after immersion; (a) 0h, (b) 10h and (c) 100h.

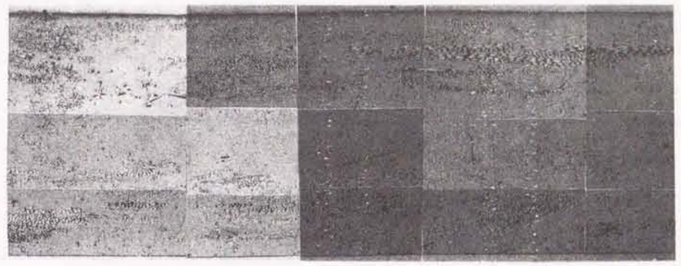

(d)

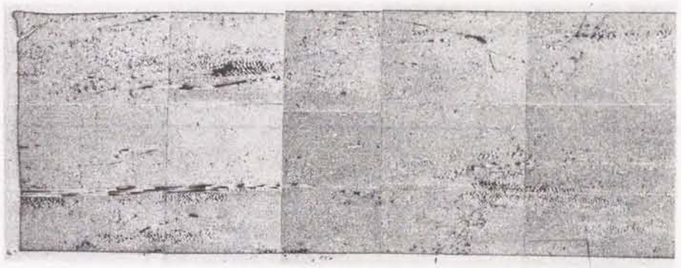

(e) 2mm

Fig.7.4 Continued; (d) 1000h and (e) 3000h.

Table 7.1 $M_g(\infty)$ and D_a obtained by approximation by eqn(2.13).

Water temperature (°C)	$M_g(\infty)$ (%)	D_a
60	0.286	0.111
80	0.313	0.084

Table 7.2 D obtained by eqn(2.15).

Water temperature (°C)	Diffusion coefficient; D (mm^2/hr)
60	9.040×10^{-3}
80	1.375×10^{-2}

Table 7.3 $M_l(\infty)$ and D_l obtained by eqn(2.23).

Water temperature (°C)	$M_l(\infty)$ (%)	D_l
60	0.139	0.036
80	0.198	0.039

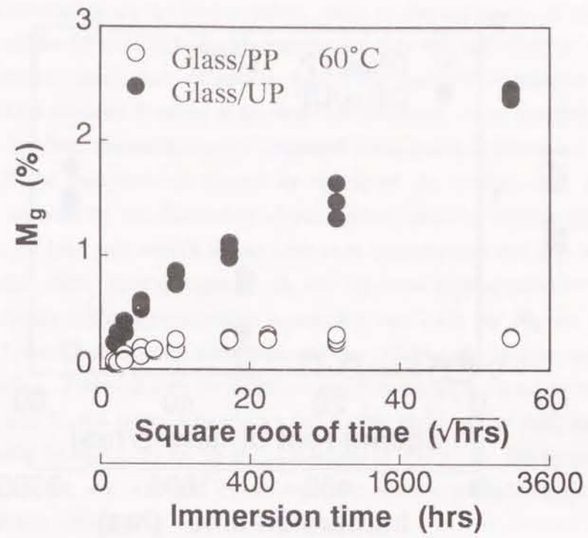

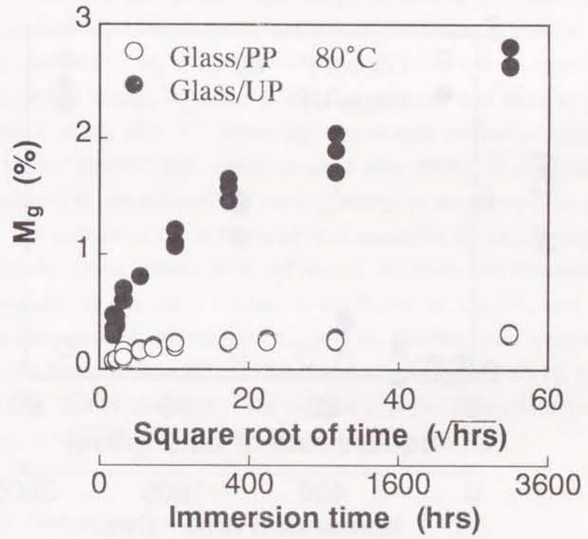

Fig.7.5 Comparison of changes of M_g against the square root of immersion time between Glass/PP and Glass/UP.

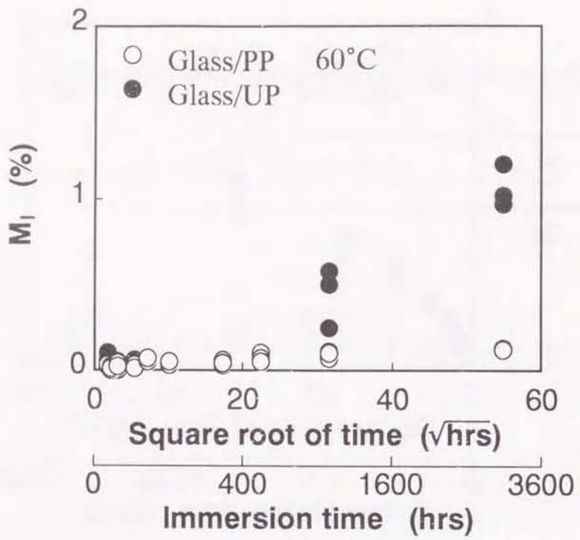

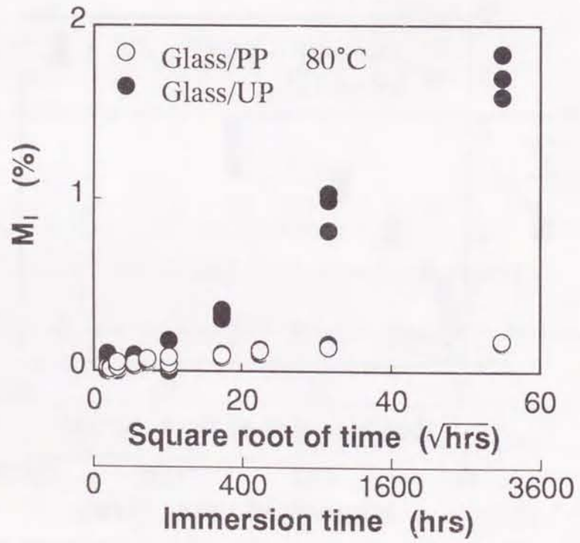

Fig.7.6 Comparison of changes of M_l against the square root of immersion time between Glass/PP and Glass/UP.

interface exists in the original dry specimen, and no cracks or debonding can be observed. In the specimens immersed for 10 and 100 h, the fiber/matrix interface still has effective bonding and the surface of the specimen maintained its smooth face. The specimens immersed for 1000 and 3000 h maintained the effective bonding at the interface, however, some materials in the form of resin particle was lost from the surface by the developed microcracks as shown in Fig.7.4(c). The glass fiber strands and their mats are formed by the aid of the binder. The microcracks are considered to be induced by the dissolution of the binders near the surface of the specimen. Therefore the weight loss was mainly induced by such phenomenon and that it led to a little increase of M_g after 300h. The changes of M_g and M_l were approximated by eqn(2.13) and eqn(2.23), respectively. The approximation results by eqn(2.13) for M_g are summarized in Table 7.1. $M_g(\infty)$ was affected by the water temperature, and $M_g(\infty)$ at higher water temperature indicated higher value. Table 7.2 lists the diffusion coefficients, D, obtained by the experimental results of M_g. The higher water temperature led to the higher D as well as $M_g(\infty)$. The approximation results by eqn(2.23) for M_l are summarized in Table 7.3. $M_l(\infty)$ was also affected by the water temperature, and $M_l(\infty)$ at higher water temperature indicated higher value, which was the same tendency with $M_g(\infty)$.

In Chapter 2, the weight change behavior of the unsaturated polyester composites was shown. This composite was different from the polypropylene composite in only the matrix resin used. Therefore the weight change behavior of these composites was compared in order to discuss the effect of the matrix resin on the weight change behavior in water environment. Fig.7.5 shows the comparison of M_g between the polypropylene composites (named as Glass/PP) and *type-A* (named as Glass/UP). M_g's in Glass/PP were extremely low compared with those of Glass/UP, and the weight change behaviors at longer immersion time were very different. In Glass/UP the increase of M_g after 30h, when M_g in neat resin reached a saturation, could be observed, while M_g in Glass/PP kept almost constant after 100h. It is considered that this difference was produced by the difference of the degradation of the fiber/matrix interface due to water immersion. The increase of M_g in Glass/UP was caused by the serious degradation of the interface, that is, the debonding between fiber and matrix. However, the fiber/matrix interface of Glass/PP little degraded by the water immersion as shown in Fig.7.4, and therefore it is considered that the increase of M_g with the dissolution of the interface never appeared in Glass/PP. The comparison of M_l between Glass/PP and Glass/UP is shown in Fig.7.6. M_l in Glass/PP was remarkably lower than that in Glass/UP. The debonding at the fiber/matrix interface, which induced the increase of M_l in Glass/UP, never appeared as shown in Fig.7.4.

7.3.3 Weight change mechanism

From these results, the phase division proposed in Chapter 2 is considered for Glass/PP. In phase III, the debonding at the interface occurred, and as a result, the remarkable increase of M_l is caused. However, such phenomenon never occurred in Glass/PP. The weight loss in Glass/PP is caused by the loss of resin particle from the surface. It is considered that the loss of the resin

particle is originated in the microcracks at the surface of the material. Therefore it can be concluded that phase III in Glass/PP never exists and that the weight changes of Glass/PP belong to phase I and phase II within the immersion time evaluated here. In this chapter the weight changes of the neat polypropylene resin were not measured. Therefore the weight change behavior cannot be divided accurately into phase I and phase II. From the experimental results, however, it can be roughly supposed that the boundary time between phase I and phase II is about 100h both at 60°C and 80°C. Based on this supposition the water temperature little affects the boundary time in Glass/PP, and the time within phase II is longer. The absorbed water in Glass/PP is much less than that in Glass/UP, and as a result, the water reached to the interface is also very little. Consequently the degradation of the fiber/matrix interface never occurs in Glass/PP. Therefore it can be concluded that Glass/PP has a good water resistance in a viewpoint of the weight changes.

7.4 Mechanical Properties

7.4.1 Experimental procedure

In order to evaluate the changes of the bending properties due to water immersion, the three point bending tests were performed for the specimen after water immersion. Geometry of the bending specimen was 80mm × 15mm. Water immersion was conducted at 80°C with a temperature controlled water bath. Immersion time was 3, 10, 30, 100 and 300h. Three point bending was performed at a constant cross-head speed of 2 mm/min with a 60 mm span at room temperature, using an Instron universal testing machine (type 4206).

7.4.2 Results and discussion

Fig.7.7 shows the dependence of bending modulus on the immersion time. The moduli were almost constant up to 100 h. At 300h the modulus decreased a little. The water immersion hardly affected on the changes of the bending modulus. The amount of absorbed water was very little, and the degradation of matrix and interface hardly occurred. The modulus may decrease gradually if the immersion time becomes much longer. Fig.7.8 shows the dependence of bending strength on the immersion time. The bending strength was almost constant up to 30 h as well as the modulus, however, the strength decreased gradually after 30 h.

The changes of the bending properties are closely related to the weight change behavior. In the following, the relation between weight changes and bending properties is discussed with comparison between Glass/PP and Glass/UP. Figs.7.9 and 10 show the relation between bending modulus and net weight gain (M_g) and weight loss (M_l) respectively for Glass/PP and Glass/UP. These figures indicated that the relation between the modulus and M_g or M_l was depended on the used materials. The reduction in the modulus for Glass/UP was related to M_g up to about 1.0 %, and it kept constant over 1.0 %. The same tendency was found out in the relation between modulus and M_l for Glass/UP. On the other hand, the modulus for Glass/PP was

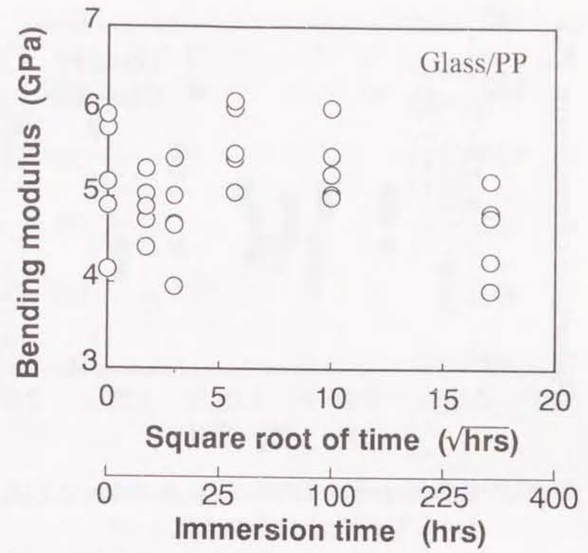

Fig.7.7 Changes of bending modulus as a function of the square root of immersion time.

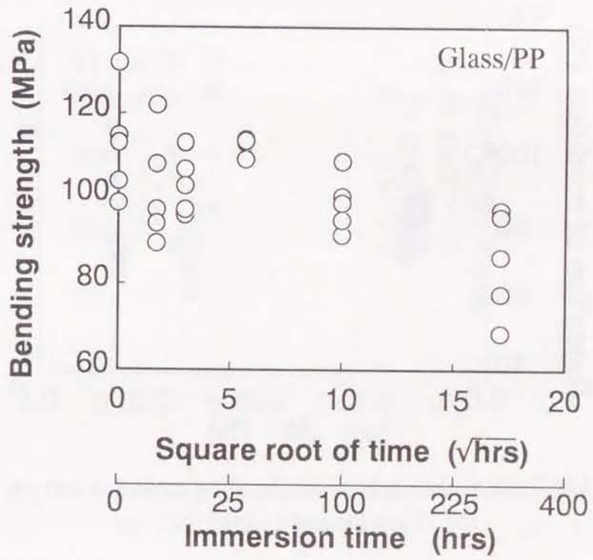

Fig.7.8 Changes of bending strength as a function of the square root of immersion time.

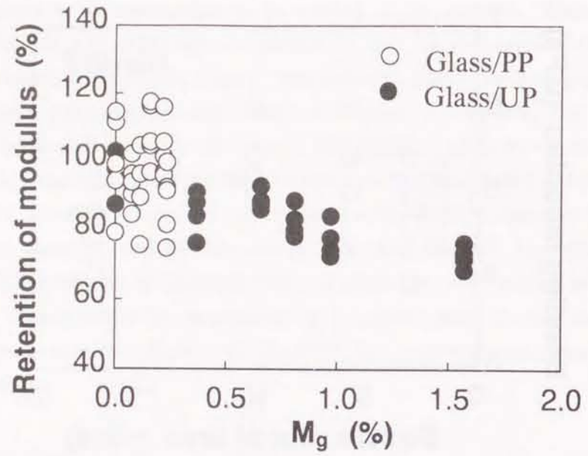

Fig.7.9 Relation between bending modulus and M_g for Glass/PP and Glass/UP.

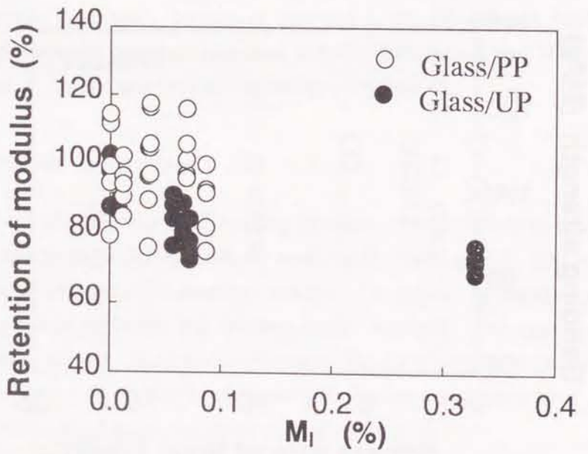

Fig.7.10 Relation between bending modulus and M_l for Glass/PP and Glass/UP.

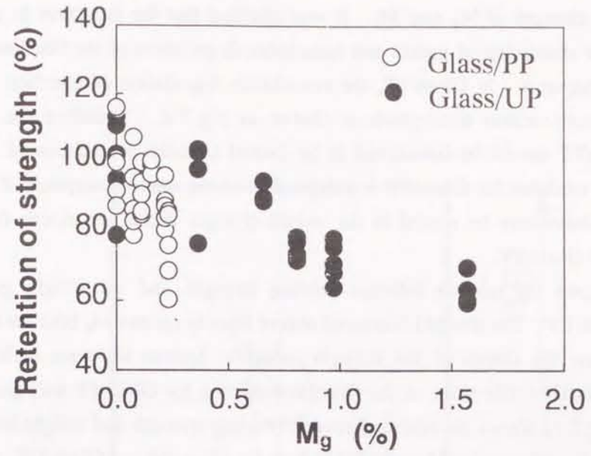

Fig.7.11 Relation between bending strength and M_g for Glass/PP and Glass/UP.

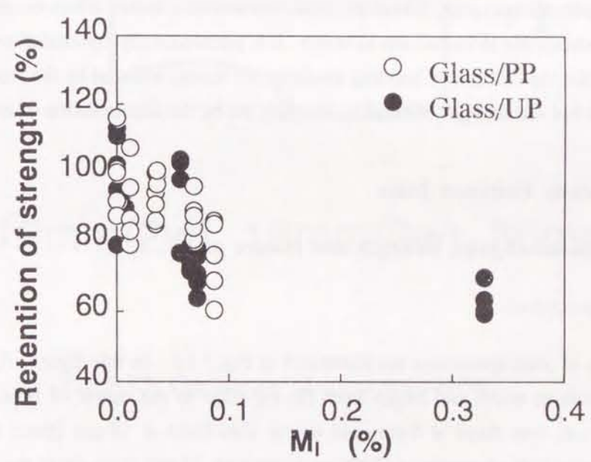

Fig.7.12 Relation between bending strength and M_l for Glass/PP and Glass/UP.

independent of the changes of M_g and M_l. It was clarified that the reduction in modulus was caused by the water absorption of matrix and remarkable degradation of the fiber/matrix interface as mentioned in Chapter 4. In Glass/PP, the remarkable degradation of interface could not be observed in the cross-section micrograph as shown in Fig.7.4. Therefore the reduction in modulus for Glass/PP should be considered to be caused by only degradation of matrix resin. From this fact, the modulus for Glass/PP is independent of the water absorption of matrix resin. However, the modulus may be related to the weight changes if the remarkable degradation of interface occurs for Glass/PP.

Fig.7.11 shows the relation between bending strength and net weight gain (M_g) for Glass/PP and Glass/UP. The strength decreased almost linearly against M_g both for Glass/PP and Glass/UP, however, the slopes of the strength reduction against M_g were different between Glass/PP and Glass/UP. The slope of the strength reduction for Glass/PP was greater than that for Glass/UP. Fig.7.12 shows the relation between bending strength and weight loss (M_l). The strength decreased linearly against M_l up to 0.1 % both for Glass/PP and Glass/UP, and the slopes of the strength reduction against M_l were almost the same, independent of the used materials. The strength reduction is closely related to the weight loss due to immersion in water for these materials. From the microscopic observation of cross-section after immersion, the weight loss of Glass/PP is considered to be caused by the development of microcracks on the surface of the specimen as shown in Fig.7.4. Therefore the strength reduction of Glass/PP occurs due to the accumulation of such microcracks, however, these microcracks never affect on the changes of bending elastic modulus due to immersion in water. It is phenomenally concluded rom the above-mentioned results that the changes of bending modulus are mainly affected by the water absorption of matrix resin and that the changes of bending strength are by the accumulation of microcracks.

7.5 Mechanically Fastened Joint

7.5.1 Experiment of joint strength and failure mode

i) Experimental procedure

Geometries of joint specimens are illustrated in Fig.7.13. In this figure, d, w and e are hole diameter, specimen width and length from the top-edge to the center of hole, respectively. The hole diameter, d, was fixed at 6 mm and e was also fixed at 18 mm (three times the hole diameter; 3e). Three kinds of specimen width were adopted; 12 mm (two times the hole diameter; 2w), 18 mm (three times the hole diameter; 3w) and 30 mm (five times the hole diameter; 5w). These are called as 2w3e, 3w3e and 5w3e joints for short. Figs.7.14 and 15 illustrate the geometries of the notched specimen and the bearing test specimen.

Water immersion was conducted at 60 °C and 80 °C. The periods of immersion were fixed at 1, 3, 18, 60, 120 and 300 h. Tensile test of joint specimen was performed with a double lap joint at constant cross-head speed of 1mm/min by an Instron testing machine (type 4206) as same manner with in Chapter 6. Tensile tests of the notched specimen were performed at constant

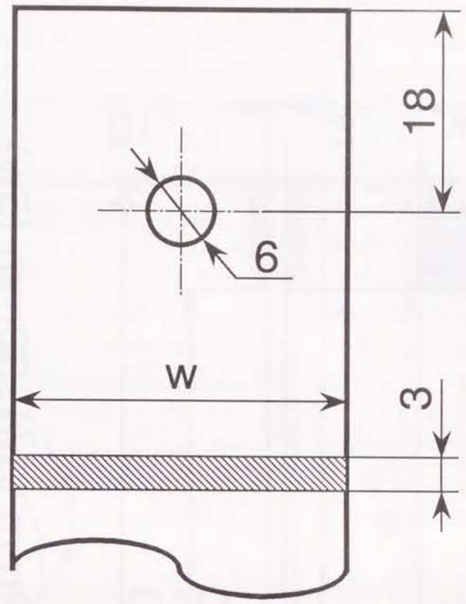

w = 12mm(2w), 18mm(3w), 30mm(5w)

Fig.7.13 Geometry of joint specimen.

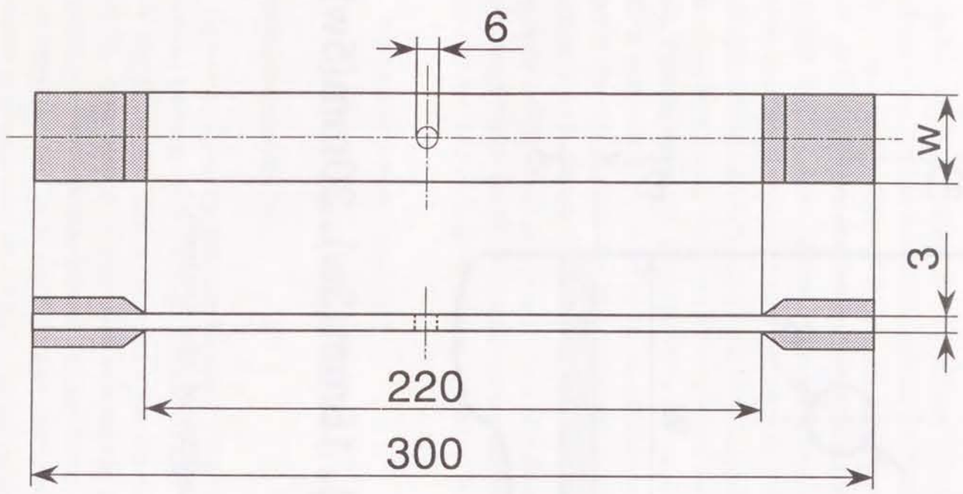

w = 12mm (2w), 18mm (3w), 30mm (5w)

Fig.7.14 Geometry of notched specimen.

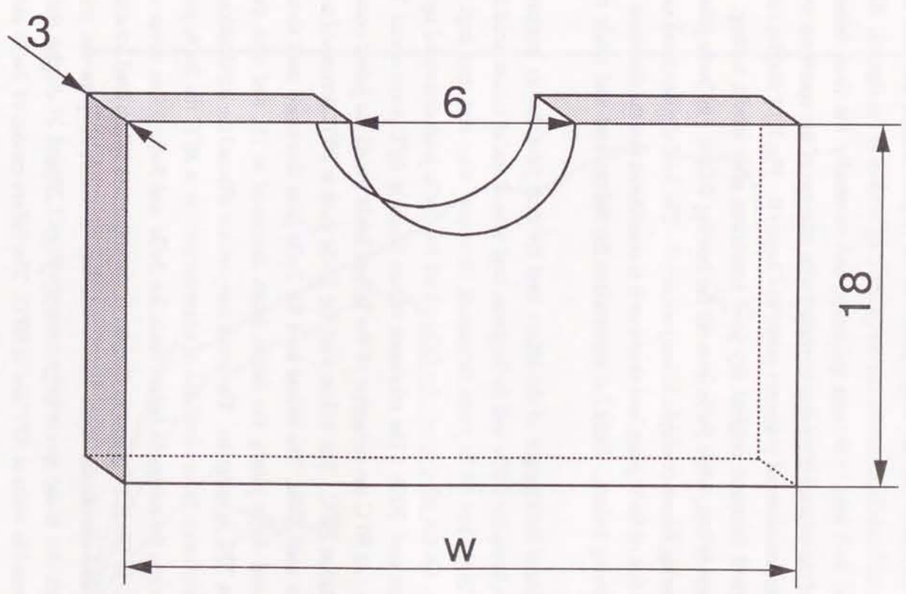

w = 12mm(2w), 18mm(3w), 30mm(5w)

Fig.7.15 Geometry of bearing test specimen.

cross-head speed of 1mm/min. The bearing test was performed at a constant cross-head speed of 0.1 mm/min.

ii) Results and discussion

Fig.7.16 displays the load-displacement curves of each original dry joint specimen. In 2w3e joint the load linearly increased, and it dropped rapidly after reaching peak load. In 3w3e and 5w3e joints, the load increased linearly with increase of the displacements, and then the first failure points appeared in the load-displacement curves (pointed by arrows in the figure). After the first failure, however, the load kept increasing gradually, and eventually the final failure was caused. The peak loads of the original dry joints increased with increase of the specimen width as same manner with the glass/unsaturated polyester joints in Chapter 6. Fig.7.17 displays the soft X-ray photographs of typical fractured original dry joint specimens after tensile testing. 2w3e joint showed the net-tension failure, while 5w3e joint did the bearing failure. In 3w3e joint, both the net-tension and the bearing failure (multiple failure) occurred. The load-displacement curve of 3w3e joint was similar to that of 5w3e joint, and therefore it is considered that the dominant failure of 3w3e joint was the bearing failure. Table 7.4 summarizes the failure load and mode of each original dry joint.

Fig.7.18 and 19 show the changes of the failure load for each joint due to immersion in water. At 60°C the failure loads for 2w3e and 3w3e joints kept almost initial values until 3h. At 18h the failure loads for 2w3e and 3w3e joints decreased, however, after that they kept almost constant value until 300h. On the other hand, the failure load for 5w3e joint decreased up to 3h, and it kept almost constant until 300h. The minimum failure loads at 60°C were about 70% in retention for all the joints. At 80°C the reduction of the failure loads for all the joints occurred at shorter immersion time than at 60°C. The failure load for 2w3e joint at 80°C decreased until 3h, and it kept almost constant until 300h. The failure load for 2w3e joint decreased until about 60% in retention. For 3w3e and 5w3e joints, the failure loads decreased at 1h, and after that they indicated constant at about 70% in retention. The water temperature affected the acceleration of the strength reduction. The minimum failure load due to water immersion at 80°C for 2w3e joint was lower than that at 60°C, while the minimum failure loads for 3w3e and 5w3e joints never affected by the water temperature. In Glass/UP joints in Chapter 6, the minimum failure load for each joint geometry eventually reached almost the same value, whereas in Glass/PP joint the minimum failure loads were different due to the specimen geometry. Figs.7.20 and 21 display the failure modes of the joints immersed in water at 60°C and at 80°C. The failure modes of 2w3e and 5w3e joints never changed by water immersion both at 60°C and at 80°C. The failure mode of 3w3e joint never also changed at 60°C, while that changed from the multiple failure to the net-tension failure at 80°C with longer immersion. The original dry 2w3e joint showed the net-tension failure, and their strength decreased remarkably due to water immersion at 80°C. On the other hand, the strength of 3w3e joint, of which failure mode changed from the multiple to net-tension, never showed a greater reduction. It is considered that this difference of the strength reduction is

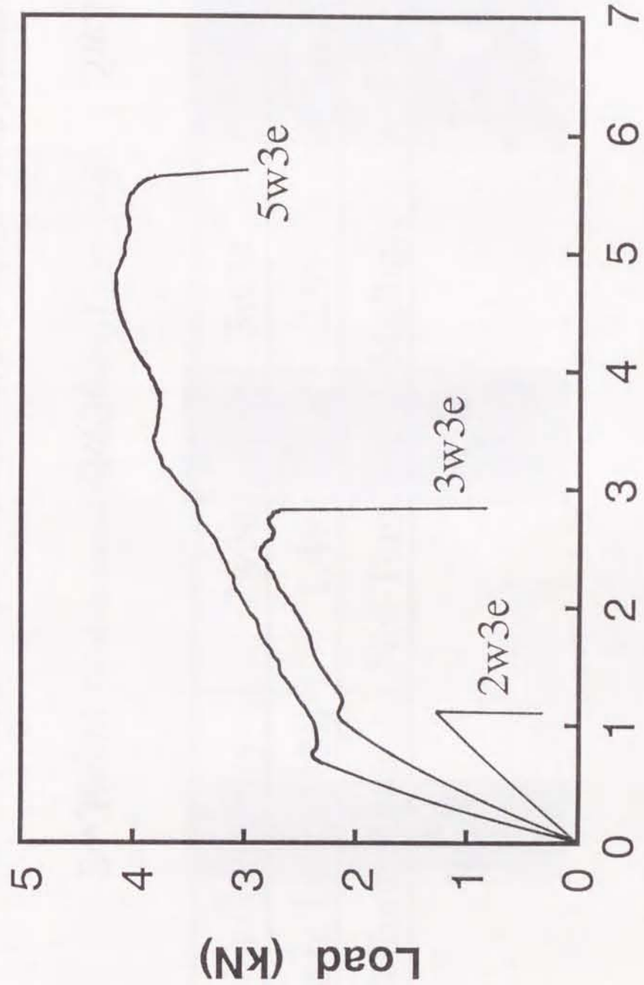

Fig.7.16 Comparison of load-displacement curves for virgin joints in tensile test.

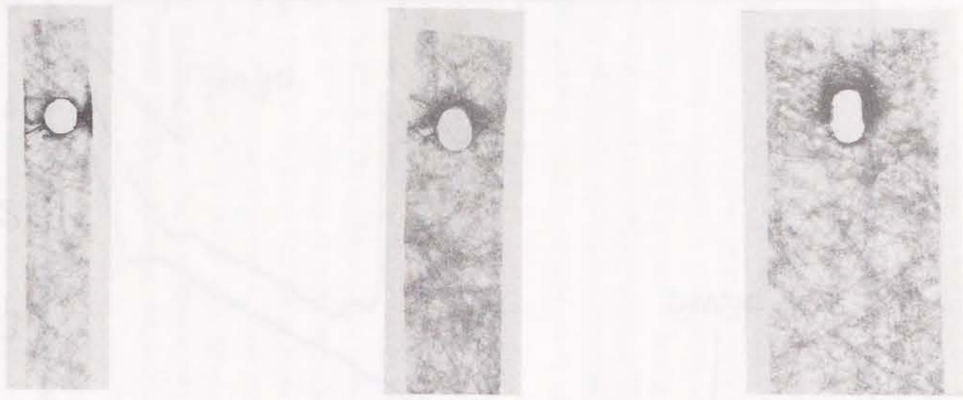

Fig.7.17 Soft X-ray photographs of typical fractured virgin joints in tensile test.

Table 7.4 Failure loads and failure modes of virgin joints.

Joint Geometry	2w3e	3w3e	5w3e
Failure Load (kN)	1.49	2.99	4.33
Failure Mode	Net-Tension	Multiple	Bearing

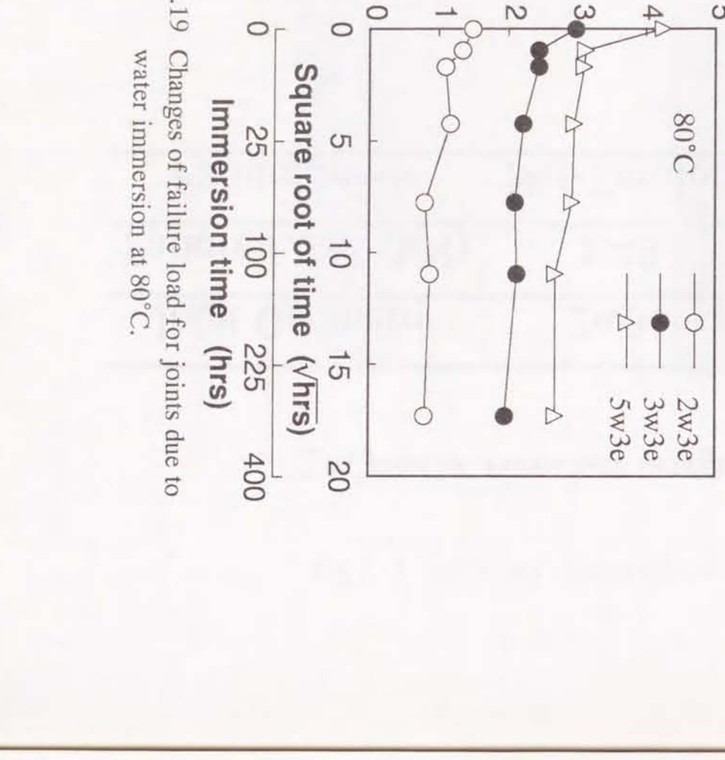

Fig.7.18 Changes of failure load for joints due to water immersion at 60°C.

Fig.7.19 Changes of failure load for joints due to water immersion at 80°C.

Immersion time / Specimen geometry	1	3	18	60	120	300
5w3e	B	B	B	B	B	B
3w3e	M	M	M	M	M	M
2w3e	N	N	N	N	N	N

Failure mode

B: Bearing failure M: Multiple failure N: Net-tension failure

Fig.7.20 Failure modes of joints immersed in water at 60°C.

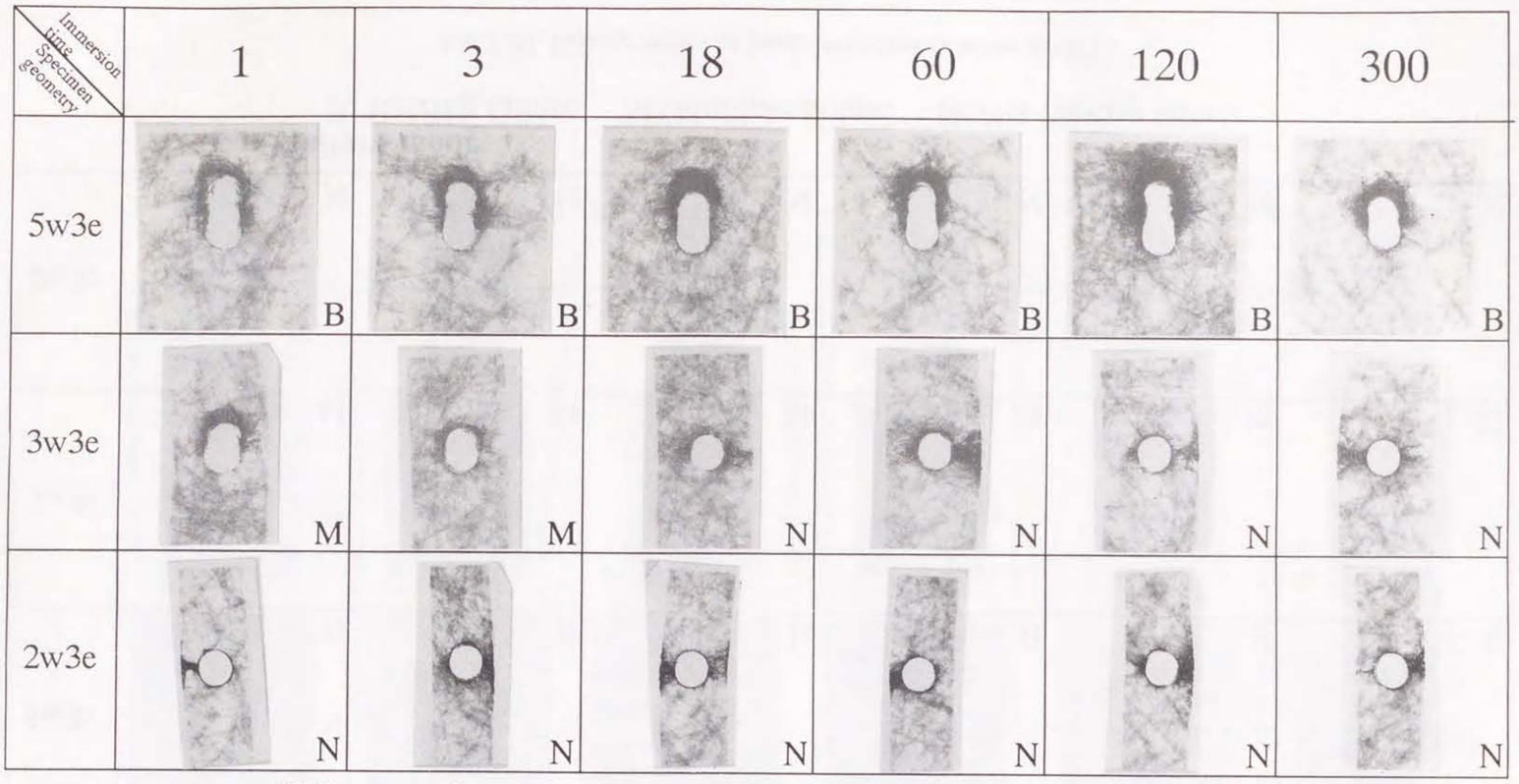

Failure mode

B: Bearing failure M: Multiple failure N: Net-tension failure

Fig.7.21 Failure modes of joints immersed in water at 80°C.

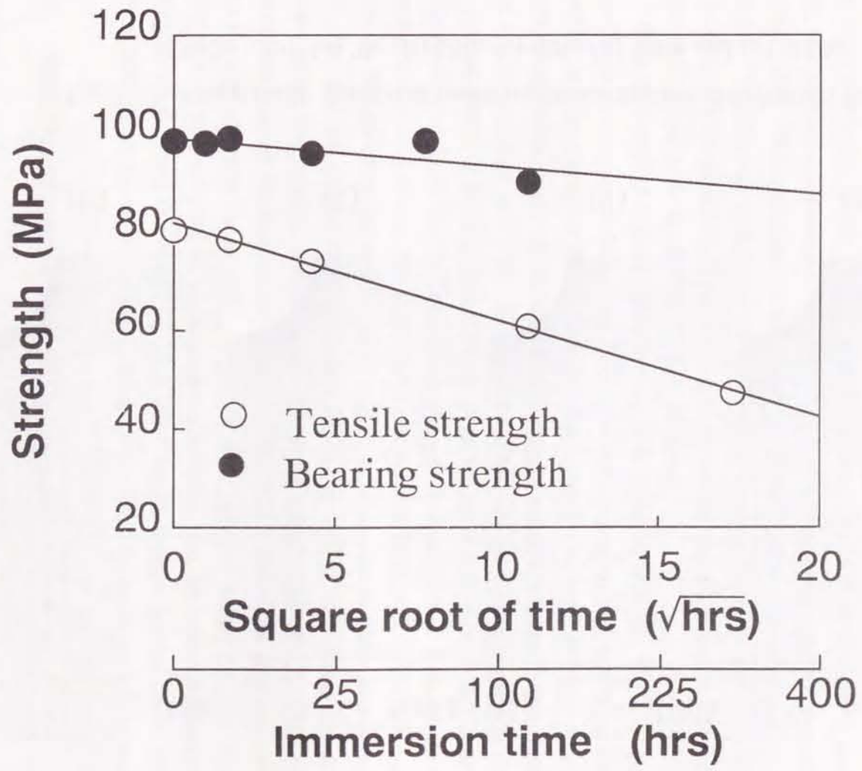

Fig.7.22 Changes of tensile strength of notched specimen and bearing strength.

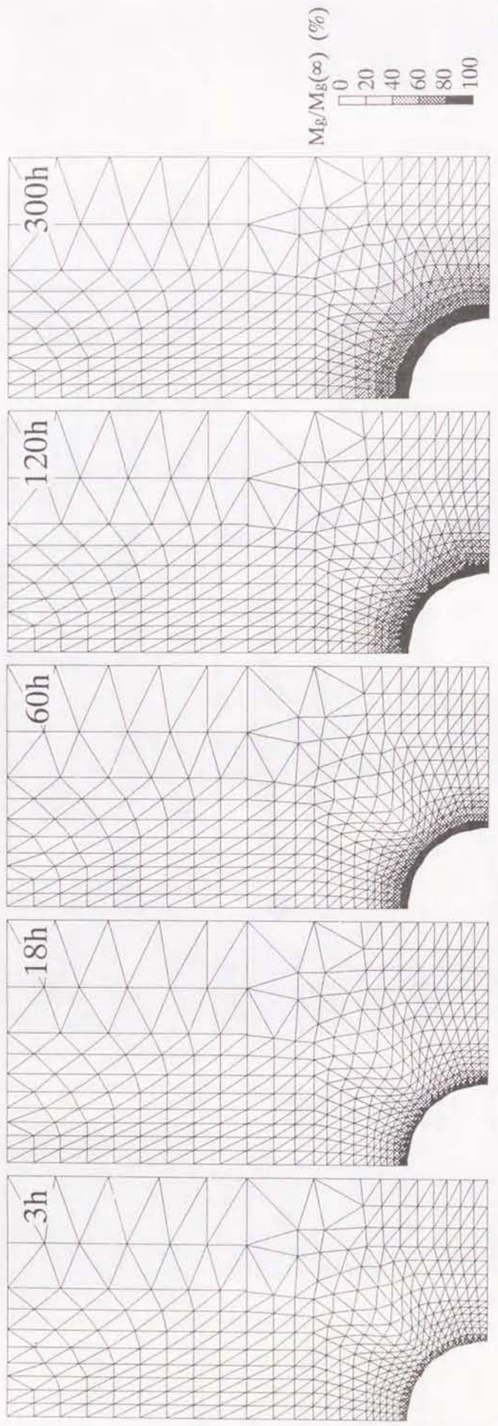

Fig.7.23 Analytically generated moisture concentration distribution for 3w3e joint; (a) 3h, (b) 18h, (c) 60h, (d) 120h and (e) 300h.

induced by the difference of the specimen width. The crack in 3w3e joint must propagate longer distance than in 2w3e joint, and therefore, it is necessarily different in the strength reduction. In Glass/UP joints the failure mode changed from the multiple failure to the bearing failure due to long water immersion, and this tendency was quite different from Glass/PP joint. Such difference in changing the failure mode may produce the difference in the minimum failure load due to water immersion between Glass/UP and Glass/PP joints. The bearing failure is the failure localized around the hole, and therefore the failure load in bearing failure eventually reaches the same value due to water immersion. On the other hand, the crack propagates in width direction in net-tension failure, and therefore it is considered that the failure load with net-tension failure depends on the specimen width. Then, the minimum failure load in Glass/PP joint is different due to the joint geometry. The difference in changing the failure mode between Glass/UP and Glass/PP joints may be caused by the difference in the tensile and the bearing strength reduction. Therefore the changes of the failure mode are discussed in next paragraph.

Here, the change of failure mode of 3w3e joint is discussed in detail. Fig.7.22 shows the changes of the tensile strength for notched specimen and the bearing strength at 80 ℃ in relation to the 3w3e joint. The changes of the tensile and bearing strength were quite different. The bearing strength reduction was small. On the other hand, the tensile strength decreased linearly against the square root of immersion time. The changes of the tensile and the bearing strength in Glass/PP were quite the reverse of those in Glass/UP. In Glass/UP the bearing strength decreased greater than the tensile strength, so that the failure mode changed from the multiple failure to the bearing failure due to water immersion. Therefore in Glass/PP the remarkable reduction in tensile strength leads to the changes of the failure mode from multiple to net-tension in 3w3e joint immersed at 80 °C. The moisture concentration distribution around the hole at each immersion time was calculated by the finite element analysis of diffusion in the same manner with that in Chapter 6. The calculated moisture distributions are displayed in Fig.7.23. The rate of diffusion was slow, so that the edge effect on the moisture distribution never appeared within the immersion time adopted here. Thus, the progress of the moisture diffusion was the same independent of the diffusing direction. From this result, it is considered that the water absorption affects the crack growth in width direction, and as a result, the greater reduction of the tensile strength is caused.

7.5.2 Prediction of joint strength and failure mode

i) Prediction method

The failure mode of 3w3e joint changed from the multiple failure to the net-tension failure. In order to understand the mechanism of changing mode, the failure strength and mode analysis were performed for 3w3e joints at 80°C. The prediction method of the failure strength and mode was the same with that proposed in Chapter 6. This prediction method was based on the failure criterion and the characteristic length. The finite element analyses were performed for the joint specimen, the notched specimen and the bearing test specimen. Fig.7.24 shows the finite element divisions for the notched specimen, the bearing test specimen and the joint specimen. The

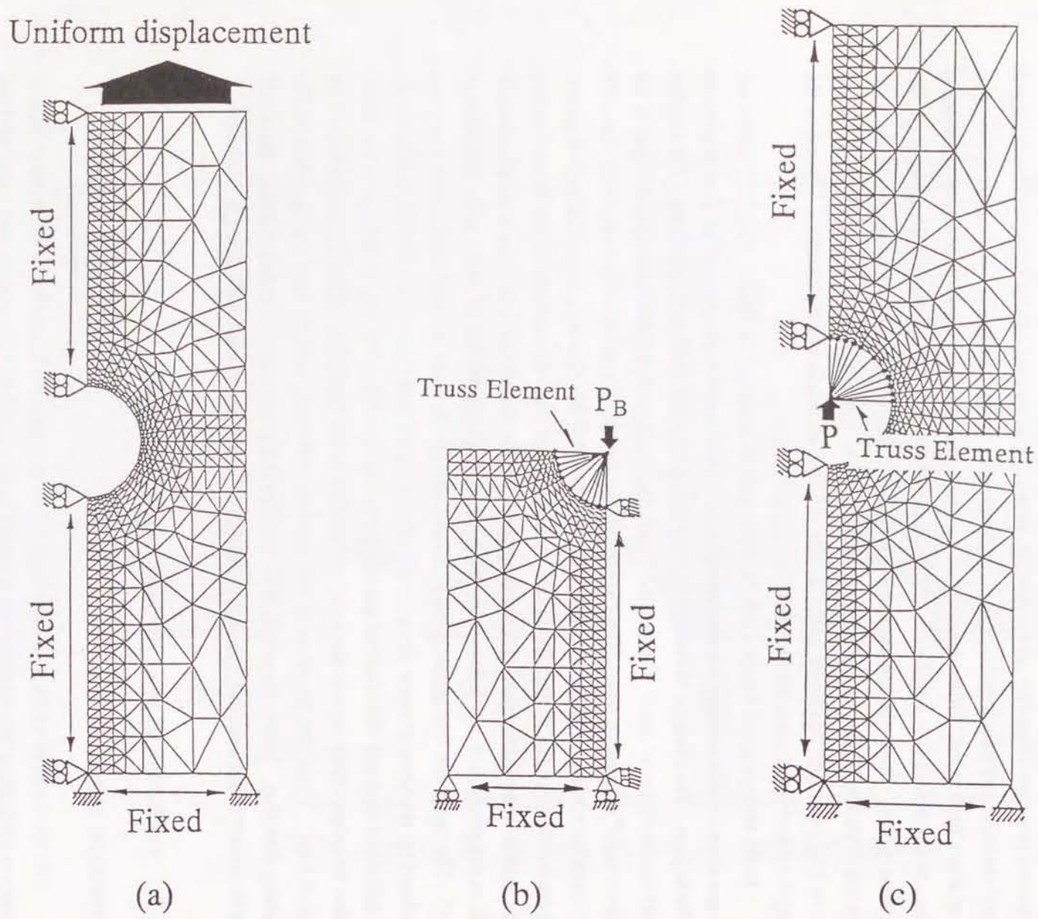

Fig.7.24 Finite element divisions and boundary conditions for (a) notched specimen, (b) bearing test specimen and (c) mechanically fastened joint.

Table 7.5 Material constants for finite element analyses.

Immersion time (hrs)	Tensile modulus (GPa)	Poisson's ratio	Tensile strength (MPa)
0	5.983	0.327	84.2
1	5.945	0.403	83.8
3	6.529	0.338	65.6
18	5.161	0.373	68.7
60	5.530	0.320	63.5
120	5.100	0.407	56.2
300	5.180	0.359	51.8

boundary conditions in the analyses are also shown in Fig.7.24. In analysis of the notched specimen, the fixed displacements were applied to the nodes at the upper edge and the total reaction force at their nodes was the failure load in the experiment shown in Fig.7.22. In the analysis of the bearing test specimen, the failure load shown in Fig.7.22 was applied to the node at the center of the notch. From these analyses, the characteristic curve was obtained. Based on these results, the analysis of the joint was performed until final failure. In the analysis of joint, the load was applied to the node at the center of a hole until the final failure condition. Table 7.5 summarizes the material constants employed for the finite element analyses.

ii) Results and discussion

Table 7.6 and Fig.7.25 show the characteristic length in tension (a_{0t}) and in bearing (a_{0b}) obtained by the finite element analyses. a_{0t} and a_{0b} increased at 1h, and it kept almost constant until 120h. At 300h a_{0t} increased remarkably, while a_{0b} decreased a little. Figs.7.26 shows the characteristic curves obtained from a_{0t} and a_{0b} on the moisture concentration distributions at each immersion time. The characteristic curves did not depend on the progress of the water absorption, and were almost the same independent of the immersion time, that is, the progress of degradation. The failure strength and mode of joint were predicted using these data. Table 7.7 summarizes the predicted results of the maximum loads and the failure modes of joints in comparison with the experimental results. Fig.7.27 shows the comparison of the maximum loads between the prediction and the experiment. The remarkable error (20.3%) appeared between the prediction and the experiment in the original dry joint, while the predicted failure loads after 1h showed good agreement with the experimental ones. However, the predicted failure modes were different from the experimental ones. Fig.7.28 shows the changes of maximum F values both in tension side and in compression side with the immersion time. The maximum F value in compression side of the original dry joint was about 0.65, and was remarkably lower than that in tension side. After 1h, the difference of the maximum F value between tension side and compression side became smaller, however, the maximum F value in tension side was almost saturated at about 0.8. Fig.7.29 illustrates the analytically obtained failure region in the joints at each immersion time. This result suggests that the fracture region in tension side enlarges greater than in compression side as the immersion became longer. Thus, the fracture progress in tension side is more affcted by the water immersion than that in compression side. This tendency corresponds to the changes of the failure mode in the experiment, that is, from the multiple to the net-tension failure. However, the fracture in tension side does not lead to the final failure of joint, and therefore the final failure mode in the prediction is different from that in the experiment. The modulus of glass/PP composites is relatively low in comparison with glass/UP composites, and moreover the stress-strain curve of glass/PP often indicates the remarkable non-linearity. However, the modulus was treated as a constant in the analyses, and this may be a reason why the final failure modes in the prediction did not correspond to those in the experiment. Therefore, it seems that the non-linear stress-strain behavior must be considered to predict the failure mode of glass/PP joints.

Table 7.6 a_{0t} and a_{0b} obtained by finite element analyses.

Immersion time (hrs)	a_{0t} (mm)	a_{0b} (mm)
0	2.32	0.70
1	2.52	0.93
3	2.51	0.88
18	2.57	0.92
60	2.37	0.88
120	2.32	0.90
300	3.25	0.77

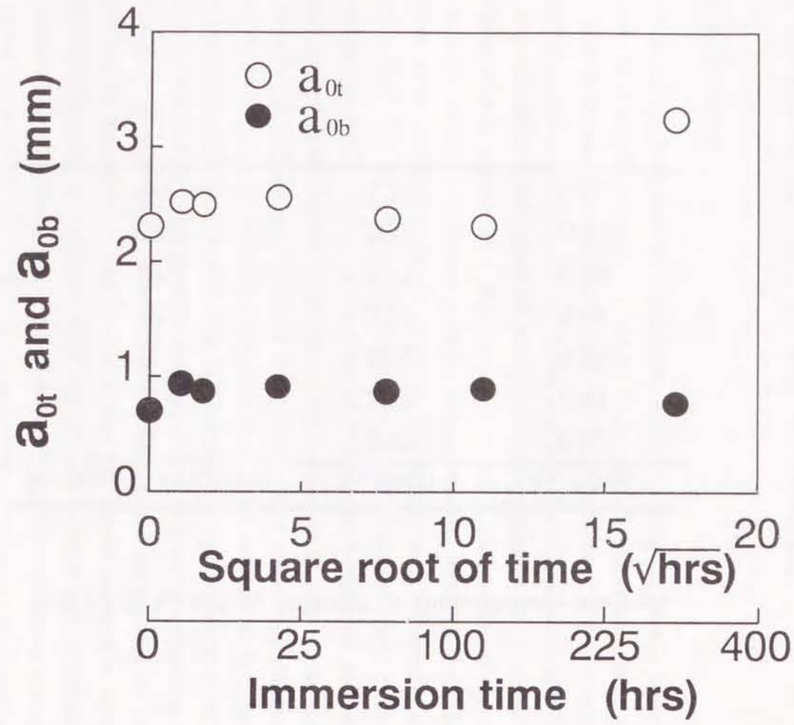

Fig.7.25 Changes of a_{0t} and a_{0b} obtained by finite element analyses against the square root of immersion time.

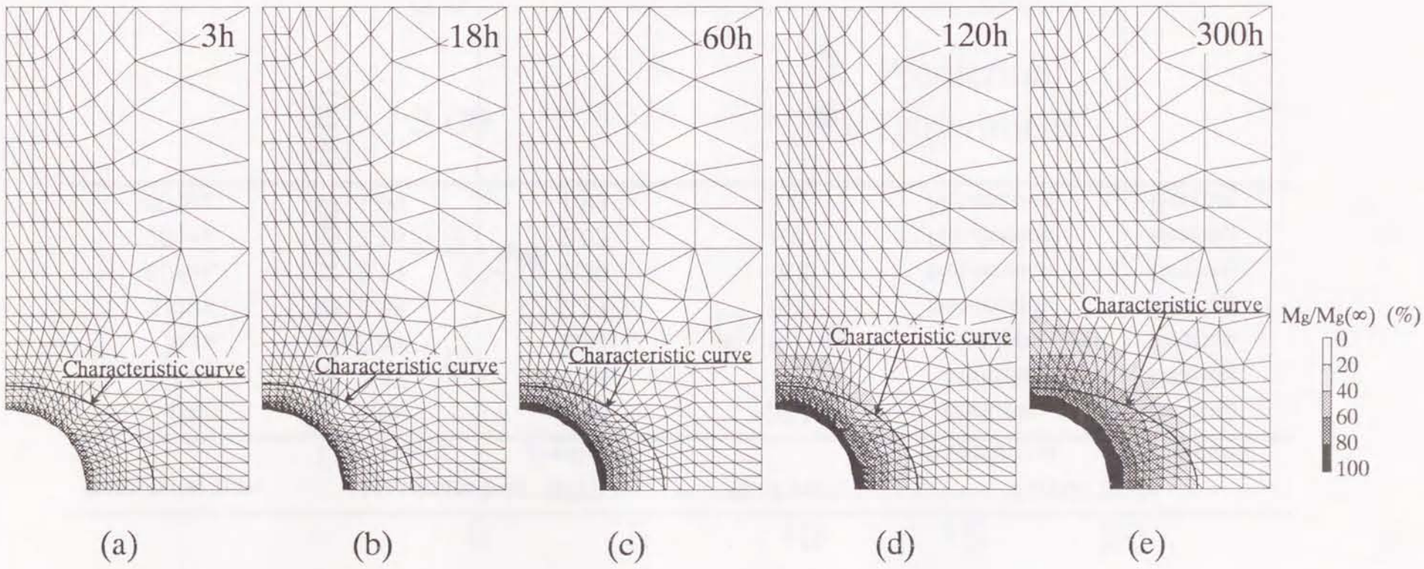

Fig.7.26 Characteristic curves obtained from a_{0t} and a_{0b} on moisture concentration distribution; (a) 3h, (b) 18h, (c) 60h, (d) 120h and (e) 300h.

Table 7.7 Predicted and experimental results for joint strength and failure modes.

Immersion time	Maximum load (kN)		% of error	Failure mode	
	Experiment	Prediction		Experiment	Prediction
0 hr.	3.05	2.43	20.3	Multiple	Bearing
1 hr.	2.49	2.43	2.4	Multiple	Bearing
3hrs.	2.48	2.25	9.3	Multiple	Bearing
18hrs.	2.28	2.27	0.4	Net-tension	Bearing
60 hrs.	2.14	2.20	-2.8	Net-tension	Bearing
120 hrs.	2.16	2.03	6.0	Net-tension	Bearing
300 hrs.	1.99	1.93	3.0	Net-tension	Bearing

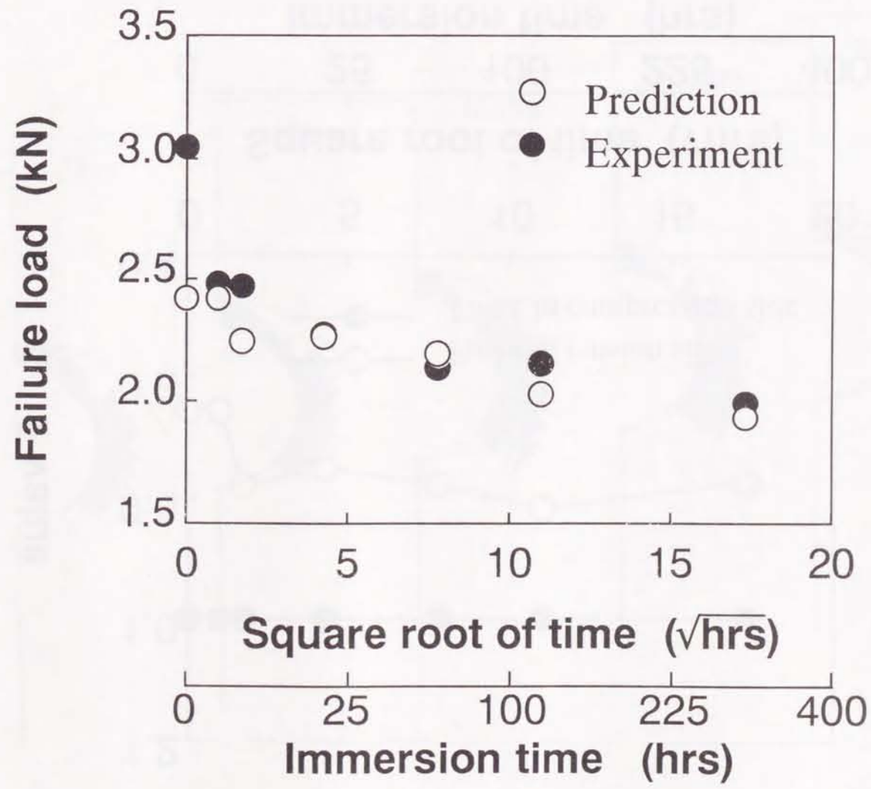

Fig.7.27 Comparison between predicted and experimental failure loads.

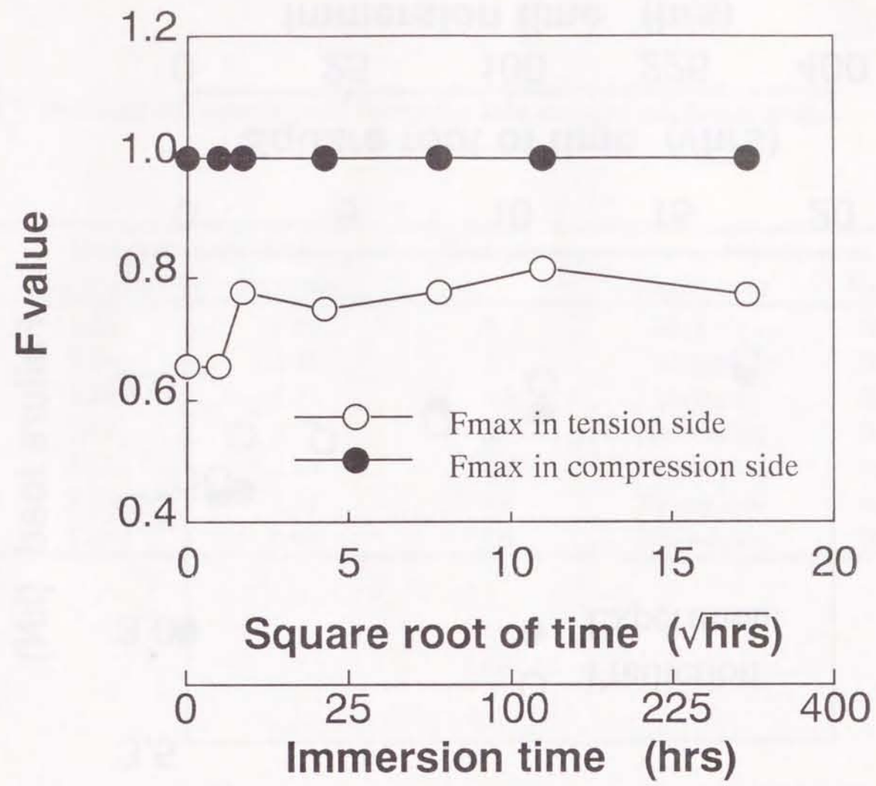

Fig.7.28 Changes of maximum F value both in tension and in compression sides due to water immersion.

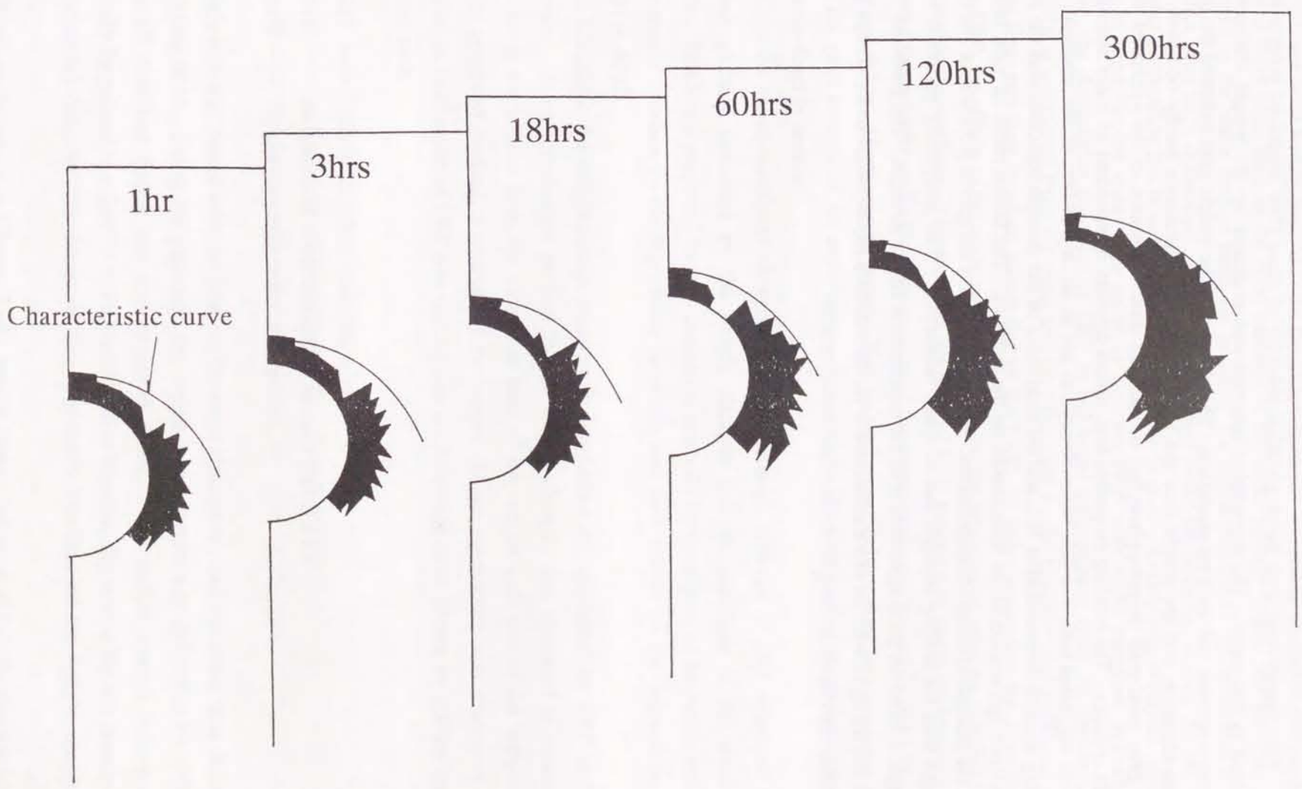

Fig.7.29 Analytically generated failure maps.

7.6 Conclusion

This chapter dealt with the degradation behavior of glass fiber reinforced polypropylene immersed in hot water. The degradation behavior was evaluated by the weight changes, the bending properties and the joint properties. The changes of the weight gain indicated the typical Fickian diffusion, and the weight loss due to the interfacial degradation hardly occurred. The glass fiber reinforced polypropylene has an excellent water resistance in the viewpoint of the weight changes. The bending properties kept almost constant independent of water immersion, and this originated both in a little water absorption and in no degradation of the interface. The bending strength decreased after 30h, and the main cause of the strength reduction was the matrix degradation (generation of the microcracks on the surface). The failure mode of joint changed from the multiple to the net-tension failure. This was caused by the greater reduction of the tensile strength than the bearing strength due to water immersion. The analytically predicted failure strength showed the good agreement with the experimental failure strength. The predicted failure mode did not agree with the experiment, however, the tendency of the failure mode change in the prediction corresponded roughly to the experimental results.

Chapter 8 Conclusions

FRP has been widely applied to the structural materials in various corrosive environments. FRP panels have been used as the main member of the water storage tanks. As the FRP tanks have spread as the water storage tanks for housing, the improvements of the performance of the water tanks have been demanded. In the water storage tanks for housing, storing the hot water with higher temperature has been demanded. FRP must have an excellent hygrothermal resistance in order to store the hot water. In order to develop FRP with more excellent hygrothermal resistance, the degradation behavior of FRP in hot water environment must be understood in detail. FRP is composed from the resin and the fiber, and so the hygrothermal resistance of the resin, the fiber and their interface affects that of the FRP. In order to develop the hygrothermal resistant FRP, the effects of the resin and the interface on the degradation must be clarified by the suitable evaluation methods. Moreover the life time of FRP structure in water environment must be predicted theoretically under the consideration of the degradation mechanism in order to ensure the structural safety. However, the present life time prediction has been done by experience on the basis of the great amount of the experimental data, and the life time prediction method has never been standardized in present.

From the above-mentioned viewpoints, the degradation behavior of FRP immersed in hot water was globally discussed by the weight changes and the reduction of the mechanical properties. This study proposed the new evaluation methods for the effects of the matrix resin and the fiber/matrix interface on the degradation behavior, and their effects on the degradation were discussed in detail.

In Chapter 2, the weight change behavior is macroscopically discussed for FRP immersed in hot water. A new evaluation method for the weight changes was proposed to discuss the weight change mechanism from the viewpoint both of the weight gain and of the weight loss. Using the proposed method, a concept of the weight change mechanism was discussed. The weight change mechanism of FRP was divided into the following three phases by comparing with that of neat resin:

Phase I ----- Only resin matrix absorbed water.
Phase II ----- Saturation of water absorption in resin part of FRP.
Phase III ----- Weight loss with water absorption.

The weight loss was caused with the delay to the water absorption, and this delay was defined as the delay time of M_l. Using this parameter the weight loss behavior was defined as the diffusion behavior of dissolved matter into environmental water. The weight change behavior was theoretically formulated in reference to Fickian diffusion kinetics. By comparing this concept with the experimental data, the importance of the fiber/matrix interface on the weight change was clarified.

Based on the results in Chapter 2, the weight change behavior of the fiber/matrix interface was microscopically discussed. A quantitative evaluation system for measuring the weight

changes of the fiber/matrix interface was proposed. In this system the weight change of the interface was defined as the difference of the weight change between FRP and its resin part. It was clarified by the chemical analyses that the weight loss of the interface was originated from the dissolution of the binder, the silane coupling agent and the fiber existing in the interfacial region. Into this dissolved interfacial region the water penetrated. Such phenomena occurred after the water absorption of the resin part reached a saturation, and they affected the weight change behavior of FRP at longer immersion time. This suggested that the amount of the interface greatly affected the long-term weight changes of FRP in water environment. Thus, the design of the interface was very important to reduce the weight changes of FRP used in water environment.

As mentioned in Chapter 2 and Chapter 3, the significant weight changes are caused in FRP by the water immersion. It can be easily supposed that such weight changes affect the mechanical properties of FRP. Therefore Chapter 4 and Chapter 5 dealt with the changes of the elastic property and the strength of FRP immersed in hot water, which was used in Chapter 2 and Chapter 3. The reduction processes of the mechanical properties were discussed from the relation between the weight changes and the mechanical properties.

In Chapter 4, the changes of the elastic property were discussed for FRP immersed in hot water. The elastic modulus decreased linearly against the weight gain due to water absorption, and it was not affected macroscopically by the weight loss in phase I and phase II. From the experimental results, it was supposed that the main cause of the modulus reduction was the degradation of the interface between fiber bundle and matrix and in fiber bundle. The effect of the interfacial degradation on the modulus reduction was estimated by the finite element analyses introducing the damage mechanics. As a result of the numerical analyses, it was verified that the main cause of the modulus reduction of FRP immersed in water was the debonding between fiber and matrix.

Chapter 5 dealt with the fracture mechanisms and the strength reductions of FRP immersed in hot water. The origin of the strength reduction owing to the water immersion was roughly clarified by the relation between the weight changes and the strength, and the fracture process during loading was discussed by introducing the AE technique and the microscopic observation. Fracture initiation was the debonding between fiber bundle and matrix in the virgin specimen, while it was the debonding inside the fiber bundles in the immersed specimen. The strength reduction due to water immersion was caused both by the degradation of the matrix and by the gradual degradation of the fiber/matrix interface in phase I and phase II. In phase III the strength was reduced by the debondings between fiber bundle and matrix and inside the fiber bundles. By introducing the AE technique the magnitude of the fracture could be estimated by both AE amplitude and AE energy. This fracture evaluation method by AE could be applied to the evaluation of the fracture mode changes of FRP immersed in hot water. This concept for AE was applied to the estimation of the material soundness of FRP during Kaiser test.

In case that FRP is applied as the structural component, FRP member is often joined with the other member. In the water storage tanks FRP panels are joined each other by the mechanically fastened joints. Therefore the effect of water on the joint properties must be clarified

to assure the structural safety of the water storage tanks. Then, Chapter 6 dealt with the degradation behavior of mechanically fastened FRP joints immersed in hot water. The used material was the same with that in Chapter 2 to Chapter 5. The joint strength with bearing failure decreased remarkably due to water immersion, while that with net-tension failure decreased a little due to water immersion. This difference was caused by the remarkable reduction of the bearing property, and as a result, all the joints eventually came to fail in the bearing failure mode. Therefore the changes of the bearing property in this joint must be considered to assure the safety design of the FRP structures with mechanically fastened joints. The prediction method of the joint strength and the failure mode of the FRP joint was proposed, and it was applied to the prediction of the degradation behavior of FRP joints immersed in hot water. This prediction method was the combination of the point stress analysis and the macroscopic failure criterion. The predicted results showed good agreement with the experimental results, and it was verified that the proposed prediction method could be applied to the design of the structures under water environment.

The materials investigated in Chapter 2 to Chapter 6 were randomly oriented glass fiber continuous strand mat reinforced unsaturated polyester resins, which were thermosetting composites. In recent years, the disposal of the waste of fiber reinforced thermosettings becomes an issue since the reuse and the recycling of thermosetting composites are very difficult. Therefore the thermoplastics have gotten much attention as recyclable matrix resins for FRP. In order to replace thermosetting composites to thermoplastic composites in the structures, the various properties of thermoplastic composites must be understood. Therefore Chapter 7 dealt with the property changes of the long fiber reinforced thermoplastics (polypropylene) immersed in hot water. The degradation behavior was evaluated by the weight changes, the bending properties and the joint properties. The changes of the weight gain indicated the typical Fickian diffusion, and the weight loss due to interfacial degradation hardly occurred. The glass fiber reinforced polypropylene had more excellent water resistance than the glass fiber reinforced unsaturated polyester in the viewpoint of the weight changes. The bending modulus kept almost constant independent of water immersion, and this originated both in a little water absorption and in no degradation of the interface. However, the bending strength decreased after 30h, and this was caused by the matrix degradation such as the generation of the microcracks on the surface. The reduction of the joint strength in glass/polypropylene composites was smaller than that in glass/polyester composites. The failure mode of joint changed from the multiple to the net-tension failure. This was caused by the greater reduction of the tensile strength than the bearing strength due to water immersion. From these results, it can be concluded that the water resistance of thermoplastic composites is superior to that of thermosetting composites. Therefore the thermoplastic composites should come to be widely applied in water environment near future if the thermoplastics with higher mechanical properties is developed.

In this paper the degradation behavior of FRP in hot water environment was discussed from the various viewpoints. From these theoretical and the experimental results in Chapter 2 to Chapter 6, the improvement of the water resistance of FRP is discussed.

The degradation of FRP in water environment is dominated by the water resistance of the matrix resin and the fiber/matrix interface. In particular, the matrix resin greatly affects the water resistance of FRP as mentioned in Chapter 7. Thus, the water resistance of thermoplastic composites is superior to that of thermosetting composites. In general, however, the mechanical properties of thermoplastic composites are inferior to those of thermosetting composites. Therefore it is difficult to apply the thermoplastic composites to the primary structures such as the water tanks. In addition to this, the alteration of the matrix resin in FRP may be led to the major modification of the fabrication method, and so this is very difficult problem. Therefore, the improvement of the water resistance of the fiber/matrix interface must be considered at present because the interface mainly affects the long-term property changes such as weight changes and the reduction of mechanical properties. The glass fiber of the randomly oriented fiber mat is treated by the primary and the secondary binders in addition to the silane coupling agent in order to enhance the ease of molding of FRP panels. As mentioned in Chapter 3, the undesirable degradation at the interface is caused by the dissolution of the binders and the silane coupling agent. Consequently the degradation behavior of the interface is dominated by the water resistance of the binders and the coupling agent. From this fact, it is considered that the fiber is treated by no binder and the coupling agent with unhydrated group in the ideally designed interface. However, the binder must be used in consideration of the handling and the impregnation at the compression molding. The silane coupling agent must be usually selected in consideration of the reactivity with matrix resin. Consequently the development of the binder with excellent water resistance is essential to improve the water resistance of FRP in water environment. Moreover the reduction of the binder content is also important to reduce the dissolution and to avoid the damage generation at the interface. Thus, it is concluded that the optimum design of the fiber/matrix interface is essential to improve the water resistance of FRP in water environment.

References

1. *Fukugo zairyo kogaku*, ed. Hayashi, T., Nikka Giren, Tokyo, 1971 (in Japanese).
2. Hull, D., *An introduction to composite materials*, Cambridge University Press, Cambridge, 1981.
3. *Environmental effects on composite materials*, ed. Springer, G. S., Technomic, Westport, 1981.
4. *Environmental effects on composite materials*, Vol.2, ed. Springer, G. S., Technomic, Lancaster, 1984.
5. Shen, C. H. and Springer, G. S., "Moisture absorption and desorption of composite materials", *J. Compos. Mater.*, 10(1976), 2-20.
6. Springer, G. S., "Moisture content of composites under transient condition", *J. Compos. Mater.*, 11(1977), 107-124.
7. Loos, A. C. and Springer, G. S., "Moisture absorption of graphite-epoxy composition immersed in liquids and in humid air", *J. Compos. Mater.*, 13(1979), 131-147.
8. Loos, A. C., Springer, G. S., Sanders, B. A. and Tung, R. W., "Moisture absorption of polyester-E glass composites", *J. Compos. Mater.*, 14(1980), 142-154.
9. Verpoest, I. and Springer, G. S., "Moisture absorption characteristics of aramid-epoxy composites", *J. Reinf. Plast. Compos.*, 7(1988), 2-22.
10. Shen, C. H. and Springer, G. S., "Effects of moisture and temperature on the tensile strength of composite materials", *J. Compos. Mater.*, 11(1977), 2-16.
11. Shen, C. H. and Springer, G. S., "Environmental effects on the elastic moduli of composite materials", *J. Compos. Mater.*, 11(1977), 250-264.
12. Springer, G. S., Sanders, B. A. and Tung, R. D., "Environmental effects on glass fiber reinforced polyester and vinylester composites", *J. Compos. Mater.*, 14(1980), 213-232.
13. Wang, Q. and Springer, G. S., "Moisture absorption and fracture toughness of PEEK polymer and graphite fiber reinforced PEEK", *J. Compos. Mater.*, 23(1989), 434-447.
14. Harper, J. F. and Naeem, M., "The effect of temperature and humidity on glass fibre reinforced vinyl ester resin", *14th Reinf. Plast. Congr.*, 1984, 173-176.
15. Schmid, R., "Effect of humidity and temperature on physical properties of matrix resins and carbon fibre composites", in *High Tech - the Way into the Nineties*, ed. Brunsch, K., Golden, H. D. and Herkert, C. M., Elsevier, Amsterdam, 1986, 311-320.
16. Gopalan, R., Rao, R. M. V. G. K. and Murthy, M. V. V., "Diffusion studies on advanced fibre hybrid composites", *J. Reinf. Plast. Compos.*, 5(1986), 51-61.
17. Ellis, B. and Found, M. S., "The effects of water absorption on a polyester/chopped strand mat laminate", *Composites*, 14(1983), 237-243.
18. Lau, C. H., Hodd, K. A. and Wright, W. W., "Water absorption characteristics of aramid-epoxy composites", *17th National SAMPE Tech. Conf.*, 1985, 179-189.
19. Singh, K. S., Singh, P. N. and Rao, R. M. V. G. K., "Hygrothermal effects on chopped fibre/woven fabric reinforced epoxy composites. Part A: Moisture absorption characteristics", *J. Reinf. Plast. Compos.*, 10(1991), 446-456.

20. Pritchard, G. and Speake, S. D., "The use of water absorption kinetic data to predict laminate property changes", *Composites*, 18(1987), 227-232.
21. Berens, A. R. and Hopfenberg, H. B., "Diffusion and relaxation in glassy polymer powders: 2. Separation of diffusion and relaxation parameters", *Polymer*, 19(1978), 489-496.
22. Wright, W. W., "The effect of diffusion of water into epoxy resins and their carbon-fibre reinforced composites", *Composites*, 12(1981), 201-205.
23. Mijovic, J. and Weinstein, S. A., "Moisture diffusion into a graphite-epoxy composite", *Polym. Commun.*, 26(1985), 237-239.
24. Apicella, A., Migliaresi, C., Nicodemo, L., Nicolais, L., Iaccarino, L. and Roccotelli, S., "Water sorption and mechanical properties of a glass-reinforced polyester resin", *Composites*, 13(1982), 406-410.
25. Ankara, A., Weisgerber, D. and Vilsmeier, J., "Influence of thermal spiking on properties of carbon fibre reinforced plastic", *Mater. Sci. Technol.*, 2(1986), 1081-1085.
26. Hahn, H. T., "Hygrothermal damage in graphite/epoxy laminates", *J. Eng. Mater. Technol.*, 109(1987), 3-11.
27. Neumann, S. and Marom, G., "Prediction of moisture diffusion parameters in composite materials under stress", *J. Compos. Mater.*, 21(1987), 68-80.
28. Marom, G. and Broutman, L. J., "Moisture penetration into composites under external stress", *Proc. 36th Annual Conf.*, SPI(1981), 17-E:1-5.
29. Avena, A. and Bunsell, A. R., "Effect of hydrostatic pressure on the water absorption of glass fibre-reinforced epoxy resin", *Composites*, 19(1988), 355-357.
30. Aditya, P. K. and Sinha, P. K., "Diffusion coefficients of polymeric composites subjected to periodic hygrothermal exposure", *J. Reinf. Plast. Compos.*, 11(1992), 1035-1047.
31. Springer, G. S., "Numerical procedures for the solution of one dimensional fickian diffusion problems", in *Environmental Effects on Composite Materials,*, ed. Springer, G. S., Technomic, Westport, 1981, 166-199.
32. Rao, R. M. V. G. K., Chanda, M. and Balasubramanian, N., "A fickian diffusion model for permeable fibre polymer composites", *J. Reinf. Plast. Compos.*, 2(1983), 289-299.
33. Miller, R. K., "Multi-material model moisture analysis for steady-state boundary conditions", in *Environmental Effects on Composite Materials, Vol.2*, ed. Springer, G. S., Technomic, Lancaster, 1984, 162-169.
34. Bonniau, P. and Bunsell, A. R., "A comparative study of water absorption theories applied to glass epoxy composites", in *Environmental Effects on Composite Materials, Vol.2*, ed. Springer, G. S., Technomic, Lancaster, 1984, 209-229.
35. Collings, T. A., "Moisture management and artificial ageing of fibre reinforced epoxy resins", *Proc. 5th Int. Conf. Compos. Mater.*, 1985, 213-239.
36. Collings, T. A., "The use of resin hybrids to control moisture absorption in fibre-reinforced plastics", *Composites*, 22(1991), 369-372.
37. Blikstad, M., "Three-dimensional moisture diffusion in graphite/epoxy laminates", *J. Reinf. Plast. Compos.*, 5(1986), 9-18.

38. Kondo, K. and Taki, T., "Moisture diffusivity of unidirectional composites", in *Environmental Effects on Composite Materials, Vol.2*, ed. Springer, G. S., Technomic, Lancaster, 1984, 288-299.
39. Janas, V. F. and McCullough, R. L., "Moisture absorption in unfilled and glass-filled, cross-linked polyester", *Compos. Sci. Technol.*, 29(1987), 293-315.
40. Dewas, J. N. and Favre, J. P., "Prevision of CFRP moisture absorption from data on neat resin", *Proc. 5th Int. Conf. Compos. Mater.*, 1985, 1059-1069.
41. Lee, M. c. and Peppas, N. A., "Models of moisture transport and moisture-induced stresses in epoxy composites", *J. Compos. Mater.*, 27(1993), 1146-1171.
42. Vaughan, D. J., Peck, Jr. R. C. and Creech, Jr. M. H., "The importance of the interface on water absorption in glass reinforced epoxy composites", *Proc. 39th Annual Conf.*, SPI(1984), 4-G, 1-4.
43. Woo, M. and Piggott, M. R., "Water absorption of resins and composites: IV. Water transport in fiber reinforced plastics", *J. Compos. Technol. Research*, 10(1988), 20-24.
44. Drzal, L. T., "Composite interphase characterisation", *Proc. 28th National SAMPE Symp.*, 1983, 1057-1068.
45. Drzal, L. T., "Interfacial behavior of aramid and graphite fibers in an epoxy matrix", *Proc. 15th National SAMPE Tech. Conf.*, 1983, 190-201.
46. Bascom, W. D., Jensen, R. M. and Cordner, L. W., "The adhesion of carbon fibres to thermoplastic polymers", *Proc. 6th Int. Conf. Compos. Mater.*, 1987, 5.424-438.
47. Sawada, Y., Shindo, A. and Nakanishi, Y., "Interfacial adhesion in a carbon fiber-polyimide composite", *Proc. 6th Int. Conf. Compos. Mater.*, 1987, 5.448-457.
48. Baillie, C. A. and Bader, M. G., "The influence of fibre surface treatment on the adhesion of carbon fibres in epoxy resin", *Proc. 8th Int. Conf. Compos. Mater.*, 1991, 11-B:1-10.
49. Ivens, J., Wevers, M. and Verpoest, I., "Influence of the carbon fiber surface treatment on the mode I fracture toughness in CFRP", *Proc. 8th Int. Conf. Compos. Mater.*, 1991, 11-C:1-11.
50. Suzuki, Y., Maekawa, Z., Hamada, H., Yokoyama, A., Sugihara, T. and Hojo, M., "Influence of silane coupling agents on interlaminar fracture in glass fiber fabric reinforced unsaturated polyester laminates", *Proc. 8th Int. Conf. Compos. Mater.*, 1991, 11-K:1-11.
51. Galiotis, C., "A study of mechanism of stress transfer in continuous- and discontinuous-fibre model composites by laser raman spectroscopy", *Compos. Sci. Technol.*, 48(1993), 15-28.
52. Baxevanakis, C., Jeulin, D. and Valentin, D., "Fracture statistics of single-fibre composite specimens", *Compos. Sci. Technol.*, 48(1993), 47-56.
53. Hamada, H., Ikuta, N., Maekawa, Z., Ichihashi, H. and Nishida, N., "Evaluation of the interfacial properties in the embedded-single-fibre coupon test", *Compos. Sci. Technol.*, 48(1993), 81-85.
54. Bader, M. G., Pickering, K. L., Buxton, A., Rezaifard, A. and Smith, P. A., "Failure micromechanisms in continuous carbon-fibre/epoxy-resin composites", *Compos. Sci. Technol.*, 48(1993), 135-142.

55. Zhou, L. M., Kim, J. K. and Mai, Y. W., "Micromechanical characterisation of fire/matrix interfaces", *Compos. Sci. Technol.*, 48(1993), 227-236.
56. Garg, A. C. and Paliwal, V., "Effect of water on the fracture behaviour of glass fibre reinforced polyesters", *Fiber Sci. Technol.*, 17(1982), 63-69.
57. Phani, K. K. and Bose, N. R., "Temperature dependence of hydrothermal ageing of CSM-laminate during water immersion", *Compos. Sci. Technol.*, 29(1987), 79-87.
58. Misaki, T. and Iwatsu, T., "Effect of boiling water aging on strength and fracture properties of chopped strand mat-polyester laminate", *J. Appl. Polym. Sci.*, 30(1985), 1083-1093.
59. Valentin, D., Paray, F. and Guetta, B., "The hygrothermal behaviour of glass fibre reinforced Pa66 composites", *J. Mater. Sci.*, 22(1987), 46-56.
60. Allred, R. E., "The effect of temperature and moisture content on the flexural response of Kevlar/epoxy laminates: Part I. [0/90] filament orientation", in *Environmental Effects on Composite Materials, Vol.2*, ed. Springer, G. S., Technomic, Lancaster, 1984, 27-42.
61. Birger, S., Moshonov, A. and Kenig, S., "The effects of thermal and hygrothermal ageing on the failure mechanisms of graphite-fabric epoxy composites subjected to flexural loading", *Composites*, 20(1989), 341-348.
62. Kellas, S., Morton, J. and Curtis, P., "The effect of hygrothermal environments upon the tensile and compressive strengths of notched CFRP laminates, Part 1: Static loading", *Composites*, 21(1990), 41-51.
63. Haque, A., Mahmood, S., Walker, L. and Jeelani, S., "Moisture and temperature induced degradation in tensile properties of Kevlar-graphite/epoxy hybrid composites", *J. Reinf. Plast. Compos.*, 10(1991), 132-145.
64. Doxsee, Jr., L. E., Janssens, W., Verpoest, I. and Meester, P. D., "Strength of aramid-epoxy composites during moisture absorption", *J. Reinf. Plast. Compos.*, 10(1991), 645-655.
65. Haque, A. and Jeelani, S., "Environmental effects on the compressive properties; Thermosetting vs. thermoplastic composites", *J. Reinf. Plast. Compos.*, 11(1992), 146-157.
66. Johannesson, T. and Blikstad, M., "Influence of moisture and resin ductility on delamination", *Compos. Sci. Technol.*, 24(1985), 33-46.
67. Watanabe, M., "Effect of water environment on fatigue behavior of fiberglass reinforced plastics", *Compos. Mater. 5th Conf.*, 345-367.
68. Hofer, K. E., Skaper, G. N., Bennett, L. C. and Rao, N., "Effect of moisture on fatigue and residual strength losses for various composites", *J. Reinf. Plast. Compos.*, 6(1987), 53-65.
69. Marshetti, M., Tizzi, S. and Tesei, C. "Creep behaviour of graphite-epoxy composites: temperature and moisture effects", *Adv. Fract. Res.*, 4(1984), 3029-3036.
70. Aveston, J., Kelly, A. and Sillwood, J. M., "Long term strength of glass reinforced plastics in wet environment", in *Advances in Composite Materials*, ed. Bunsell, A. R. et al., Pergamon Press, Oxford, 1990, 556-568.

71. Wang, C. S. and Wang, A. S. D., "Creep behavior of glass-epoxy composite laminates under hygrothermal conditions", in *Advances in Composite Materials*, ed. Bunsell, A. R. et al., Pergamon Press, Oxford, 1990, 569-583.
72. Kellas, S., Morton, J. and Curtis, P., "The effect of hygrothermal environments upon the tensile and compressive strengths of notched CFRP laminates, Part 2: Fatigue loading", *Composites*, 21(1990), 52-62.
73. Singh, K. S., Singh, P. N. and Rao, R. M. V. G. K., "Hygrothermal effects on chopped fibre/woven fabric reinforced epoxy composites. Part B: Degradation studies", *J. Reinf. Plast. Compos.*, 10(1991), 457-462.
74. Chateauminois, A., Chabert, B., Soulier, J. P. and Vincent, L., "Hygrothermal ageing effects on the static fatigue of glass/epoxy composites", *Composites*, 24(1993), 547-555.
75. Komai, K., Shiroshita, S., Kinoshita, S. and Grenestedt, J., "Influence of water on tensile and fatigue strength of angle-ply aramid/epoxy composites", *J. Soc. Mater. Sci., Japan*, 38(1989), 1329-1335 (in Japanese).
76. Komai, K., Shiroshita, S. and Kinoshita, S., "Influence of water on fatigue strength under reversed tension and compression of aramid/epoxy composites", *J. Soc. Mater. Sci., Japan*, 39(1989), 341-346 (in Japanese).
77. Komai, K. and Shiroshita, S., "The influence of water and test frequency on the fatigue strength of aramid/epoxy composites", *J. Soc. Mater. Sci., Japan*, 41(1992), 1427-1433 (in Japanese).
78. Komai, K. and Shiroshita, S., "The influence of hot water on the fatigue strength of aramid/epoxy composites", *J. Soc. Mater. Sci., Japan*, 41(1992), 1539-1544 (in Japanese).
79. Heitman, R. E. and Lindstrom, R. S., "A method for predicting the strength degradation in an underground environment of polyester fiberglass laminates", *Proc. 19th Annual Meeting*, SPI(1964), 4-F:1-10.
80. Phillips, M. G., "Prediction of long-term stress-rupture life for glass fibre-reinforced polyester composites in air and in aqueous environments", *Composites*, 14(1983), 270-275.
81. Aveston, J. and Sillwood, J. M., "Prediction of long-term strength of glass-reinforced plastics in wet environments", *Trans. Inst. Mater. Eng. C. Conf.*, 97(1985), 143-147.
82. Chung, T. J. and Bradshaw, R. J.. "Irreversible hygrothermomechanical behavior and numerical analysis in anisotropic materials", *J. Compos. Mater.*, 15(1981), 502-520.
83. Flaggs, D. L. and Crossman, F. W., "Analysis of the viscoelastic response of composite laminates during hygrothermal exposure", in *Environmental Effects on Composite Materials, Vol.2*, ed. Springer, G. S., Technomic, Lancaster, 1984, 363-380.
84. Hirai., T., Katayama, T., Itoh, S., Inoguchi, H. and Araki, J., "Study on micro-interface of FRTP laminate made of fiberous thermoplastic resin and reinforcement strands in hot water environment", *J. Soc. Mater. Sci., Japan*, 39(1990), 989-995 (in Japanese).
85. Honzyo, T. and Nakanishi, Y., "Examination of deterioration behavior of carbon fiber-matrix interface owing to water absorption by torsional braid analysis", *J. Soc. Mater. Sci., Japan*, 40(1991), 464-469 (in Japanese).

86. Phani, K. K. and Bose, N. R., "Hydrothermal ageing of CSM-laminate during water immersion - an acousto-ultrasonic study", *J. Mater. Sci.*, 21(1986), 3633-3637.
87. Chang, F. K., Scott, R. A. and Springer, G. S., "Strength of mechanically fastened composite joints", *J. Compos. Mater.*, 16(1982), 470-494.
88. Chang, F. K., Scott, R. A. and Springer, G. S., "Failure of composite laminates containing pin loaded holes - Method of solution", *J. Compos. Mater.*, 18(1984), 255-278.
89. Chang, F. K., Scott, R. A. and Springer, G. S., "Design of composite laminates containing pin loaded holes", *J. Compos. Mater.*, 18(1984), 279-289.
90. Wilson, D. W. and Tsujimoto, Y., "On phenomenological failure criteria for composite bolted joint analysis", *Compos. Sci. Technol*, 26(1986), 283-305.
91. Serabian, S. M. and Oplinger, D. W., "An experimental and finite element investigation into the mechanical response of 0/90 pin-loaded laminates", *J. Compos. Mater.*, 21(1987), 631-649.
92. Swanson, S. R. and Burns, J. S., "Analysis of pin loading of carbon/epoxy plates", *Proc. 31st Int. SAMPE Symp.*, 1986, 1078-1086.
93. Agarwal, B. L., "Static strength of bolted joint in composite material", *AIAA Journal*, 18(1980), 1371-1375.
94. Smith, P. A. and Pascoe, K. J., "Fatigue of bolted joints in (0/90) CFRP laminates", *Compos. Sci. Technol.*, 29(1987), 45-69.
95. Marshall, I. H., Arnold, W. S., Wood, J. and Mousley, R. F., "Observations on bolted connections in composite structures", *Compos. Sci. Technol.*, 13(1989), 133-151.
96. Abd-El-Naby, S. F. M. and Hollaway, L., "The experimental behaviour of bolted joints in pultruded glass/polyester material. Part 1: Single-bolt joints", *Composites*, 24(1993), 531-538.
97. Kaji, A., Hamada, H., Maekawa, Z. and Nagamori, M., "Influence of temperature on the strength of FRP bolted joint", *Reinforced Plastics*, 30(1984), 429-437.
98. Norton, F. M., Hodgson, M. E. and Backwith, S. W., "Pinned, thick-wall composite carbon/epoxy joint behavior subjected to thermal and humidity exposure", *Proc. 31st Int. SAMPE Symp.*, 1986, 1820-1834.
99. Crank, J., *Mathematics of diffusion*, Oxford University Press, London, 1956.
100. *Fukugo zairyo handbook*, ed. Japan Society for Composite Materials, Nikkan Kogyo Shinbunsha, Tokyo, 1989.
101. Reifsnider, K. L. and Carman, G., "The micromechanics of damage evolution in composite material system," AMD-Vol.150, AD-Vol.32, *Damage mechanics in composites*, ASME, 1992, 1-11.
102. Renard, J. and Thionnet, A., "Meso-macro approach to predict the damage evolution of transverse cracking in laminated composite," AMD-Vol.150, AD-Vol.32, *Damage mechanics in composites*, ASME, 1992, 31-52.

103. Walker, K. P., Freed, A. D. and Jordan, E. H., "Accuracy of the generalized self-consistent method in modeling the elastic behavior of periodic composites," AMD-Vol.150, AD-Vol.32, *Damage mechanics in composites*, ASME, 1992, 107-131.
104. Ju, J. W. and Chen, T. M., "Effective moduli of elastic composites containing microcracks or microvoids," AMD-Vol.150, AD-Vol.32, *Damage mechanics in composites*, ASME, 1992, 181-190.
105. Gosz, M., Moran, B. and Achenbach, J. D., "Matrix cracking in transversely loaded fiber composites with compliant interphases," AMD-Vol.150, AD-Vol.32, *Damage mechanics in composites*, ASME, 1992, 133-140.
106. Hogg, P. J., "A model for stress corrosion crack growth in glass reinforced plastics", *Comp. Sci. Technol.*, 38, 1990, 23-42.
107. Kawamoto, K. and Ono, K., "Pattern recognition analysis of acoustic emission signals from carbon fiber/epoxy composites", *Proc. 3rd Int. Symp. Acoustic Emission from Composite Materials*, 1989, 230-239.
108. Yamaguchi, K., Oyaizu, H., Johkaji, J. and Kobayashi, Y., "Recognition on fracture modes and behavior in FRP by AE waveform-microdata", *Proc. 3rd Int. Symp. Acoustic Emission from Composite Materials*, 1989, 268-277.
109. Weng, T., Hiltner, A. and Baer, E., "Damage analysis in reinforced LCP composites by acoustic emission location techniques", *J. Compos. Mater.*, 24(1990), 103-121.
110. Chow, C. L., Xian, X. J. and Lam, J., "Experimental investigation and modelling of damage evolution/propagation in carbon/epoxy laminated composites", *Compos. Sci. Technol.*, 39(1990), 159-184.
111. Berthelot, J. M., "Relation between amplitudes and rupture mechanisms in composite materials", *J. Reinf. Plast. Compos.*, 7(1990), 284-299.
112. Berthelot, J. M. and Rhazi, J., "Acoustic emission in carbon fibre composites", *Compos. Sci. Technol.*, 37(1990), 411-428.
113. Faudree, M., Baer, E., Hiltner, A. and Collister, J., "Characterization of damage and fracture processes in short fiber BMC composites by acoustic emission", *J. Compos. Mater.*, 22(1988), 1170-1195.
114. Kau, C., Hiltner, A., Baer, E. and Huber, L., "Damage processes in reinforced reaction injection molded polyurethanes", *J. Reinf. Plast. Comp.*, 8(1989), 18-102.
115. "Standard guide for acoustic emission examination of fiberglass reinforced plastic resin (RP) tanks/vessels," *American Society for Testing Materials*, E-1067.
116. "Acoustic emission examination of fiber reinforced plastic vessels," Section V, Article 11, Boiler and Pressure Vessel Code, *American Society of Mechanical Engineers*.
117. Collings, T. A., "Experimentally determined strength of mechanically fastened joints", in *Joining fiber resinforced plastics*, ed. Matthews, F. L., Elsevier Applied Science, Essex, 1986.
118. Matthews, F. L., "Theoretical stress analysis of mechanically fastened joints". in *Joining fiber resinforced plastics*, ed. Matthews, F. L., Elsevier Applied Science, Essex, 1986.

119. Whitney, J. M. and Nuismer, R. J., "Stress fracture criteria for laminated composite containing stress concentration", *J. Compos. Mater.*, 8(1974), 253-265.
120. Yamada, S. E. and Sun, C. T., "Analysis of laminate strength and its distribution", *J. Compos. Mater.*, 12(1974), 275-284.

Nomenclatures

A_m	Moisture content
$A_m(0)$	Initial moisture content
$A_m(t)$	Moisture content after immersion
$A_m(\infty)$	Maximum moisture content
a_{0b}	Characteristic length in bearing
a_{0t}	Characteristic length in tension
c	Moisture concentration
c_0	Moisture concentration at surface of material
$c_{0\infty}$	Moisture concentration around material
c_i	Initial moisture concentration inside material
D	Damage accumulation in material
D	Diffusion coefficient
D_a	Apparent diffusion coefficient
D_F	Apparent diffusion coefficient for FRP
D_l	Diffusion coefficient for weight loss
D_{lF}	Diffusion coefficient for weight loss for FRP
D_{lR}	Diffusion coefficient for weight loss for resin part of FRP
D_R	Diffusion coefficient in resin part of FRP
D_S	Initial slope of weight loss vs $\sqrt{t}$
E_1	Longitudinal modulus of unidirectional lamina
E_2	Transverse modulus of unidirectional lamina
E_f	Elastic modulus of fiber
E_m	Elastic modulus of matrix
$\bar{E}$	Elastic modulus of randomly oriented FRP
F	Rate of transfer per unit area of section
G_{12}	Shear modulus of unidirectional lamina
G(t)	Ratio of amount of moisture at time t to at saturation
h	Thickness of material
M(0)	Initial weight gain
M(t)	Weight gain at immerssion t
$M(\infty)$	Weight gain at saturation
$M_a(t)$	Apparent weight gain for FRP after immerssion for time t
M_C	Constant in eqn(2.24)
$M_g(t)$	Net weight gain for FRP after immerssion for time t
$M_{gF}(t)$	Net weight gain for FRP in phase I and II
$M_{gF}(\infty)$	Net weight gain for FRP at saturation in phase I and II
$M_{gI}(t)$	Net weight gain of fiber/matrix interface after immersion for time t
$M_{gI}^{A}(t)$	Net weight gain of interface by water absorption

$M_{gI}^{P}(t)$	Net weight gain of interface by water penetration
M_{gI}	Weight gain related to M_I
$M_{gR}(t)$	Net weight gain of the resin part of FRP after immerssion for time t
$M_{gR}(\infty)$	Net weight gain of the resin part of FRP at saturation
$M_{gr}(t)$	Net weight gain for neat resin after immerssion for time t
$M_I(t)$	Weight loss for FRP after immerssion for time t
$M_I(\infty)$	Weight loss for FRP at saturation
$M_{IF}(t)$	Weight loss for FRP after immerssion for time t
$M_{IF}(\infty)$	Maximum weight loss for FRP
$M_{II}(t)$	Weight loss of fiber/matrix interface after immersion for time t
$M_{IR}(t)$	Weight loss of the resin part of FRP after immerssion for time t
$M_{IR}(\infty)$	Maximum weight loss of the resin part of FRP
$M_{Ir}(t)$	Weight loss for neat resin after immerssion for time t
P_b	Maximum load of bearing test
P_{nt}	Maximum load of notched specimen in tensile test
P	Damage parameter
Q_{11}, Q_{12}, Q_{22}, Q_{66}	Reduced stiffness of unidirectional lamina
$\overline{Q_{11}}$	Transformed reduced stiffness of unidirectional lamina
$r_c(\theta)$	Characteristic curve
t	Immersion time
t_0	Delay time of M_I
t_{0F}	Delay time of M_I for FRP
t_{0R}	Delay time of M_I for resin part of FRP
V_f	Fiber volume fraction in FRP
$W_d(t)$	Weight of dried FRP after immersion for time t
$W_{dr}(t)$	Weight of dried neat resin after immersion for time t
W_f	Fiber weight fraction in FRP
W_i	Initial material weight
$W_m(t)$	Weight of absorbed water
W_i	Initial material (FRP) weight
W_{ir}	Initial neat resin weightInitial material (FRP) weight
$W_w(t)$	Weight of wet FRP after immersion for time t
$W_{wr}(t)$	Weight of wet neat resin after immersion for time t
x	Space coordinate normal to section
ε_1, ε_2	Strain in longitudinal and transverse direction
γ_d	Density of dissolved matter
γ_w	Density of water (moisture)
ν_{12}	Poisson's ratio given by $-\varepsilon_2/\varepsilon_1$
ν_{21}	Poisson's ratio given by $-\varepsilon_1/\varepsilon_2$
σ_b	Bearing strength

σ_{nt}	Tensile strength of notched specimen in tensile test

Published Paper on This Thesis

Chapter 2

1. Morii, T., Tanimoto, T., Hamada, H., Maekawa, Z., Hirano, T. and Kiyosumi, K.
   "Weight changes of a randomly oriented GRP panel in hot water"
   Composites Science and Technology, Vol.49(1993), pp.209-216.

2. Morii, T., Hamada, H., Maekawa, Z., Tanimoto, T., Hirano, T. and Kiyosumi, K.
   "Weight change mechanism of randomly oriented GFRP panel immersed in hot water"
   Composite Structures, Vol.25(1993), pp.95-100.

Chapter 3

3. Morii, T., Hamada, H., Maekawa, Z., Tanimoto, T., Hirano, T., Kiyosumi, K. and Tsujii, T.
   "Weight changes of the fibre/matrix interface in GRP panels immersed in hot water"
   Composites Science and Technology, Vol.50(1994), pp.373-379.

Chapter 4

4. Morii, T., Tanimoto, T., Hamada, H., Maekawa, Z., Hirano, T. and Kiyosumi, K.
   "Relation between weight changes and bending properties of GFRP panel immersed in hot water"
   Polymers and Polymer Composites, Vol.1(1993), pp.37-44.

5. Hamada, H., Maekawa, Z., Morii, T., Tanimoto, T. and Yokoyama, A.
   "Damage mechanics on hydrothermal aged FRP"
   American Society for Testing and Materials, Special Technical Publication (submitted)

Chapter 5

6. Morii, T., Tanimoto, T., Hamada, H., Maekawa, Z., Hirano, T. and Kiyosumi, K.
   "Fracture and acoustic emission characteristics of glass fiber reinforced plastics panels for hot water"
   Polymer Composites, Vol.15(1994), pp.206-216.

Chapter 6

7. Hamada, H., Maekawa, Z., Hirano, T., Morii, T. and Haruna, K.
   "Hot water degradation of mechanically fastened GFRP joints"
   Transactions of the Japan Society of Mechanical Engineers, Vol.57(1991), pp.591-596.

8. Morii, T., Hamada, H., Maekawa, Z., Tanimoto, T., Hirano, T. and Haruna, K.
   "Degradation behavior of mechanically fastened joints of glass-reinforced cross-linked polyester immersed in hot water"
   Polymer Composites (in press)

Chapter 7

9. Morii, T., Tanimoto, T., Hamada, H. and Maekawa, Z.
   "Degradation behaviour of glass fibre reinforced polypropylene immersed in hot water"
   Polymers and Polymer Composites, Vol.1(1993), pp.175-182.

10. Morii, T., Hamada, H., Maekawa, Z. and Tanimoto, T.
    "Hydrothermal effects on mechanically fastened glass/polypropylene composite joint"
    Polymer Composites (in press)

Acknowledgment

The author would like to express his sincere appreciation and acknowledgment to Prof. Z. Maekawa and Dr. H. Hamada (Kyoto Institute of Technology) for their continuous guideline and encouragement throughout the conduct of this research. The author also would like to express his heartfelt thanks to Prof. T. Tanimoto (Shonan Institute of Technology) and Dr. A. Yokoyama (Mie University) for their valuable suggestions and helpful discussions concerning this study. The author would like to thank Prof. T. Matsuo and Prof. E. Jinen (Kyoto Institute of Technology) for their useful advice to improve the quality of this thesis. The author wishes to express his gratitude to Mr. T. Hirano and Mr. K. Kiyosumi (Sekisui Plant System Co., Ltd.) for their useful discussions and advice on all aspects of the present study. The author is very grateful to Mr. T. Tsujii (Perkin Elmer Japan Co., Ltd.), Mr. S. Mori and Mr. H. Ashida (ex-undergraduate students at Kyoto Institute of Technology), and Mr. N. Akasaka, Mr. S. Hayashi, Mr. H. Fujita and Mr. M. Narita (ex-undergraduate students at Shonan Institute of Technology) for their valuable supports to this research. Additional thanks are due to every one of the polymer mechanics laboratory at Kyoto Institute of Technology and of Tanimoto laboratory at Shonan Institute of Technology for their helpful supports.